

A Thesis Submitted for the Degree of PhD at the University of Warwick

Permanent WRAP URL:

<http://wrap.warwick.ac.uk/88438>

Copyright and reuse:

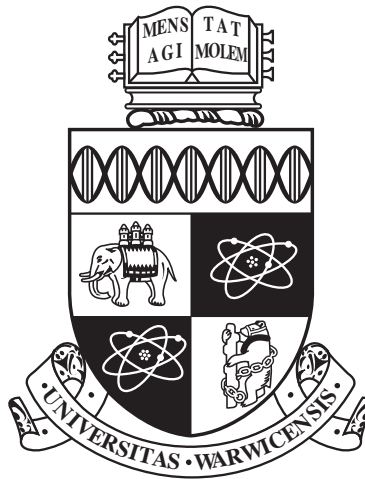
This thesis is made available online and is protected by original copyright.

Please scroll down to view the document itself.

Please refer to the repository record for this item for information to help you to cite it.

Our policy information is available from the repository home page.

For more information, please contact the WRAP Team at: wrap@warwick.ac.uk



**Turbulent skin-friction drag reduction control by
spanwise motion**

by

Qiang Yang

Thesis

Submitted to the University of Warwick

for the degree of

Doctor of Philosophy

School of Engineering

May 2016

THE UNIVERSITY OF
WARWICK

In memory of my grandfather.

Contents

List of Tables	iv
List of Figures	v
Acknowledgments	x
Declarations	xii
Abstract	xiii
Abbreviations	xiv
Chapter 1 Introduction	1
Chapter 2 Literature Review	4
2.1 Near wall turbulence dynamics	4
2.1.1 The law of wall	4
2.1.2 Near wall coherent structures	4
2.1.3 Very large scales motions	6
2.1.4 Inner-outer interaction	8
2.1.5 Self-sustained process	9
2.2 3D turbulent boundary layer	11
2.3 Turbulent drag reduction control	12
2.3.1 Spanwise wall oscillation	13
2.3.2 Lorentz force actuators	19
2.3.3 DBD plasma actuators	20
2.3.4 Reynolds number effect	23
Chapter 3 Methodology	28
3.1 Fully implicit frictional step method	29

3.2	Coherent structure identification	36
3.3	Proper orthogonal decomposition	39
3.4	Grid resolution and domain size test	44
3.4.1	No control baseline cases study	44
3.4.2	Control baseline cases study	50
Chapter 4	Drag Reduction by Spanwise Wall Oscillation	56
4.1	Uni-direction wall motion	57
4.2	Spanwise wall oscillation	66
4.2.1	Turbulence statistics	68
4.2.2	Stokes layer	71
4.2.3	Phase modulation	75
4.2.4	Streaks variation	80
4.3	Conclusions	86
Chapter 5	Drag Reduction by spanwise Lorentz Force	88
5.1	Lorentz force model	89
5.2	Wave configurations	91
5.3	Preliminary study	93
5.3.1	Effect of force parameters	93
5.3.2	Oblique oscillation	93
5.3.3	Spatial transient response	95
5.4	Oblique travelling waves	99
5.5	Streamwise and spanwise travelling waves	103
5.5.1	\mathcal{DR} maps	103
5.5.2	Power budget	108
5.5.3	Lorentz force induced Stokes layer	110
5.5.4	Statistics and spectra	115
5.5.5	λ_2 structures	118
5.6	Conclusions	122
Chapter 6	Drag Reduction by DBD Plasma Actuators	124
6.1	Plasma actuator model and its validation	124
6.2	Multiple actuators	130
6.3	Travelling wave configurations	133
6.4	Drag reduction maps	139
6.5	Turbulence statistics	146
6.6	Effect of flow symmetry	153

6.7	The application	154
6.8	Conclusion	157
Chapter 7	Influence of the VLSMs at High Reynolds Numbers	159
7.1	Reynolds number effect	160
7.2	Some further observations from the literature	163
7.2.1	VLSMs definition and visualisation	163
7.2.2	Wavenumber and convection velocity modulation	167
7.2.3	Phase modulation in Stokes layer	170
7.3	Change in the \mathcal{DR} map	173
7.3.1	Wall shear stress spectra	173
7.3.2	\mathcal{DR} deterioration rate	174
7.3.3	Influence of the superimposition effect	177
7.3.4	Influence of the modulation effect	182
7.4	Conclusions	186
Chapter 8	Conclusions and Future Works	187
8.1	Conclusions	187
8.2	Future works	189
Appendix A	Estimation of flight Reynolds number	191
Appendix B	Density spectra	192
Appendix C	\mathcal{DR} asymptotic at $\omega = 0$ ($T = \infty$)	194
Appendix D		196
Appendix E	Analytical solution for the Laminar LGSL	198
Appendix F	Parameter selection for starting vortex comparison	201
Appendix G	Validation of the VLSMs definition	203
Appendix H	Uncertainty quantification for VLSMs statistics	205
Appendix I	Derivation of FIK for each wave component	207

List of Tables

2.1	Travelling wave forms in literature.	14
2.2	Assumptions to evaluate the plasma body force in PIV	23
3.1	Contributions to turbulent kinetic energy k from different POD modes.	42
3.2	Grid resolution and domain size used in literature.	45
3.3	Tested grid resolutions in x , y and z directions separately	46
3.4	Final grid resolution and domain size for the four Reynolds numbers	50
3.5	Grid resolution and domain size test for flow controls	55
4.1	Drag reduction mechanisms by spanwise wall oscillation in literature.	58
5.1	Travelling wave of Lorentz force studied in the literature.	92
5.2	Main case parameters with $A_f = 0.5$, $\Delta^+ = 10$	105
6.1	Configurations for ST and SO	139
6.2	Energy budget estimation for control † in wind and water tunnels.	147
7.1	Conditioned wall shear stress, $\overline{\tau_w}$ and relative drag reduction, \mathcal{DR}	184
C.1	$\mathcal{DR}(\phi)$ in the first 1/4 period at $A_w^+ = 12$	195
H.1	Wall shear stress statistics from different sample lengths.	206

List of Figures

2.1	Near wall streaks at $y^+ = 9.6$ visualised by hydrogen bubbles	6
2.2	(a) Ensemble averaged coherent structures (Jeong et al., 1997); . . .	7
2.3	Inner-outer interaction, taken from Marusic et al. (2010).	9
2.4	A schematic of the three dimensional turbulent boundary layers . . .	11
2.5	Spanwise oscillation by plasma actuators at four different phases . .	24
3.1	Sketch of the geometry and coordinate of a channel flow	29
3.2	Structure of matrix \mathbf{A}	34
3.3	A typical identified λ_2 structure	37
3.4	Ensemble averaged λ_2 structures ($\lambda_2^+ = -0.005$)	38
3.5	Patterns of Reynolds stresses in a yz plane ($x = 0$)	40
3.6	Skin-friction associated with: (a) positive λ_2 structure	40
3.7	The first four POD modes for velocity fluctuations, u' , v' , w'	43
3.8	The characteristic eddy identified in CH200 case	44
3.9	Comparison of turbulent statistics between present baseline case . .	45
3.10	Sensitivity of calculated friction Reynolds number Re_τ	47
3.11	Sensitivity of statistics peak values to grid resolutions	47
3.12	Comparison of two dimensional pre-multiplied density spectra	48
3.13	Comparison of one dimensional accumulated density spectra	49
3.14	Turbulent kinetic energy k budgets comparison	51
3.15	Comparison of two dimensional pre-multiplied density spectra	52
3.16	Time history of skin-friction for three types of flow control cases . .	53
4.1	Schematics of skin-friction control by spanwise wall velocity.	57
4.2	Time history of skin-friction coefficient C_f for uni-direction	59
4.3	Turbulent kinetic and enstrophy profiles during the transient	60
4.4	Streamwise and spanwise production terms profiles during the transient	60
4.5	One-dimensional pre-multiplied streamwise spectra for UA12O	61
4.6	Ensemble averaged (a) positive and (b) negative λ_2 structures	62

4.7	Transient time history for skin-friction, turbulent kinetic energy . . .	63
4.8	Drag increase for different spanwise wall moving velocities	64
4.9	Spanwise mean velocity profiles for different spanwise	65
4.10	Comparison of the Reynolds stress profiles	66
4.11	Ensemble averaged positive (yellow) and negative (red) λ_2 structures	66
4.12	Skin-friction coefficient C_f time history for spanwise wall oscillation	67
4.13	\mathcal{DR} asymptotic for spanwise wall oscillation at $Re_\tau = 200$, $A_w^+ = 12$.	69
4.14	Turbulence statistics at four oscillation frequencies	70
4.15	Comparison of the Stokes layers between the laminar and turbulent .	72
4.16	Phase variation of $\partial \widetilde{v'w'}^+ / \partial y^+$, ordered as in figure 4.15.	72
4.17	Comparison between turbulent and laminar Stokes layers	73
4.18	Drag reduction \mathcal{DR} against Stokes layer thickness δ^+	74
4.19	Ensemble averaged λ_2 structure changes at 16 equally separated phases	76
4.20	The measured properties from ensemble averaged	77
4.21	Ensemble averaged λ_2 structures in lower wall region	78
4.22	Phase modulation in Reynolds shear stress $-\widetilde{u'v'}$	79
4.23	Phase variation for $\omega^+ = 0.03$ ($T^+ = 209$)	80
4.24	Streamwise velocity fluctuation u' from instantaneous flow fields . .	82
4.25	The characteristic eddies variation at 16 equally separated phases . .	83
4.26	Variation of different angles at $y^+ = 10$ during one oscillation period	84
4.27	Streaks angles as a function of oscillation frequency (period)	85
4.28	\mathcal{DR} as a function of (a) streaks angles γ ; and (b) normalised	86
5.1	Schematics of skin-friction control by travelling wave	89
5.2	Wave configurations for: (a) oblique oscillation with an angle γ . . .	94
5.3	Effect on drag reduction \mathcal{DR} from (a) Lorentz force strength A_f . .	95
5.4	Effect of oscillating Lorentz force direction γ	96
5.5	Near wall streaks at $y^+ \approx 5$	96
5.6	Skin-friction coefficient C_f distribution along streamwise direction .	97
5.7	Spatial response of normalised Skin-friction coefficient $C_f/C_{f,0}$. . .	98
5.8	Instantaneous flow field visualisation around the trailing edge	99
5.9	Instantaneous velocity magnitude $\sqrt{u^2 + v^2 + w^2}$ at $y^+ \approx 5$	101
5.10	\mathcal{DR} against travelling wave angle θ for oblique travelling waves . . .	102
5.11	Turbulence statistics in transformed coordinate	103
5.12	Drag reduction maps for (a) streamwise travelling wave	104
5.13	Drag reduction for (a) spanwise oscillation cases	106
5.14	\mathcal{DR} comparison for travelling wave cases	107

5.15	Power calculation for the laminar case in figure 5.18	109
5.16	Power spent (P_{sp}) maps	109
5.17	Net energy saving (P_{net}) mapsse	111
5.18	(a) Spanwise mean velocity profiles for OC case	112
5.19	Spanwise mean velocity profiles for travelling wave cases.	113
5.20	δ^+ maps for: (a) streamwise travelling wave	114
5.21	\mathcal{DR} against δ^+ for both streamwise and spanwise travelling waves	114
5.22	R.m.s. of the velocity and vorticity fluctuations comparison	116
5.23	R.m.s. of vorticity fluctuations for FST	117
5.24	2D and 1D pre-multiplied streamwise velocity spectra $k_x k_z E_{uu}$	117
5.25	One-dimensional pre-multiplied spectra over the half channel	118
5.26	Conditional averaged positive λ_2 structure	120
5.27	End view of the characteristic eddy	120
5.28	Conditional averaged positive and negative λ_2 structures	121
5.29	Correlation between \mathcal{DR} with the structure tilting angles	122
6.1	Schematics of skin-friction control by plasma actuators	125
6.2	Schematics of a DBD plasma actuator viewed from a cross section	127
6.3	Plasma body force distribution of a single DBD plasma actuator	128
6.4	Horizontal velocity contour u	130
6.5	Vorticity field (contour) and velocity vectors for the starting vortex	131
6.6	Starting vortices at the leading edge of the plasma actuators	132
6.7	Spatial evolution of the starting vortex core	133
6.8	Time history of skin-friction coefficient C_f for different	134
6.9	DBD plasma actuators configurations for (a) spanwise travelling wave	135
6.10	Time variation for: (a) voltage; and (b) plasma body force	136
6.11	Comparing simulation results with three different step functions	137
6.12	Effect of duty cycle \mathcal{D} for spanwise oscillation	137
6.13	Spectrum and the first two most energetic Fourier modes	139
6.14	Drag reduction maps	140
6.15	Time history of skin-friction coefficient C_f for ST1	141
6.16	Vortical structures in SO3 case at $\phi = 0, \pi/2, \pi, 3\pi/2$	143
6.17	Drag reduction \mathcal{DR} against the oscillation frequency ω^+	143
6.18	Power spent (P_{sp}) maps for (a) ST1; (b) SO1; and (c) SO4.	144
6.19	Net energy saving, P_{net} maps for (a) ST1; (b) SO1; and (c) SO4.	145
6.20	\mathcal{DR} against P_{sp} at $\omega^+ \approx 0.06$ ($T^+ \approx 105$) comparison among	146
6.21	Streamwise mean velocity profiles comparison	148

6.22	Two-dimensional streamwise velocity contour	148
6.23	Comparison between no control and control cases	149
6.24	2D pre-multiplied spectra $k_x k_z \Phi_{uv}$ for no control case, ST1 and SO4	150
6.25	Pre-multiplied 1D energy spectra (a) $k_x \Phi_{uv}$ and (b) $k_z \Phi_{uv}$	150
6.26	Correlation R_{uu} , R_{vv} and R_{uv}	151
6.27	Correlation R_{uu} , R_{vv} and R_{uv} for SO4 at $y^+ = 20$	152
6.28	Structure angles for R_{uu} (line with upper triangles), R_{vv}	152
6.29	Drag reduction dependency on the body force penetration depth Δ^+	154
6.30	The spanwise mean velocity profiles for steady body force cases	155
6.31	(a) Schematics of operation mode with two groups of DBD	156
6.32	A concept of implementing DBD plasma actuators on a car body	157
7.1	\mathcal{DR} deterioration at high Reynolds numbers	160
7.2	Schematics of skin-friction control by streamwise travelling wave	161
7.3	Drag reduction map at $Re_\tau = 800$	162
7.4	Drag reduction at four Reynolds numbers	163
7.5	A 3D graphic view of (a) the near wall small scale structures	165
7.6	Instantaneous streamwise velocity fluctuation contour	166
7.7	The characteristic eddy in the yz plane	166
7.8	Wall shear stress fluctuation for (a) no control case	167
7.9	(a) Instantaneous view of the small scales under SS_P and SS_N	168
7.10	Wavenumber-frequency spectra of wall shear stress fluctuation	169
7.11	Schematics of modulation effects from VLSMs	170
7.12	Conditional averaged small scale wall shear stress fluctuation	171
7.13	Instantaneous near wall λ_2 structures	171
7.14	Conditional averaged near wall quasi-streamwise vortices	172
7.15	Conditioned spanwise mean velocity for spanwise wall oscillation	173
7.16	2D pre-multiplied spectra for (a) wall shear stress fluctuation	175
7.17	\mathcal{DR} contribution from the inner and outer regions	176
7.18	Mean wall shear stress contribution from spanwise length scales	176
7.19	(a) Pre-multiplied spectra for mean wall shear stress $\overline{\tau_w}$	177
7.20	1D pre-multiplied spectra for wall shear stress fluctuation	178
7.21	Same as in figure 7.20, but for streamwise wavelength, λ_x^+	179
7.22	Maps for wall shear stress fluctuation reduction	180
7.23	Wavelength dependent convection velocity of τ'_w	181
7.24	Correlation between drag reduction \mathcal{DR} and wall shear stress r.m.s.	182
7.25	The probability density function of the VLSMs	183

7.26	Reduction rate maps for mean wall shear stress $\overline{\tau_w}$	185
D.1	Ensemble averaged λ_2 structures at 8 equally separated phases . . .	196
D.2	The characteristic eddies changes in the first half period	197
F.1	Comparison of the starting vortex	202
G.1	Streamwise velocity fluctuation, u' contour at $y^+ = 15$, $Re_\tau = 1600$.	203
G.2	Comparison of the decomposed streamwise velocity profiles	204
H.1	Typical time history of C_f , with the wall shear stress	205
H.2	Reproducing (a) figure 7.22(b); (b) figure 7.26(a)	206

Acknowledgments

Fist of all, I sincerely thank my PhD supervisor, Professor Yongmann M. Chung for guiding me into the turbulence world. He always uses vivid examples to explain complex turbulent phenomena, making the discussion so fruitful. I enjoyed the tea time with him for some casual discussions. Thank him for giving me all the freedom to explore the research points I was interested in during the late stage of my PhD. I admire his research attitude: always calm, cautious and motivated; I appreciate the spiritual, material and financial helps he offered to me whenever in need. Thank him for the understanding and supports in my struggling time.

My thanks also goes to my co-supervisor, Professor Duncan Lockerby for offering me the PhD position at the first instance. I like his smartness and humour. Particularly, I enjoyed the Wales hiking experience with him, and other fluid group members. In the mean time, I thank my master supervisor Professor Jin Zhou at the National University of Defence Technology for encouraging me to come abroad for my PhD study, helping me get such an opportunity, and providing me supports during the whole journey.

Then I would like to thank those people who provided me endless help during my PhD life in UK: Edward Hurst, who guided me from English language to his spanwise travelling wave control research; Jenny and Steve Arnold, who kindly let me enjoy their cosy house during my whole PhD study; our FATNODE dinner group members: Julia Choe, Jasmine Desmond, Chimie Gamot, Yuanwei Xu, Aaron Finney, Chinedu Nwaigwe and Salvatore Cosseddu, for the good food and happy moment we had together; my officemates: Carlos Duque-Daza, Tony Wang, Minsuok Kim, Ashwin Rajan, Iresha Atthanayake, Max Grabner and Toon Sirilapanan, for

the research discussion and help in every detail; CSC secretary Vida Glanville, for the delicious cookies and cakes every Friday; CSC technician Olav Smorholm, for the assistant on Paraview installation on Minerva, making figure 7.5 possible; Professor Kwing-So Choi for providing the PIV data in figure 6.4 for our DBD plasma actuator model development.

I particularly benefited from the lunch seminar at Centre for Scientific Computing and the fluid seminar at School of Engineering. Thanks for the organisers and all the speakers. Without the scholarship from China Scholarship Council and the University of Warwick, none of the above could happen, thanks!

Last, but not least, I would like to thank my parents and other family members for keeping supporting me to be focusing on my PhD study. For my loved grandpa, I will always be feeling sorry for not being able to see him in the last moment.

Declarations

This thesis, and the materials in it, is my own work. It has not been submitted for a degree at any other university. As part of the work carried out, the work was presented at the following conferences:

Q. Yang and Y. M. Chung. Large-scale structure in skin friction drag reduction by a spanwise wall oscillation. In *UK Turbulence Consortium*, 22-23 September, London, U.K., 2014.

Q. Yang and Y. M. Chung. Numerical study of reducing turbulent skin-friction drag using DBD plasma actuators. In *European Drag Reduction and Flow Control Meeting*, 23-26 March, Cambridge, U.K., 2015a.

Q. Yang and Y. M. Chung. Turbulent skin-friction drag reduction by travelling waves induced by spanwise Lorentz force. In *European Turbulence Conference 15*, 25-28 August, Delft, The Netherlands, 2015b.

Q. Yang and Y. M. Chung. Influence of VLSTMs in drag reduction by streamwise travelling wave of spanwise wall velocity. In *UK Turbulence Consortium*, 3-4 September, Southampton, U.K., 2015c.

Abstract

Three types of actuators, *i.e.*, oscillating walls, Lorentz force actuators and DBD plasma actuators, were used to actively control turbulent boundary layer for the turbulent skin-friction drag reduction with Direct Numerical Simulations. The main object is to understand drag reduction mechanism in simple spanwise wall oscillation case (Jung et al., 1992), then implement the control using more practical Lorentz force actuators and plasma actuators. A large amount of $40 \pm 2\%$, $30 \pm 2\%$ and $20 \pm 2\%$ drag reduction was observed at $Re_\tau = 200$ turbulent channel for oscillating walls, Lorentz force actuators and plasma actuators, respectively. Different configurations for Lorentz force and plasma actuators were intensively studied, with a new configuration proposed for DBD plasma actuators. The present study suggests a good prospective of skin-friction drag reduction by using Lorentz force actuators for ocean transportation, and DBD plasma actuators for land and air transportation. However, no net energy saving was obtained for both actuators considering the fluid power required for flow control, and this situation was even worse if the electric efficiency of the actuators was accounted for. For all three types of actuators, the interaction between the actuators and the near wall turbulent structure is presented using ensemble averaged method. DNS control cases were also performed at moderate Reynolds numbers, *i.e.*, $Re_\tau = 800$ and 1600 , to understand the role of recently discovered very large scale motions (VLSMs). The result suggests that the control of the VLSMs in the outer region is necessary for maximising drag reduction at high Reynolds number turbulent flows.

Abbreviations

ρ	fluid density
μ	dynamics viscosity
ν	kinematic viscosity
x, y, z	Cartesian coordinate for streamwise, wall normal and spanwise directions
u, v, w	velocity component for x, y, z directions
U, V, W	mean velocity component for x, y, z directions
L_x, L_y, L_z	domain size in x, y, z directions
N_x, N_y, N_z	total grid points in x, y, z directions
t	time
Δt	time step size
$\Delta x, \Delta y, \Delta z$	grid resolution in x, y, z directions
δ_{99}	boundary layer thickness
δ_θ	boundary layer momentum thickness
h	half channel height
R, D	pipe radius, diameter
δ	h or R or δ_{99}
τ_w	wall shear stress
u_τ	friction velocity, $\tau_w = \sqrt{\frac{\tau_w}{\rho}}$
U_m	bulk mean velocity
U_c	centreline velocity for channel and pipe

U_∞ free streamwise velocity for boundary layer
 C_f skin friction coefficient, $C_f = \frac{\tau_w}{\frac{1}{2}\rho U_m^2}$
 k turbulent kinetic energy, $k = u'^2 + v'^2 + w'^2$
 Re bulk Reynold number, $Re = U_m \delta / \nu$
 Re_τ friction Reynolds number, $Re_\tau = u_\tau \delta / \nu$
 Re_{cr} critical Reynolds number
 δ_ν viscous length scale
 y^+ coordinate non-dimensionalised by wall unit, $y^+ = y / \delta_\nu$
 u^+ velocity non-dimensionalised by wall unit, $u^+ = u / u_\tau$
 t^+ time non-dimensionalised by wall unit, $t^+ = u / (\delta_\nu / u_\tau)$
 \mathcal{U}_c convection velocity
 k_x, k_z wavenumber in x, z directions
 λ_x, λ_z wave length in x, z directions
 ω angular frequency
 γ_s mean velocity angle, $\gamma_s = \tan^{-1}(W/U)$
 γ_τ shear stress angle, $\gamma_\tau = \tan^{-1}(\overline{uv}/\overline{vw})$
 γ_g shear stress angle, $\gamma_g = \tan^{-1}(d\overline{U}/dy/d\overline{W}/dy)$
 a_1 structure parameter, $a_1 = (\overline{uv} + \overline{vw} + \overline{uw}) / (\overline{u_2} + \overline{v_2} + \overline{w_2})$
 A_w amplitude of spanwise wall velocity
 A_f amplitude of Lorentz force (or plasma force) strength
 \mathbf{E} electric field
 ρ_c charge density distribution
 \mathcal{DR} drag reduction
 \mathcal{DI} drag increase
 P_{sp} power spent
 P_{net} net energy saving
DNS Direct Numerical Simulation

LES Large-eddy Simulation
PIV Particle Image Velocimetry
CS Coherent Structures
LSM Large Scale Motion
VLSM Very Large Scale Motion
POD Proper Orthogonal Decomposition
DBD Dielectric Barrier Discharge
LGSL Lorentz force Generated Stokes Layer
PGSL Plasma actuators Generated Stokes Layer

Chapter 1

Introduction

The fluid flow settles down at two states, *i.e.*, laminar or turbulent, depending on whether a non-dimensionalised number, known as Reynolds number (Reynolds, 1883), is below or above a critical value, Re_{cr} . One big difference between the two flow states is the higher skin-friction associated with turbulent state at the same mass flow rate. This is due to the thin turbulent boundary layer (Prandtl, 1925), where the streamwise velocity profile is much steeper. If we can reduce the turbulent drag, it will bring a huge economical and environmental impact. “A 1% reduction in drag on a jet airliner in cruise conditions translates roughly to a 0.75% reduction in fuel consumption, implying a potential reduction in emitted CO_2 of nine million tonnes per 1% drag reduction” (Leschziner et al., 2011). “A 1% drag decrease corresponds approximately, to a 5 ~ 10% increase in payload” (Bushnell, 2003).

There are two types of drags in turbulent flow, *i.e.*, skin-friction drag due to viscosity, and pressure drag due to interference, roughness, lift, shock wave. The latter drag is important when the turbulent flow has regions with flow separations. For the modern streamline airliner in cruising condition, about 60% of the total drag comes from the skin-friction drag. Many different methods have been proposed to reduce turbulent skin-friction. Based on whether the control needs energy input or not, they can be categorized into passive and active controls. Active drag reduction methods can achieve higher drag reduction if the energy input is not considered, thus they are more attractive. For instance, spanwise wall oscillation can achieve as much as 40% drag reduction at low Reynolds number (Jung et al., 1992; Baron and Quadrio, 1996; Choi and Graham, 1998). The drag reduction achievable by passive control, such as riblets, is typically around 7 ~ 8% (García-Mayoral and Jiménez, 2011a,b). All the drag reduction control methods also suffer from their

own drawbacks. For example, the space size for riblets and the hole size for blowing and suction are scaled in wall units. At flight Reynolds number, the viscous length scale is extremely small, $O(1\mu m)$ (see appendix A for the estimation), and this makes the design of these control devices very difficult. Moreover, the riblet valley and the blowing and suction holes can be easily filled by dusts in such a small scale, which can significantly deteriorate the control efficiency.

Spanwise wall oscillation is a prospective drag reduction control method, because it does not need small scale surface sensors or actuators on the wall. Some smart wall surfaces are under design in the laboratory (Gatti et al., 2015a; Bird et al., 2015). However, for an optimal drag reduction by spanwise wall oscillation, the wall needs to oscillate at a very high frequency, and this is still a challenge for the mechanical structure. Thanks to the electrical devices, like Lorentz force actuators and plasma actuators, they bring an alternative way to create spanwise wall oscillation. Lorentz force actuators requires the fluid to be electric conductive, thus they are ideal for transportations in the ocean; while plasma actuators need to ionize the fluid first, thus they are suitable for transportation on the land and in the air.

Even though some experiments and numerical simulations have been conducted to investigate the drag reduction by using Lorentz force actuators and plasma actuators (Berger et al., 2000; Choi et al., 2011), there are two questions remaining unclear: 1) What is the whole picture of drag reduction by travelling wave of Lorentz force in a three dimensional wavenumber-frequency space, *i.e.*, $k_x - k_z - \omega$? 2) How should we configure the plasma actuators to achieve skin-friction drag reduction? These are the focus of the current work in order to take spanwise wall oscillation drag reduction control from laboratory to engineering applications. Apart from the implication, another two questions associated with spanwise wall oscillation itself are also needed to be addressed: 1) What is the drag reduction mechanism for spanwise wall oscillation? 2) Why does the drag reduction deteriorate when the Reynolds number goes high? A better understanding about these two questions is directly linked to whether we can successfully apply the skin-friction drag reduction control by Lorentz force and plasma actuators to our ships, land vehicles and aircrafts.

With these four key questions in mind, the thesis is organised as follows: Chapter 2 is a literature survey about the current state-of-the-art in turbulent flow and its skin-friction drag reduction controls. Chapter 3 introduces the numerical scheme and analysis methods used for the DNS datasets. Chapter 4 focuses on the drag reduction mechanism of spanwise wall oscillation from structures' point of view. Chapter 5 is a systematic study of turbulent skin-friction drag reduction by

Lorentz force actuators and explores the whole drag reduction picture in a three dimensional parameter space, *i.e.*, $k_x - k_z - \omega$ for a variety of travelling waves. Chapter 6 explores six different configurations of plasma actuators for turbulent skin-friction drag reduction, and demonstrates the successful way to achieve skin-friction drag reduction. Chapter 7 studies the Reynolds number effect in spanwise wall oscillation at the highest Reynolds number, *i.e.*, $Re_\tau = 1600$, with a particular emphasize on the role of the very large scale motions. Chapter 8 summarises the works done in this study and gives the suggestions for the future works.

Chapter 2

Literature Review

2.1 Near wall turbulence dynamics

2.1.1 The law of wall

Channel, pipe and boundary layer flows are three canonical wall bounded turbulent flows. They are comparable to each other at the same Reynolds number when the proper flow characteristic scales are chosen for reference. Based on the law of the wall, wall turbulent flow can be divided into an inner region and an outer region. In the inner region, viscosity dominates, so the flow is scaled in the viscous length scale, *i.e.*, $\delta_\nu = \nu/u_\tau$, where, u_τ is the friction velocity. This layer contains a viscous sublayer ($y^+ < 5$, superscript $+$ indicates the scaling using wall units) and a buffer layer $5 < y^+ < 30$. The outer region is dominated by the inertia of the flow, and the effect of the viscosity is negligible, thus the flow is scaled in the outer unit, δ (half channel height h , pipe radius R , or boundary layer thickness δ_{99}) (Von Kármán, 1930). The overlap region between the inner and the outer regions needs to satisfy both the scaling laws, and this leads the streamwise mean velocity profile to be logarithmic, *i.e.*, $u^+ = \frac{1}{\kappa} \ln y^+ + B$, where κ is the von Kármán constant and B is another constant. For the turbulent boundary layer, there is a wake region beyond the logarithmic region, and the velocity-defect law is applied, *i.e.*, $\frac{U_\infty - U}{u_\tau} = \frac{1}{\kappa} \left\{ -\ln \left(\frac{y}{\delta} \right) + 2\Pi \left[1 - \sin^2 \left(\frac{\pi y}{2\delta} \right) \right] \right\}$, where U_∞ is the free stream velocity, and Π is the wake strength parameter (Coles, 1956).

2.1.2 Near wall coherent structures

After Kline et al. (1967) found the near wall high- and low-speed streaks (figure 2.1), the structures' view of the turbulent flow started to form. Kline et al. (1967) found the average spanwise spacing of the streaks was fixed in wall units, *i.e.*, $\lambda_z^+ \approx 100$,

which was also confirmed in the later DNS study (Kim et al., 1987). These near wall streaks were found to be responsible for the production of the new turbulence and the transport of the turbulence within the boundary layer. This effect was studied through the quadrant analysis of the streamwise Reynolds shear stress, $-u'v'$ by Lu and Willmarth (1973). They divided $-u'v'$ into four quadrant events based on the sign of u' and v' , and showed that the ejection event (Q2) contributes to 77% of $-u'v'$. Bogard and Tiederman (1986) compared different burst-detection algorithms, and found that the quadrant technique was the most effective. Blackwelder and Eckelmann (1979) showed that these bursting phenomena were associated with pairs of counter-rotating quasi-streamwise vortices in the boundary layer based on the hot-film measured statistics. Head and Bandyopadhyay (1981) used the smoke visualisation to show the vortical structures in different regions of the turbulent boundary layer. They identified horseshoe vortices or vortex loops in the low Reynolds number region and vortex pairs or hairpins in the high Reynolds number region. More varieties of the vortical structures were named in the literature, such as, hairpin eddies, pancake eddies, surfboard eddies, typical eddies, vortex rings, mushroom eddies, arrowhead eddies (Jeong et al., 1997). Generally, they all refer to the same type of coherent structure with different forms. A nice review about these coherent structures was given by Robinson (1991). Unfortunately, there is no such a general definition of the coherent structure. Below was one used by Robinson (1991):

“It is a three-dimensional region of the flow over which at least one fundamental flow variable (velocity component, density, temperature, etc.) exhibits significant correlation with itself or with another variable over a range of space and/or time that is significantly larger than the smallest scales of the flow.”

DNS provides an ideal tool to study the coherent structures in the turbulent flow, due to the availability of the high accurate 3D flow fields (Kim et al., 1987). With the visualisation technique, Zhou et al. (1999) successfully identified the symmetrical hairpin type structure, which had two legs, connecting with the head through the two necks. Jeong et al. (1997) proposed an education method to get the ensemble averaged hairpin structure through “the forest of hairpins” (Wu and Moin, 2009) in a fully developed turbulent channel flow. And they identified that the general shape of the coherent structures in the near wall region ($y^+ < 60$) was two highly elongated counter-rotating quasi-streamwise vortices, which were reminiscent of the legs of the hairpin structures. Jeong et al. (1997) showed that the positive (clockwise rotating) and the negative (anti-clockwise rotating) quasi-streamwise vortices were inclined in the xy plan with an angle of 9° and tilted in

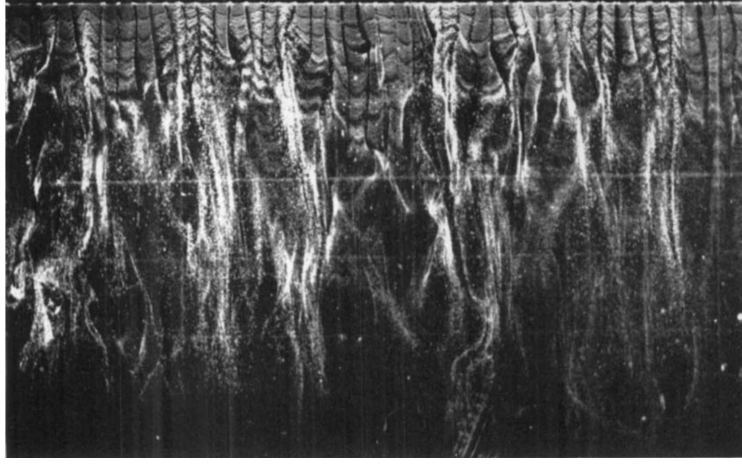


Figure 2.1: Near wall streaks at $y^+ = 9.6$ visualised by hydrogen bubbles, taken from Kline et al. (1967).

the xz plane with angles of $\mp 4^\circ$, respectively. The positive and the negative quasi-streamwise vortices had a diameter of around 25 in wall units, and extended to around 200 wall units in length. Both of them generated the sweep on one side and the ejection on the other side, and they were stagger arranged in the flow, thus forming very long high- and low-speed streaks, typically 1000 in wall units (figure 2.2(a)). This conceptual model is consistent with the exact coherent structure (or the travelling wave solution to the Navier-Stokes equations (Waleffe, 2001) shown in figure 2.2(b)), and it shed some light on many turbulent phenomena, such as the length scale of the low-speed streaks, the quadrant events of the streamwise Reynolds shear stress, the energy transferring in the buffer layer *etc.* (Jeong et al., 1997). The quasi-streamwise vortices acted as engines in the buffer layer to extract energy from the mean flow and dissipate it close to the wall. Kravchenko et al. (1993), Orlandi and Jiménez (1994), Solbakken and Andersson (2004) and Ge et al. (2011) showed that the quasi-streamwise vortices were the origin of the high skin-friction in the turbulent boundary layer. Adrian et al. (2000) found that 2 \sim 3 individual hairpin structures could form hairpin packets. This “bottom-up” model gave a nice explanation about the turbulent bulge (Head and Bandyopadhyay, 1981) and the uniform momentum zone (Meinhart and Adrian, 1995) in the outer region.

2.1.3 Very large scales motions

The very large scale motions (VLSMs) are the third scale apart from the near wall streaks ($\lambda_x^+ \approx O(10^3)$) and the turbulent bulges (or large scale motions (LSMs), $\lambda_x \approx O(2\delta \sim 3\delta)$). The VLSMs can typically reach $\lambda_x \approx 10\delta$ long. They were

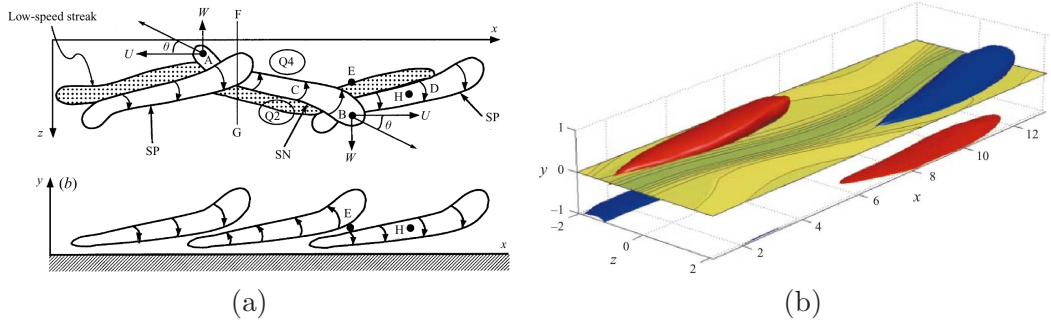


Figure 2.2: (a) Ensemble averaged coherent structures (Jeong et al., 1997); and (b) exact coherent structures (Waleffe, 2001).

first observed by Kim and Adrian (1999) in a turbulent pipe flow with the Reynolds number, $Re_\tau = 3175$. A bi-mode pattern was found in the 1D pre-multiplied energy spectrum for the streamwise velocity fluctuation. The peak in the high wavenumber end (also known as an inner peak) was well understood, which was associated with the near wall cycle; while the peak in the low wavenumber end (also known as an outer peak) was associated with much larger length scales. Kim and Adrian (1999) found that the longest VLSMs exceeded 14 pipe radii. Jiménez (1998) studied the spectra of the $Re_\tau = 590$ DNS channel data, and termed the VLSMs as “global modes”. Hutchins and Marusic (2007b) also reported as long as 20 boundary layer thickness structures in their high Reynolds number wind tunnel up to $Re_\tau = 19960$. These structures were termed as “superstructures” by the authors. Two new features were reported about the superstructures: 1) the superstructures had a meandering feature, which made the real length of these structures even longer; 2) the superstructures had footprints in the near wall region, and tended to influence the near wall cycle. Hutchins and Marusic (2007b) offered a clear explanation about the rising of the near wall peak of the streamwise velocity fluctuation intensity for the first time. Monty et al. (2007), Monty et al. (2009) compared the VLSMs in the internal flows, *i.e.*, channel and pipe, and the superstructure in the external flow, *i.e.*, boundary layer flow at the similar Reynolds number, $Re_\tau \approx 3000$, and argued that the VLSMs and the superstructures were the same type of structure, but due to the geometry difference, the VLSMs appeared further away from the wall and contained more energy in internal flows than those in the external flows. Lee and Sung (2013) compared the VLSMs in the turbulent pipe and boundary layer flows, and showed that the VLSMs in the pipe flow in average were 1.5 ~ 3.0 times longer than those in the boundary layer flow. Guala et al. (2006) and Balakumar and Adrian (2007) found that the structures ($\lambda_x > 3R$) contained not only half of

the streamwise fluctuation energy, but also more than half of the Reynolds shear stress for the pipe flow up to $Re_\tau = 7959$. In the near wall region, structures of the size $\lambda_x \approx R$ were responsible for majority of the Reynolds shear stress; while in the logarithmic region, structures with $\lambda_x \approx 5R$ were responsible for majority of the Reynolds shear stress.

2.1.4 Inner-outer interaction

At high Reynolds numbers, the VLSMs have strong footprints in the near wall region (Abe et al., 2004; Hutchins and Marusic, 2007b; Bernardini et al., 2014; Agostini and Leschziner, 2014). Hutchins and Marusic (2007a) first noticed a high correlation between the streamwise velocity signal in the near wall small scales and that in the outer large scales for the $Re_\tau = 7300$ boundary layer. The authors termed this as an amplitude modulation from the large scales to the small scales (“top-down effect”). Mathis et al. (2009) defined a one-point amplitude modulation coefficient, C_{AM} to quantify the amplitude modulation effect from the VLSMs to the near wall small scales. However, Mathis et al. (2011b) later showed that there was a similarity between C_{AM} and the term $\overline{3u_L u_S^2}$ in the skewness. To solve this dilemma, Bernardini and Pirozzoli (2011) proposed a two-point amplitude modulation coefficient, C_{AM}^{2p} to quantify the amplitude modulation effect from the VLSMs on the near wall small scales. In the 2D plot for C_{AM}^{2p} , a second outer peak was formed at the higher Reynolds number, which was the indication of the amplitude modulation effect. This two-point amplitude modulation coefficient was used by Pirozzoli et al. (2011), Ahn et al. (2013) and Nadeem et al. (2015) for the VLSMs study. Based on the superimposition and the amplitude modulation effect, Marusic et al. (2010) and Mathis et al. (2011a) proposed a predictive model to estimate the near wall velocity signal by only measuring the velocity signal in the outer region (figure 2.3). The predicted result agreed well with the measured data at $Re_\tau = 2800, 7300, 19000$ for up to the fifth order moment of turbulent channel, pipe and boundary layer (Mathis et al., 2011a). Similarly, Mathis et al. (2013) further developed the predictive model to predict the wall shear stress fluctuation. However, Agostini and Leschziner (2014) noticed that the modulation effect for the small scales differed greatly under the positive VLSMs region and the negative VLSMs region. One particular argument was that the near wall velocity fluctuation should be scaled in the local wall units, rather than the global wall units, which was also supported by Jiménez (2012) and Hwang (2013). Hwang (2013) showed that the near wall peak of the streamwise velocity fluctuation was scaled very well in the global wall units in a narrow channel, where the wide outer motions were artificially removed by the

domain size restriction. Agostini and Leschziner (2014) and Agostini and Leschziner (2015) redefined the universal near wall signal with the consideration of the local effect from the VLSMs, and managed to collapse the probability density functions for all the three velocity components of the universal field.

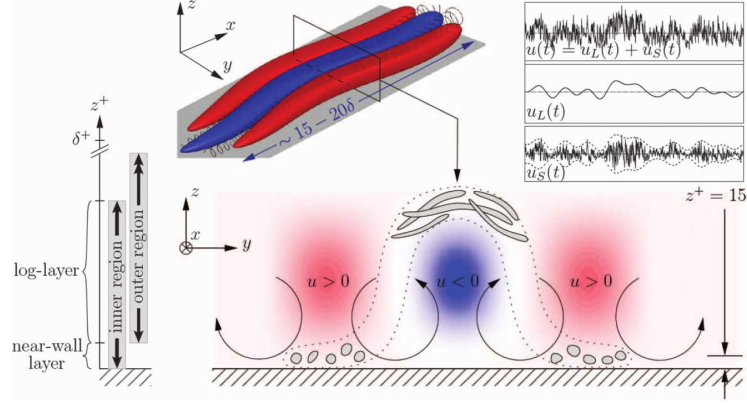


Figure 2.3: Inner-outer interaction, taken from Marusic et al. (2010).

Talluru et al. (2014) found that the VLSMs not only just modulated the amplitude of the near wall small scales in the streamwise velocity component, but also in the spanwise and wall normal velocity components. The modulation manner was very similar to that reported by Hutchins and Marusic (2007a). Ganapathisubramani et al. (2012) reported the frequency modulation from the large scales to the small scales as well: under the positive large scales, the small scales had a higher frequency; while under the negative large scales, the small scales had a lower frequency. The authors also identified a phase modulation, *i.e.*, a phase lag between the envelop of the small scales and the large scales. These frequency and phase modulations were further studied by Jacobi and McKeon (2013) and Baars et al. (2015).

A bigger picture about the inner-outer structure interaction was given by Toh and Itano (2005) from a streamwise confined channel simulation at $Re_\tau = 349$. A “co-supporting cycle” was conjugated that “*the large scale structures are generated by the collective behaviour of near wall structures and that the generation of the latter is in turn enhanced by the large scale structures*”.

2.1.5 Self-sustained process

There is a widely accepted regeneration cycle in the near wall region. Jiménez and Moin (1991) performed the DNS in a minimum size channel to study the dynamics of the near wall streaks and the quasi-streamwise vortices, and found that the

streaks and the quasi-streamwise vortices could still exist if the box is wider than the typical spanwise spacing of the near wall streaks, *i.e.*, $\lambda_z^+ \approx 100$, and the turbulent statistics in the near wall region calculated from the minimum channel unit was reasonably accurate. However, for the box size narrower than 100 in wall unit, the near wall dynamics could not sustain. Jiménez and Pinelli (1999) explicitly filtered the outer motions in a minimum channel box and showed that the near wall structures could still survive. This clearly demonstrated a cycle in the near wall region. Different mechanisms were used to explain the near wall cycle, for example, the streak instability (Swearingen and Blackwelder, 1987; Hamilton et al., 1995), the parent-offspring of hairpin structures (Zhou et al., 1999). A detailed review was given by Panton (2001).

However, for the regeneration of the outer VLSMs, active debates are still going on. When Kim and Adrian (1999) first observed the VLSMs, they conjectured that the VLSMs was the consequence of the gathering of the hairpin packets (so called “bottom-up” effect). Lee et al. (2014) defined “preserving”, “merging”, “breaking”, “shortening”, “creating” and “extincting” six events in a turbulent boundary layer and showed that “merging” event was dominant in the outer region. From the auto-correlation of the streamwise velocity at various wall normal location in the pipe, Bailey et al. (2008) and Bailey and Smits (2010) found that the large scale motions (LSMs) were detached from the wall in the outer region and attached from the wall in the logarithmic region, thus it was conjectured that the VLSMs should be formed from the detached LSMs, rather than the attached one. Iwamoto et al. (2004) artificially blocked the energy transfer from the mean flow to the large scales with $\lambda_z > 0.6h$ in a $Re_\tau = 1160$ numerical channel, and showed that the VLSMs could not be formed. Thus, they argued that the small scales did not agglomerate autonomously to form the VLSMs, but became clustered with the advective effect of the low-speed large scale structures.

In the other end, Hwang and Cossu (2010) quenched the near wall small scale structures by using an elevated Smagorinsky constant in the LES channel flow, and found that the large scale structures could still be self-sustained. However, if the box size was reduced to be shorter than $3h$ long, or narrower than $1.5h$ wide, then the large scale self-sustained mechanism was not active. Using the same technique, Hwang and Cossu (2011) and Hwang (2015) further showed that there was a full range of scales that could be self-sustained in the channel flow. Similarly, Mizuno and Jiménez (2013) replaced the wall boundary with an off-wall boundary condition, and found that the buffer layer did not exist, but the logarithmic region and other turbulent statistics were predicted reasonably well, which supported that the

dynamics of the VLSMs was independent from the near wall small scale structures. Analogous to the minimal flow unit for the buffer layer, Flores and Jiménez (2010) studied the minimum channel for the large scale structures in the logarithmic layer, and showed the turbulent structures were “healthy” from the wall to the layer whose thickness scaled with the width of channel.

2.2 3D turbulent boundary layer

In reality, the turbulent boundary layer flow can be three dimensional subjected to the spanwise pressure gradient, the surface curvature or the rotation, which means the mean velocity changes the direction across the wall normal direction (see figure 2.4). Understanding 3D turbulent boundary layer is crucial for developing accurate turbulent models (Coleman et al., 1996) and controlling the turbulence.

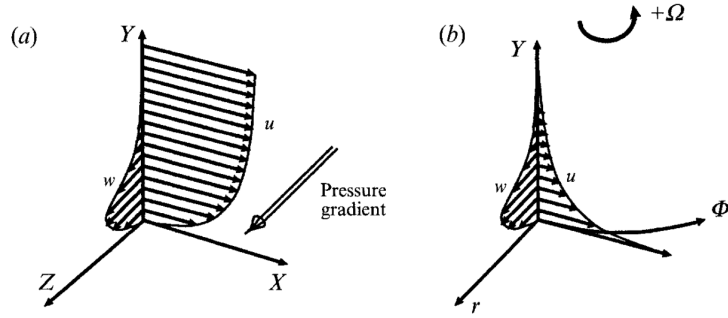


Figure 2.4: A schematic of the three dimensional turbulent boundary layers induced by (a) spanwise pressure gradient and (b) rotating disk, taken from Littel and Eaton (1994).

Bradshaw and Pontikos (1985) investigated the 3D turbulent boundary layer on a swept wing. The main effort was spent on measuring the phase lag between the shear stress angle, γ_τ and the mean velocity gradient angle, γ_g , and also the variation of the structure parameter, a_1 , because the lag between γ_τ and γ_g could not be predicted by the isotropic eddy viscosity models. The data confirmed that a_1 decreased in the 3D turbulent boundary layer, which eventually led to the discovery of the spanwise wall oscillation for the turbulent skin-friction control (Jung et al., 1992). Moin et al. (1990) studied the 3D turbulent boundary layer in a numerical channel with the spanwise pressure gradient and showed a decrease in the turbulent production and an increase in the turbulent dissipation, thus the decrease in the turbulent kinetic energy. Eaton (1995) used an upstream facing wedge to produce the spanwise pressure gradient and generated a 3D turbulent boundary layer in

the experiment. They showed that the two types of quasi-streamwise vortices were affected very differently by the spanwise mean flow, one of which was strongly inhibited. This vortex dynamics was intensively analysed by Sendstad and Moin (1992). Littel and Eaton (1994) conditioned the streamwise velocity fluctuation based on the strong sweep and ejection events, and found a strong asymmetry in the correlation profiles, thus they argued that the two types of quasi-streamwise vortices were modulated differently in the flow.

Le et al. (2000) imposed the transverse wall motion in a numerical channel to create a 3D turbulent boundary layer. The authors observed that the wall shear stress experienced three stages: the early reduction, the later reduction and the recovery. During the recovery stage, the lag angle between γ_τ and γ_g became negligible. The asymmetry in the conditioned strong quadrant events was also observed, which again suggested that the positive (clockwise rotating) and the negative (anti-clockwise rotating) quasi-streamwise vortices associated with the sweep and ejection were modulated differently in a 3D turbulent boundary layer. Kang et al. (1998) studied the same rotating disk experiment, and also found the asymmetry in both the spanwise velocity correlation coefficient and the conditioned strong quadrant events. Coleman et al. (2000) used a domain deformation method to create a 3D turbulent boundary layer. Holstad et al. (2010) and Holstad et al. (2012) studied the three dimensionality of the Couette-Poiseuille flow. The ensemble averaged λ_2 structures were found to be asymmetric compared to the 2D turbulent boundary layer case, thus the streamwise Reynolds shear stress was transferred to the spanwise and the wall normal components. The authors argued that the staggered λ_2 structure model should also hold in the 3D turbulent boundary layer. The ensemble averaged λ_2 structures were used to analyse the 3D turbulent boundary layer in a concentric annulus with a rotating inner cylinder by Jung and Sung (2006). Despite the slight curvature effect, the positive and the negative λ_2 structures showed a similar asymmetry as those in the flat plate 3D turbulent boundary layer.

2.3 Turbulent drag reduction control

Various drag reduction control methods have been developed. In general, they can be divided into two types depending on whether the control needs energy input or not: the passive controls (no energy input) and the active controls (with energy input). Typical passive controls include riblets (Choi et al., 1993; García-Mayoral and Jiménez, 2011b), random wall roughness (Sirovich and Karlsson, 1997), super-hydrophobic surface texture (Jelly et al., 2014; Lee et al., 2015), vortex generators

(Hutchins and Choi, 2001), polymers (Graham, 2014). Typical active controls include blowing and suction (Choi and Moin, 1994; Chung and Talha, 2011; Deng et al., 2014, 2015; Bai et al., 2014; Kametani et al., 2015), wall deformation (Endo et al., 2000; Tamano and Itoh, 2012), spanwise wall oscillation (Jung et al., 1992; Gatti et al., 2015a), rotating disk (Ricco and Hahn, 2013; Wise et al., 2014), artificial forcing (Handler et al., 1993; Satake and Kasagi, 1996; Schoppa and Hussain, 1998; Lee and Kim, 2002; Iwamoto et al., 2005; Xu et al., 2007; Fukagata et al., 2010).

One particular popular skin-friction control scheme is travelling wave. The wave can be generated in various ways, and travels in the streamwise, the spanwise or the oblique directions. A summary of all the travelling wave forms in the literature is given in table 2.1. All these skin-friction control methods can achieve a significant amount of drag reduction. Some led to re-laminarisation (Mamori et al., 2014) or even to sub-laminar state (Min et al., 2006; Xu et al., 2007).

Fukagata and Kasagi (2002) provided a powerful tool to analyse the skin-friction contribution from the streamwise Reynolds shear stress. By triple integration of the streamwise momentum equation, the skin-friction was found to consist of three parts: the laminar contribution; the turbulence contribution; and the contribution due to the inhomogeneity, the unsteadiness and the body force. This revealed that the turbulent skin-friction control was mainly to reduce the second part. To quantify the drag reduction, the flow control was applied under either constant flow rate (CFR) or constant pressure gradient (CPG). Under CFR condition, a drag reduction corresponds to a decrease of the driven pressure gradient and also wall shear stress; under CPG condition, the wall shear stress does not change, and a drag reduction corresponds to an increase of the mass flow rate. Frohnäpfel et al. (2012) considered both the energy saving and the pumping time into the cost function, and defined a constant pumping power (CPP) control, which might give larger benefit in reality when the time cost was important.

2.3.1 Spanwise wall oscillation

Jung et al. (1992) and Akhavan et al. (1993) observed that 40% skin-friction drag could be achieved in a numerical channel at $Re_\tau = 180$, when a spanwise oscillatory crossflow or spanwise oscillating wall was imposed. For spanwise wall oscillation, the control scheme is as following:

$$W_w = A_w \sin(\omega t) = A_w \sin\left(\frac{2\pi}{T}t\right), \quad (2.1)$$

Table 2.1: Travelling wave forms in literature.

Wave form	Formula	Source
By blowing and suctions		
Streamwise	$v_w = A_f \cos(\kappa_x x - \omega t)$	Lee et al. (2008) Lieu et al. (2010)
Spanwise	$v_w = A_f \cos(\kappa_z z - \omega t)$	Bai et al. (2014)
By wall deformation		
Streamwise	$a_x = A_a \cos(\kappa_x x - \omega t)$	Nakanishi et al. (2012)
Spanwise	$a_z = A_a \cos(\kappa_z z - \omega t)$	Zhao et al. (2004) Itoh et al. (2006) Klumpp et al. (2011) Tomiyaama and Fukagata (2013) Koh et al. (2015)
By wall motion		
Streamwise	$w_w = A_w \sin(\kappa_x x - \omega t)$	Quadrio et al. (2009)
Spanwise	$w_w = A_w \sin(\kappa_z z - \omega t)$	Quadrio and Xie (2015)
By Lorentz force		
Streamwise	$f_z = A_f e^{-y/\Delta} \sin(\kappa_x x - \omega t)$	Huang et al. (2010)
	$f_y = A_f e^{-y/\Delta} \sin(\kappa_x x - \omega t)$	Mamori et al. (2014)
Spanwise	$f_z = A_f e^{-y/\Delta} \sin(\kappa_z z - \omega t)$	Du and Karniadakis (2000) Du et al. (2002)
Bi-direction	$f_z = A_f e^{-y/\Delta} \sin(\kappa_x x + \kappa_z z - \omega t)$	Huang et al. (2014)
By plasma actuators		
Spanwise	-	Whalley and Choi (2014) Choi et al. (2011)

where A_w is the maximum wall velocity and ω (or T) is the oscillation frequency (or period). Or equivalently,

$$W_w = D_m \cos(\omega t) = D_m \cos\left(\frac{2\pi}{T}t\right), \quad (2.2)$$

where $D_m (= 2A_w/\omega)$ is the maximum wall displacement. The optimal wall oscillation period was found to be $T_{opt}^+ \approx 100$. Baron and Quadrio (1996) showed that around 10% net energy saving was possible by spanwise wall oscillation, which was a similar level to the passive drag reduction controls, such as riblets. And the authors argued that the induced Stokes layer by spanwise wall oscillation displaced the high- and low-speed streaks relative to the quasi-streamwise vortices, thus reducing the generation of streamwise Reynolds shear stress. Similar amount of drag reduction

was observed in a numerical pipe by Quadrio and Sibilla (2000). In a numerical boundary layer flow, Lardeau and Leschziner (2013) found 25% drag reduction at $Re_\tau = 520$, and the optimal oscillation period was at $T_{opt}^+ = 80$, lower than the channel and pipe cases. A 36.8% drag reduction was found in a numerical boundary layer with higher maximum spanwise wall velocity of $A_w^+ = 18$ (Yudhistira and Skote, 2011). The drag reduction by the spanwise wall oscillation was confirmed experimentally by Laadhari et al. (1994), Trujillo et al. (1997), Choi et al. (1998), Bogard et al. (2000), Choi and Clayton (2001), Choi (2002), Di Cicca et al. (2002), Ricco (2004) and Ricco and Wu (2004) for the flat plate wall and by Choi and Graham (1998) for the circular pipe.

The two control parameters, *i.e.*, the maximum wall velocity A_w^+ and the oscillation frequency ω^+ were intensively explored for a scaling law of the drag reduction. The drag reduction value was not simply scaled by the maximum wall displacement D_m^+ nor the oscillation frequency ω^+ . Choi and Graham (1998) experimentally studied the drag reduction in a circular pipe at two Reynolds numbers, $Re_\tau = 650$ and 1000, and found that the maximum wall velocity A_w^+ gave a better scaling than the oscillation frequency ω^+ . Choi et al. (2002) proposed a combined number V_c with a thickness l^+ , an acceleration rate a^+ , the maximum wall velocity A_w^+ , and the Reynolds number Re_τ : $V_c = a^+ l^+ / A_w^+ Re_\tau^{-0.2}$, and the authors found that the drag reduction was scaled in a quadratic form of V_c^+ , *i.e.*, $\mathcal{DR} = 1000V_c^{+2} + 50V_c^+$. Similarly, Quadrio and Ricco (2004) proposed a combined parameter $S^+ = a^+ l^+ / A_w^+$ without the consideration of the Reynolds number effect. The authors found that the drag reduction was scaled linearly well with S^+ , when the oscillation period was small, *i.e.*, $T^+ < 150$, which was also the accurate prediction regime of the model-based approach by Moarref and Jovanović (2012). Ricco and Quadrio (2008) further explored the parameter space $T^+ - A_w^+$ and $T^+ - D_m^+$ for the drag reduction region and also for the net energy saving condition at $T^+ < 150$, where the linear scaling correlation is held.

Vodop'yanov et al. (2013) imposed riblets on the oscillation wall, and found that the drag reduction effect was larger than the effect of either the spanwise oscillation of a smooth wall or a stationary riblet surface, when each was used separately. Mito and Kasagi (1998) generated the spanwise oscillation by the vertical wall deformation, rather than the spanwise wall velocity. The authors observed that the coherent structures were modulated significantly and the skin-friction fluctuated around the mean value of the no control case, but no long term sustained drag reduction was observed. Mishra and Skote (2015) used a square wave to replace the sinusoidal wave in order to save the power input for the control, and 18% net energy

saving was achieved. More generally, Cimarelli et al. (2013) considered 9 temporal waveforms for the spanwise wall oscillation, and they found that the optimal wave form depended on the control parameters. However, at the optimal amplitude and oscillation frequency, the maximum net energy saving was achieved by a sinusoidal wave.

To investigate the initial response by the spanwise wall oscillation, Quadrio and Ricco (2003) studied the flow immediately after the wall started to oscillate. They found that the spanwise Stokes layer was formed just after one oscillation period, but the response of the skin-friction was much slower, and it depended on the applied maximum spanwise wall velocity. The turbulent flow went through a non-monotonic process to reach its new equilibrium state. Skote (2012) compared the spatial and the temporal transient responses in a turbulent boundary layer subjected to the spanwise wall oscillation. Up to the first $3/4$ oscillation period, the temporal transient response followed that of the spatial one very well by using a convection velocity $\mathcal{U}_c^+ = 10$. As in the channel case, the temporal response went through a non-monotonic process, but this process was not observed in the spatial response. This difference was explained to be caused by the pressure-strain term in the turbulent budget. Xu and Huang (2005) investigated the turbulent budget terms during the first two oscillation periods, and noticed a sustained attenuation of the pressure-strain terms for the spanwise and the wall normal Reynolds stress components, and this eventually led to the reduction of the streamwise normal Reynolds stress $\overline{u'u'}$ and the Reynolds shear stress $\overline{u'v'}$.

The drag reduction mechanism has been partially understood, with different models coexisted. The earliest one was that the spanwise wall oscillation generated the Stokes layer, and it shifted the position of the low-speed streaks relative to the quasi-streamwise vortices (Akhavan et al., 1993; Baron and Quadrio, 1996). Galionis and Hall (2005) theoretically studied the unstable Görtler vortex on a concave surface subjected to the spanwise wall oscillation. The growth rate of the most amplified Görtler vortex was found to be significantly reduced. Dhanak and Si (1999) considered a single coherent quasi-streamwise vortex dipole in a spanwise oscillation flow, and argued that the spanwise wall oscillation deformed the quasi-streamwise vortices and increased the mixing of the high- and low-speed streaks, resulting in the drag reduction. Negi et al. (2015) used a localized volume forcing to generate the low-speed streaks in a laminar boundary layer, and studied the interaction between the low-speed streaks and the spanwise wall oscillation. The authors found that the drag reduction values had a better correlation with the wall normal velocity fluctuations, which was also observed by Hurst (2013). Using a generalized optimal

perturbation (GOP) approach, Blesbois et al. (2013) found that in a spanwise oscillating turbulent boundary layer, the GOP modes were infinitely long structures with certain angles to the mean flow, and the angle and the amplitude of the structures jumped suddenly at a certain instant during the oscillation period, which was consistent with the conditioned streaks angle in the DNS by Toubert and Leschziner (2012) and the quasi-streamwise vortices tilting angle in the DNS by Hurst (2013). Yakeno et al. (2014) performed the ensemble average of the quasi-streamwise vortices and the associated quadrant events, and the authors argued that the drag reduction for the cases with small oscillation periods was due to the suspension of the Q2 event; while the drag increase for the cases with large oscillation periods was due to the enhancement of the Q4 event. Considering these two effects, the authors proposed a combined parameter, which gave a good scaling of the drag reduction for various oscillation periods and spanwise wall velocity amplitudes. Iuso et al. (2003) observed that there was an increase in the streak width, the spanwise spacing and the waviness, but a reduction of the streak strength, thus the authors interpreted that these were due to the density reduction of the unstable low-speed streaks, which weakened the near wall cycle. Toubert and Leschziner (2012) compared the turbulent statistics between the spanwise wall oscillation case and the no control case in much detail, and the authors argued that the origin of the statistics changes was the spanwise distortion of the near wall streaks. This mechanism was further supported by Agostini et al. (2014) at a higher Reynolds number. Ricco et al. (2012) calculated the turbulent kinetic energy and the enstrophy balance, and argued that the drag reduction by the spanwise wall oscillation was due to the increase of the turbulent enstrophy and dissipation in the transient process. Dugdale et al. (2007) studied the proper orthogonal decomposition (POD) modes for the spanwise wall oscillation in a pipe flow, and showed that the Stokes layer pushed the propagating mode away from the wall, resulting in a higher convection velocity and shorter interaction time between the propagating modes and the roll modes, thus reducing the production of the Reynolds shear stress and the skin-friction.

Viotti et al. (2009) found the spatial form of spanwise wall oscillation, *i.e.*, streamwise oscillation of spanwise wall velocity (also known as stationary wave), which has the formula as below:

$$W_w = A_w \sin(\kappa_x x) = A_w \sin\left(\frac{2\pi}{\lambda_x} x\right), \quad (2.3)$$

where κ_x (or λ_x) is the streamwise wavenumber (or wavelength). The stationary wave can be linked to the spanwise wall oscillation by a convection velocity $\mathcal{U}_c^+ = 10$.

The stationary wave case achieved slightly higher drag reduction than the spanwise wall oscillation at the same maximum wall velocity and Reynolds number. The optimal streamwise wavelength was found to be $\lambda_x^+ \approx 1000 \sim 1250$. Skote (2011) implemented the stationary wave into a boundary layer, and achieved around 50% drag reduction. Yakeno et al. (2009) performed a large number of channel DNS cases to create the drag reduction map $A_w^+ - T^+$ for the spanwise wall oscillation and $A_w^+ - \lambda_x^+$ for the stationary wave, and showed that stationary wave was more efficient than spanwise wall oscillation. Similar comparison was carried out in a turbulent boundary layer by Skote (2013). As in the channel case, they confirmed that the stationary wave case was more efficient in reducing skin-friction than the spanwise wall oscillation.

Quadrio et al. (2009) combined the spanwise wall oscillation and the stationary wave, and proposed the streamwise travelling wave of the spanwise wall velocity,

$$W_w = A_w \sin(\kappa_x x - \omega t) = A_w \sin\left(\frac{2\pi}{\lambda_x} x - \frac{2\pi}{T} t\right). \quad (2.4)$$

The wave travelling speed was defined as $c \equiv \omega/\kappa_x$ (or $c \equiv \lambda_x/T$). Positive (or negative) c corresponded to the forward (or backward) streamwise travelling wave. A total number of 250 simulation cases were performed at fixed $A_w^+ = 12$, $Re_\tau = 200$ to construct the drag reduction map in the $\kappa_x - \omega$ parameter space. It was found that the drag increase region was a cone passing the origin with a travelling wave speed equal to the convection velocity of the near wall coherent structures, *i.e.*, $c^+ = \mathcal{U}_c^+ = 10$. The optimal drag reduction was about 48% appearing at $(\omega^+, \kappa_x^+) = (0.02, 0.008)$, and this drag reduction value was higher than the optimal drag reduction by either purely the spanwise wall oscillation or the stationary wave. A maximum net power saving of 18% was found at $(\omega^+, \kappa_x^+) = (0.02, 0.005)$. Quadrio and Ricco (2011) analysed the generalized Stokes layer, and showed that the drag reduction scaled with the Stokes layer thickness when c is sufficiently different from the turbulent convection velocity \mathcal{U}_c . The optimal Stokes layer thickness for the drag reduction was found to be $\delta^+ \approx 6.5$, and a minimum thickness of $\delta^+ \approx 1$ was required for the drag reduction. Duque-Daza et al. (2012) were able to generate a similar \mathcal{DR} map using the linearised Navier-Stokes equations, and extent the \mathcal{DR} map to a much higher Reynolds number $Re_\tau = 2594$. However, the linearised Navier-Stokes approach relied on a careful selection of the cost function and an optimization plane, and the base flow required a superimposition of a generalised Stokes layer profile in the spanwise direction, which was assumed to be independent from the streamwise mean flow. As stated by the authors, this approach needed

an empirical calibration in order to be reliable. Auteri et al. (2010) designed an experiment using 60 individual controlled pipe segments to generate the streamwise travelling wave of spanwise wall velocity and verified the numerical result by Quadrio et al. (2009). As a discrete spatial wave form, the experiment achieved a maximum 33% drag reduction. Quadrio and Xie (2015) further proposed a spanwise travelling wave of the spanwise wall velocity (see table 2.1), but all the explored cases were found to be not as good as purely the spanwise wall oscillation. A review about the drag reduction using various wall motions (oscillation, stationary wave and travelling wave) was given by Quadrio (2011).

2.3.2 Lorentz force actuators

Lorentz force is an electro-magnetic force applied for electro-conductive fluids, for example sea water. Berger et al. (2000) performed the DNS for the drag reduction using Lorentz actuators to create the spanwise oscillation, in a similar fashion to the spanwise wall oscillation. 40% drag reduction was reported at $Re_\tau = 100$, with an optimal oscillation period of $T_{opt}^+ = 100$. The effect of the Lorentz actuators was treated as a body force coupled into the momentum equation of the fluid motion. By solving the Maxwell equation with an ideal boundary condition, the magnitude of the Lorentz force is formulated as

$$f_z = A_f e^{-\frac{y}{\Delta}}, \quad (2.5)$$

where A_f is the strength of the Lorentz force, Δ is the penetration depth of the Lorentz force. Due to the simplicity, this explicit expression of the Lorentz force was widely used in the numerical study (Du et al., 2002; Huang et al., 2010). The drag reduction by Lorentz force actuators was experimentally confirmed by Pang and Choi (2004) and Pang et al. (2004), who observed more than 40% drag reduction with control parameters, $A_f^+ \approx 210$ and $T^+ \approx 100$. Pang et al. (2004) argued that the drag reduction was due to the stretching of the quasi-streamwise vortices in the near-wall region.

Du and Karniadakis (2000) and Du et al. (2002) conducted experiments and DNSs for the spanwise travelling wave generated by the Lorentz force (see table 2.1), and more than 30% drag reduction was achieved. The authors noticed that most of the near wall streaks were eliminated, and a wide ribbon of the low-speed velocity was formed. This wide ribbon pattern was found to be caused by the the Lorentz force induced streamwise vortices, and the control cases with wider ribbons corresponded to higher drag reduction. Xie and Quadrio (2013) performed around

1000 DNS cases in the $\omega - \kappa_z - A_f - \Delta$ 4D parameter space for the spanwise travelling wave by the spanwise Lorentz force. Their results suggested: 1) the spanwise travelling wave by the Lorentz force generated a non-negligible spanwise mass flow rate for most of the cases; 2) the spanwise travelling wave was always less efficient than the corresponding temporal oscillation case.

Other travelling wave forms by the Lorentz force were also studied in the literature (see table 2.1). Huang et al. (2010) proposed the streamwise travelling wave of the spanwise Lorentz force, and obtained 42% drag reduction for the optimal cases. An oscillation frequency dependent optimal streamwise wavenumber $\kappa_{x,opt}^+$ was observed. Mamori et al. (2014) applied the Lorentz force in the wall normal direction to create the blowing and suction effect, and the wave travelled in the streamwise direction. The results suggested that drag reduction only happened when the wave was stationary. It was argued that the spanwise rollers were responsible for the creation of the negative Reynolds shear stress, resulting in the drag reduction. Huang et al. (2014) studied the effect of the travelling wave angle to the mean flow, and the streamwise travelling wave was found to be more effective than the spanwise travelling wave.

One drawback of Lorentz force actuators is the low efficiency in converting the electric power into the fluid power, which is the order of $O(10^{-3})$ based on the current technology (Berger et al., 2000). This makes Lorentz force actuators unlikely to achieve a net energy saving at this moment.

2.3.3 DBD plasma actuators

The Dielectric Barrier Discharge (DBD) plasma actuator consists of an upper electrode, a lower electrode and a dielectric barrier layer in between. When the high voltage ($\sim 1kV$) AC (alternative current) is applied, the air in the vicinity of the electrode is ionized, and the ions and the neutral gas particles strongly collide with each other to exchange the momentum and energy, resulting in an electric wind. The thickness of the upper and lower electrodes is normally measured in μm and the response frequency is in several kHz . DBD plasma actuators are very light, cheap, and easy to be implemented on wall surfaces. All these features make DBD plasma actuators a perfect candidate for the flow control of air vehicles. After the DBD plasma actuator was first developed by Roth et al. (2000), it was quickly used for the flow separation control of the air-foils (Roth, 2003). Some reviews about the plasma actuators were given by Moreau (2007), Corke et al. (2010), Caruana (2010) and Wang et al. (2013).

Unlike Lorentz force actuators, the physical process of the air discharge is

very complicated, thus no explicit formula was available to describe the force distribution. Several groups have tried to model the DBD plasma actuators. From the first principle, Boeuf and Pitchford (2005), Jayaraman et al. (2006), Unfer and Boeuf (2009), Unfer and Boeuf (2010), Nishida and Abe (2011) and Likhanskii et al. (2008) considered the time dependent continuity and momentum equations for the electrons and ions, and numerically modelled the plasma force distribution. This model captured the discharge details, including the microseconds scale discharge filaments and the strong unsteadiness of the plasma force field. However, in this model, the time step was extremely small, *i.e.*, in picoseconds, and this led to a multi-scale problem for the flow control. To simplify the problem, Jayaraman et al. (2006) only used a frozen pre-calculated plasma force field at phase $\phi = \pi/2$ to avoid the multi-scale problem. Suzen et al. (2005), Suzen et al. (2007) and Belson et al. (2012) derived the simplified Maxwell equations for the electric field \mathbf{E} and the charge density distribution ρ_c , and proposed some empirical boundaries (Gaussian distribution) for \mathbf{E} and ρ_c , thus they could get the time dependent plasma force field. In this model, the equations for the plasma actuators were only solved once, and the force field varied according the AC current wave form. Orlov and Corke (2006), Mertz and Corke (2009) and Mertz and Corke (2011) improved the boundary condition for the dielectric material from Suzen et al. (2005) using a lumped-element circuit model. In this mode, the increasing rate of the maximum velocity as the $7/2$ law of the applied peak-peak voltage ($V_{p-p}^{7/2}$ scaling (Murphy et al., 2013)) was correctly predicted. The modelled space-time variation of the current showed a very high correlation with the space-time variation of the plasma light emission observed in the experiment. Interestingly, the model could also predict the directivity pattern of the acoustic. Abdollahzadeh et al. (2014) empirically approximated the thrust to match the $V_{p-p}^{7/2}$ scaling. A simple linear model for DBD plasma actuators was proposed by Shyy et al. (2002). In this mode, the plasma force was distributed in a triangle region, where the plasma could be observed by naked eyes in the experiment. The electric field \mathbf{E} was assumed linearly decreasing from the maximum on the surface between the upper and the lower electrodes, and the charge density ρ_c was evaluated from the experiment. Instead of treating the DBD plasma actuator effect as a body force, Marziali Bermudez et al. (2011) modelled the plasma actuator effect in the fluid flow as a slip wall boundary condition within the plasma region.

As the increase in the accuracy of the modern PIV (Particle Image Velocimetry) technique, some PIV measurement based plasma models were developed. The idea is to solve an inverse problem governed by the momentum equation. However, due to the lack of the pressure field from PIV, an additional assumption is needed

to close the problem. Using the PIV data, both the total thrust and the spatial distribution can be estimated. To estimate the thrust force, Durscher and Roy (2012) and Kotsonis et al. (2010) assumed the pressure was uniform along the two horizontal boundaries of the control volume. With this assumption, the evaluated plasma actuator thrust matched the trend of the directly measured data by the load cell. In order to evaluate the spatial distribution of the plasma body force, different assumptions are available from the literature, and they are summarized in table 2.2. Kotsonis et al. (2010) assumed that at the initial stage when the plasma actuators were actuated, the dominant terms in the momentum equations were the unsteady term and the plasma body force term, thus the plasma force could be directly calculated. This method needed actuate time resolved PIV measurement. Wilke (2009) assumed the pressure gradient term was much smaller than the plasma body force when the plasma induced flow became steady, thus the plasma body force was directly balanced by the convection term and the viscous term. Kotsonis et al. (2010) also proposed a “pressure gradient” method by considering the time derivative of the momentum equation, and assuming the plasma body force was steady. After the pressure gradient was known, the plasma body force could be evaluated from the original momentum equation. Therefore, the “pressure gradient” method also relied on the high resolution time resolved PIV data. Albrecht et al. (2011) instead considered the vorticity equation directly, where no pressure gradient term was involved. The authors proposed an order of magnitude relation between the gradient term of the two plasma body force components, then the plasma body force could be calculated. A comparison of these PIV measurement based plasma body force models was given by Kriegseis et al. (2013). In general, the spatial plasma body force distributions among all the PIV measurement based methods are very similar. Based on this, Maden et al. (2013) proposed an empirical formulation to parametrise the plasma body force, and also compared the plasma induced wall jet profiles among different methods. The linear model by Shyy et al. (2002) and the PIV measurement based models could predict the jet profile very well in the downstream, while the PIV measurement based models had better prediction in the vicinity of the tip of the upper electrode. Suzen et al. (2005)’s model almost failed to predict the jet profile at any location.

The main property of the plasma actuators is the induced wall jet, which was carefully studied in experiments by Jukes et al. (2006a), Jukes et al. (2008), Whalley and Choi (2012) and Jukes and Choi (2013). The plasma wall jet is an ideal candidate to replace the conventional vortex generator for the flow separation control (Jukes and Choi, 2012; Jukes et al., 2012). However, due to the discrete

Table 2.2: Assumptions to evaluate the plasma body force in PIV measurement based methods.

Assumptions	Source	Remarks
$NS : \underbrace{\frac{\partial u_i}{\partial t}}_{\textcircled{1}} + u_j \underbrace{\frac{\partial u_i}{\partial x_j}}_{\textcircled{2}} = \underbrace{\frac{f_i}{\rho}}_{\textcircled{3}} - \underbrace{\frac{1}{\rho} \frac{\partial p}{\partial x_i}}_{\textcircled{4}} + \nu \underbrace{\frac{\partial^2 u_i}{\partial x_j^2}}_{\textcircled{5}}$		
$\textcircled{2} \rightarrow 0; \textcircled{4} \rightarrow 0; \textcircled{5} \rightarrow 0.$	Kotsonis et al. (2010)	For initial stage
$\textcircled{1} \rightarrow 0; \textcircled{4} \rightarrow 0.$	Wilke (2009)	For steady stage
$\textcircled{1} \rightarrow 0; \partial \textcircled{3} / \partial t \rightarrow 0.$	Kotsonis et al. (2010)	Time derivative
$\textcircled{1} \rightarrow 0; \partial f_1 / \partial y \gg \partial f_2 / \partial x.$	Albrecht et al. (2011)	Curl of NS equations

nature of the plasma body force, the application of the plasma actuators for the turbulent skin-friction control is not straightforward. Wilkinson (2003) did the first attempt to generate the spanwise oscillation by the DBD plasma actuators for the turbulent skin-friction drag reduction control. Unfortunately, due to the limitation of the spanwise plasma wind speed achievable, the wind tunnel test for the drag reduction was unable to be carried out. This concept was followed by Jukes et al. (2006b), who managed to get 45% skin-friction drag reduction by the oscillating plasma force at $Re_\tau = 380$ (see figure 2.5). The authors argued that the drag reduction was due to the interaction between the plasma body force induced streamwise rollers with the near wall quasi-streamwise vortices in the turbulent boundary layer. This drag reduction was confirmed in the DNS by Elam (2012). Inspired by the spanwise travelling wave of the Lorentz force (Du and Karniadakis, 2000), Whalley and Choi (2011) and Whalley and Choi (2014) proposed the spanwise travelling wave configuration using the streamwise aligned plasma actuator array, and 30% drag reduction was reported. Similar “ribbon” structures as the spanwise travelling wave by the Lorentz force were observed. A review of the drag reduction by the plasma actuators with the spanwise oscillation and the spanwise travelling wave was given by Choi et al. (2002). Recently, Li et al. (2015) reported the drag reduction by the spanwise aligned plasma actuator array (same configuration as in (Ibrahim and Skote, 2014)).

2.3.4 Reynolds number effect

It has been observed that the turbulent skin-friction drag reduction efficiency deteriorates with increasing Reynolds number (Berger et al., 2000; Iwamoto et al., 2002; Choi et al., 2002), which is known as the Reynolds number effect in the

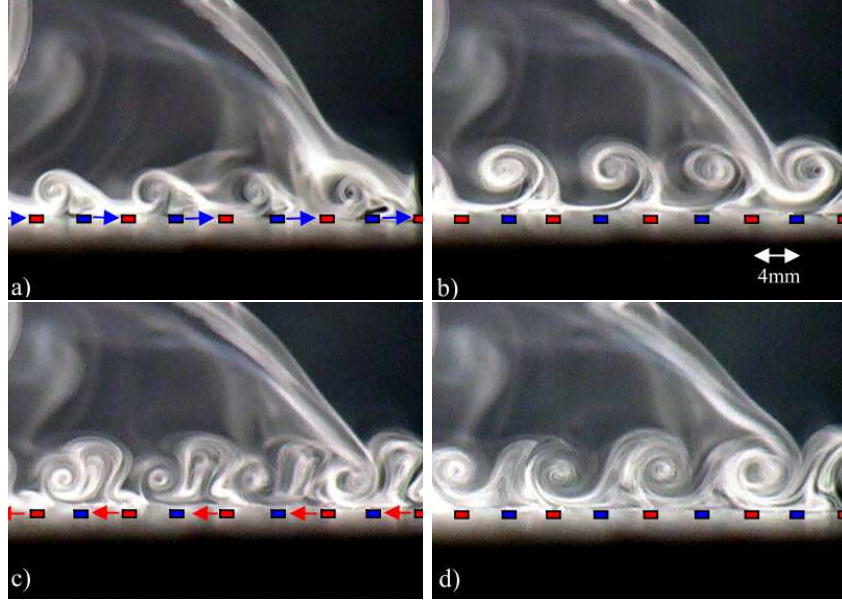


Figure 2.5: Spanwise oscillation by plasma actuators at four different phases, taken from Jukes et al. (2006a).

turbulent skin-friction drag reduction control. Due to the computational power restriction in the DNS and the measurement accuracy limitation in the experiment, the Reynolds number for the flow control research in laboratories is typically the order of $Re_\tau \sim O(10^3)$, while the applications for the skin-friction control are at the Reynolds number $Re_\tau \sim O(10^4)$ and above. Therefore, it is very important to address whether a certain amount of drag reduction is still achievable at high Reynolds numbers.

Berger et al. (2000) reported that the drag reduction control efficiency by the spanwise oscillating Lorentz force control decreased as increasing Reynolds number in a range of $Re_\tau = 100 \sim 400$. Iwamoto et al. (2002) studied the drag reduction by the V-control blowing and suction, and reported the decrease in the drag reduction from 20% at $Re_\tau = 110$ to 12% at $Re_\tau = 650$. Koh et al. (2015) studied the drag reduction using the spanwise surface wave at $Re_\tau = 540, 906, 1908$ and 2250 turbulent boundary layers. The drag reduction decreased from 11% at $Re_\tau = 540$ to 1% at $Re_\tau = 2250$. For the spanwise travelling wave, Choi et al. (2002) reported the optimal drag reduction decreased from 44.5% at $Re_\tau = 100$ to 34.1% at $Re_\tau = 400$. The authors proposed a power law scaling $\mathcal{DR} \sim Re_\tau^{-\alpha}$ ($\alpha = 0.2$) to quantify the drag reduction deterioration. The Reynolds number effect was also confirmed by Ricco and Quadrio (2008) at the similar Reynolds number and by Toubert and Leschziner (2012) at the Reynolds number up to $Re_\tau = 1000$ for the spanwise wall oscillation.

It was also observed that the drag reduction decreased with increasing the Reynolds number by the spanwise wall oscillation in the turbulent boundary layer (Skote, 2012). However, the Reynolds number effect was less clear in the experiment due to the uncertainty in the measurement (Ricco and Wu, 2004; Choi and Graham, 1998). Gatti et al. (2013) performed small box-size channel flow DNSs up to $Re_\tau = 2100$ for the streamwise travelling wave, and reported the performance loss. However, the authors observed that the energy input for the streamwise travelling wave decreased with the Reynolds number ($P_{sp} \sim Re_\tau^{-0.136}$), thus they argued that a net energy saving by the streamwise travelling wave at the high Reynolds number was still possible. The drag reduction deterioration by the streamwise travelling wave of the spanwise wall velocity was also confirmed by Hurst et al. (2014) in the large box-size channel DNSs with the Reynolds number ranging from $Re_\tau = 200 \sim 1600$. The authors also noticed some other interesting phenomena: 1) the optimal control parameter shifted towards a higher oscillation frequency for the spanwise wall oscillation, and towards a higher streamwise wavenumber for the streamwise stationary wave; 2) the power law scaling parameter α was found to be control-parameters (ω, κ_x) dependent, but α was positive for all the drag reduction cases, which suggested a drag reduction deterioration.

The Reynolds number effect explored in the DNS is typically for a small range of Reynolds numbers, namely $Re_\tau < 1000$, thus the prediction for even higher Reynolds number is normally done with theoretical works (or affordable approaches). For example, Iwamoto et al. (2005) derived an explicit formula for the drag reduction with the turbulent fluctuation in the near wall layer below a threshold location y_d completely damped, and showed that a 35% drag reduction was still achievable at the Reynolds number up to $Re_\tau = 10^5$. Fukagata et al. (2006) applied the same argument to the drag reduction control by the superhydrophobic surface, and a large drag reduction was predicted to be possible at the Reynolds number $Re_\tau = 10^5 \sim 10^6$. For the streamwise travelling wave by the spanwise wall velocity, Duque-Daza et al. (2012) used the linearised Navier-Stokes to predict the drag reduction map at the high Reynolds number $Re_\tau = 2594$, which was found to be very similar to the one at $Re_\tau = 200$, with only $\sim 5\%$ difference in \mathcal{DR} (more precisely the streaks amplification). Similarly, a perturbation analysis was carried out by Belan and Quadrio (2013), who suggested a much weaker \mathcal{DR} deterioration as the Reynolds number increased, and also an asymptotic value for the constant drag reduction above a threshold Reynolds number. Quadrio and Gatti (2015) and Gatti et al. (2015b) assumed the change of the constant B in the log law from the no control case to the streamwise travelling wave cases, is Reynolds number independent,

thus the authors estimated that the drag reduction at high Reynolds number was possible. Skote (2014) proposed an argument about the scaling of the streamwise mean velocity profile for the near wall control strategies without changing the fluid properties and the outer layer. The theory prediction agreed well with the available DNS data, but the constant B is \mathcal{DR} dependent. Those predictions are very optimistic for the drag reduction control community, though it may take some time for the DNS and the experimental validation.

The Reynolds number effect suggests that the control parameters are not scaled in the inner units at high Reynolds numbers, similar to the inner scaling failure for the turbulent statistics of the no control high Reynolds number flows (DeGraaff and Eaton, 2000). Toubert and Leschziner (2012) pointed out that the Reynolds number effect in the spanwise wall oscillation was due to the VLSMs in the outer region, which clearly caused the difference between the near wall streaks under the positive and the negative VLSMs. The superposition and modulation effects by the VLSMs were also used to explain the Reynolds number effect in the blowing and suction control at $Re_\tau = 1000$ by Deng et al. (2015). The VLSMs carry a significant amount of Reynolds shear stress (Guala et al., 2006; Deck et al., 2014), and it was found that by purely controlling the large scale structures, it gave as much as 20% drag reduction (Schoppa and Hussain, 1998; Fukagata et al., 2010; Pujals et al., 2010; Schlatter et al., 2015). However, Iwamoto et al. (2002) showed that for the opposition control, the \mathcal{DR} deterioration was only strong for $Re_\tau < 300$, and \mathcal{DR} became insensitive to the Reynolds number for $Re_\tau > 300$. The asymptotic behaviour of \mathcal{DR} was also observed by Hurst et al. (2014) for the stationary wave of the spanwise wall velocity (see their figure 10(b)). Skote et al. (2015) thus suggested a power law scaling to replace the log law for the \mathcal{DR} scaling in the spanwise wall oscillation control. Using FIK identity, Hurst et al. (2014) showed that the \mathcal{DR} deterioration mainly came below the critical layer ($y^+ < 2Re_\tau^{1/2}$), while the \mathcal{DR} contribution from the outer region was almost constant from $Re_\tau = 200$ to 1600. This finding was consistent with Iwamoto et al. (2005), who showed that the Reynolds number effect was mild if the near wall turbulence was completely damped, though the damping layer thickness needed to increase slightly with the Reynolds number for the same amount of \mathcal{DR} . These results suggested the importance of the scale interaction across the wall normal direction. Iwamoto et al. (2002) demonstrated this point using the Karhunen-Loeve decomposition, and they showed that at $Re_\tau = 110$ and 300, the largest contribution to the skin-friction came from the structures within $15 < y^+ < 30$, but the contribution from $30 < y^+ < 75$ is also important for $Re_\tau = 300$. The structures within $30 < y^+ < 75$ was beyond the

direct control, but can transfer the energy to those structures within $15 < y^+ < 30$, causing the \mathcal{DR} deterioration. Thus the authors suggested the control of the structures within $30 < y^+ < 75$ was necessary at high Reynolds numbers. Iwamoto et al. (2002) claimed that the structures at $y^+ > 75$ remained inactive in terms of contributing to the skin-friction, and this might be due to the limitation of the highest Reynolds number studied, *i.e.*, $Re_\tau = 300$. Very recently, de Giovanetti et al. used three different approaches, *i.e.*, FIK identity analysis, spanwise domain confinement and artificial scale damping, and showed that the scales with $0.2h \leq \lambda_z \leq 1h$ contributed the most to the skin friction at $Re_\tau = 2000$. The turbulent structures within this scale range are in the logarithmic region, and they form a hierarchy of the self-similar attached eddies (Flores and Jiménez, 2010; Hwang, 2015).

It is clear the outer structures (including the logarithmic structures, LSMs and VLSMs) play an important role in the \mathcal{DR} deterioration by indirectly transferring energy to the near wall structures, causing the control on the near wall structure to be less effective. But whether or not we need to control the large scales from the outer region for a better \mathcal{DR} performance still remains open.

Chapter 3

Methodology

In the present study, the incompressible Newtonian fluid in a channel geometry is considered. The flow is governed by the Navier-Stokes equations, shown as below,

$$\begin{aligned}\frac{\partial u_i}{\partial t} + u_j \frac{\partial u_i}{\partial x_j} &= -\frac{\partial p}{\partial x_i} + \frac{1}{Re} \frac{\partial^2 u_i}{\partial x_j^2} + f_i, \\ \frac{\partial u_i}{\partial x_i} &= 0.\end{aligned}\tag{3.1}$$

Here all the variables are non-dimensionalised by half channel height h and bulk mean velocity U_m , thus the Reynolds number is defined as $Re = U_m h / \nu$, where ν is the kinematic viscosity. Both subscripts i, j vary in $\{1, 2, 3\}$, representing $\{x, y, z\}$ directions, respectively. When the same subscript appears more than once in one term, a summation from 1 to 3 is automatically taken, *i.e.*, $\frac{\partial^2 u_i}{\partial x_j^2} \equiv \frac{\partial^2 u_i}{\partial x_1^2} + \frac{\partial^2 u_i}{\partial x_2^2} + \frac{\partial^2 u_i}{\partial x_3^2}$, $\frac{\partial u_i}{\partial x_i} \equiv \frac{\partial u_1}{\partial x_1} + \frac{\partial u_2}{\partial x_2} + \frac{\partial u_3}{\partial x_3}$. Unless stated otherwise, x_1, x_2 and x_3 represent the coordinates x (streamwise), y (wall normal) and z (spanwise) directions, respectively; and u_1, u_2 and u_3 represent the velocity components u, v and w in three directions, respectively. f_i represents the body force component in x ($i = 1$), y ($i = 2$) and z ($i = 3$) directions, respectively. In the present study, the body force is either generated by Lorentz force actuators or plasma actuators.

A sketch of the channel geometry and coordinate system is shown in figure 3.1. The channel is bounded by two flat plates on top and bottom, where no slip boundary condition is applied. In the other two directions, the flow is assumed to be homogeneous, thus periodic boundary conditions are applied. The origin of the coordinate is located on the bottom wall, therefore the domain size in wall normal direction is $0 < y < 2$.

In this chapter, a fully implicit finite volume method for solving equation

(3.1) is explained first, then the coherent structure identification and the proper orthogonal decomposition (POD) methods are addressed separately for the data analysis in the following chapters. In the end, a series of grid resolution and domain size tests are conducted for both no control and control baseline cases.

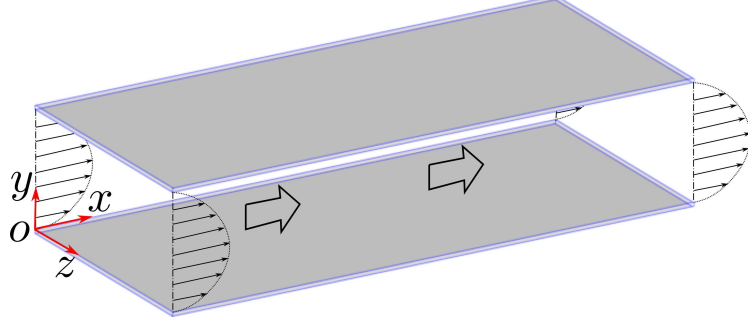


Figure 3.1: Sketch of the geometry and coordinate of a channel flow. The channel length, width and height are L_x , L_z and 2, respectively.

3.1 Fully implicit frictional step method

Fractional step method (FSM) is one way to decouple the pressure field from the velocity field in solving the Navier-Stokes equations. Depending on whether FSM is applied for the continuous N-S equations or the discrete form, the method can be viewed as time splitting (Temam, 1991; Kim and Moin, 1985) or approximate factorisation (Dukowicz and Dvinsky, 1992; Perot, 1993). From time splitting point of view, the physical interpolation for the two sub time steps is clear: 1) solving the momentum equations for an intermediate velocity field with the pressure term excluded; 2) projecting the intermediate velocity field into a divergence free space. The disadvantage is that a proper boundary condition for the intermediate velocity field is needed (Kim and Moin, 1985). In the other hand, approximate factorisation is based on discrete N-S equations with the physical boundary condition matrix stored separately, thus no boundary condition is required for the intermediate velocity field (Perot, 1993). FSM guarantees the mass conservation, but introduces an additional error terms into the momentum equations, by modifying the original pressure term (Temam, 1991). For example, Kim and Moin (1985) showed that the equation linking the original pressure and the modified pressure is $p = \phi + (\Delta t / 2Re) \nabla^2 \phi$. If the modified pressure ϕ is directly used to approximate the original pressure p , this gives a first-order time accuracy for the FSM (Perot, 1993).

The code used in the present study is based on an approximate factorisation

FSM developed by Kim et al. (2002). The authors employed Beam & Warming procedure to linearise the convection term first, then used Crank-Nicholson discretisation for all the spatial terms, thus a fully implicit scheme was achieved. This fully implicit FSM was implemented into our in-house channel flow code by Talha (2012), and was parallelised by Hurst (2013) using a 2DECOMP&FFT library developed by Li and Laizet (2010). To make the methodology complete, the overall numerical method is briefly summarised in this section.

For convenience, the Navier-Stokes equations (equation (3.1)) are written in a vector form, as below,

$$\begin{aligned}\frac{\partial \mathbf{u}}{\partial t} + H\mathbf{u} &= -Gp + \frac{1}{Re}L\mathbf{u} + \mathbf{f}, \\ D\mathbf{u} &= 0,\end{aligned}\tag{3.2}$$

where G is the gradient operator; L is the linear viscosity operator; H is the convective operator and D is the divergence operator. And each of them is defined as below,

- $Gp := \nabla p$;
- $L\mathbf{u} := \frac{1}{Re}\nabla^2\mathbf{u}$;
- $H\mathbf{u} := (\mathbf{u} \cdot \nabla)\mathbf{u}$;
- $D\mathbf{u} := \nabla \cdot \mathbf{u}$.

For x -momentum equation,

$$\frac{\partial u_1}{\partial t} + Hu_1 = -\frac{\partial p}{\partial x_1} + \frac{1}{Re}Lu_1 + f_1,\tag{3.3}$$

using Crank-Nicholson scheme for discretisation, this gives,

$$\frac{u_1^{n+1} - u_1^n}{\Delta t} + \frac{1}{2}(Hu_1^n + Hu_1^{n+1}) = -\frac{\partial p^{n+1/2}}{\partial x_1} + \frac{1}{2Re}(Lu_1^n + Lu_1^{n+1}) + f_1,\tag{3.4}$$

where superscript n represents the information in the previous time step, which is known; while superscript $^{n+1}$ represents the information in the current time step, and superscript $^{n+1/2}$ represents the information in the half time step, both of which are unknown. The body force used in the present study is decoupled from the velocity and pressure fields, thus it is evaluated through $f_1 = f_1^{n+1/2}$, and this information at each time step is known. The pressure field is half a time step staggered of the velocity fields, and this is to make the splitting in the fractional step method second-order accuracy (Kim et al., 2002), as shown later.

For the convective term Hu_1^{n+1} , the Beam & Warming scheme is used as below,

$$\begin{aligned}
u_i^{n+1}u_j^{n+1} &= (u_i^n + (u_i^{n+1} - u_i^n)) (u_j^n + (u_j^{n+1} - u_j^n)) \\
&= u_i^{n+1}u_j^n + u_i^n u_j^{n+1} - u_i^n u_j^n + (u_i^{n+1} - u_i^n)(u_j^{n+1} - u_j^n), \\
&= u_i^{n+1}u_j^n + u_i^n u_j^{n+1} - u_i^n u_j^n + \Delta u_i^{n+1} \Delta u_j^{n+1}, \\
&= u_i^{n+1}u_j^n + u_i^n u_j^{n+1} - u_i^n u_j^n + O(\Delta t^2),
\end{aligned} \tag{3.5}$$

which gives the second-order accuracy in time. Thus,

$$\begin{aligned}
Hu_1^{n+1} &= (\mathbf{u}^{n+1} \cdot \nabla) u_1^{n+1} = \frac{\partial(u_1^{n+1}u_1^{n+1})}{\partial x_1} + \frac{\partial(u_2^{n+1}u_1^{n+1})}{\partial x_2} + \frac{\partial(u_3^{n+1}u_1^{n+1})}{\partial x_3} \\
&= \frac{\partial(u_1^{n+1}u_1^n)}{\partial x_1} + \frac{\partial(u_1^n u_1^{n+1})}{\partial x_1} - \frac{\partial(u_1^n u_1^n)}{\partial x_1} + \\
&\quad \frac{\partial(u_2^{n+1}u_1^n)}{\partial x_2} + \frac{\partial(u_2^n u_1^{n+1})}{\partial x_2} - \frac{\partial(u_2^n u_1^n)}{\partial x_2} + \\
&\quad \frac{\partial(u_3^{n+1}u_1^n)}{\partial x_3} + \frac{\partial(u_3^n u_1^{n+1})}{\partial x_3} - \frac{\partial(u_3^n u_1^n)}{\partial x_3} + O(\Delta t^2) \\
&= \frac{\partial(u_1^{n+1}u_1^n)}{\partial x_1} + \frac{\partial(u_1^n u_1^{n+1})}{\partial x_1} + \frac{\partial(u_2^{n+1}u_1^n)}{\partial x_2} + \frac{\partial(u_2^n u_1^{n+1})}{\partial x_2} + \\
&\quad \frac{\partial(u_3^{n+1}u_1^n)}{\partial x_3} + \frac{\partial(u_3^n u_1^{n+1})}{\partial x_3} - Hu_1^n + O(\Delta t^2).
\end{aligned} \tag{3.6}$$

An approximate non-linear operator N is introduced, so that,

$$\begin{aligned}
Nu_1^{n+1} &= \frac{1}{2} \left(\frac{\partial(u_1^{n+1}u_1^n)}{\partial x_1} + \frac{\partial(u_1^n u_1^{n+1})}{\partial x_1} + \frac{\partial(u_2^{n+1}u_1^n)}{\partial x_2} + \frac{\partial(u_2^n u_1^{n+1})}{\partial x_2} + \right. \\
&\quad \left. \frac{\partial(u_3^{n+1}u_1^n)}{\partial x_3} + \frac{\partial(u_3^n u_1^{n+1})}{\partial x_3} \right) \approx \frac{1}{2} (Hu_1^{n+1} + Hu_1^n).
\end{aligned} \tag{3.7}$$

Therefore, equation (3.4) can be rearranged as below,

$$\left(\frac{1}{\Delta t} + N - \frac{1}{2Re} L \right) u_1^{n+1} + \frac{\partial}{\partial x_1} p^{n+1/2} = \left(\frac{1}{\Delta t} + \frac{1}{2Re} L \right) u_1^n + f_1. \tag{3.8}$$

With the introducing of a combined operator $M = N - \frac{1}{2Re} L$, and the pressure increase $\delta p^{n+1/2} = p^{n+1/2} - p^{n-1/2}$, equation (3.8) can be further rearranged as

below,

$$\left(\frac{1}{\Delta t} + M\right) u_1^{n+1} + \frac{\partial}{\partial x_1} \delta p^{n+1/2} = \left(\frac{1}{\Delta t} + \frac{1}{2Re} L\right) u_1^n - \frac{\partial}{\partial x_1} p^{n-1/2} + f_1. \quad (3.9)$$

Similarly, the time discretisation for the momentum equations in y and z directions are shown as below,

$$\left(\frac{1}{\Delta t} + M\right) u_2^{n+1} + \frac{\partial}{\partial x_2} \delta p^{n+1/2} = \left(\frac{1}{\Delta t} + \frac{1}{2Re} L\right) u_2^n - \frac{\partial}{\partial x_2} p^{n-1/2} + f_2. \quad (3.10)$$

$$\left(\frac{1}{\Delta t} + M\right) u_3^{n+1} + \frac{\partial}{\partial x_3} \delta p^{n+1/2} = \left(\frac{1}{\Delta t} + \frac{1}{2Re} L\right) u_3^n - \frac{\partial}{\partial x_3} p^{n-1/2} + f_3. \quad (3.11)$$

Up to this point, the original Navier-Stokes equations are discretised fully implicitly into equations (3.9), (3.10), (3.11), and subjected to the continuity equation constrain. Those equations can be then discretised in space using second-order finite volume method. The boundary conditions are:

- x direction: periodic boundary, *i.e.*,
 $u_i(L_x, y, z) = u_i(0, y, z)$ and $p(L_x, y, z) = p(0, y, z)$.
- y direction: no slip wall boundary, *i.e.*,
 1) $u_i(x, 0, z) = 0$ and $\partial p(x, 0, z)/\partial y = 0$ for bottom wall;
 2) $u_i(x, 2, z) = 0$ and $\partial p(x, 2, z)/\partial y = 0$ for top wall;
 3) corresponding wall velocity is applied if the wall is not stationary, *e.g.*, spanwise wall motion (chapter 4), travelling wave by spanwise wall velocity (chapter 7).
- z direction: periodic boundary, *i.e.*,
 $u_i(x, y, L_z) = u_i(x, y, 0)$ and $p(x, y, L_z) = p(x, y, 0)$.

The number of grid points in x , y and z directions of the interior domain are N_x , N_y and N_z , respectively, and a vector of freedom of $3N_x N_y N_z$ can be formed for the velocity, *i.e.*,

$$\begin{aligned} \mathbf{v}^{n+1} &= ((\mathbf{v}_1^{n+1})^T, (\mathbf{v}_2^{n+1})^T, (\mathbf{v}_3^{n+1})^T)^T \\ &= (u_{1|i=1}^{n+1}, u_{1|i=2}^{n+1}, \dots, u_{1|i}^{n+1}, \dots, u_{1|i=N_x N_y N_z - 1}^{n+1}, u_{1|i=N_x N_y N_z}^{n+1}, \\ &\quad u_{2|i=1}^{n+1}, u_{2|i=2}^{n+1}, \dots, u_{2|i}^{n+1}, \dots, u_{2|i=N_x N_y N_z - 1}^{n+1}, u_{2|i=N_x N_y N_z}^{n+1}, \\ &\quad u_{3|i=1}^{n+1}, u_{3|i=2}^{n+1}, \dots, u_{3|i}^{n+1}, \dots, u_{3|i=N_x N_y N_z - 1}^{n+1}, u_{3|i=N_x N_y N_z}^{n+1})^T. \end{aligned}$$

And a vector of freedom of $N_x N_y N_z$ can be formed for the pressure increase, *i.e.*,

$$\delta \mathbf{p}^{n+1/2} = (\delta p_{|i=1}^{n+1/2}, \delta p_{|i=2}^{n+1/2}, \dots, \delta p_{|i}^{n+1/2}, \dots, \delta p_{|i=N_x N_y N_z-1}^{n+1/2}, \delta p_{|i=N_x N_y N_z}^{n+1/2})^T.$$

Therefore, the temporal and spatial discretised Navier-Stokes equations can be written in the following matrix form,

$$\begin{pmatrix} \mathbf{A} & \mathbf{G} \\ \mathbf{D} & \mathbf{0} \end{pmatrix} \begin{pmatrix} \mathbf{v}^{n+1} \\ \delta \mathbf{p}^{n+1/2} \end{pmatrix} = \Delta t \begin{pmatrix} \mathbf{r} \\ \mathbf{0} \end{pmatrix} + \begin{pmatrix} \mathbf{mbc} \\ \mathbf{cbc} \end{pmatrix}, \quad (3.12)$$

$$\mathbf{A} = \mathbf{I} + \Delta t \mathbf{M},$$

$$\mathbf{r} = \frac{\mathbf{v}^n}{\Delta t} - G \mathbf{p}^{n-1/2} + \frac{1}{2Re} L \mathbf{v}^n + \mathbf{f},$$

where \mathbf{mbc} and \mathbf{cbc} store the boundary information for the momentum and continuity equations, respectively. \mathbf{A} is a matrix with size of $(3N_x N_y N_z)^2$.

An LU matrix approximation is employed to solve the above large matrix inversion problem. With a new notation $\delta \mathbf{v}^* = \mathbf{v}^* - \mathbf{v}^n$, where \mathbf{v}^* is the intermittent velocity field, equation (3.12) can be split into the following two equations,

$$\begin{pmatrix} \mathbf{A} & \mathbf{0} \\ \mathbf{D} & -\Delta t \mathbf{DG} \end{pmatrix} \begin{pmatrix} \delta \mathbf{v}^* \\ \delta \mathbf{p}^{n+1/2} \end{pmatrix} = \Delta t \begin{pmatrix} \mathbf{R} \\ \mathbf{0} \end{pmatrix} + \begin{pmatrix} \mathbf{mbc} \\ \mathbf{cbc} \end{pmatrix} + \begin{pmatrix} \Delta t \mathbf{MG} \delta \mathbf{p}^{n+1/2} \\ \mathbf{0} \end{pmatrix}, \quad (3.13)$$

$$\mathbf{R} = \mathbf{r} - \mathbf{A} \mathbf{v}^n.$$

$$\begin{pmatrix} \mathbf{I} & \Delta t \mathbf{G} \\ \mathbf{0} & \mathbf{I} \end{pmatrix} \begin{pmatrix} \mathbf{v}^{n+1} \\ \delta \mathbf{p}^{n+1/2} \end{pmatrix} = \begin{pmatrix} \mathbf{v}^* \\ \delta \mathbf{p}^{n+1/2} \end{pmatrix}. \quad (3.14)$$

Since the pressure is introduced in a δ form, the error term in the above approximation is second-order (Kim et al., 2002).

Finally, the procedure to solve the velocity and pressure is clear, and is listed as below:

- 1) solve $\delta \mathbf{v}^*$ using equation (3.13), and get \mathbf{v}^* subsequently;
- 2) solve pressure difference $\delta \mathbf{p}^{n+1/2}$ using equation (3.13);
- 3) solve velocity \mathbf{v}^{n+1} using equation (3.14);
- 4) get pressure $\mathbf{p}^{n+1/2}$.

The above procedure is essentially the same as the FSM used by Kim and Moin (1985), except that they need to consider the boundary condition for \mathbf{v}^* , and solve a scalar function for $\mathbf{p}^{n+1/2}$.

Since the coefficient matrix $\mathbf{A} = \mathbf{I} + \Delta t \mathbf{M}$ has the size of $(3N_x N_y N_z)^2$, the difficulty lies in how to invert the coefficient matrix \mathbf{A} efficiently in step 1). Matrix

\mathbf{A} can be written into small block matrix format as below,

$$\mathbf{A} = \mathbf{I} + \Delta t \mathbf{M} = \begin{pmatrix} \mathbf{I} + \Delta t \mathbf{M}_{11} & \Delta t \mathbf{M}_{12} & \Delta t \mathbf{M}_{13} \\ \Delta t \mathbf{M}_{21} & \mathbf{I} + \Delta t \mathbf{M}_{22} & \Delta t \mathbf{M}_{23} \\ \Delta t \mathbf{M}_{31} & \Delta t \mathbf{M}_{32} & \mathbf{I} + \Delta t \mathbf{M}_{33} \end{pmatrix}, \quad (3.15)$$

where \mathbf{M}_{ij} contains all the coefficients for the j^{th} velocity component δu_j in the i^{th} momentum equation. The structure of matrix \mathbf{A} is shown in figure 3.2.

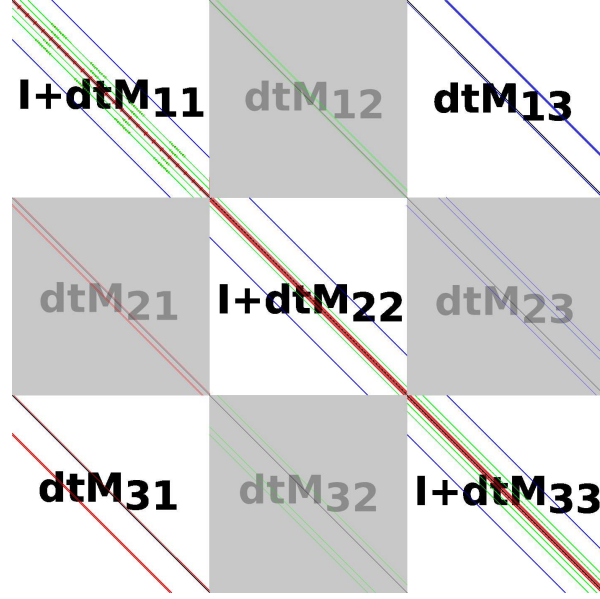


Figure 3.2: Structure of matrix \mathbf{A} . Coefficients in front of δu^* , δv^* and δw^* are coloured red, green and blue, respectively.

This matrix can again be approximated using LU matrices with a second-order accuracy (Kim et al., 2002),

$$\mathbf{A} = \begin{pmatrix} \mathbf{I} + \Delta t \mathbf{M}_{11} & \mathbf{0} & \mathbf{0} \\ \Delta t \mathbf{M}_{21} & \mathbf{I} + \Delta t \mathbf{M}_{22} & \mathbf{0} \\ \Delta t \mathbf{M}_{31} & \Delta t \mathbf{M}_{32} & \mathbf{I} + \Delta t \mathbf{M}_{33} \end{pmatrix} \begin{pmatrix} \mathbf{I} & \Delta t \mathbf{M}_{12} & \Delta t \mathbf{M}_{13} \\ \mathbf{0} & \mathbf{I} & \Delta t \mathbf{M}_{23} \\ \mathbf{0} & \mathbf{0} & \mathbf{I} \end{pmatrix} + \begin{pmatrix} O(\Delta t^2) \mathbf{J} \\ O(\Delta t^2) \mathbf{J} \\ O(\Delta t^2) \mathbf{J} \end{pmatrix}. \quad (3.16)$$

To further reduce the computational cost, the matrix $\mathbf{I} + \Delta t \mathbf{M}_{ii}$ can be approximated with a second-order accuracy (Kim et al., 2002) as below,

$$\begin{aligned} \mathbf{I} + \Delta t \mathbf{M}_{ii} &= \mathbf{I} + \Delta t \mathbf{M}_{ii}^z + \Delta t \mathbf{M}_{ii}^y + \Delta t \mathbf{M}_{ii}^x \\ &= (\mathbf{I} + \Delta t \mathbf{M}_{ii}^z)(\mathbf{I} + \Delta t \mathbf{M}_{ii}^y)(\mathbf{I} + \Delta t \mathbf{M}_{ii}^x) + O(\Delta t^2) \mathbf{J}. \end{aligned} \quad (3.17)$$

where $\mathbf{I} + \Delta t \mathbf{M}_{ii}^x$ only contains the coefficient for δu_1^* , $\mathbf{I} + \Delta t \mathbf{M}_{ii}^y$ only contains the coefficient for δu_2^* , $\mathbf{I} + \Delta t \mathbf{M}_{ii}^z$ only contains the coefficient for δu_3^* , and \mathbf{J} is the matrix of ones. Thus, the original inversion of a $(3N_x N_y N_z)^2$ size matrix \mathbf{A} is transferred to be the inversion of multiple tri-diagonal or pena-diagonal matrices with size of N_x^2 , or N_y^2 or N_z^2 .

Overall, the procedure to find $\delta \mathbf{v}^*$ in equation (3.13) is listed as below:

- $\delta \mathbf{v}_1^{**} = (\mathbf{I} + \Delta t \mathbf{M}_{11}^x)^{-1} (\mathbf{I} + \Delta t \mathbf{M}_{11}^y)^{-1} (\mathbf{I} + \Delta t \mathbf{M}_{11}^z)^{-1} \Delta t \mathbf{R}_1;$
- $\delta \mathbf{v}_2^{**} = (\mathbf{I} + \Delta t \mathbf{M}_{22}^x)^{-1} (\mathbf{I} + \Delta t \mathbf{M}_{22}^y)^{-1} (\mathbf{I} + \Delta t \mathbf{M}_{22}^z)^{-1} \Delta t (\mathbf{R}_2 - \mathbf{M}_{21} \delta \mathbf{v}_1^{**});$
- $\delta \mathbf{v}_3^{**} = (\mathbf{I} + \Delta t \mathbf{M}_{33}^x)^{-1} (\mathbf{I} + \Delta t \mathbf{M}_{33}^y)^{-1} (\mathbf{I} + \Delta t \mathbf{M}_{33}^z)^{-1} \Delta t (\mathbf{R}_3 - \mathbf{M}_{31} \delta \mathbf{v}_1^{**} - \mathbf{M}_{32} \delta \mathbf{v}_2^{**});$
- $\delta \mathbf{v}_3^* = \delta \mathbf{v}_3^{**};$
- $\delta \mathbf{v}_2^* = \delta \mathbf{v}_2^{**} - \Delta t \mathbf{M}_{23} \delta \mathbf{v}_3^{**};$
- $\delta \mathbf{v}_1^* = \delta \mathbf{v}_1^{**} - \Delta t \mathbf{M}_{12} \delta \mathbf{v}_2^{**} - \Delta t \mathbf{M}_{13} \delta \mathbf{v}_3^{**};$

In step 2), the Poisson equation for pressure (equation (3.13)) raised from the continuity constrain, needs to be solved. To be noticed, in the time splitting approach, the scalar in the Poisson equation is the modified pressure (Temam, 1991; Kim and Moin, 1985), *i.e.*, $G \delta p^{n+1/2} = G \delta \phi^{n+1/2} + \Delta t \mathbf{M} \mathbf{G} \delta \phi^{n+1/2}$. It has to be mentioned that, we approximate $\mathbf{B} = \Delta t \mathbf{I}$ in the “generalized block LU decomposition” (Perot, 1993), which traditionally only gives first-order accuracy, but it is the staggered in time arrangement of pressure that makes the error term $\Delta t \mathbf{M} \mathbf{G} \delta \phi^{n+1/2}$ second-order small, thus the overall splitting second-order accuracy (Kim et al., 2002). For a single pressure control volume, the governing equation is written as below,

$$\Delta t D G \delta p = D \delta \mathbf{u}^* - cbc. \quad (3.18)$$

Since \mathbf{u}^n is divergence free, *i.e.*, $D \mathbf{u}^n = 0$, equation (3.18) is equivalent to the one below,

$$D G \delta p = \frac{1}{\Delta t} (D \mathbf{u}^* - cbc) \equiv g. \quad (3.19)$$

Equation (3.19) can be transformed into Fourier space shown as below,

$$-k_x^2 \hat{\delta p}(k_x, y, k_z) + \frac{\partial^2 \hat{\delta p}(k_x, y, k_z)}{\partial y^2} - k_z^2 \hat{\delta p}(k_x, y, k_z) = \hat{g}(k_x, y, k_z), \quad (3.20)$$

where $\hat{\cdot}$ indicates the Fourier coefficient, and k_x, k_z are the streamwise and spanwise wavenumbers, respectively. Using finite volume to discretise the term $\frac{\partial^2 \hat{p}(k_x, y, k_z)}{\partial y^2}$, an algebra equation can be written as,

$$a_1 \hat{p}(k_x, y, k_z)_{i,j-1,k} + (a_2 - k_x^2 - k_z^2) \hat{p}(k_x, y, k_z)_{i,j,k} + a_3 \hat{p}(k_x, y, k_z)_{i,j+1,k} = \hat{g}(k_x, y, k_z), \quad (3.21)$$

where a_1, a_2 and a_3 are the derived coefficients. Once $\hat{p}(k_x, y, k_z)$ is solved, the pressure in physical space can be obtained by the inverse Fourier transform.

Up to this point, the whole procedure for the implicit fractional step method is finished. There are three second-order accuracy approximations, *i.e.*, equations (3.13), (3.16) and (3.17), thus it gives an overall second-order temporal accuracy. A minimum second-order central difference is used for the spatial discretisation, therefore it gives an overall spatial accuracy of second-order as well. The temporal and spatial accuracy tests were given by Kim et al. (2002) and Talha (2012), respectively.

To avoid the checkerboard effect, a staggered mesh is used, *i.e.*, the three velocity components are defined on different surfaces of the mesh cell, and the pressure is defined in the cell centre. The body force vector is treated in the same way as the velocity vector. For detailed staggered mesh arrangement, please refer to (Talha, 2012).

To make the code capable for high Reynolds number flow simulation, it is paralleled using the MPI library. Since direct solvers are used for all the matrix inversions, a 2DECOMP&FFT library (Li and Laizet, 2010) is implemented to satisfy this requirement, and also to guarantee the scalability of the code. Details about the implementation can be found in Hurst (2013). The paralleled code is highly scalable up to 1024 cores tested.

3.2 Coherent structure identification

The λ_2 criterion proposed by Jeong and Hussain (1995) is used in the present study to identify the vortex structures. λ_2 is the second largest eigenvalue of the gradient tensor $\mathbf{S}^2 + \mathbf{\Omega}^2$, where \mathbf{S} is the strain tensor, *i.e.*, $S_{ij} = \frac{1}{2} \left(\frac{\partial u_i}{\partial x_j} + \frac{\partial u_j}{\partial x_i} \right)$, and $\mathbf{\Omega}$ is the vorticity tensor, *i.e.*, $\Omega_{ij} = \frac{1}{2} \left(\frac{\partial u_i}{\partial x_j} - \frac{\partial u_j}{\partial x_i} \right)$. According to Jeong and Hussain (1995), the vortex cores correspond to regions, where the gradient tensor $\mathbf{S}^2 + \mathbf{\Omega}^2$ has at least two negative eigenvalues, equivalent to $\lambda_2 < 0$. Figure 7.5(a) shows a snapshot of the quasi-streamwise vortices in the buffer region identified by negative λ_2 value at $Re_\tau = 800$. Some hairpin structures can be observed, but majority of them are

single legged (Robinson, 1991). Essentially, there are two types of structures: the positive one rotating in clockwise direction ($\omega'_x > 0$) and the negative one rotating in anti-clockwise direction ($\omega'_x < 0$). However, the high population density and irregular shapes of these near wall structures make the view very difficult. Jeong et al. (1997) proposed an ensemble average method to extract the shapes of the positive and negative structures. This ensemble average method is adopted in the present study with a certain improvement. Detail of the ensemble average method and its validation is given in the following part.

Generally, the ensemble average method includes two procedures: 1) identifying the cores of the vortex structures; 2) selecting the identified vortex structures and conditionally average them. To identify the vortex cores, the local minima of the λ_2 value in a small window with a diameter of $D_c^+ = 20$ are detected in every yz plane. The two local minima in two adjacent yz planes are connected if they satisfy the following two criteria: a) the two points form a vector which has a streamwise angle $-45^\circ < \theta < 45^\circ$; b) the signs of the streamwise vorticity fluctuation ω'_x are the same at the two points. A typical identified λ_2 structure is shown in figure 3.3. This is a negative λ_2 structure, since $\omega'_x < 0$ for all the identified local minima. The quasi-streamwise vortices are within the buffer layer and have a typical length of $\lambda_x^+ \approx 300$, which can be read through the energy peak in pre-multiplied density spectrum $k_x k_z \Phi_{vv}$ (figure 3.12(b)), thus only those structures longer than $\lambda_x^+ = 150$ and within the near wall region $y^+ < 60$ are selected for the next procedure.

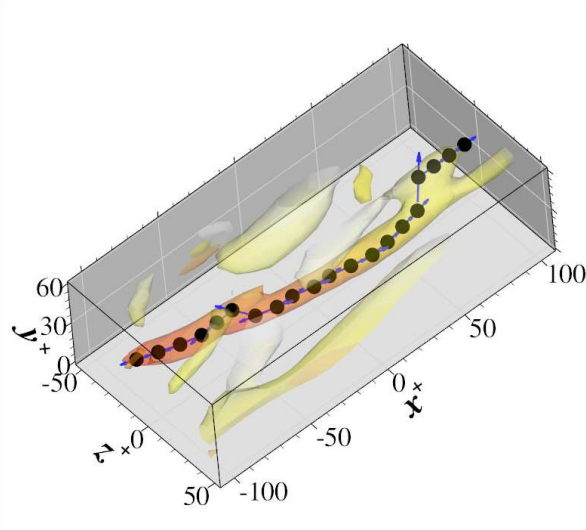


Figure 3.3: A typical identified λ_2 structure. Iso-surface is $\lambda_2^+ = -0.01$ coloured by wall distance. Black spheres indicate the selected local minima on each yz plane and blue arrows indicate the searching directions.

Once the positive (negative) λ_2 structures in the flow field are all identified, a crude averaged positive (negative) structure can be obtained by simply aligning the streamwise centres of the positive (negative) λ_2 structures and taking the average. Then the correlation between the crude positive (negative) averaged structure and each individual positive (negative) structure is calculated in a window size of $150 \times 60 \times 40$ wall units by shifting the individual positive (negative) structure for up to 30 wall units in x and z directions, while the y location is kept unchanged. If the maximum correlation is higher than 0.4, then the individual positive (negative) structure is retained; otherwise it is discarded. The remaining positive (negative) individual structures are averaged again by aligning the streamwise centre points of the structures. This procedure can be repeated for more than once to make sure the the remaining individual positive (negative) structures are highly correlated. At the same time, the velocity and pressure fields associated with each individual positive (negative) structure are also averaged to get the ensemble averaged flow fields. The final ensemble averaged positive (negative) λ_2 structures are calculated based on the ensemble averaged velocity field.

The ensemble averaged positive and negative λ_2 structures are shown in figure 3.4. A total of 10 well separated flow fields in time are used, and the total number of selected positive and negative λ_2 structures are 1601 and 1609, respectively. As observed from figure 3.4, the positive and negative structures are highly symmetric about streamwise direction. A rough measure by eyes suggests a $\pm 5^\circ$ tilting angle for positive and negative λ_2 structures; and a 10° inclination angle for both. This result is very close to the $\mp 4^\circ$ tilting angles, 9° inclination angle reported by Jeong et al. (1997), and the $\mp 6^\circ$ tilting angles, 9° inclination angle reported by Jung and Sung (2006).

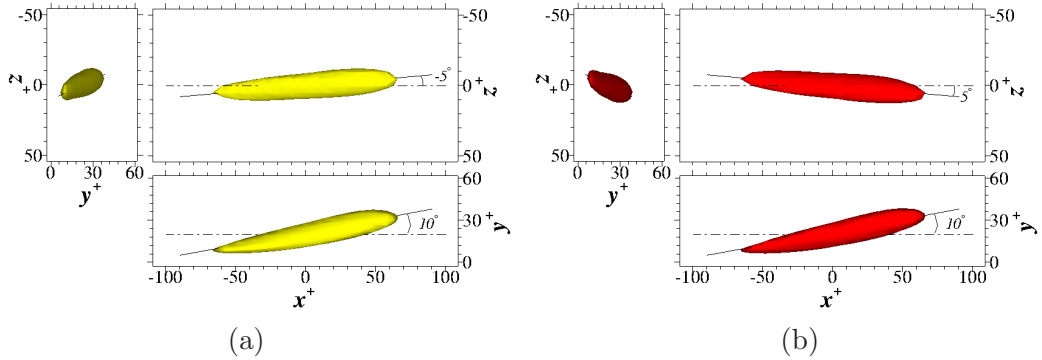


Figure 3.4: Ensemble averaged λ_2 structures ($\lambda_2^+ = -0.005$) in yz , xz and xy plane views: (a) positive one; and (b) negative one.

The quasi-streamwise vortices are Reynolds stress carrying eddies. The patterns for the three velocity fluctuation components, *i.e.*, u' , v' , w' , and the three Reynolds shear stress components, *i.e.*, $-u'v'$, $-v'w'$, $-u'w'$ in a yz plane cutting through the streamwise centre of the ensemble averaged λ_2 structures ($x = 0$) are shown in figure 3.5. Again, these patterns are symmetric or anti-symmetric between the positive and negative λ_2 structures. The Reynolds shear stress components show a very good agreement with the ensemble averaged data shown by Jeong et al. (1997) (figure 13 of their paper). The high- and low-speed streaks can be well observed on both sides of the λ_2 structures, with the high-speed streak peaking at $y^+ \approx 23$ and the low-speed streak peaking at $y^+ \approx 11$. The high-speed streak is associated with Q4 event (sweep), and the low-speed streak is associated with Q2 event (ejection). Both Q4 and Q2 create positive streamwise Reynolds shear stress $-\overline{u'v'}$, as shown by two positive peaks in the left and right sides of the positive and negative λ_2 structures in figure 3.5(d). The negative contribution to $-\overline{u'v'}$ from Q3 and Q1 events are on the top and bottom sides of the λ_2 structures. The different peak locations of the high- and low-speed streaks agree with the quadrant analysis result by Kim et al. (1987), who reported that sweep events dominated in the near wall region, and ejection events dominated in the region further away from the wall, with the crossing point at $y^+ \approx 12$. The high skin-friction region associated with the λ_2 structures is clearly displayed in figure 3.5.

3.3 Proper orthogonal decomposition

Proper orthogonal decomposition (POD), also known as Karhunen-Lo  ve decomposition (KL) provides a set of bases to study multi-scale turbulent flow (Berkooz et al., 1993), in the sense that the energy decays the fastest across all the modes. In this case, the key turbulent dynamics can be captured by a small number of leading order POD modes. The modes in POD are not pre-fixed, but in the periodic direction the POD modes are statistically equivalent to Fourier modes. In the present numerical channel flow, POD is only used for the wall normal direction, while direct Fourier transform is used for streamwise and spanwise directions.

For the one dimensional POD modes in wall normal direction, the three velocity fluctuation components form a vector $\phi(y)$ as below,

$$\begin{aligned} \phi(y) = [& u'(y_1), u'(y_2), \dots, u'(y_j), \dots, u'(y_{N_y-1}), u'(y_{N_y}), \\ & v'(y_1), v'(y_2), \dots, v'(y_j), \dots, v'(y_{N_y-1}), v'(y_{N_y}), \\ & w'(y_1), w'(y_2), \dots, w'(y_j), \dots, w'(y_{N_y-1}), w'(y_{N_y})]^T. \end{aligned} \quad (3.22)$$

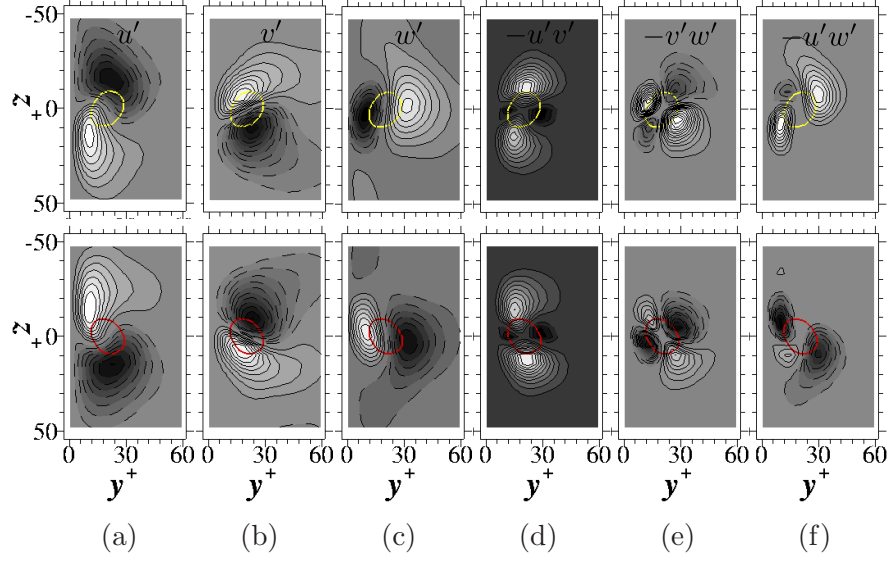


Figure 3.5: Patterns of Reynolds stresses in a yz plane ($x = 0$) cutting through the streamwise centres of the ensemble averaged positive (top row) and negative (bottom row) λ_2 structures: (a) u' ; (b) v' ; (c) w' ; (d) $-u'v'$; (e) $-v'w'$ and (f) $-u'w'$. λ_2 structures in the yz planes are indicated by contour lines $\lambda_2^+ = -0.005$. Bright (dark) colour is for high (low) value. Negative contour lines are dashed.

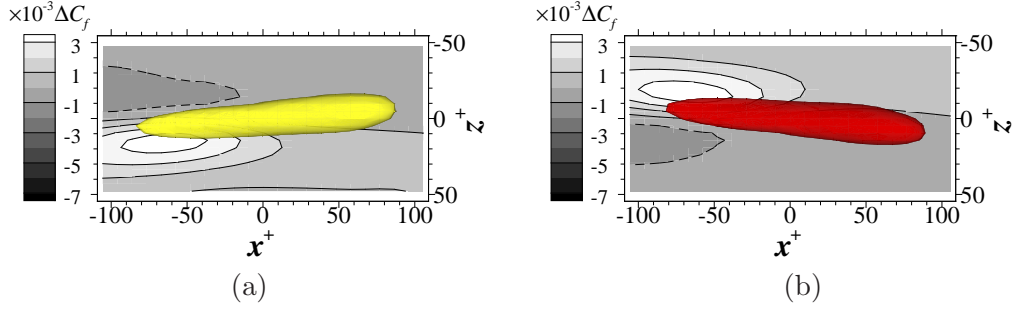


Figure 3.6: Skin-friction associated with: (a) positive λ_2 structure; and (b) negative λ_2 structure. Full wall surface averaged C_f has been subtracted.

Thus the POD modes are defined in the sense to give the fastest spectrum decay rate for the turbulent kinetic energy, $k = \frac{1}{2} \|\phi(y)\|^2$. A space and time averaged correlation tensor can be defined, $\mathbf{R} = \langle \phi(y) \phi(y')^T \rangle_{x,z}$ for the velocity vector $\phi(y)$. The POD essentially solves the following eigenvalue problem,

$$\int_0^1 \mathbf{R} \psi^{(n)}(y) dy = \lambda^{(n)} \psi^{(n)}(y), \quad (3.23)$$

where $\psi^{(n)}(y)$ and $\lambda^{(n)}$ are the n^{th} eigenfunction and eigenvalue. $\psi^{(n)}(y)$ represents

the n^{th} POD mode, and $\lambda^{(n)}$ represents the energy associated with the n^{th} POD mode, and

$$\|\phi(y)\|^2 = \sum_{n=1}^{3N_y} \lambda^{(n)}. \quad (3.24)$$

Since the correlation tensor \mathbf{R} is Hamiltonian, all the eigenvectors are orthogonal to each other. Moreover, they are normalised, so that,

$$\int_0^1 \psi^{(n)}(y) \psi^{(m)}(y) dy = \begin{cases} 1, & \text{if } m = n, \\ 0, & \text{if } m \neq n. \end{cases} \quad (3.25)$$

To be noticed that, this decomposition can be applied in any wall normal region $[y_{min}, y_{max}]$. The smaller $(y_{max} - y_{min})$ is, the faster convergence can be achieved. The NAG[®] library is employed to solve equation (3.23). Since a non-uniform grid is used in the y direction (equation (3.30)), following Moin and Moser (1989) and Ball et al. (1991), a coordinate transformation is employed to preserve the symmetry of \mathbf{R} , thus equation (3.23) can be transformed to a symmetric matrix problem, *i.e.*,

$$\left(\zeta^{1/2} \mathbf{R}_{ij} \zeta^{1/2} \right) \left(\zeta^{1/2} \psi^{(n)} \right) = \lambda^{(n)} \left(\zeta^{1/2} \psi^{(n)} \right), \quad (3.26)$$

where $\zeta = \zeta^{1/2} \zeta^{1/2} = [\Delta y_1, \Delta y_2, \dots, \Delta y_{N_y}, \Delta y_1, \Delta y_2, \dots, \Delta y_{N_y}, \Delta y_1, \Delta y_2, \dots, \Delta y_{N_y}]^T$.

The above approach is called direct POD method, which is suitable for low freedom vector ϕ (Berkooz et al., 1993). For example, in the present one dimensional case, the freedom of ϕ is $3N_y$, and the size of \mathbf{R} is $(3N_y)^2$. However, when the freedom of vector ϕ is large, which is especially true for two dimensional and three dimensional turbulent databases, solving equation (3.23) is computational expensive. Fortunately, in two or three dimensional cases, the number of available flow fields (snapshots) N_t is typically lower than the freedom of a single flow field, thus the snapshot method can be used to save the computational cost (Sirovich, 1987). The idea is to change the kernel in equation (3.23) from a spatial correlation tension \mathbf{R} to a temporal correlation tensor \mathcal{K} , which is defined as below,

$$\mathcal{K}_{ij} = \int_0^1 \phi(y, t_i) \phi(y, t_j) dy. \quad (3.27)$$

Thus, equation (3.23) becomes

$$\int_t \mathcal{K} \varphi^{(m)}(t) dt = \lambda^{(m)} \varphi^{(m)}(t), \quad (3.28)$$

where $\max\{m\} = N_t$, smaller than the eigenvector space in the direct POD method. Then the final eigenvector can be calculated by projecting all the snapshots $\phi(y, t)$ into the vector $\varphi^{(m)}(t)$, *i.e.*,

$$\psi^{(m)}(y) = \int_t \phi(y, t) \varphi^{(m)}(t) dt. \quad (3.29)$$

For more detailed theory, please refer to Sirovich (1987).

Figure 3.7 shows the first four POD modes for streamwise, wall normal and spanwise velocity fluctuation components, u' , v' and w' . Following the assumption given by Moin and Moser (1989), w' is taken to be uncorrelated with u' and v' in the current channel flow, thus w' is set to be zero in $\phi(y)$ when calculating the POD modes for u' and v' ; similarly, both u' and v' are set to be zeros in $\phi(y)$ when calculating the POD modes for w' . Both direct POD and snapshot POD methods are used for this calculation, and they show a very good agreement with each other, and also with the result from Moin and Moser (1989) at a slightly lower Reynolds number, $Re_\tau = 180$. The peak locations calculated by Moin and Moser (1989) are all slightly closer to the wall, which may come from the effect of different wall normal coordinate used. Similar to the Fourier modes, higher POD mode has more local minima and maxima.

Table 3.1 shows the turbulent kinetic energy contributions from the first four POD modes compared with Moin and Moser (1989), Sen et al. (2007). A reasonable agreement is achieved. To capture 90% total kinetic energy, 15 POD modes are needed for the present data, while only 10 POD modes for Moin and Moser (1989), Sen et al. (2007), which suggests that POD is indeed a powerful tool for turbulent dimension reduction analysis.

Table 3.1: Contributions to turbulent kinetic energy k from different POD modes.

Case	$\lambda_1/(2k)$	$\lambda_2/(2k)$	$\lambda_3/(2k)$	$\lambda_4/(2k)$	90% of TKE
Present study	0.291	0.155	0.085	0.059	15
Moin and Moser (1989)	0.32	0.16	0.08	-	10
Sen et al. (2007)	0.28	0.16	0.085	0.05	10

Even though snapshot POD can significantly reduce the computational cost, the convergence rate is slow for three dimensional flow fields. By taking advantage of the periodic boundary in the streamwise and spanwise directions, the three dimensional POD can be reduced to a one dimensional POD in Fourier space for each wave pair (m, n) , where m and n are the integer numbers of sinusoidal waves in the

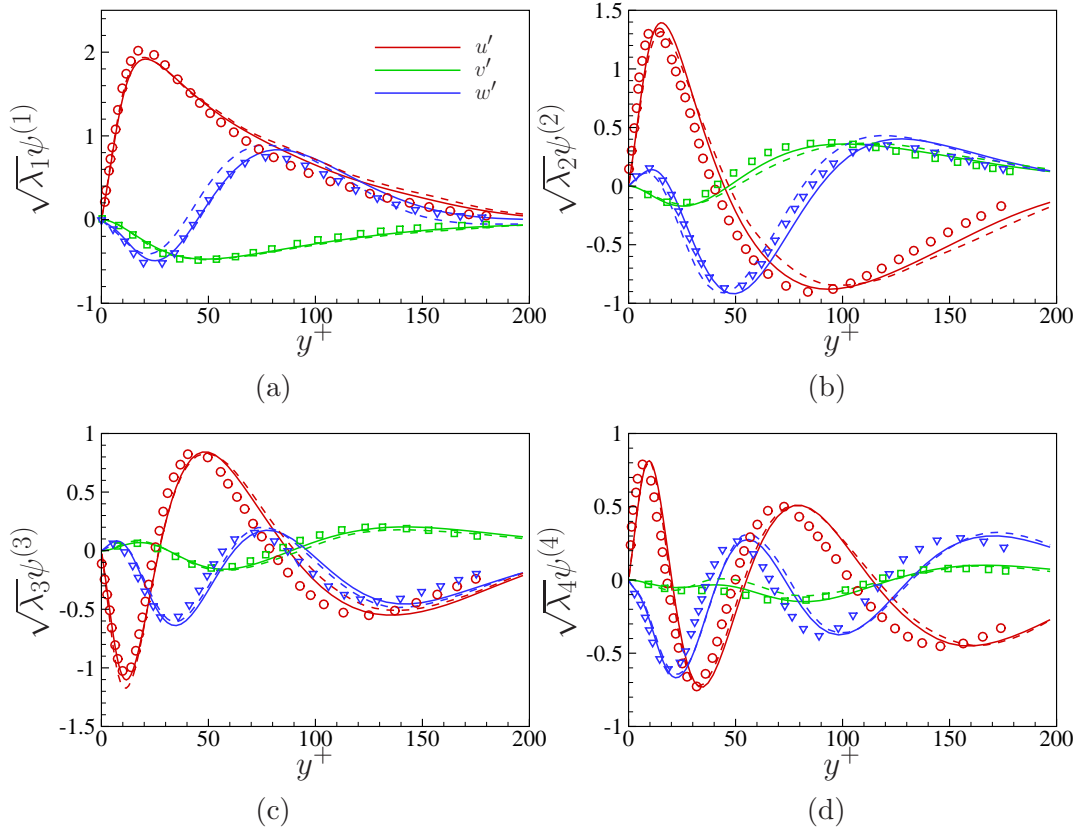


Figure 3.7: The first four POD modes for velocity fluctuations, u' , v' , w' : (a) first mode $\sqrt{\lambda_1}\psi^{(1)}$; (b) second mode $\sqrt{\lambda_2}\psi^{(2)}$; (c) third mode $\sqrt{\lambda_3}\psi^{(3)}$; and (d) fourth mode $\sqrt{\lambda_4}\psi^{(4)}$. Solid lines are calculation using direct POD method; dashed lines are calculated using snapshot POD method; and symbols are data from Moin and Moser (1989).

streamwise and spanwise directions, *i.e.*, $\lambda_x = \frac{L_x}{m}$, $\lambda_z = \frac{L_z}{n}$. Then equations (3.22) to (3.26) can be written in the complex space for vector $\hat{\phi}(m, n, y)$ (see detail in Moin and Moser (1989), Ball et al. (1991)). After solving the eigenvalue problem, a total number of q (an integer number) POD modes in y direction are found for each (m, n) pair. Thus a single three dimensional POD mode is indicated by a quantum group (m, n, q) . Considering the first POD mode in wall normal direction $q = 1$ for all the wave pairs (m, n) , this gives the characteristic eddy in the turbulent field, as defined by Moin and Moser (1989). Figure 3.8 shows the characteristic eddy in a three dimensional view when the phase difference between each mode and its reference phase is zero. It shows a high-speed streak with two low-speed streaks accompanying aside. From a yz plan view, the spanwise spacing between the high- and low-speed streaks is $\lambda_z^+ \approx 50$ in the near wall region, but the spacing increases

as the wall normal distance becomes larger. The high-speed streak has a very long tail in the near wall region, and a round head in the channel centre. This agrees with that channel turbulence becomes more isotropic as it leaves the near wall region to the channel centre, and again it is reminiscent of Townsend’s double cone eddies (Townsend, 1976). Due to the homogeneity of the flow in the spanwise direction, when a phase difference of π is used between each POD mode with its reference phase, a similar characteristic eddy is expected, but the high- and low-speed streaks swap positions in the spanwise direction. The captured characteristic eddy is similar to those shown by Moin et al. (1989) and Moarref and Jovanović (2012), and it is a perfect low dimensional structure for understanding the effect of flow control, which is going to be discussed in the following chapters.

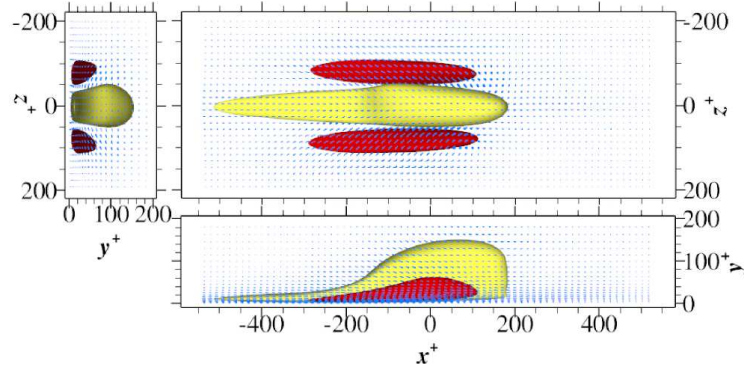


Figure 3.8: The characteristic eddy identified in CH200 case. Iso-surfaces are $u' = -0.35$ (red) and $u' = 0.35$ (yellow).

3.4 Grid resolution and domain size test

3.4.1 No control baseline cases study

A survey of the grid resolution and domain size for DNS channel at low Reynolds numbers is shown in table 3.2. Based on the grid study by Hurst (2013), who used the same code as the present one, the baseline simulation in the present study C0 is set as in table 3.2. The turbulent statistics for the baseline case C0 gives a very good agreement with literature data, as shown in figure 3.9 for the streamwise mean velocity, velocity fluctuation, Reynolds shear stress and vorticity fluctuation profiles.

As C0 case working as the baseline, the grid resolution in each direction, x , y and z is reduced separately. It is noticed that, a hyper-tangent function is used in the wall normal direction, and the grid coordinate is controlled by the total number

Table 3.2: Grid resolution and domain size used in literature.

Source	Re_τ	$\Delta x^+ \times (\Delta y_{min}^+ \sim \Delta y_{max}^+) \times \Delta z^+$	$L_x \times L_y \times L_z$
1 [†]	180	$12 \times (0.05 \sim 4.4) \times 7$	$4\pi \times 2 \times 2\pi$
2 [†]	180	$17.7 \times (0.05 \sim 5.9) \times 4.4$	$4\pi \times 2 \times 4\pi/3$
3 [†]	180	$8.9 \times (? \sim 6.1) \times 4.5$	$12\pi \times 2 \times 4\pi$
4 [†]	200	$15.7 \times (0.8 \sim 5.4) \times 6.5$	$4\pi \times 2 \times 4\pi/3$
5 [†]	200	$17 \times (0.7 \sim 6.2) \times 8.3$	$4\pi \times 2 \times 2\pi$
C0	196	$5.0 \times (0.1 \sim 2.5) \times 2.5$	$16 \times 2 \times 6$

[†] 1: Kim et al. (1987); 2: Moser et al. (1999); 3: del Álamo and Jiménez (2003); 4: Quadrio and Ricco (2003); 5: Touber and Leschziner (2012).

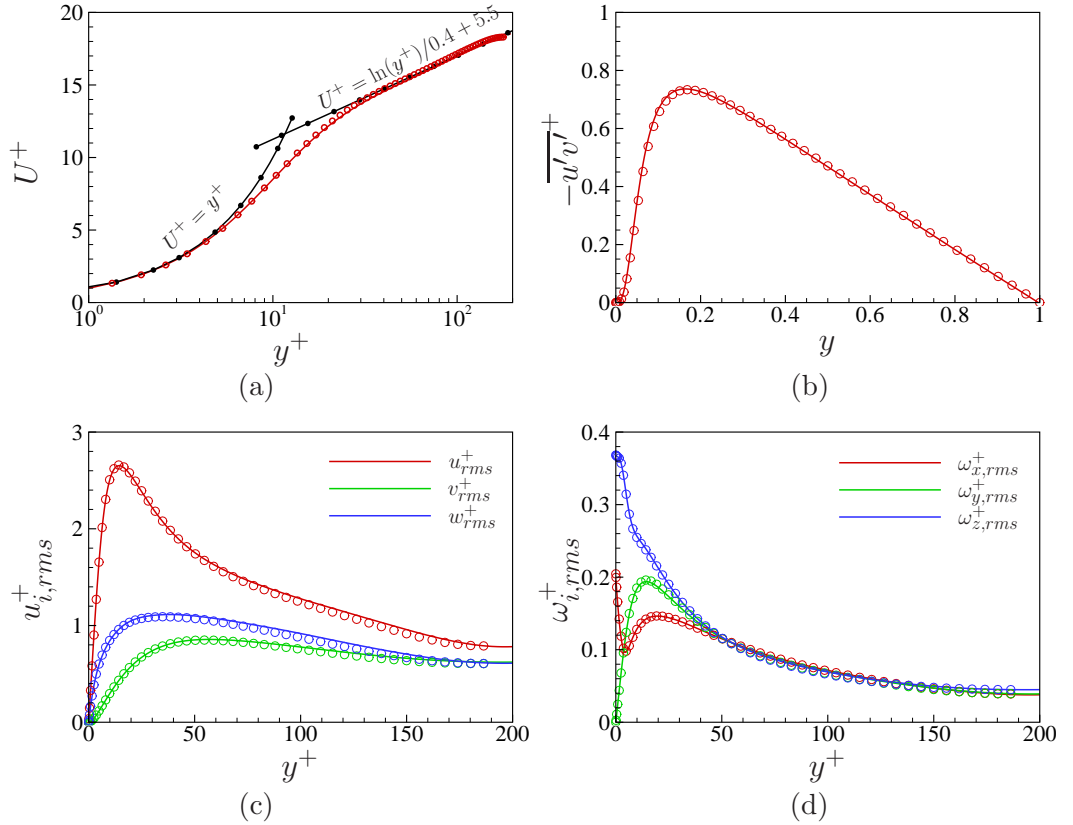


Figure 3.9: Comparison of turbulent statistics between present baseline case C0 at $Re_\tau = 200$ (lines) with del Álamo and Jiménez (2003) at $Re_\tau = 180$ (symbols): (a) U ; (b) $-\overline{u'v'}^+$, (c) $u_{i,rms}^+$ and (d) $\omega_{i,rms}^+$.

of grid points N_y and a stretching parameter α , shown as below,

$$y_j = \frac{\tanh \left[\alpha \left(\frac{2(j-1)}{N_y} - 1 \right) \right]}{\tanh(\alpha)}. \quad (3.30)$$

The grid resolutions considered are given in table 3.3. A parameter χ is defined for the grid resolution change, *i.e.*, $\chi = \Delta x^+ / \Delta x_{C0}^+$ for the x direction; $\chi = \Delta y_{min}^+ / \Delta y_{min,C0}^+$ and $\chi = \Delta y_{max}^+ / \Delta y_{max,C0}^+$ for the y direction; and $\chi = \Delta z^+ / \Delta z_{C0}^+$ for the z direction. Figure 3.10 shows the actual friction Reynolds number Re_τ for a fixed bulk mean Reynolds number $Re = U_m h / \nu = 3150$. According to Dean's correlation (Dean, 1978), *i.e.*, $C_f = 0.073(2Re)^{-1/4}$ (or $Re_\tau = 0.175Re^{7/8}$), it gives the corresponding friction Reynolds number of $Re_\tau = 201.6$. As shown in figure 3.10, $Re_\tau = 196$ is calculated for the baseline case C0, and it is very sensitive to the streamwise grid resolution, while it only has a small variation for a wide range of the grid resolutions in the spanwise and wall normal directions. The changes of u_{rms}^+ and ω_y^+ peaks are shown in figure 3.11. It is obvious that: 1) the grid resolution change in the y direction has a very weak effect on the u_{rms}^+ and $\omega_{y,rms}^+$ peaks for the χ range considered; 2) u_{rms}^+ peak is more sensitive to Δx^+ , while ω_y^+ peak is more sensitive to Δz^+ . Overall the grid test result suggests that the baseline case C0 achieves a similar accuracy as the spectra code by del Álamo and Jiménez (2003), and the present simulation accuracy is acceptable for $\chi \leq 2.0$.

Table 3.3: Tested grid resolutions in x , y and z directions separately. (\dagger indicates the grid resolution used for the baseline case C0.)

Δx^+	2.5	5.0 \dagger	7.5	10.0	12.5	15.0	20.0
Δz^+	2.5 \dagger	3.75	5	6.25	7.5	10.0	
Δy_{min}^+	0.1 \dagger	0.2	0.3	0.4	0.5	0.6	0.7
$\hookrightarrow \alpha$	2.04	1.95	1.73	1.58	1.42	1.34	1.25
Δy_{max}^+	2.5 \dagger	3.0	4.0	5.0	6.0	7.0	8.0
$\hookrightarrow \alpha$	2.04	2.38	2.54	2.64	2.73	2.84	2.92

To check the effect of domain size, the domain size for C0 is doubled but with the same grid resolution (CH200L, see table 3.4), then the two dimensional spectra are checked (The definition of the density spectra is given in appendix B). Figure 3.12 shows the comparison between the present CH200, CH200L cases and the $Re_\tau = 180$ data from del Álamo and Jiménez (2003): 1) The present simulation data at $Re_\tau = 200$ for both CH200 and CH200L cases shows a very good agreement with the canonical DNS database for all the Reynolds stress components ($\overline{v'u'}$ and $\overline{u'w'}$ are zero for the canonical turbulent channel). 2) Even though the turbulent statistics show a very good agreement with literature data (figure 3.9) for CH200, the two dimensional spectra clearly suggest that the domain is not long enough, especially for the streamwise Reynolds stress $\overline{u'u'}$. However, the width of the domain

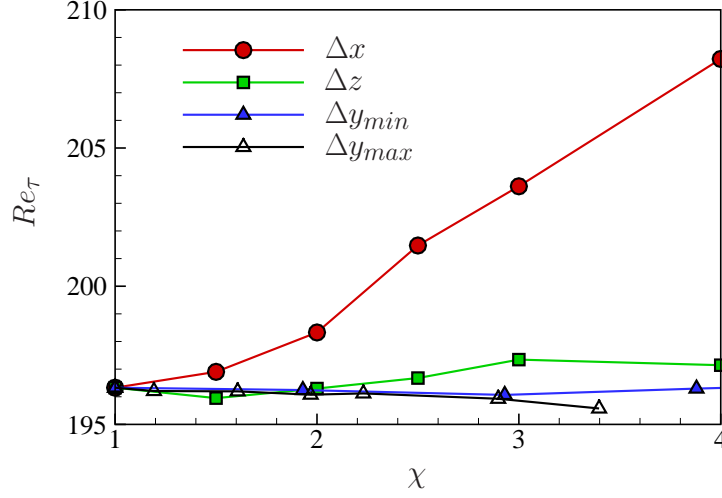


Figure 3.10: Sensitivity of calculated friction Reynolds number Re_τ to grid resolutions.

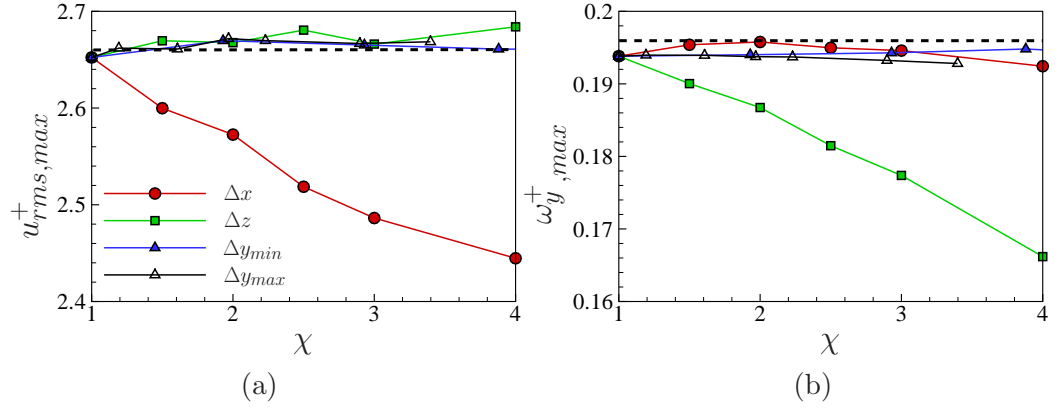


Figure 3.11: Sensitivity of statistics peak values to grid resolutions: (a) u_{rms}^+ and (b) ω_y^+ . Dashed lines indicate the corresponding values from del Álamo and Jiménez (2003).

for CH200 is large enough, apart from the spanwise Reynolds stress $\overline{w'w'}$, for which a small amount of energy is contained in scales wider than $\lambda_z^+ = 1200$. 3) It is well known that the size of the near wall streaks in the buffer region is scaled in wall units, *i.e.*, $\lambda_x^+ \approx 10^3$ and $\lambda_z^+ \approx 10^2$, which are clearly shown as a dominant energy peak in figure 3.12(a). At the present low Reynolds number, the domain length in wall units is even too small for both the CH200L and the case by del Álamo and Jiménez (2003) ($L_x = 12\pi$ and $L_z = 4\pi$, see table 3.2), since the spectrum tails at long wavelength for $k_x k_z \Phi_{uu}$ and $k_x k_z \Phi_{uv}$ are clearly chopped beyond the

domain length. However, the domain length seems to be just long enough for the wall normal and spanwise Reynolds stresses, *i.e.*, $\overline{v'v'}$, $\overline{w'w'}$.

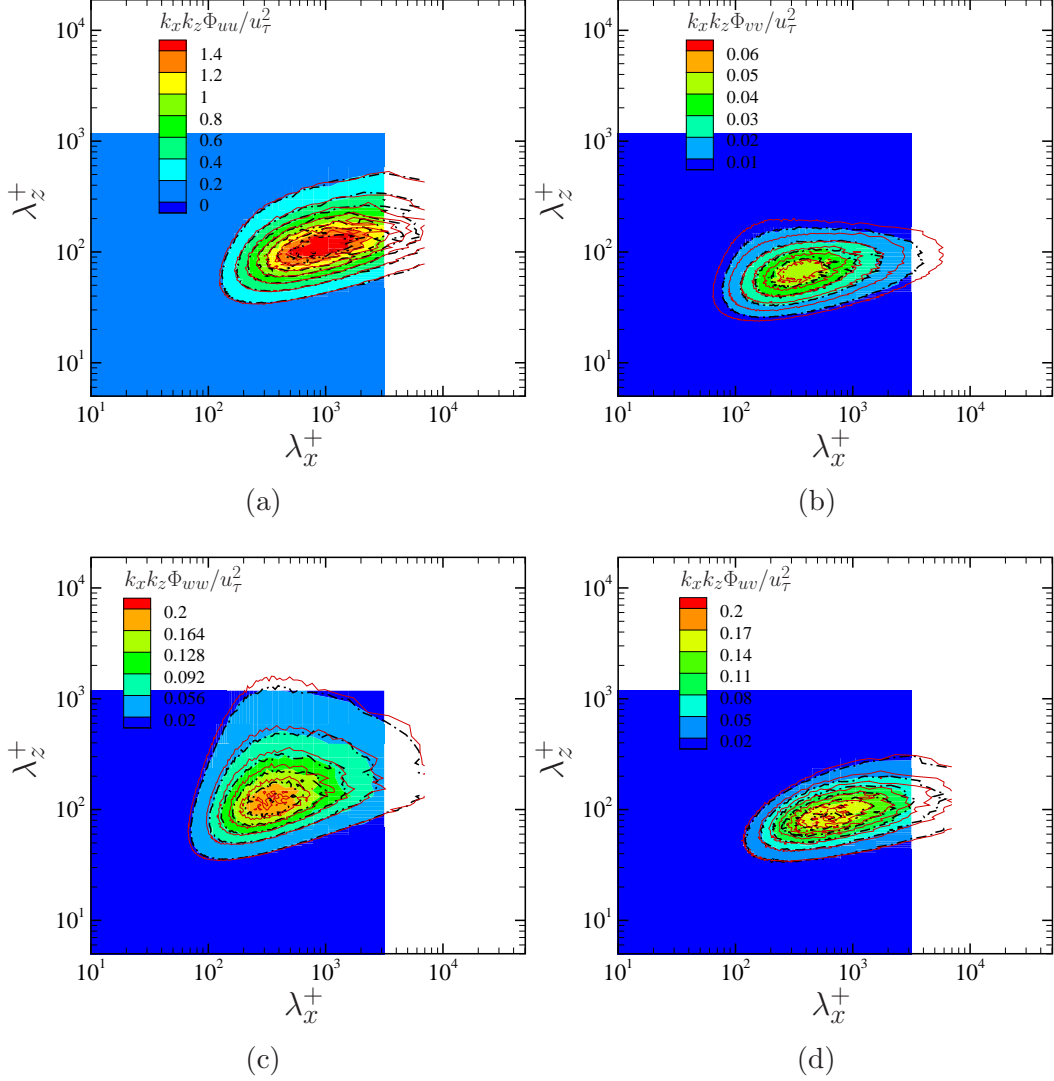


Figure 3.12: Comparison of two dimensional pre-multiplied density spectra at $y^+ \approx 15$ among CH200 (shaded contour), CH200L (dash-dotted contour lines) and literature data at $Re_\tau = 180$ from del Álamo and Jiménez (2003) (solid contour lines) for (a) $k_x k_z \Phi_{uu}$, (b) $k_x k_z \Phi_{vv}$, (c) $k_x k_z \Phi_{ww}$, and (d) $k_x k_z \Phi_{uv}$.

The accumulative one dimensional density spectra along streamwise and spanwise wavelengths are shown in figure 3.13. This is done by integrating the density spectrum in a wavenumber range of $(0, k_x]$ or $(0, k_z]$, so that, a quantitative comparison of the accumulated energy can be made starting from the largest scale to the scale considered. In these plots, the total Reynolds stress $\overline{u'_i u'_j}$ can be read

at the smallest wavelength λ_x^+ (or λ_z^+) (a direct comparison with figures 3.9(b) and 3.9(c)). Due to the restriction of available online data, the one dimensional spectra are compared at $y^+ \approx 10$, and the literature data is taken from Moser et al. (1999) at $Re_\tau = 180$, where a smaller domain was used ($L_x = 4\pi$ and $L_z = 4\pi/3$) compared to del Álamo and Jiménez (2003). Since a staggered grid is used in the present simulation, no attempt is tried to interpolate the spectrum, thus the wall normal location for the spectra of $\overline{u'u'}$ and $\overline{w'w'}$ is half grid shifted from that of $\overline{v'v'}$. Therefore, the total energy of $\overline{v'v'}$ is slightly lower than that given by Moser et al. (1999), but the agreement in $\overline{u'u'}$ and $\overline{w'w'}$ is very good. The spectrum of $\overline{u'v'}$ is not given by Moser et al. (1999), and the negative portion in figure 3.13(b) is truncated. As can be seen from 3.13, the domain size affects the energy distribution among different scales. For example, the tails of the largest wavelengths are lifted up when the domain size is reduced, while the domain size effect on the small wavelength side is nearly negligible. Overall, a large enough domain size is important for scales interaction study in the turbulent field, but the scale integrated turbulent statistics, such as Reynolds stresses, are less sensitive to the domain size when the domain is larger than CH200 case.

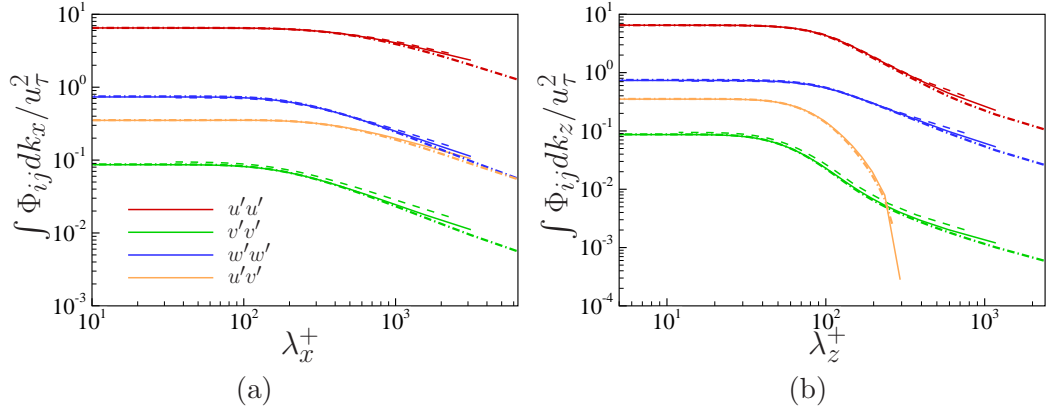


Figure 3.13: Comparison of one dimensional accumulated density spectra at $y^+ \approx 10$ among CH200 (solid lines), CH200L (dash-dotted lines) and literature data at $Re_\tau = 180$ from Moser et al. (1999) (dashed lines) for (a) streamwise wavelength λ_x^+ and (b) spanwise wavelength λ_z^+ .

Based on the baseline case (C0) study, the final grid resolution and domain size are chosen for another three higher Reynolds numbers, as shown in table 3.4. It can be noticed that the grid resolution and domain size are slightly reduced in the streamwise and spanwise directions at three higher Reynolds numbers, which is due to the consideration of computational cost. A check of the turbulent kinetic energy

budgets ($k = \frac{1}{2}(u'^2 + v'^2 + w'^2)$) is shown in figure 3.14. The agreement between the present high Reynolds number simulations and the literature data from del Álamo and Jiménez (2003), Hoyas and Jiménez (2006) is still very good. The two dimensional pre-multiplied density spectra for the streamwise Reynolds stress $k_x k_z \Phi_{uu}$ at $Re_\tau = 400, 800$ and 1600 are shown in figure 3.15. As Reynolds number increases, the dominant peak is better captured in the domain. However, the footprints of the large outer scale motions become more and more important, as can be seen in figure 3.15(c) at $Re_\tau = 1600$. For the canonical channel flow at high Reynolds numbers, much larger domain size has been used in literature, for instant, $L_x = 8\pi$, $L_z = 4\pi$ at $Re_\tau = 550$ (del Álamo and Jiménez, 2003), $L_x = 8\pi$, $L_z = 3\pi$ at $Re_\tau = 950$ (Hoyas and Jiménez, 2006), and $L_x = 8\pi$, $L_z = 3\pi$ at $Re_\tau = 2000$ (Hoyas and Jiménez, 2006). As a careful interpolation of the large scale effect in the following chapters, a domain size doubled case at $Re_\tau = 800$ is also performed, *i.e.*, CH800L.

Table 3.4: Final grid resolution and domain size adopted for the four Reynolds numbers studied.

Case	Re_τ	Re	Δx^+	Δy_{min}^+	Δy_{max}^+	Δz^+	Δt^+	L_x	L_z
CH200	196	3150	5.0	0.4	6.0	2.5	0.2	16.0	6.0
CH200L	196	3150	5.0	0.4	6.0	2.5	0.2	32.0	12.0
CH400	397	7000	10.0	0.4	7.2	5.0	0.2	16.0	6.0
CH800	801	15700	10.0	0.4	9.7	5.0	0.2	12.0	4.0
CH800L	797	15700	5.0	0.4	9.7	5.0	0.2	24.0	8.0
CH1600	1609	34500	10.0	0.4	9.2	5.0	0.2	12.0	4.0

3.4.2 Control baseline cases study

A fully developed turbulent flow field from the no control baseline case C0 is used as the initial field for the flow control. In the present studies, we consider three different types of spanwise motions generated by 1) spanwise wall velocity; 2) spanwise Lorentz force; and 3) spanwise plasma actuators. Figure 3.16 shows the response of the normalised skin-friction after the control is activated (at $t = 0$). All the three controls show two separated stages: 1) a transient response, and 2) a new equilibrium stage. As has been noticed by Quadrio and Ricco (2003) and Ricco and Hahn (2013), the length of the transient period depends on both the control parameters and the final skin-friction state. Generally, a higher drag reduction case has a longer transient period. The longest transient period appears for ST1 configuration using plasma actuators, because a steady plasma body force is used, and it

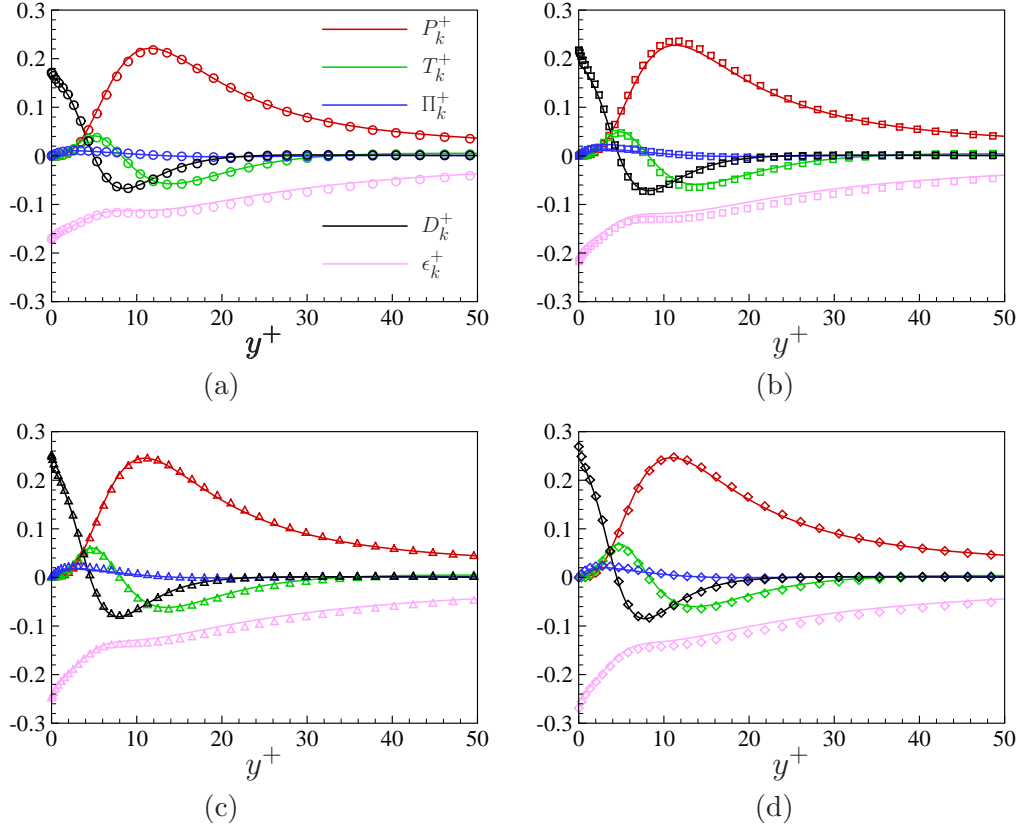


Figure 3.14: Turbulent kinetic energy k budgets comparison between present simulation at four Reynolds numbers (lines) with those from literature (symbols): (a) $Re_\tau = 200$; (b) $Re_\tau = 400$; (c) $Re_\tau = 800$ and (d) $Re_\tau = 1600$. The symbols in (a)(b)(c)(d) are for $Re_\tau = 180$ (del Álamo and Jiménez (2003)), $Re_\tau = 395$ (Moser et al. (1999)), $Re_\tau = 950$ (Hoyas and Jiménez (2006)) and $Re_\tau = 2000$ (Hoyas and Jiménez (2006)), respectively.

takes a very long time for the spanwise mean velocity profile to be developed. After the mean level of C_f settles down, the C_f trajectories show an oscillation with two different time scales: a small one associated with the control forcing, and a large one associated with the outer large scale motions (Touber and Leschziner, 2012). One particular case (W-OC, $A_w^+ = 12$, $\omega^+ = 0.01$) is chosen to show the very large C_f variation caused by the control when the forcing period is low. This kind of behaviour makes the C_f prediction expensive due to a long sampling time required. Hurst et al. (2014) has shown a big variation in the \mathcal{DR} prediction among literature data for the spanwise wall oscillation case, even when the control parameters are very close to each other.

In the present study, all the flow controls are applied at a constant mass flow

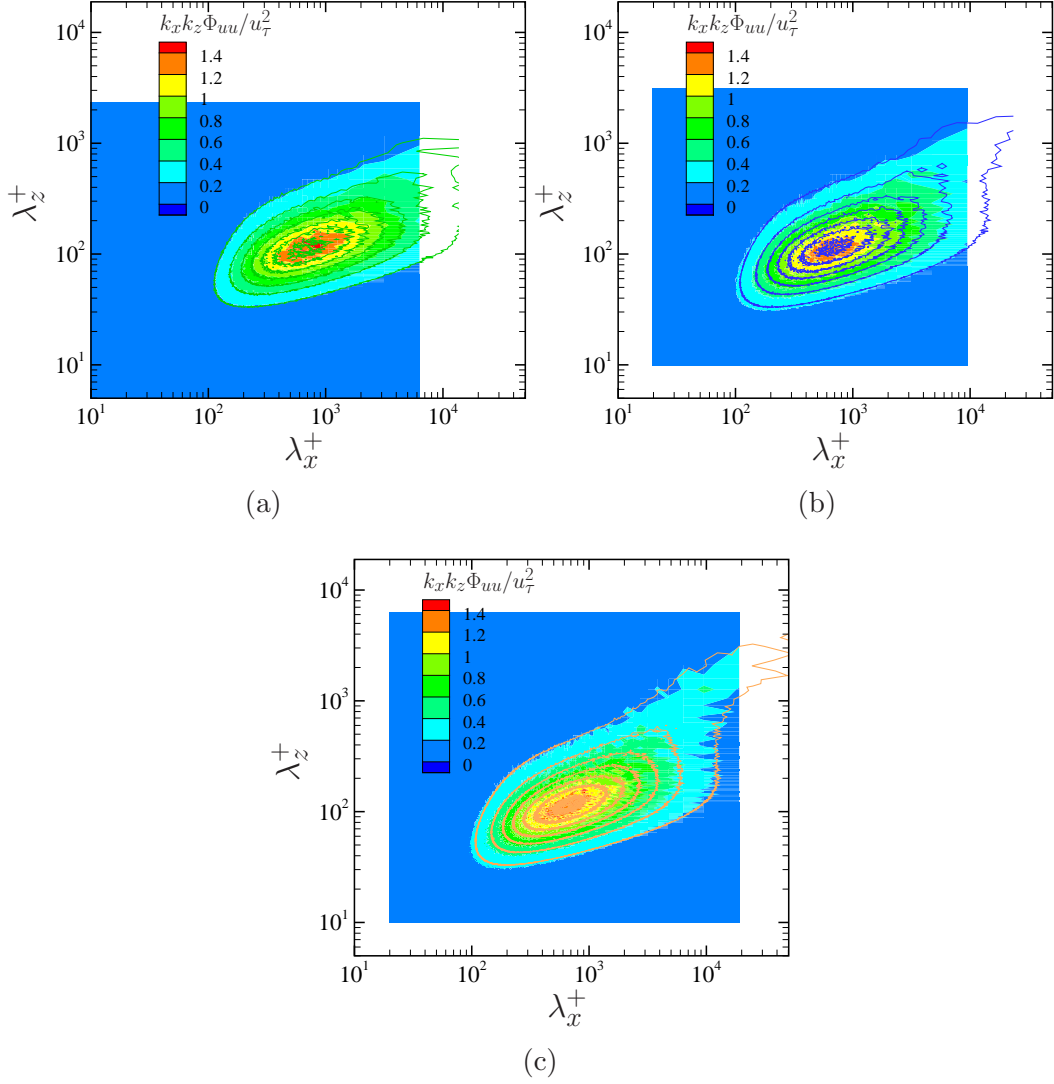


Figure 3.15: Comparison of two dimensional pre-multiplied density spectra for streamwise velocity $k_x k_z E_{uu}$ at $y^+ \approx 15$ between present data (shaded contour) and literature data (contour lines) at (a) $Re_\tau = 400$; (b) $Re_\tau = 800$ and (c) $Re_\tau = 1600$. The literature data are from the same source as in figure 3.14.

rate, thus a drag reduction corresponds to a decrease in skin-friction. The long term drag reduction is defined as below,

$$\mathcal{DR} = \frac{1}{t_f - t_i} \int_{t_i}^{t_f} \frac{C_{f,0} - C_f}{C_{f,0}} dt \times 100(\%), \quad (3.31)$$

where C_f and $C_{f,0}$ are xz plane averaged skin-friction coefficient of the controlled and no control cases, respectively. t_i and t_f are the starting and ending time for

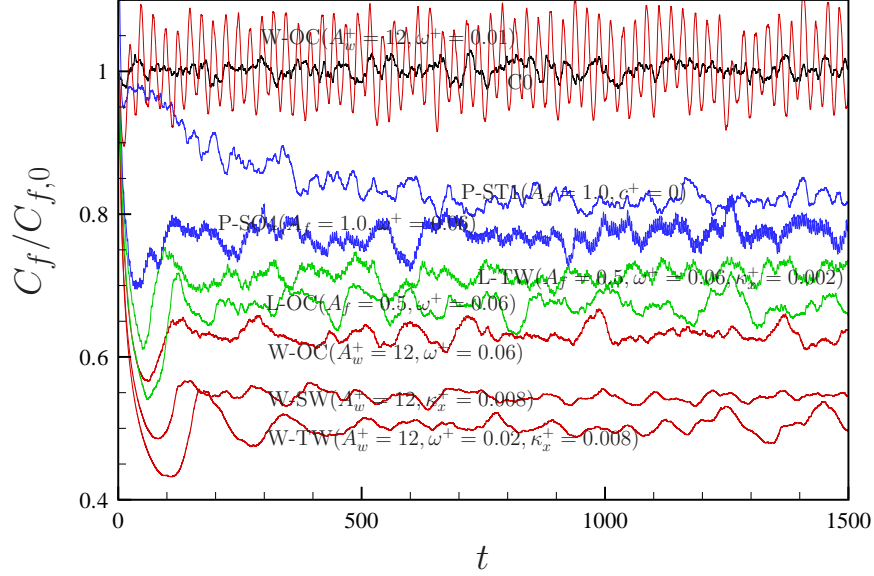


Figure 3.16: Time history of skin-friction for three types of flow control cases: wall motion (“W”, red lines), Lorentz force (“L”, green lines), and plasma actuators (“P”, blue lines).

the time average. Correspondingly, the drag increase is defined as $\mathcal{DI} = -\mathcal{DR}$. t_i is the time instance after the transient period of the flow control, and the value is determined by eyes from the C_f time history plot (the values of t_i are listed in table 3.5). Similar procedure was used by Quadrio and Ricco (2004) and Ricco and Hahn (2013). However, for turbulent statistics calculation, the transient period is set to be longer by monitoring the streamwise total shear stress profiles in a window size of $\Delta T \approx 300$, since the flow response in the channel center is slower than u_τ response on the wall (Jung and Chung, 2012).

To quantify the uncertainty in \mathcal{DR} caused by the grid resolution and the domain size, a systematic check has been conducted for typical cases of each control. They are listed in table 3.5, and the control parameters for each case are given at the bottom of the table. Here the grid resolution test only focuses on the streamwise and spanwise directions, since the turbulence statistics for the no control case is not sensitive to the y grid resolution (see figures 3.10 and 3.11), and also the study by Hurst (2014) suggested that for the same code, the \mathcal{DR} and turbulence statistics for the control by spanwise wall velocity did not change when doubling the wall normal resolution or the time step. Therefore, the same wall grid resolution as C0 case is used for all the test simulations, and the time step is fixed at $\Delta t^+ = 0.2$.

For spanwise wall motion, three baseline cases are tested, *i.e.*, optimal spanwise wall oscillation (W-OC), optimal stationary wave (W-SW), and optimal streamwise travelling wave case (W-TW). An additional set of tests is also performed at $Re_\tau = 400$ to check the Reynolds number effect. The largest change in \mathcal{DR} is 1.7% for the optimal travelling wave case. For spanwise Lorentz force control, the streamwise and spanwise resolution and domain size tests are done for the optimal oscillation case (L-OC), and the travelling wave case (L-TW) with the highest drag increase. The largest \mathcal{DR} difference is around 1.5%. For plasma actuators, the tests are done for two configurations, *i.e.*, ST1 and SO4, and the largest \mathcal{DR} different due to the grid resolution and the domain size is around 1% for ST1 and 1.4% for SO4. According to the typical control cases study, we give a 2% error bar for the \mathcal{DR} values in the present study.

Table 3.5: Grid resolution and domain size test for flow controls by spanwise motion: wall motion (W), Lorentz force (L) and plasma actuators (P).

Case	Re_τ	$L_x \times L_z$	$\Delta x^+ \times \Delta z^+$	t_i	$C_f \times 10^3$	$ \Delta C_f (\%)^\dagger$	$\mathcal{DR}(\%)$
W-OC ¹	200	16×6	5×2.5	200	4.93	-	36.1
W-OC	200	16×6	5×5	200	4.94	0.06	36.1
W-OC	200	16×6	10×5	200	5.05	0.02	34.6
W-OC	200	32×12	5×2.5	200	5.03	0.02	34.9
W-OC	400	16×6	5×5	100	4.46	-	29.8
W-OC	400	16×6	10×5	100	4.49	0.01	29.2
W-OC	400	32×12	5×5	100	4.42	0.01	30.4
W-SW ²	200	16×6	5×2.5	250	4.25	-	45.0
W-SW	200	16×6	5×5	250	4.27	0.01	44.8
W-SW	200	16×6	10×5	250	4.30	0.01	44.3
W-SW	200	32×12	5×2.5	250	4.31	0.01	44.3
W-TW ³	200	16×6	5×2.5	350	3.94	-	49.1
W-TW	200	16×6	10×5	350	3.96	0.01	48.8
W-TW	200	32×12	5×2.5	350	4.06	0.03	47.4
L-OC ⁴	200	16×6	5×2.5	200	5.57	-	27.9
L-OC	200	16×6	10×2.5	200	5.59	0.01	27.6
L-OC	200	16×6	2.5×2.5	200	5.68	0.02	26.4
L-OC	200	16×6	5×5	200	5.60	0.01	27.5
L-OC	200	16×6	5×1.25	200	5.63	0.01	27.1
L-OC	200	32×6	5×2.5	200	5.68	0.02	26.4
L-OC	200	16×12	5×2.5	200	5.61	0.01	27.3
L-TW ⁵	200	16×6	5×2.5	50	10.11	-	-30.8
L-TW	200	16×6	2.5×2.5	50	10.22	0.89	-32.0
L-TW	200	16×6	5×1.25	50	10.14	0.34	-31.3
L-TW	200	32×6	5×2.5	50	10.11	0.01	-30.8
L-TW	200	16×12	5×2.5	50	10.12	0.13	-31.0
P-SO4 ⁶	200	16×6	5×2.5	140	6.08	-	21.3
P-SO4	200	16×6	2.5×2.5	140	6.16	1.28	20.3
P-SO4	200	16×6	5×1.25	140	6.10	0.35	21.0
P-SO4	200	16×12	5×2.5	140	6.09	0.11	21.2
P-ST1 ⁷	200	16×6	5×2.5	650	6.43	-	16.8
P-ST1	200	16×6	2.5×2.5	650	6.54	1.68	15.4
P-ST1	200	16×6	5×1.25	650	6.49	0.98	16.0
P-ST1	200	16×12	5×2.5	650	6.51	1.26	15.8

1 - $A_w^+ = 12$, $\omega^+ = 0.06$ ($T^+ = 105$); 2 - $A_w^+ = 12$, $\kappa_x^+ = 0.008$ ($\lambda_x^+ \approx 800$); 3 - $A_w^+ = 12$, $\omega^+ = 0.02$ ($T^+ = 314$), $\kappa_x^+ = 0.008$ ($\lambda_x^+ \approx 800$); 4 - $A_f = 0.5$, $\omega^+ = 0.06$ ($T^+ = 105$); 5 - $A_f = 0.5$, $\omega^+ = 0.06$ ($T^+ = 105$), $\kappa_x^+ = 0.008$ ($\lambda_x^+ \approx 800$); 6 - $A_f = 1.0$, $s^+ = 50$, $\omega^+ = 0.06$ ($T^+ = 105$); 7 - $A_f = 1.0$, $s^+ = 50$, $c^+ = 0$.

[†] percentage change of C_f with respect to the baseline case (indicated by a superscript) for each control.

Chapter 4

Drag Reduction by Spanwise Wall Oscillation

In this chapter, the spanwise wall motion refers to any form of spanwise velocity imposed on the wall, W_w (figure 4.1). It can be a uni-direction spanwise wall velocity (Le et al., 2000), or a temporal oscillating spanwise wall velocity (Jung et al., 1992), or a spatial modulated spanwise wall velocity (Viotti et al., 2009; Quadrio et al., 2009), or a uniform spanwise wall velocity of an arbitrary temporal wave form (Cimarelli et al., 2013). Here we investigate the first two spanwise wall velocity forms in this chapter. A mathematics formula for these two spanwise wall velocities are shown as below,

$$W_w = A_w, \quad (4.1)$$

or,

$$W_w = A_w \sin(-\omega t) = A_w \sin\left(-\frac{2\pi}{T}t\right), \quad (4.2)$$

where A_w is the magnitude of the spanwise wall moving velocity, and ω (T) is the spanwise wall oscillation frequency (period).

The aim of this chapter is to explore skin-friction drag reduction mechanism and the near wall structure modulation by spanwise wall motion. Even though spanwise wall oscillation control has been proposed for more than 20 years, and both DNSs and experiments have confirmed its drag reduction effect at low Reynolds numbers, the drag reduction mechanism is explained from different aspects (see table 4.1 for a brief summary), and some views are still in debate. A particular focus of the

present study is on the near wall structures directly conditioned from a DNS channel database, following the work of Hurst (2013), and this gives us a clear insight into the near wall structure response to the initial impose of spanwise wall motion, and the cyclic behaviour in the new equilibrium state. The findings provide a guide to the study of skin-friction drag reduction by practical wall attached actuators in the following two chapters, *i.e.*, Lorentz force actuators and DBD plasma actuators.

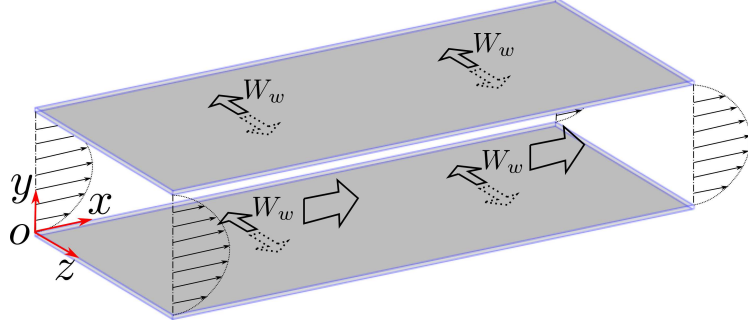


Figure 4.1: Schematics of skin-friction control by spanwise wall velocity.

4.1 Uni-direction wall motion

Uni-direction wall motion is an ideal case to study the drag reduction at the initial stage of the spanwise wall motion (Le et al., 2000). We consider a wide range of spanwise wall velocities, *i.e.*, $A_w^+ = 1 \sim 20$, and the scenario when the top and bottom walls move in the same direction (in phase) or in opposite directions (out of phase). For all the cases in the present study, the x direction mass flow rate is kept constant by dynamically adjusting the streamwise mean pressure gradient dP/dx .

Figure 4.2 shows the long time and short time history of skin-friction coefficient C_f for four typical cases, UA6 ($A_w^+ = 6$, in phase), UA12 ($A_w^+ = 12$, in phase), UA6O ($A_w^+ = 6$, out of phase), UA12O ($A_w^+ = 12$, out of phase) after the wall starts to move in the spanwise direction at $t^+ = 0$. The flow passes a transient process and then settles down at a new equilibrium state. The in phase cases, *i.e.*, UA6 and UA12 experience some longer time C_f drop after hitting the peak values, compared to the out of phase cases, *i.e.*, UA6O and UA12O. However, the short term transient process ($t^+ < 300$) does not depend on the phase of the wall motion, but purely on A_w^+ (figure 4.2(b)). Though all the control cases finally settle down at a higher C_f state, there is an initial C_f drop for $t^+ < 100$. The length of the initial C_f decay seems not to be scaled in wall units, instead it is A_w^+ dependent: $t^+ \approx 60$ for $A_w^+ = 6$; and $t^+ \approx 80$ for $A_w^+ = 12$. Le et al. (2000) used $t^+ = 60$ to define the

Table 4.1: Drag reduction mechanisms by spanwise wall oscillation in literature.

Source	Mechanism
Baron and Quadrio (1996)	Spanwise wall oscillation disrupts the spatial coherence between streamwise vortices ($10 < y^+ < 50$) and low-speed streaks ($y^+ < 10$).
Choi et al. (1998)	Negative spanwise vorticity is created in both positive and negative movement of spanwise wall oscillation, reducing velocity gradient in the near wall region.
Xu and Huang (2005)	The global turbulence suppression is caused by the sustained attenuation of the pressure-strain term in the turbulent budget.
Duggeby et al. (2007)	The coherent vorticity structures are pushed away from the wall into higher speed flow, causing a shorter time interaction between the propagating wave modes and the roll modes, thus less Reynolds shear stress production.
Ricco et al. (2012)	Turbulent dissipation rate is largely enhanced during the transient process, which leads to drag reduction in the new quasi-equilibrium state.
Touber and Leschziner (2012)	The unsteady cross-flow straining causes major spanwise distortions in the streaks, and the reduction in wall normal and shear stresses.
Agostini et al. (2014)	The drag reduction process is linked to the rate of change in the Stokes strain in the upper region of the viscous sublayer where streaks are the strongest.
Yakeno et al. (2014)	Spanwise wall oscillation suppresses the near-wall streamwise vortices rotating in the opposite direction, and also tilt the structures into spanwise direction.

C_f minimum in their case ($A_w^+ = 8.5$). They further divided the transient process into three periods, *i.e.*, the early reduction period ($t^+ < 20$); the late reduction period ($20 < t^+ < 60$); and the recovery period ($t^+ > 60$). This C_f reduction and recovery process is very important for understanding the drag reduction mechanism for a wide range of spanwise motions studied in this thesis.

We focus on UA12O case, and run simulations for the transient process using 10 different initial flow fields, then get the ensemble averaged statistics at each time instance as indicated by the dashed line in figure 4.2(b). The wall normal profiles

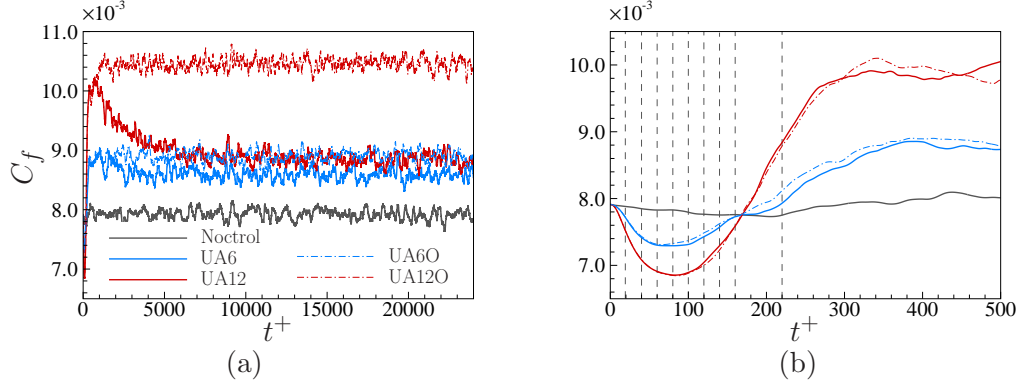


Figure 4.2: Time history of skin-friction coefficient C_f for uni-direction spanwise wall motion: (a) long time history; and (b) transient process.

for the turbulent kinetic energy ($q \equiv 2k \equiv \langle u'_i u'_i \rangle$) and the enstrophy ($\langle \omega'_i \omega'_i \rangle$) are shown in figure 4.4 for t^+ up to 220 with a time interval of $\Delta T^+ = 20$. The $\langle u'_i u'_i \rangle$ across the whole channel decreases up to $t^+ = 60$, then starts to increase, which is very consistent with the C_f drop. On the contrary, $\langle \omega'_i \omega'_i \rangle$ increases sharply at $t^+ = 20$, especially shows a peak at $y^+ \approx 8$, which indicates the enhancement of turbulent dissipation at the start of the wall motion. After $t^+ = 20$, the near wall enstrophy starts to follow the change of $\langle u'_i u'_i \rangle$ to establish the energy balance in the new state. A more pronounced change happens to the streamwise and spanwise production terms, *i.e.*, $-2\langle u'v' \rangle dU/dy$ and $-2\langle v'w' \rangle dW/dy$. The streamwise production terms decreases for up to $t^+ \approx 40$ then starts to recovery, in the mean time the spanwise production term keeps increasing due to the increase of spanwise mean shear. Therefore, both the reduction of production and the increase of dissipation counted for the initial C_f drop (Moin et al., 1990). More precisely, in a 3D turbulent boundary layer, Coleman et al. (1996) showed that small scales are more quickly affected by the initial wall motion than the large scales, thus the imposed wall motion enhanced the small scales, resulting in the turbulent dissipation increase. To verify this point, we show the streamwise velocity spectra $k_x \Phi_{uu}$ at four time instances, *i.e.*, $t^+ = 0, 20, 40$ and 60 in figure 4.5. It is clear to see that at $t^+ = 20$ a small protrusion at $\lambda_x^+ \approx 130$ starts to form, while the energy at $\lambda_x^+ \approx 1000$ becomes weaker. It is also noticeable that the most energetic site is pushed away from the wall (from $y^+ = 14$ to 19). This is consistent with the upward shift of the $\langle \omega'_i \omega'_i \rangle$ peak. The upward shift of the small scales enhances the dissipation in the region $y^+ < 20$. In the present study and the 3D boundary layer studies by Moin et al. (1990) and Coleman et al. (1996), the spanwise wall velocity (or pressure gradient) are imposed suddenly, thus there is a big jump in w at the first time step. However,

recently Agostini and Leschziner (2014) studied the transient enstrophy response for spanwise wall oscillation, where the spanwise wall velocity gradually increased from 0, and they also observed an initial enstrophy increase during $0 < t^+ < 10$. After $t^+ = 20$, turbulent kinetic energy starts to transfer from the original stream-wise aligned streaks to the new oblique streaks (see also figure 7 in (Coleman et al., 1996)). The new energetic site in the $k_x \Phi_{uu}$ spectrum is just the x projection of the new streaks. Therefore, the very important phenomenon in the transient process is the breaking down of the streaks. It leads to the drop of the turbulent kinetic energy and more near wall small scale structures to enhance the turbulent dissipation.

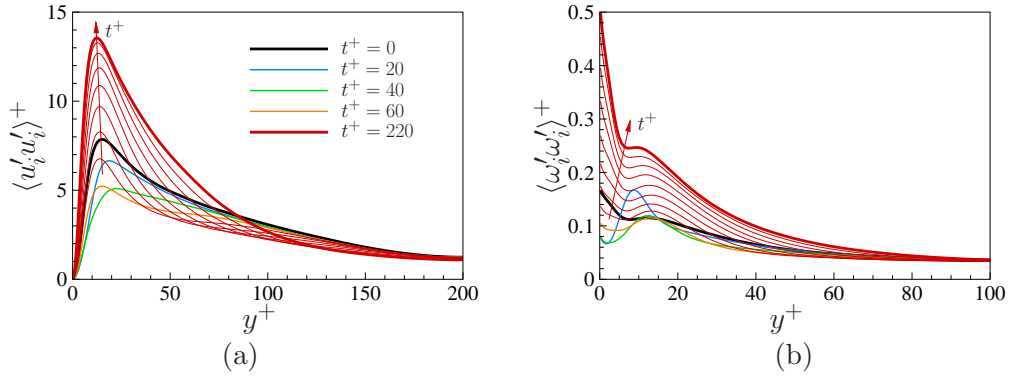


Figure 4.3: Wall normal profiles during the transient process of UA12O for (a) turbulent kinetic energy ($\langle u'_i u'_i \rangle^+$); and (b) turbulent enstrophy ($\langle \omega'_i \omega'_i \rangle^+$).

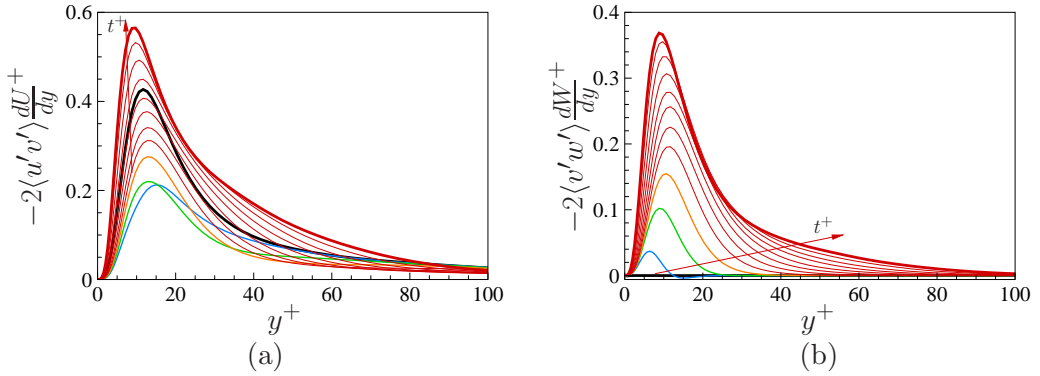


Figure 4.4: Wall normal profiles during the transient process of UA12O for (a) streamwise turbulent production ($-2\langle u'v' \rangle \frac{dU}{dy}$); and (b) spanwise turbulent production ($-2\langle v'w' \rangle \frac{dW}{dy}$).

We investigate the streaks breaking down during the transient process using the conditioned λ_2 structures, because those near structures form a regeneration

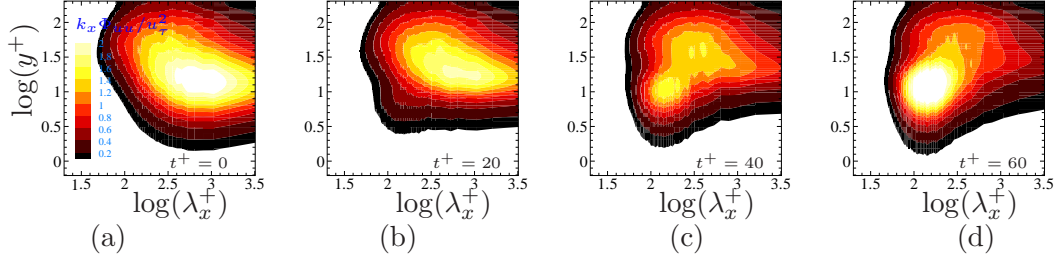


Figure 4.5: One-dimensional pre-multiplied streamwise spectra for UA12O at (a) $t^+ = 0$, (b) $t^+ = 20$, (c) $t^+ = 40$ and (d) $t^+ = 60$.

cycle with the near wall streaks (Hamilton et al., 1995). The procedure to extract these λ_2 structures has been explained in details in section 3.2 for the canonical channel flow. For UA12O case, we apply the same procedure to each time instance at $t^+ = 0 \sim 220$ with an interval of $\Delta T^+ = 20$. The ensemble averaged positive and negative λ_2 structures at $t^+ = 20, 40, 60, 80, 100, 120, 140$ and 220 are shown in figure 4.6. Comparing to the canonical flow case (figure 3.4), the λ_2 structures are strongly affected by the spanwise wall motion: 1) Both positive and negative λ_2 structures are tilted into negative z direction, since the head and tail of the λ_2 structures are convected at different spanwise velocities. 2) Positive and negative λ_2 structures response in different ways to the spanwise wall motion. Immediately after the impose of the spanwise wall velocity, the positive λ_2 structure starts to become weaker and moves upward, with the weakest period at $t^+ = 80 \sim 120$. The negative λ_2 structure generates spanwise velocity underneath in the same direction as the wall motion, and its strength is enhanced at $t^+ = 20$, then weakened afterwards up to $t^+ = 120$. In the canonical channel flow, the positive and negative λ_2 structures are highly symmetric about the flow direction (see $t^+ = 0$ in figure 4.6), and they are responsible for the near wall long streaks (Jeong et al., 1997). With the spanwise wall motion, this symmetry between the positive and negative λ_2 structures is broken up, leading to the breaking up of the near wall streaks as well (see figure 4.5).

The skin-friction in the domain ($L_x^+ \times L_y^+ \times L_z^+ = 200 \times 60 \times 100$) of the conditioned λ_2 structures are sampled (see figure 3.6 for the skin-friction pattern for the canonical case). The skin-friction associated with the positive (C_{f+}) and the negative (C_{f-}) λ_2 structures is normalised by C_f at $t^+ = 0$, and plotted in figure 4.7, together with the volume integrated turbulent kinetic energy and enstrophy. C_{f+} and C_{f-} follow closely C_f . At $t^+ = 20$, the positive λ_2 structure is pushed away, thus generates less skin-friction; negative λ_2 structure generates less skin-friction mainly due to the spanwise tilting, though its strength actually increases

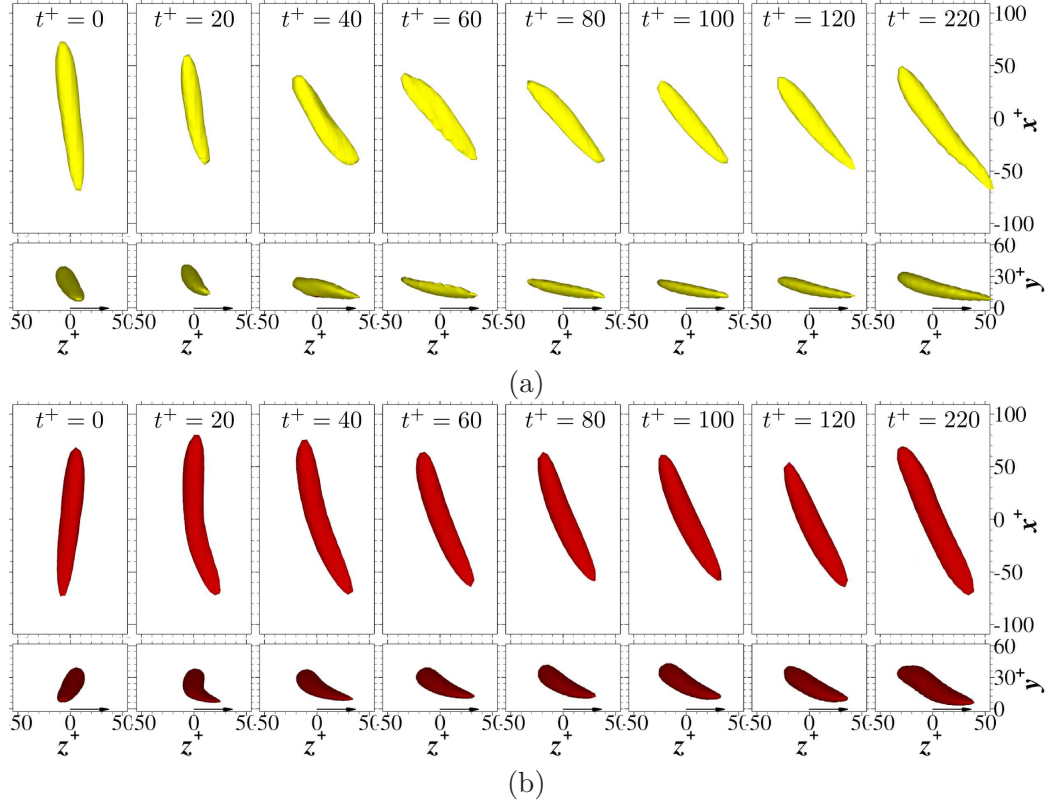


Figure 4.6: Ensemble averaged (a) positive and (b) negative λ_2 structures during the transient period for UA12O at $t^+ = 0, 20, 40, 60, 80, 100, 120$ and 220 . λ_2 structures are visualised with $\lambda_2^+ = -0.005$. Arrows indicate the wall moving direction.

at this time instance. However, C_{f+} starts to recovery at $t^+ = 60$, earlier than C_{f-} , which recovers at $t^+ = 100$. At $t^+ = 120$, the two structures are almost aligned in the same direction as the mean flow (see figure 4.6), and generate the same level of skin-friction. The turbulent kinetic energy and enstrophy start to recover earlier than skin-friction, and this is due to the $w'w'$ and $\omega'_x\omega'_x$ components, which are directly generated by the spanwise mean strain $\partial W/\partial y$. Figure 4.7 also compares the time trace of the volume integrated enstrophy between UA12O and spanwise wall oscillation data at $T^+ = 100$ from (Ricco et al., 2012) and $T^+ = 200$ from (Agostini et al., 2014). All three datasets show an initial enstrophy increase. This increasing period is $t^+ \approx 13, 10$, and 25 for UA12O, (Agostini and Leschziner, 2014) and (Ricco et al., 2012), respectively. The difference in this time scale might be due to the fact that the simulation in (Ricco et al., 2012) was operated at a constant pressure gradient, in contrast to the other two, which were at a constant mass flow rate. For UA12O, the enstrophy increase period is around $1/6$ of the C_f dropping period, and for the other $5/6$ time the enstrophy is below the original level.

On the contrary, the summation of streamwise and spanwise productions does not recovery to the original level until $t^+ \approx 90$, matching the C_f decay period. Thus it suggests that the production decrease is more directly related to the initial C_f decay compared to the transient enstrophy increase, at least for the present uni-direction wall motion situation. The time scale for the λ_2 structures to realign themselves in the new flow direction matches well with the C_f decay period. From structures' point of view, this is the tilting of the λ_2 structure that breaks down the low-speed streaks, reducing the production of the streamwise Reynolds shear stress and the turbulent kinetic energy.

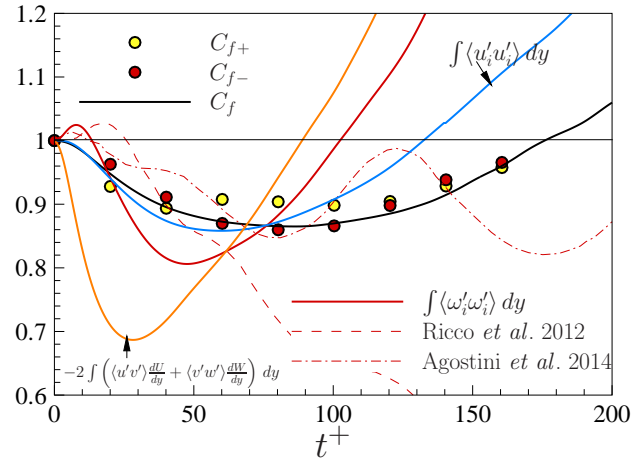


Figure 4.7: Transient time history for skin-friction, turbulent kinetic energy and enstrophy. The thin lines are enstrophy data from (Ricco et al., 2012) at $T^+ = 100$, and (Agostini and Leschziner, 2014) at $T^+ = 200$ for spanwise wall oscillation.

The C_f decay period for UA12O, *i.e.*, $T^+ \approx 80$, matches reasonably well with half of the optimal oscillation period T_{opt}^+ in the spanwise wall oscillation, which is going to be shown later. Quadrio and Ricco (2004) first linked T_{opt}^+ with the Lagrangian time scale, $T^+ \approx 60$ for the longest-lived and statistically significant turbulent structures. A similar optimal time scale from generalized optimal perturbation (GOP) approach, $T_{GOP}^+ \approx 80$ has also been predicted (Blesbois et al., 2013). Recently, Cimarelli et al. (2013) has shown that the optimal oscillation period $T_{opt}^+ = 125$ was almost fixed for many different temporal spanwise oscillation waves. This implies that the near wall structures only adjust themselves to the new state within $T^+ \approx 80$, and beyond that they start to recovery the strength and generate higher skin friction. We have run simulations for a wide range of spanwise wall velocity amplitude, $A_w^+ = 1 \sim 20$, and all the cases end with drag increase (see figure

4.8). If the wall alternates its moving direction before $t^+ \approx 80$, then a reflected response as in figure 4.6 happens to the positive and negative λ_2 structures, and this brings the flow into a further lower C_f state. The study on the initial response by Quadrio and Ricco (2003) suggested that this process can finally settle down after $2 \sim 3$ cyclic periods. The above process is not sensitive to the exact temporal wave form of the wall motion, which is a good news for practical drag reduction applications.

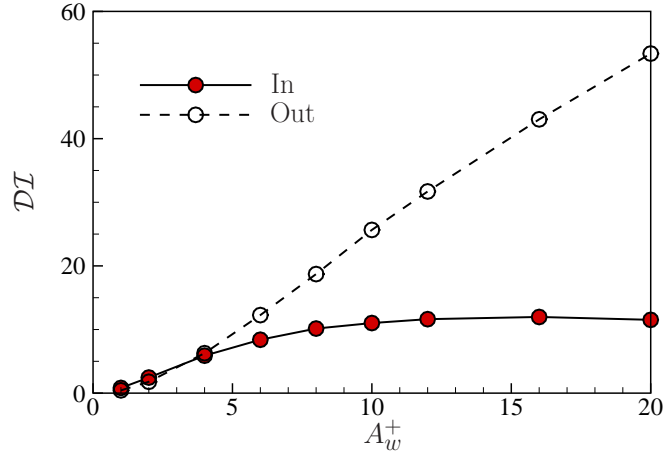


Figure 4.8: Drag increase for different spanwise wall moving velocities when the top and bottom walls move in phase or out of phase.

For uni-direction wall motion, the flow finally settles down at a C_f state depending on both A_w^+ and the moving phase between the top and bottom walls. This is clearly demonstrated in figure 4.8. For $A_w^+ \leq 4$, the DI value does not depend on the wall moving direction; while for $A_w^+ > 4$, the DI difference becomes significant. The drag increases monotonously with A_w^+ when the top and bottom walls are out of phase, but it saturates at $DI \approx 12$ when they are in phase. This DI behaviour is reflected in the spanwise mean velocity profiles, as shown in figure 4.9. The spanwise mean shear $\partial W / \partial y$ keeps increasing with A_w^+ when the two walls are out of phase; while a larger A_w^+ only leads to a higher spanwise bulk mean flow, not the mean shear $\partial W / \partial y$ when the two walls are in phase. This also suggests that the DR in channel flow controls can have different asymptotic behaviours depending on the wall moving phase.

The skin-friction increase is also reflected in the Reynolds stress components, shown in figure 4.10. As can be seen, the velocity fluctuations for the three velocity components increase significantly across the whole channel height (figure 4.10(a)).

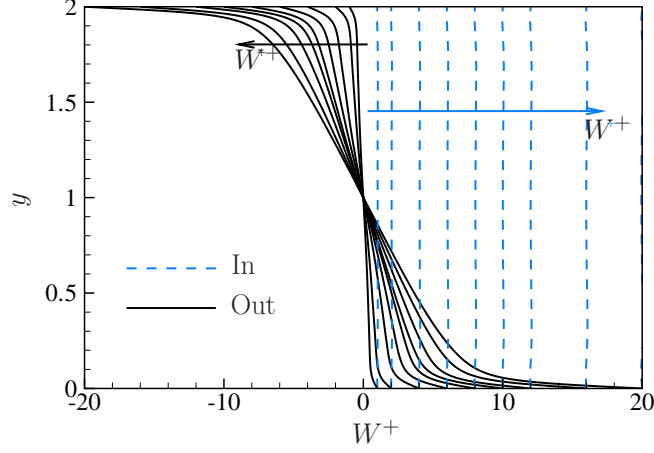


Figure 4.9: Spanwise mean velocity profiles for different spanwise wall moving velocities when the top and bottom walls are in phase or out of phase.

Higher spanwise wall moving velocity corresponds to larger increase in the $u_{i,rms}^+$ values. The spanwise wall motion also introduces the other Reynolds shear stress components, *i.e.*, $\overline{v'w'}$, $\overline{u'w'}$, which are zeros in the canonical flow (figure 4.10(b)). Fukagata et al. (2002) proposed an identity, which is now known as F.I.K. identity, to quantify the origin of the wall shear stress, and it is written as below for the channel flow,

$$C_f = \frac{6}{Re} + 6 \int_0^1 (1-y)(-\overline{u'v'})dy, \quad (4.3)$$

where the first and second terms on the right hand side are the laminar and turbulent contributions to the skin-friction. Therefore, the increase of $-\overline{u'v'}$ is directly linked to the increase of C_f .

To close this section, we show the ensemble averaged λ_2 structures for UA12O in the new steady state (figure 4.11). A comparison can be made with the case for a 2D boundary layer ($A_w^+ = 0$) in figure 3.4. The mean velocity and shear angles for UA12O vary in wall normal direction, thus the positive and negative λ_2 structures have different preferred alignment angles, and they are less symmetric. Nevertheless, the λ_2 structures in a steady 3D turbulent boundary layer is very similar to its 2D counterpart. In the following part, we are going the further investigate these λ_2 structures within an unsteady 3D turbulent boundary layer subjected to the spanwise wall oscillation.

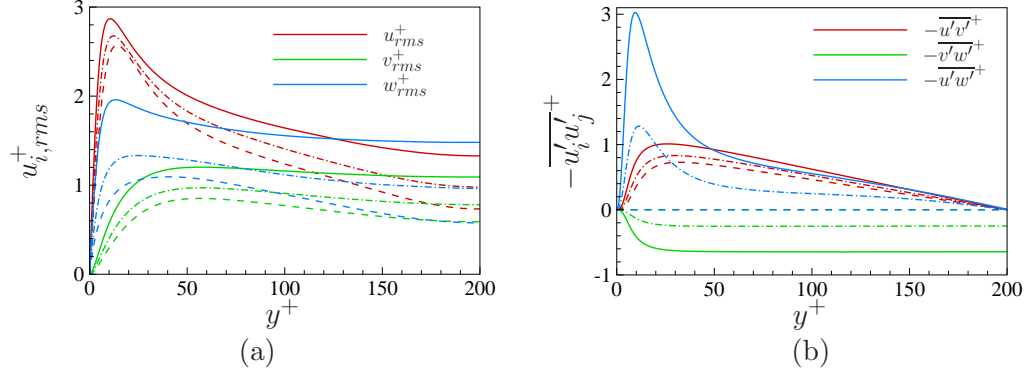


Figure 4.10: Comparison of the Reynolds stress profiles among no control case (dashed lines), UA12O (solid lines) and UA6O cases (dash-dot lines): (a) normal components, u_{rms}^+ , v_{rms}^+ , w_{rms}^+ ; (b) shear stress components, $\overline{u'v'}^+$, $\overline{v'w'}^+$, $\overline{u'w'}^+$.

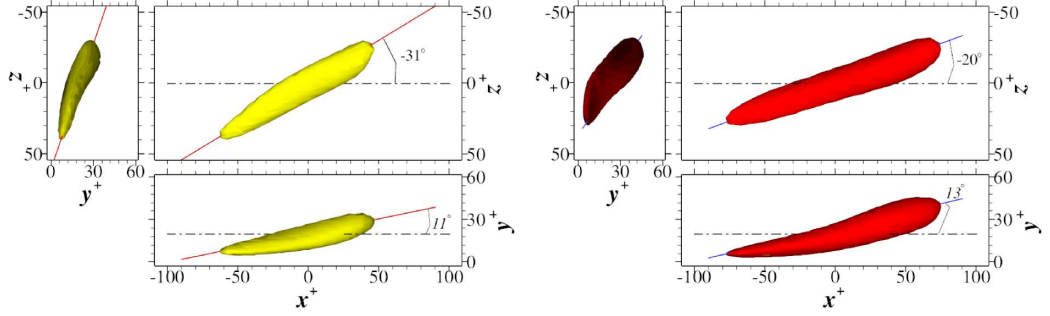


Figure 4.11: Ensemble averaged positive (yellow) and negative (red) λ_2 structures in the new equilibrium state for UA12O case. λ_2 structures are visualised with $\lambda_2^+ = -0.005$.

4.2 Spanwise wall oscillation

By continuously suppressing the positive and negative λ_2 structures, spanwise wall oscillation (equation (4.2)) can achieve a sustained drag reduction (Jung et al., 1992). One interesting phenomenon for the turbulent statistics at the lower C_f state is the phase variation (Touber and Leschziner, 2012; Agostini and Leschziner, 2014), thus the main aim of this section is to show that the phase modulation and the rich near wall turbulent phenomena can be directly linked to the positive and negative λ_2 structures. In this study, the wall oscillation amplitude is fixed at $A_w^+ = 12$, and the oscillation frequency ω^+ ranges from 0.01 to 0.12 (or $T^+ = 52 \sim 628$).

We first show the time history of the skin-friction coefficient C_f for the spanwise wall oscillation at four different oscillation frequencies, *i.e.*, $\omega^+ = 0.01$, 0.03, 0.06 and 0.12 ($T^+ = 628$, 209, 105 and 52) in figure 4.12. The flow experiences

a long time transient to the new equilibrium state. A visual by eyes from the C_f curves gives the length of the transient period to be $t^+ = 550, 1500, 1200$ and 1800 for $\omega^+ = 0.01, 0.03, 0.06$ and 0.12 ($T^+ = 628, 209, 105$ and 52), respectively. To be noticed that C_f has an undershooting behaviour, which has been taken into account for the present transient process. The initial C_f decreasing period roughly agrees with the observation by Quadrio and Ricco (2003), who gave $t^+ = 200 \sim 400$.

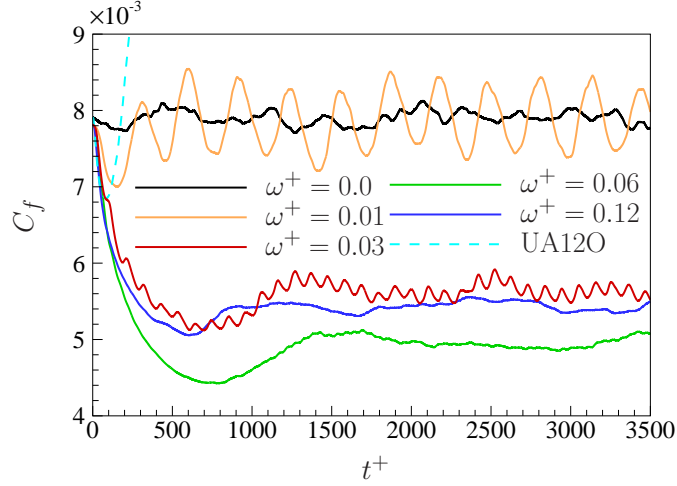


Figure 4.12: Skin-friction coefficient C_f time history for spanwise wall oscillation cases with different oscillation frequencies.

Together plotted in figure 4.12 is the initial C_f time history for UA12O case, which shows some similarity as that of $\omega^+ = 0.01$ ($T^+ = 628$) case in the first half wall oscillation period ($t^+ < 314$). When the wall starts to move, C_f decreases for $0 < t^+ < T^+/4$, then it begins to recover for $T^+/4 < t^+ < T^+/2$. The turning point is at $t^+ \approx 150$; while for UA12O case, a similar turning point is at $t^+ \approx 80$. As explained in the previous section, for $\omega^+ = 0.01$ ($T^+ = 628$) case, the wall moves in one direction for $t^+ = 314$ long, and the λ_2 structures have enough time to recover to the initial or even higher C_f level before the wall changes the moving direction. Differently, for $\omega^+ = 0.03$ ($T^+ = 209$) case, the C_f recovery period is very short, as can be seen from the local peaks in the C_f time history curve, thus the C_f level keeps decreasing in the first 3 oscillation periods. For even higher oscillation frequencies, $\omega^+ = 0.06$ and 0.12 ($T^+ = 628$ and 52), the wall changes the moving direction before the C_f recovers. After several wall oscillation periods, a new quasi-steady C_f state is reached, where C_f shows an oscillation behaviour for all the four cases. The large time scale irregular variation is due to the limited box size used, which can only capture a limited number of the very large scale structures (Touber

and Leschziner, 2012); while the small scale regular variation is associated with spanwise wall oscillation frequency. Apparently, at lower oscillation frequencies, the C_f variation associated with the wall oscillation is larger. For the highest oscillation frequency $\omega^+ = 0.12$ ($T^+ = 52$), the small C_f oscillation is almost invisible. A long time averaged C_f gives the drag reduction of $-2 \pm 2\%$, $28 \pm 2\%$, $36 \pm 2\%$ and $30 \pm 2\%$ for cases $\omega^+ = 0.01, 0.03, 0.06$ and 0.12 ($T^+ = 628, 209, 105$ and 52), respectively.

Specially, we can treat the UA12O case as a spanwise oscillation case with frequency $\omega^+ = 0$ ($T^+ = \infty$). Then the uni-direction cases with $A_w^+ = 1 \sim 12$ studied in the previous section can be used to predict the asymptotic \mathcal{DR} value at the extreme oscillation frequency (or period). It has to be pointed out that DNS is not possible for the spanwise wall oscillation at $\omega^+ = 0$ ($T^+ = \infty$), or even for finite small ω^+ (finite large T^+), because the uncertainty in C_f prediction can be very high due to the limited sampling number of the cyclic periods. At $\omega^+ = 0$ ($T^+ = \infty$), the spanwise mean velocity profiles are different depending on whether the top and bottom walls move in phase or out of phase (see figure 4.9), thus different asymptotic values are expected. The two predicted \mathcal{DR} asymptotic values are $\mathcal{DR} = -8.6$ when top and bottom walls are in phase, and $\mathcal{DR} = -16.1$ when they are out of phase. The detail about how to get these two values is given in appendix C.

Figure 4.13 shows the two asymptotic \mathcal{DR} values together with the DNS data for $\omega^+ \leq 0.03$ ($T^+ \geq 209$). The effect of the wall moving direction just start to appear as $\omega^+ \leq 0.005$ (or $T^+ \geq 1260$). A direct interpolation of this result is that the λ_2 structures only feel the effect from the opposite side wall motion when the Stokes layer is thick enough, which corresponds to a small enough oscillation frequency. The present DNS data tends to approach the two asymptotic \mathcal{DR} values, but the change in the range $\omega^+ < 0.0025$ seems to be very sharp. The DNS data from Quadrio et al. (2009) tends to get very close to the in phase asymptotic \mathcal{DR} value. The \mathcal{DR} asymptotic prediction further supports that the drag reduction in the spanwise wall oscillation is the same as the mechanism for the transient C_f decay in the uni-direction wall motion, *i.e.*, due to the breaking up of the near wall streaks. In the following sections, we are going to explore this point by focusing on the interaction between the λ_2 structures and the Stokes layer.

4.2.1 Turbulence statistics

The turbulence statistics are compared in figure 4.14 for the mean velocity, Reynolds stresses and vorticity fluctuations. All the statistics are non-dimensionalised by the wall units of the no control case. In this format, the \mathcal{DR} cases have a streamwise mean velocity decrease in the near wall region, corresponding to the thicken of the

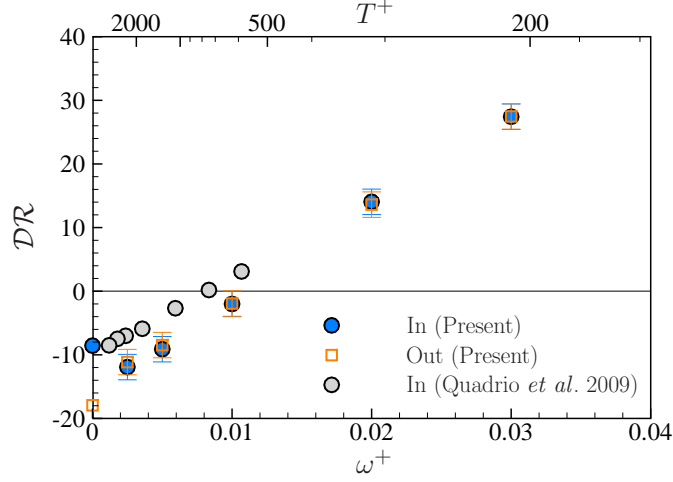


Figure 4.13: \mathcal{DR} asymptotic for spanwise wall oscillation at $Re_\tau = 200$, $A_w^+ = 12$.

viscous sublayer; and a streamwise mean velocity increase in the outer layer due to the constant mass flow constrain (Choi et al., 1998). For the first-moment statistics, a triple decomposition is used for any turbulent property ϕ , *i.e.*,

$$\phi = \tilde{\phi} + \phi' = \bar{\phi} + \hat{\phi} + \phi', \quad (4.4)$$

where $\bar{\phi} = \langle \phi \rangle_{x,z,t}$ is the time and space averaged value, and it is normally written as an upper case Φ ; $\tilde{\phi}$ is the phase averaged component, and is defined as: $\tilde{\phi}(t) = \frac{1}{N} \sum_{n=1}^N \langle \phi(t + nT) \rangle_{x,z}$ (n is an integer) for spanwise wall oscillation cases in the present chapter; $\tilde{\phi}(x) = \frac{1}{N} \sum_{n=1}^N \langle \phi(x + n\lambda_x) \rangle_{z,t}$ for streamwise stationary wave cases, $\tilde{\phi}(z) = \frac{1}{N} \sum_{n=1}^N \langle \phi(z + n\lambda_z) \rangle_{x,t}$ for spanwise stationary wave cases; and $\tilde{\phi}(x) = \langle \phi(x + ct) \rangle_{z,t}$ ($c = \omega/\kappa_x$) for streamwise travelling wave cases, and $\tilde{\phi}(z) = \langle \phi(z + ct) \rangle_{x,t}$ ($c = \omega/\kappa_z$) for spanwise travelling wave cases in the following chapters. $\hat{\phi} = \tilde{\phi} - \bar{\phi}$, and for no control case, $\hat{\phi} = 0$. ϕ' is the stochastic fluctuation.

The high order statistics are only considered for the stochastic fluctuation component. Generally, compared to the no control case, \mathcal{DR} cases by spanwise wall oscillation show a reduction in the Reynolds stress components (see figure 4.14(b), 4.14(c), 4.14(d) and 4.14(e)) and in vorticity fluctuation components as well (see figure 4.14(f), 4.14(g), 4.14(h)). As expected, all the statistics show an overall increase for the drag increase case $\omega^+ = 0.12$ ($T^+ = 52$). A better correlation is found between the \mathcal{DR} value and the wall normal components, *i.e.*, v_{rms}^+ and ω_y^+ , similar to the opposition flow control (Chung and Talha, 2011).

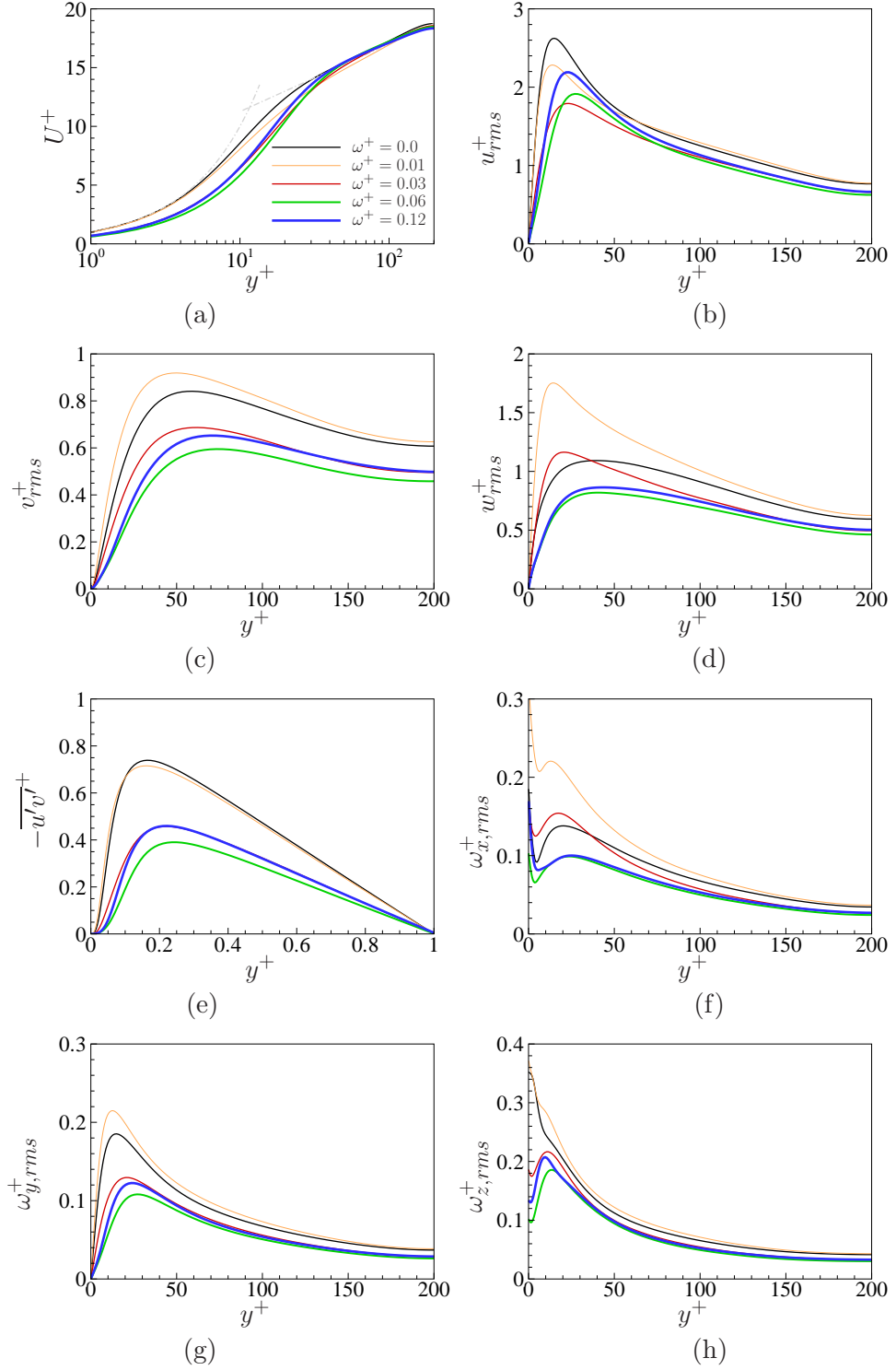


Figure 4.14: Turbulence statistics at four oscillation frequencies for: (a) U^+ ; (b) u_{rms}^+ ; (c) v_{rms}^+ ; (d) w_{rms}^+ ; (e) $-\overline{u'v'}^+$; (f) $\omega_{x,rms}^+$; (g) $\omega_{y,rms}^+$ and (h) $\omega_{z,rms}^+$.

4.2.2 Stokes layer

Spanwise wall oscillation without streamwise flow is known as Stokes' Second Problem, and the generated unsteady spanwise mean flow is called Stokes layer. It has an analytical solution in the form as below,

$$W(y, t) = A_w e^{-\eta} \cos(\omega t - \eta), \quad (4.5)$$

where $\eta = y \sqrt{\omega Re/2}$ (Schlichting, 1968). When equation (4.5) is non-dimensionalised in wall units, it becomes

$$W(y^+, t^+) = A_w^+ e^{-\eta} \cos(\omega^+ t^+ - \eta), \quad (4.6)$$

where $\eta = y^+ \sqrt{\omega^+/2}$. Therefore, the Stokes layer in wall units does not have Reynolds number effect, as already shown by Hurst et al. (2014).

The spatial and phase averaged spanwise velocity profiles at four oscillation frequencies, *i.e.*, $\omega^+ = 0.01, 0.03, 0.06$ and 0.12 ($T^+ = 628, 209, 105, 52$) are shown in figure 4.15, and compared with the laminar solution. It is clear that when the oscillation frequency is low, the turbulent Stokes layer differs significantly from the laminar solution, and they get closer to each other as ω^+ increases. This was also the observation by Toubert and Leschziner (2012), when they compared the turbulent and laminar Stokes layer profiles at $T^+ = 100$ ($\omega^+ \approx 0.063$) and $T^+ = 400$ ($\omega^+ \approx 0.016$). Ricco and Quadrio (2008) pointed out that this difference was caused by the additional Reynolds shear stress term $\frac{\partial \widetilde{v'w'^+}}{\partial y^+}$ raised from the spatial averaged spanwise momentum equation, shown as below,

$$\frac{\partial \widetilde{W}^+}{\partial t^+} = \frac{\partial^2 \widetilde{W}^+}{\partial y^{+2}} - \frac{\partial \widetilde{v'w'^+}}{\partial y^+}. \quad (4.7)$$

Ricco and Quadrio (2008) showed that $\frac{\partial \widetilde{v'w'^+}}{\partial y^+}$ was large during the transient process, reaching the maximum at $t \approx T/2$, and it became negligible once the new equilibrium state was reached after a few oscillation periods. The phase variation of $\frac{\partial \widetilde{v'w'^+}}{\partial y^+}$ after the transient process is shown in figure 4.16. It is clear that the variation of $\frac{\partial \widetilde{v'w'^+}}{\partial y^+}$ increases (especially for the region $y^+ < 20$) as ω^+ decreases, and this causes the large discrepancy between the turbulent and laminar Stokes layer profiles for $\omega^+ = 0.01$ and 0.03 ($T^+ = 628$ and 209) cases.

The laminar Stokes layer thickness is given as $\delta^+ = \sqrt{4\pi T^+}$ (or $\delta^+ = 2\pi \sqrt{2/\omega^+}$) (Schlichting, 1968), at which location the fluid motion is in phase with

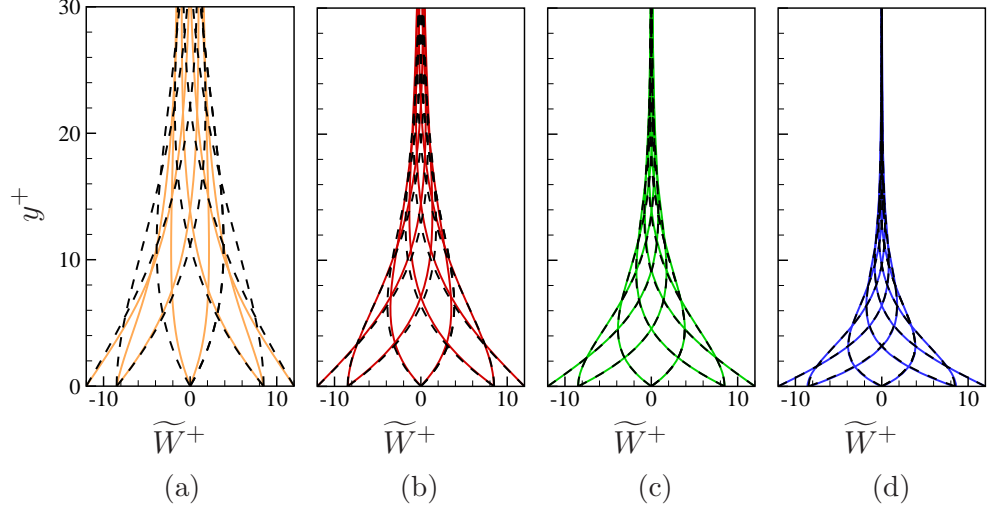


Figure 4.15: Comparison of the Stokes layers between the laminar (dashed line) and the turbulent (solid line) cases for different oscillation frequencies: (a) $\omega^+ = 0.01$ ($T^+ = 628$); (b) $\omega^+ = 0.03$ ($T^+ = 209$); (c) $\omega^+ = 0.06$ ($T^+ = 105$) and (d) $\omega^+ = 0.12$ ($T^+ = 52$).

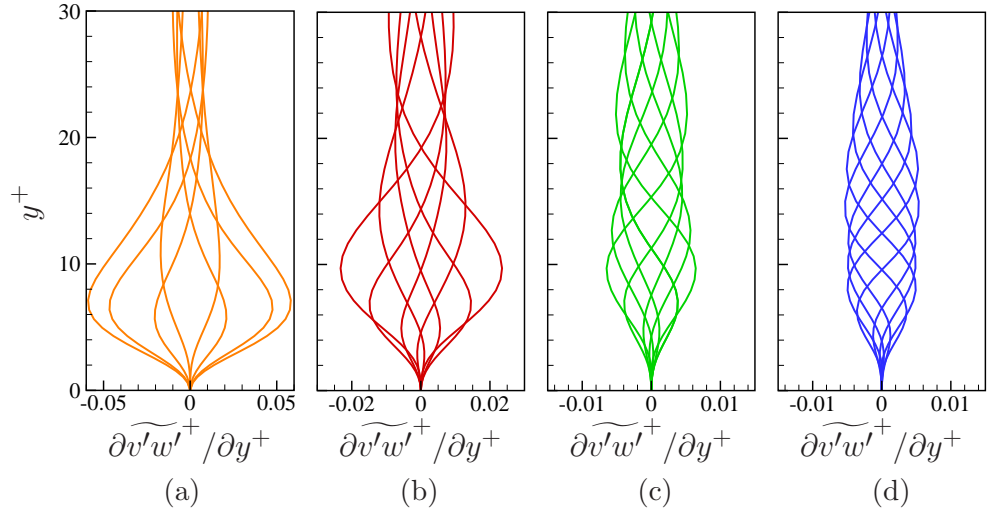


Figure 4.16: Phase variation of $\partial \widetilde{v'w'}^+ / \partial y^+$, ordered as in figure 4.15.

the wall motion, *i.e.*, $\eta(\delta^+) = 2\pi$. In the present study, we define an effective Stokes layer thickness for both the laminar and the turbulent cases as $\eta(\delta^+) = 1$, which gives $\delta^+ = \sqrt{2/\omega^+}$. This is the same definition as used by Quadrio and Ricco (2011) for the generalised Stokes layer study. A comparison between the turbulent and the laminar Stokes layer thickness is shown in figure 4.17(a). At low frequency

$\omega^+ < 0.03$ (or $T^+ > 209$), the laminar Stokes layer thickness tends to increase much faster as ω^+ decreases. At high frequency, the agreement between the laminar and the turbulent Stokes layer thickness is very good, and the change is not sensitive to the frequency when $\omega^+ > 0.15$ (or $T^+ < 42$), as has been observed in figure 4.15. It has to be pointed out that, for the turbulent case, $\delta^+(\omega^+ = 0.15)$ is the same as $\delta^+(\omega^+ = 0.18)$ in the graph, because the change of δ^+ is within the wall normal grid resolution at that height, and δ^+ can not be distinguished for these two cases.

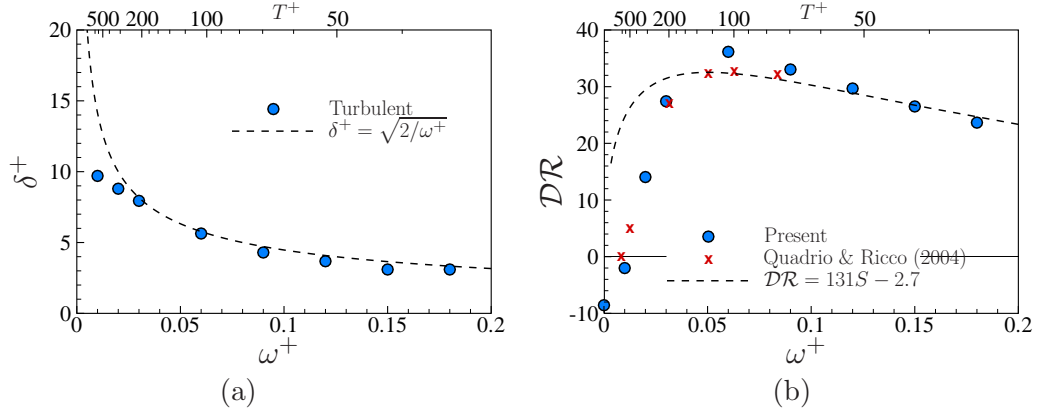


Figure 4.17: Comparison between turbulent and laminar Stokes layers for (a) thickness δ^+ ; and (b) drag reduction \mathcal{DR} .

Figure 4.17(b) shows the \mathcal{DR} change as a function of the oscillation frequency. The present data agrees reasonably well with (Quadrio and Ricco, 2004) for the same control parameters. The optimal frequency around $\omega^+ \approx 0.06$ ($T^+ \approx 105$) is indicated by both DNS datasets, although the predicted \mathcal{DR} value from the present data is around 8% higher. Together given is the prediction from the S parameter (Choi et al., 2002; Quadrio and Ricco, 2004; Ricco and Quadrio, 2008). The form of S parameter for a laminar Stokes layer is as below,

$$S = \sqrt{2\omega^+} \ln \left(\frac{A_w^+}{W_{th}^+} \right) e^{-y^+ \sqrt{\omega^+/2}}, \quad (4.8)$$

where W_{th}^+ is a threshold value for the spanwise velocity, and y^+ is the location where a threshold value for the acceleration rate is taken. Quadrio and Ricco (2004) proposed a linear correction between \mathcal{DR} and S , and used available DNS data for the linear fitting. The authors found that $\mathcal{DR} = 131S - 2.7$ ($W_{th}^+ = 1.2$, $y^+ = 6.3$) gave the best linear fitting for $T^+ < 150$. Based on the S parameter scaling, an explicit relation between \mathcal{DR} and ω^+ is established, and this is shown as the dashed line in figure 4.17(b). The optimal frequency predicted from the S parameter scaling

is $\omega_{opt}^+ = 2/y^{+2} \approx 0.05$ ($T^+ \approx 125$), very close the DNS prediction. Again it is clear that the S parameter scaling becomes worse for small ω^+ (or large T^+). Quadrio and Ricco (2004) explained that for $T^+ > 150$, half of the wall oscillation period is longer than the time period of the statistically significant turbulent structures ($t^+ \sim O(60)$), and the turbulent structures can develop their inner dynamics during half of the wall oscillation period, thus the S parameter scaling becomes invalid.

Figure 4.18 presents \mathcal{DR} as a function of the Stokes layer thickness δ^+ , compared between the DNS data and the S parameter scaling. As conjectured by Akhavan et al. (1993) and Baron and Quadrio (1996), there is an optimal Stokes layer thickness. It is $\delta^+ \approx 5.7$ from the DNS prediction, and $\delta^+ \approx 6.3$ from the S parameter prediction. As has been shown by Ricco and Quadrio (2008), the S parameter does not cross the origin, and this leads to a minimum wall oscillation amplitude A_w^+ (or displacement $D_m^+ \equiv 2A_w^+/\omega^+$) for the drag reduction. The S parameter scaling also suggests a minimum Stokes layer thickness, δ_{min}^+ , and the value is $\delta_{min}^+ \approx 1$, which has been shown by Quadrio and Ricco (2011) for the generalised Stokes layer (red solid line). For the generalised Stokes layer thickness, \mathcal{DR} scales linearly with δ^+ for small δ^+ . It is the same case for the spanwise wall oscillation suggested by the S parameter scaling. However, the present DNS data has not reached this linear regime due to the computational cost to resolve this very thin but very fast oscillating Stokes layer.

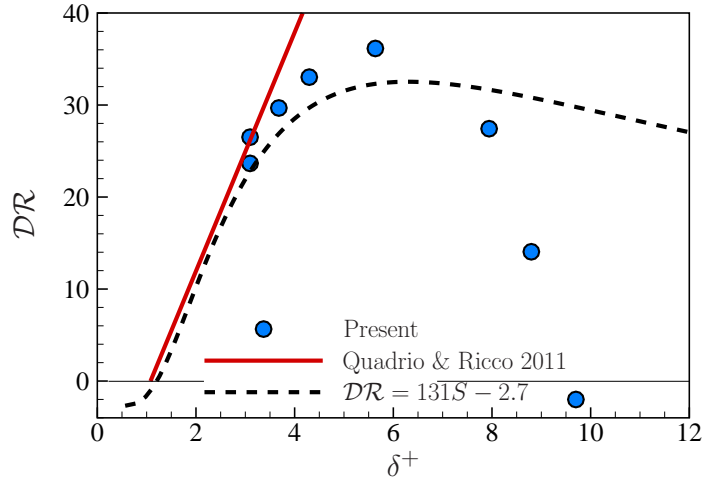


Figure 4.18: Drag reduction \mathcal{DR} against Stokes layer thickness δ^+ .

As a short summary, the spanwise wall oscillation tangles the λ_2 structures through its generated Stokes layer. If the Stokes layer is too thick (very large

oscillation period), then the scenario is the same as uni-direction wall motion, and no drag reduction is achievable. In the other end, for too thin Stokes layer (very small oscillation period), the λ_2 structures are completely outside of the Stokes layer, thus their dynamics is not affected by the wall oscillation. In this scenario, we conjecture the \mathcal{DR} is close to 0, if it is not 0 according the minimum Stokes layer δ_{min}^+ shown in figure 4.18. The available DNS data points are still quite far away from the uni-direction wall motion case, and the \mathcal{DR} asymptotic may not follow the linear prediction as in figure 4.13, thus this remains to be an interesting point to be explored in the future. For the optimal Stokes layer thickness δ_{opt}^+ , the λ_2 structures are tilted in the flow, and the Reynolds shear stress associated with the λ_2 structures is minimized (Akhavan et al., 1993; Baron and Quadrio, 1996; Yakeno et al., 2014).

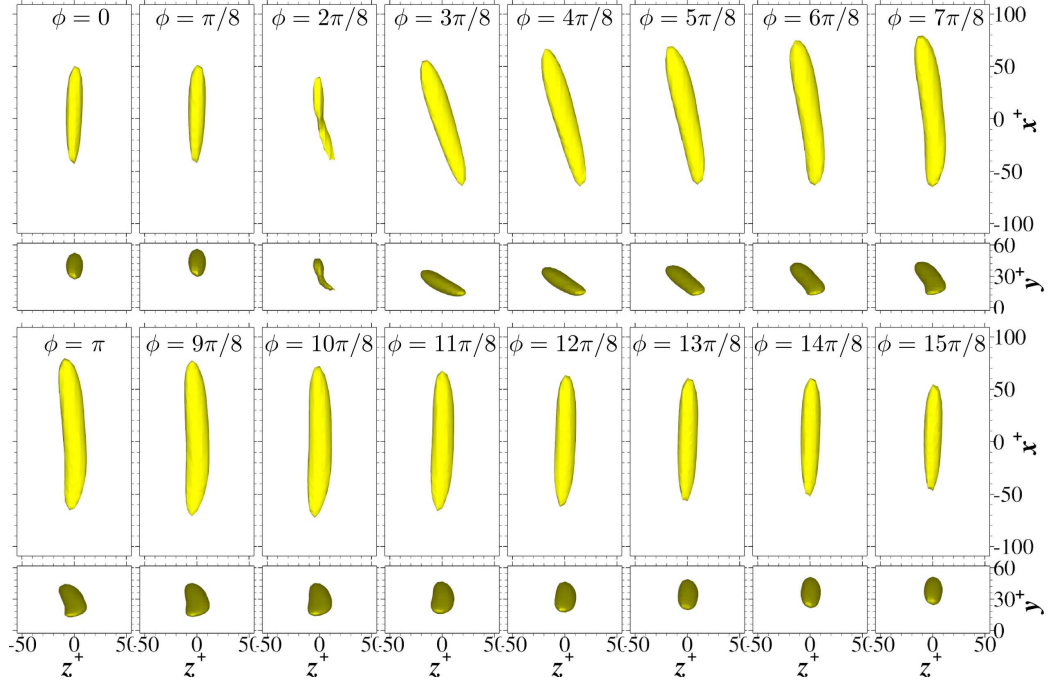
4.2.3 Phase modulation

Touber and Leschziner (2012) and Agostini and Leschziner (2014) have shown the strong phase modulation in turbulence statistics. In this section, we explore this point through the ensemble averaged λ_2 structures. The simulation is run for 10 oscillation periods in the new quasi-steady state, and instantaneous flow fields are saved at 16 equally separated phases. At each phase, the same ensemble average procedure described for the no control case in section 3.2 is employed. The final ensemble averaged λ_2 structures are shown in figure 4.19 for 16 phases. The positive and negative λ_2 structures show a dynamical variation during one oscillation period:

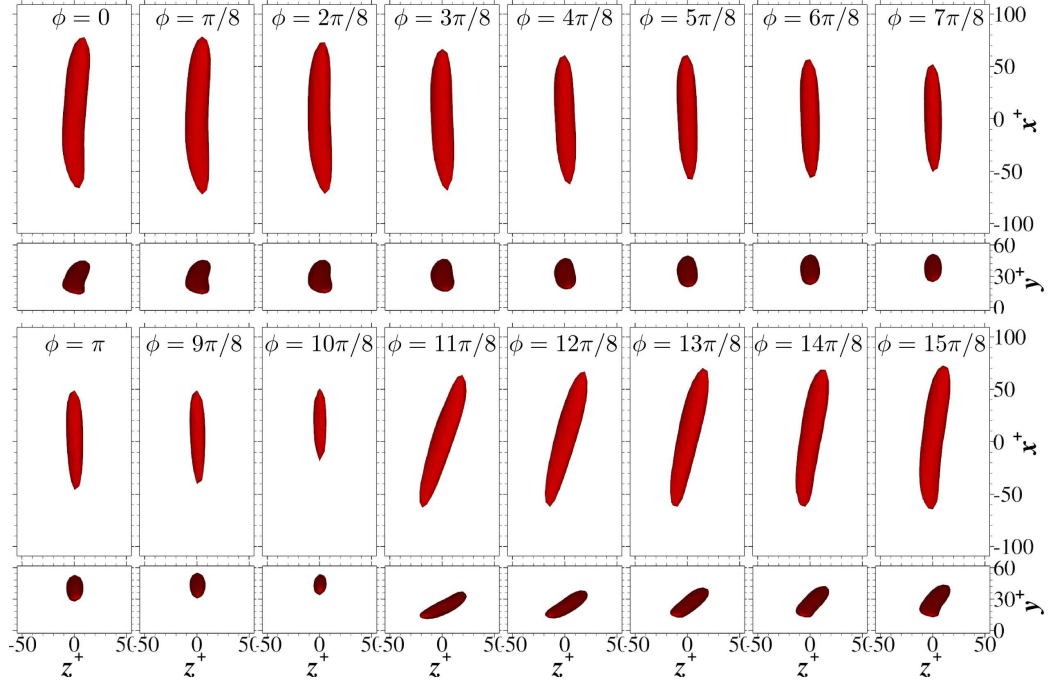
- 1) The positive and negative λ_2 structures are symmetric with half an oscillation period shift. For example, positive λ_2 structure at $\phi = 3\pi/8$ is symmetric about x direction with negative λ_2 structure at $\phi = 11\pi/8$.
- 2) From the xz plane view, the tilting angle varies from -18° to 0° for the positive structure, and from 18° to 0° for the negative structure.
- 3) From the yz plane view, both structures originate very close to the wall, then gradually move away from the wall.
- 4) The strength of the structure increases in the first $1/3$ period, then it decreases in the following $2/3$ period.

To quantitatively measure the ensemble averaged λ_2 structure properties, the centres of the ensemble averaged structures are identified, and then the wall normal location of the structure centre h^+ , the structure tilting angle α_t , the structure length l^+ , and the maximum of $-\lambda_2^+$ are plotted in figure 4.20. This again confirms the observation based on visualisation in figure 4.19.

The above λ_2 structure variation has also been studied by Hurst (2013). However, one unsolved puzzle is that the dynamics picture shown in 4.19 is not



(a)



(b)

Figure 4.19: Ensemble averaged λ_2 structure changes at 16 equally separated phases during one oscillation period at $\omega^+ = 0.06$ ($T^+ = 105$) for (a) positive structure and (b) negative structure. Structures are visualised by $\lambda_2^+ = -0.003$.

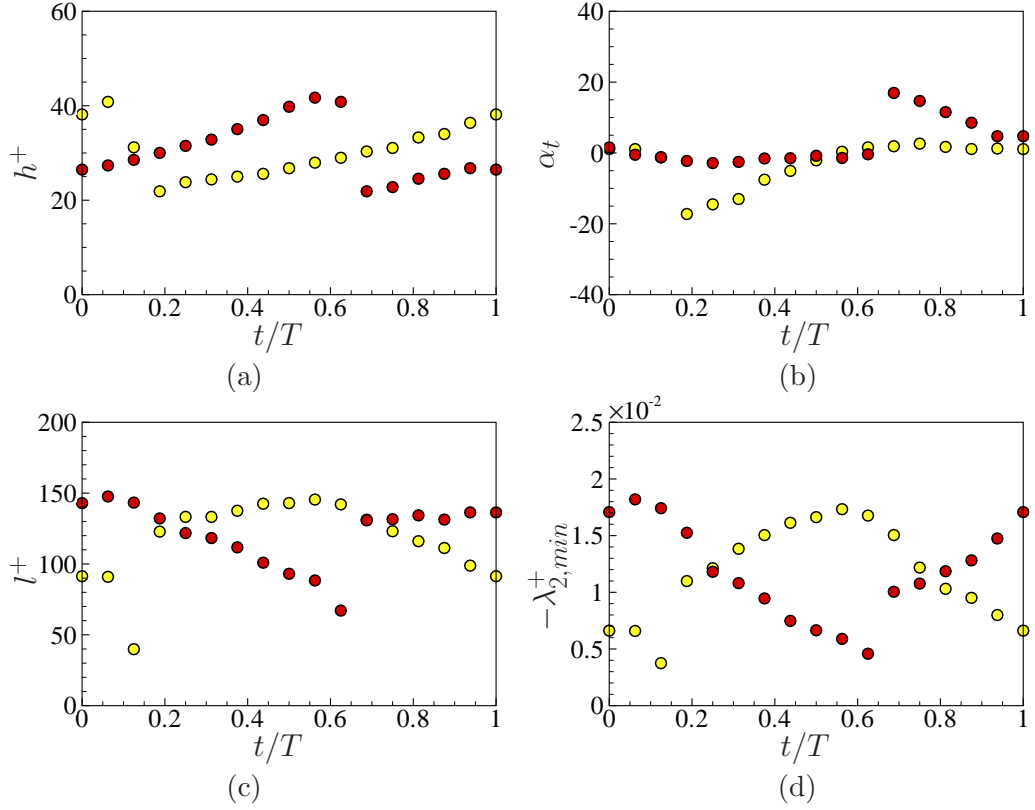


Figure 4.20: The measured properties from ensemble averaged positive (yellow symbols) and negative (red symbols) λ_2 structures: (a) the structure centre height h^+ , (b) the structure tilting angle α_t , (c) the structure length l^+ , and (d) the maximum value of $-\lambda_2^+$.

continuous, which can be even further observed from the measured structure height and tilting angle jumps in figure 4.20(a) and 4.20(b), respectively. This discontinuity was also observed for the near wall streaks angle variation by Touber and Leschziner (2012) and Blesbois et al. (2013). To answer this question, the λ_2 structures are further conditioned at phases, $\phi = \pi/8 \sim 3\pi/8$ for the positive one, and at $\phi = 9\pi/8 \sim 11\pi/8$ for the negative one. In this conditioning process, the near wall region is split into two parts: one is at $0 < y^+ < 20$, and the other is at $20 < y^+ < 60$. The new ensemble averaged λ_2 structures are shown in figure 4.21. Immediately, a stronger structure closer to the wall and a weaker structure further away from the wall can be observed. This result suggests that the ensemble averaged structure at the discontinuous phases in figure 4.19 actually represents two structures of the same kind: one is further away from the wall following the weak structure in the previous phase; the other one is closer to the wall leading the strong structure in

the next phase. Therefore, the ensemble averaged λ_2 structures monotonically move away from the wall and do not return to the wall.

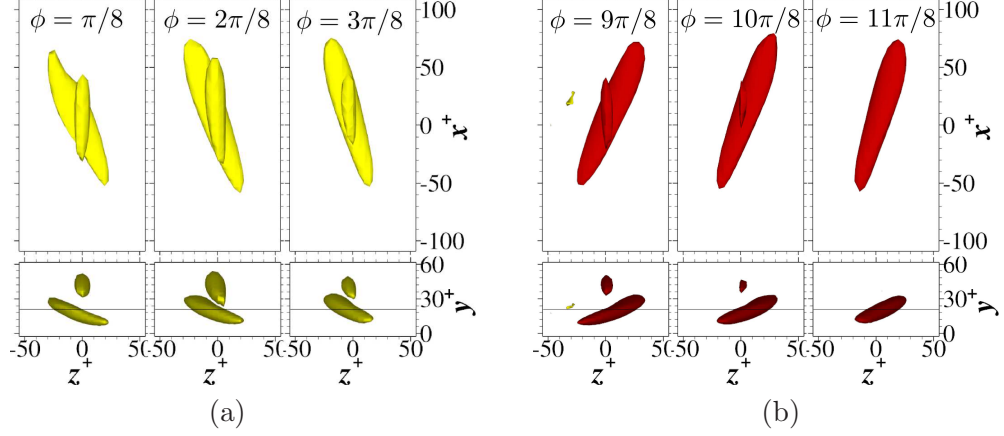


Figure 4.21: Ensemble averaged λ_2 structures in the lower wall region, *i.e.*, $0 < y^+ < 20$ and the upper wall region, *i.e.*, $20 < y^+ < 60$ for: (a) positive structures; and (b) negative structures.

The ensemble averaged λ_2 structures at the other three oscillation frequencies, *i.e.*, $\omega^+ = 0.01, 0.03$ and 0.12 ($T^+ = 628, 209$ and 52) have very similar phase variation as the one shown above for $\omega^+ = 0.06$ ($T^+ = 105$), and they are given in appendix D. In general, the tilting angle and structure height variations decrease as the wall oscillation frequency increases. This is consistent with the amplitude of the small time scale C_f variation shown in figure 4.12. At $\omega^+ = 0.01$ ($T^+ = 628$), the maximum tilting angle reaches $\alpha_{t,max} = 45^\circ$; while $\alpha_{t,max} = 9^\circ$ for $\omega^+ = 0.12$ ($T^+ = 52$) case, which is only slightly larger than the tilting angle of the no control case.

We focus on the $\omega^+ = 0.03$ ($T^+ = 209$) case to establish the link between the λ_2 structure variation and the phase modulation in the Reynolds shear stress and the skin-friction. This case is a sub optimal \mathcal{DR} case but with stronger phase variation compared to the optimal case at $\omega^+ = 0.06$ ($T^+ = 105$) (Touber and Leschziner, 2012). Figures 4.22(a) and 4.22(b) shows the full domain phase averaged turbulent shear stress $-\widetilde{u'v'}$ variation during one oscillation period for $\omega^+ = 0.06$ ($T^+ = 105$) and $\omega^+ = 0.03$ ($T^+ = 209$), respectively. As can be seen, $\omega^+ = 0.03$ ($T^+ = 209$) case has stronger phase variation than $\omega^+ = 0.06$ ($T^+ = 105$) case, which is mainly due to the stronger tilting of the λ_2 structures for $\omega^+ = 0.03$ ($T^+ = 209$) case. The $-\widetilde{u'v'}$ variation averaged within the domain ($L_x^+ \times L_y^+ \times L_z^+ = 200 \times 60 \times 100$) associated with the positive and negative λ_2 structures are shown in figures 4.22(c) and 4.22(d), respectively. There is a peak site at $y^+ \approx 20$ for positive λ_2 structure (at $\phi = 0$)

and for negative λ_2 structure (at $\phi = \pi$). This matches well with the double peak variation for the full domain statistics in figure 4.22(b). Agostini and Leschziner (2014) reported a hysteresis phenomenon in the phase variation. For example, for $-\widetilde{u'v'}$ at a fixed wall normal location y^+ in figure 4.22(b), the increasing time period tends to be shorter than the decreasing period. This was explained as the phase-wise asymmetric of the flow skewness by Agostini and Leschziner (2014). Figures 4.22(c) and 4.22(d) can offer another view about this hysteresis phenomenon, *i.e.*, the time scale for the λ_2 structure to be regenerated close to the wall is a very rapid process, and is much shorter than its decay time scale.

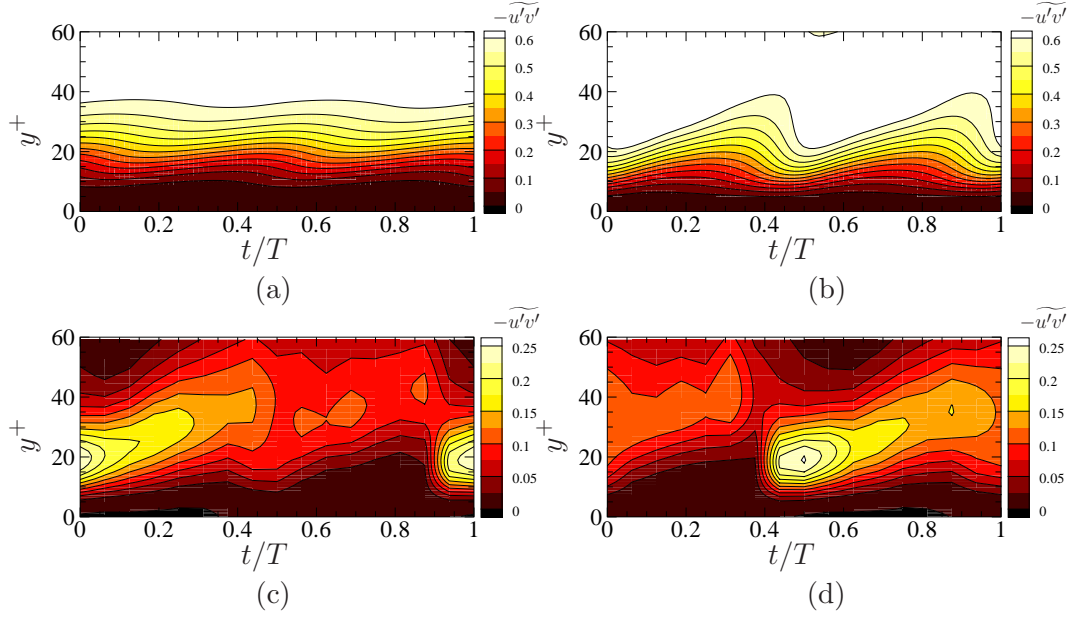


Figure 4.22: Phase modulation in Reynolds shear stress $-\widetilde{u'v'}$ for: (a) $\omega^+ = 0.06$ ($T^+ = 105$) case with full domain; and $\omega^+ = 0.03$ ($T^+ = 209$) case with (b) full domain; (c) positive λ_2 structure domain only; and (d) negative λ_2 structure domain only.

Figure 4.23 shows the phase variation for the positive and negative λ_2 structures in the identified number fraction ($\widetilde{\varphi}_+$, $\widetilde{\varphi}_-$), the skin-friction (\widetilde{C}_{f+} , \widetilde{C}_{f-}), and the weighted skin-friction ($\widehat{C}_{f_w} = \widetilde{\varphi}_+ \widetilde{C}_{f+} + \widetilde{\varphi}_- \widetilde{C}_{f-} - \overline{C_f}$). The spanwise strain favours the positive and negative λ_2 structures at different phases, which is again symmetric with half a period shifted for $\widetilde{\varphi}$ and \widetilde{C}_f associated with the positive and negative λ_2 structures. When the weighted skin-friction \widehat{C}_{f_w} is compared with that of the full domain \widehat{C}_f , a good agreement in the phase location of the peaks and troughs is observed, though \widehat{C}_{f_w} oscillates with an amplitude of $\sim 4\%$, larger than the full domain statistics ($\sim 2\%$). This is expected because the area without λ_2

structures in the full channel is not taken into account for the weighting.

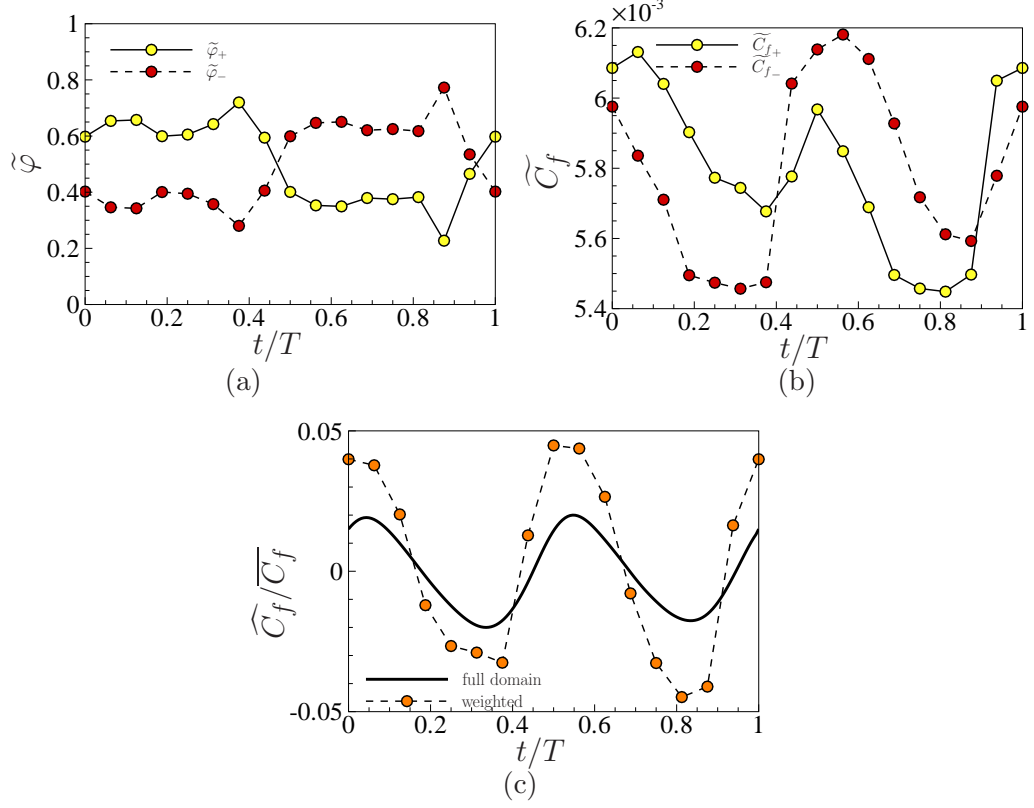


Figure 4.23: Phase variation for $\omega^+ = 0.03$ ($T^+ = 209$) in (a) identified λ_2 structure fraction $\tilde{\varphi}$; (b) skin-friction \tilde{C}_f ; and (c) weighted skin-friction \tilde{C}_{f_w} compared with the full domain case with \tilde{C}_f removed.

4.2.4 Streaks variation

The footprints of the quasi-streamwise vortices in the near wall region are the high- and low-speed streaks. We keep focusing on $\omega^+ = 0.03$ ($T^+ = 209$) case to investigate the streaks variation during one wall oscillation period. The instantaneous near wall streaks at $y^+ = 10$ and 20 for the no control case and $\omega^+ = 0.03$ ($T^+ = 209$) case are shown in figure 4.24. In the no control case, the near wall streaks are aligned in the streamwise direction and form a very long coherent pattern (see figure 2.2). The tilting angles of the positive and negative λ_2 structures (see figure D.1(b)), and the characteristics eddy (figure 4.25) are superimposed into the plots to give a visual impression about the spatial orientation between the streaks and the quasi-streamwise vortices. For $\omega^+ = 0.03$ ($T^+ = 209$) case, the streaks are significantly modulated by the wall motion. Figure 4.24(b) shows that the streaks are strongly tilted towards

one side of the flow field at phase $\phi = 0$. At this height $y^+ = 10$, the streaks tend to align between the positive and the negative λ_2 structures. However, when the cutting plane moves higher to $y^+ = 20$, the streaks become less coherent (figure 4.24(c)), and they are shorter compared to those at $y^+ = 10$. At phase $\phi = 0$, the positive and negative structures are located at very different wall normal locations, and the tilting angles are very different between them (see figure D.1(b)). This is reflected in the instantaneous flow field in figure 4.24(c): the streaks are broken up and shorter. Figure 4.24(d) shows the streaks at phase $\phi = \pi/4$, $y^+ = 10$. This is the phase that the streaks lose the orientation direction, and multiple streaks angles can be observed. Since the positive structure is closer to the wall compared to the negative one at phase $\phi = \pi/4$, the main streaks angle is dominated by the positive structure, as shown by the yellow line in the plot. However, newly generated small streaks can also be identified, for instance, in the region around $(x = 12, z = 5.5)$. These weak streaks are almost perpendicular to the main streaks in the flow field, and their angles match the alignment of the positive structure tail. The positive λ_2 structure is ‘J’ shaped at $\phi = \pi/4$, thus it can induce two different streaks angles. Le et al. (2000) conjectured ‘J’ shape and ‘S’ shape λ_2 structures in their 3D turbulent boundary layer generated by uni-direction wall motion. In the present study, the ‘J’ shape structures are directly captured from the ensemble average, and they are important in generating new streaks at a particular phase of the spanwise wall oscillation.

The near wall streaks can also be visualised by the characteristic eddy as discussed in section 3.3. Figure 4.25 shows the characteristic eddies at 16 equally separated phases for $\omega^+ = 0.03$ ($T^+ = 209$) case. Compared to the characteristic eddy in the no control case (figure 3.8), the length of them in the spanwise oscillation case becomes shorter, with the long tail disappeared. The near wall part is significantly tilted due to the Stokes layer, but the tilting is not in phase with the wall motion, which is also the case for the ensemble averaged λ_2 structure. The tilting angle of the modulated characteristic eddy represents the streaks alignment, as shown by the superimpose in figure 4.24. The yz plane view shows that the streaks angles also change with wall distance. The periodic variation of the characteristic eddy at other three frequencies, *i.e.*, $\omega^+ = 0.01$ ($T^+ = 628$), $\omega^+ = 0.06$ ($T^+ = 105$) and $\omega^+ = 0.12$ ($T^+ = 52$) are very similar, and they are given in appendix D. Two observations of these characteristic eddies are: 1) The phase difference between the characteristic eddy response and the wall motion depends on the wall oscillation frequency. For $\omega^+ = 0.01$ ($T^+ = 628$), the characteristic eddy has a long time to respond to the wall motion, thus it is almost in phase with the wall movement.

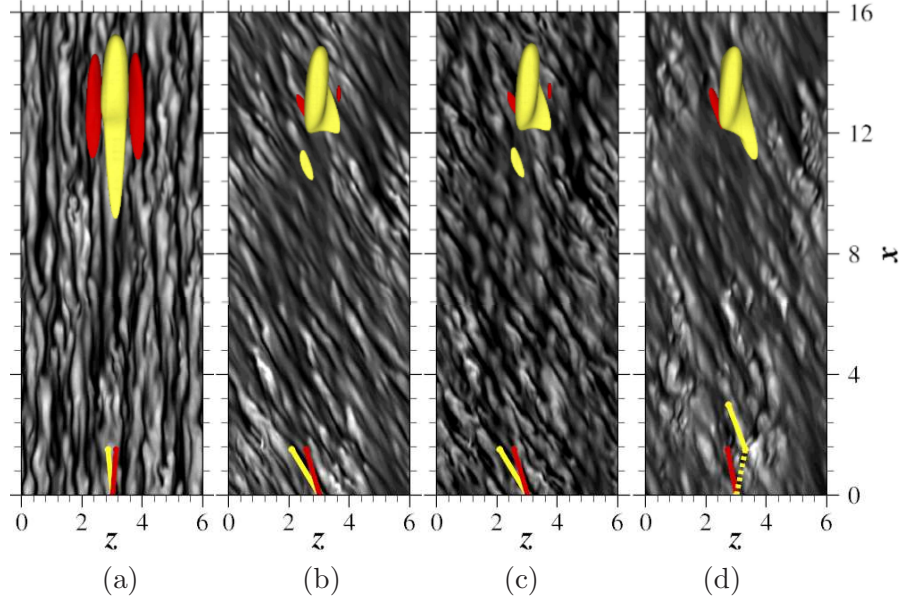


Figure 4.24: Streamwise velocity fluctuation u' from instantaneous flow fields for (a) no control case at $y^+ = 10$; and $\omega^+ = 0.03$ ($T^+ = 209$) case at (b) $y^+ = 10$, $\phi = 0$; (c) $y^+ = 20$, $\phi = 0$; (d) $y^+ = 10$, $\phi = \pi/4$. The contour is clipped at $[-0.15, 0.6]$. Dark color is for low velocity, while light colour is for high velocity. The yellow and red lines indicate the tilting angles of the ensemble averaged positive and negative λ_2 structures in figure D.1(b), respectively. The characteristic eddies from figure 4.25 are superimposed.

2) The modulation effect of the characteristic eddy by spanwise wall oscillation is larger at lower oscillation frequency, and smaller at higher oscillation frequency. For $\omega^+ = 0.12$ ($T^+ = 52$), there is almost no visible change of the characteristic eddies compared to the no control case.

We then choose the two cases with the largest streaks variation, *i.e.*, $\omega^+ = 0.03$ ($T^+ = 209$) and $\omega^+ = 0.01$ ($T^+ = 628$), for the streaks angle study. The streaks angles γ are identified from the characteristic eddy at a cutting plane of $y^+ = 10$. The phase-wise variation is compared with the mean velocity angle $\tilde{\gamma}_s$, the mean velocity gradient angle $\tilde{\gamma}_g$, and the Reynolds shear stress angle $\tilde{\gamma}_\tau$ at the same wall normal location, and the definitions of which are given as below (Jung and Sung,

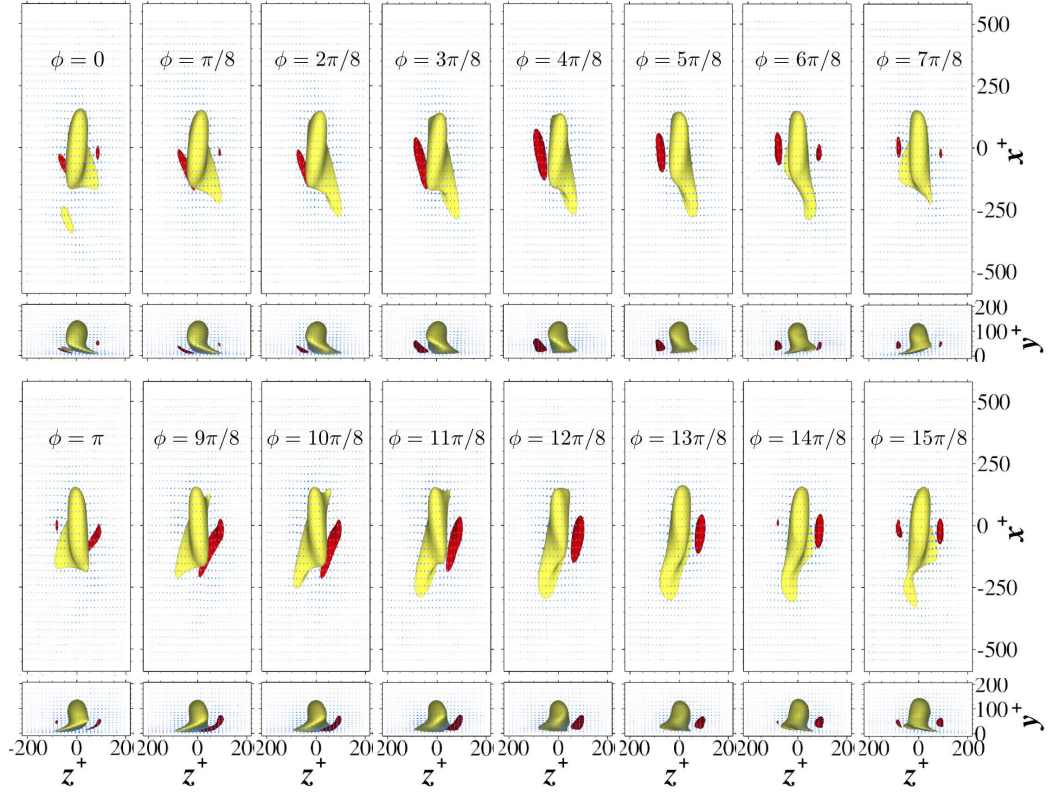


Figure 4.25: The characteristic eddies changes at 16 equally separated phases during one oscillation period at $\omega^+ = 0.03$ ($T^+ = 209$). The positive (yellow) and negative (red) eddies are visualised by $u' = 0.35$ and $u' = -0.35$, respectively.

2006),

$$\begin{aligned}
 \tilde{\gamma}_s &= \tan^{-1} \frac{\widetilde{W} - \widetilde{W}_w}{\widetilde{U}}, \\
 \tilde{\gamma}_g &= \tan^{-1} \frac{\partial \widetilde{W} / \partial y}{\partial \widetilde{U} / \partial y}, \\
 \tilde{\gamma}_\tau &= \tan^{-1} \frac{\widetilde{v'w'}}{\widetilde{u'v'}}.
 \end{aligned} \tag{4.9}$$

The comparison is shown in figures 4.26(a) and 4.26(b) for $\omega^+ = 0.03$ ($T^+ = 209$) and $\omega^+ = 0.01$ ($T^+ = 628$), respectively. As has been noticed by Touber and Leschziner (2012), Blesbois et al. (2013) and Hurst (2014), the streaks angle has two jumps during one oscillation period for $\omega^+ = 0.03$ ($T^+ = 209$) case. This jump in $\tilde{\gamma}$ is less obvious from the characteristic eddies, but it is clear that the streaks tend to stay at around one positive angle for half a period, then switch to a negative

angle. The transition period between them is very short. At $y^+ = 10$, $\tilde{\gamma}_s$, $\tilde{\gamma}_g$ and $\tilde{\gamma}_\tau$ are all phase-leading of the streaks angle $\tilde{\gamma}$. Toubert and Leschziner (2012) observed that $\tilde{\gamma}_g(y^+ = 10)$ matched $\tilde{\gamma}$ well. Figure 4.26(a) shows that $\tilde{\gamma}_\tau(y^+ = 10)$ is also a good (or even better) candidate for tracing the streaks. It is worth mentioning that Ricco (2004) proposed the maximum streaks angle γ_{max} calculation using a fixed near wall convection velocity $\mathcal{U}_c^+ = 10$. The phase variation of this indicator $\tilde{\gamma}_R = -\tan^{-1}(\tilde{W}/\mathcal{U}_c)$ is plotted in figure 4.26(a). Though with some phase difference, the maximum streaks angle prediction from $\tilde{\gamma}_R(y^+ = 10)$ agrees well with $\tilde{\gamma}$, even better than the other three angles. The same observation is also applied to $\omega^+ = 0.01$ ($T^+ = 628$) case in figure 4.26(b). At this large oscillation period, the streaks have enough time to reorganise themselves, thus the jump in the streaks angle almost disappears.

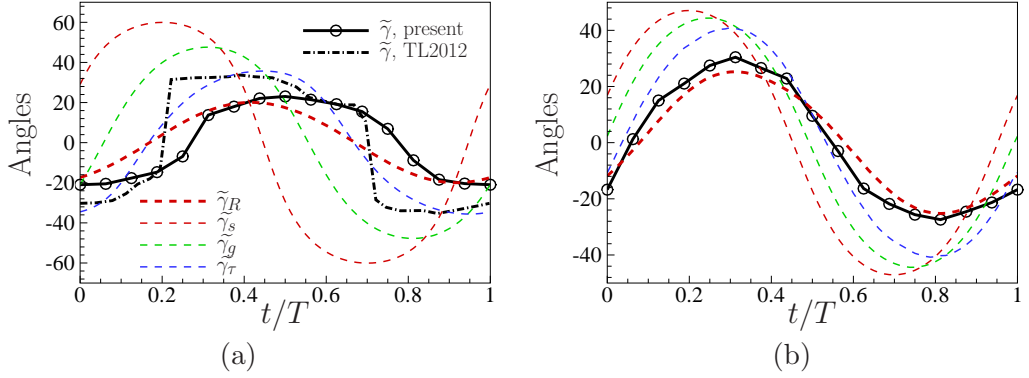


Figure 4.26: Variation of different angles at $y^+ = 10$ during one oscillation period for (a) $\omega^+ = 0.03$ ($T^+ = 209$); and (b) $\omega^+ = 0.01$ ($T^+ = 628$).

Figure 4.27 shows the change of the maximum streaks angle γ_{max} with the oscillation frequency ω^+ . As observed from the characteristic eddies, γ_{max} increases monotonously as ω^+ decrease for fixed A_w^+ . The experimental data from Ricco (2004) at three constant spanwise wall displacements D_m^+ are included for comparison. At fixed D_m^+ , the maximum streaks angle γ_{max} increases monotonously as ω^+ increases until an optimal frequency is reached, $0.08 < \omega_{opt}^+ < 0.1$ ($60 < T_{opt}^+ < 80$). An optimal oscillation frequency for the maximum γ_{max} is also observed by the $\gamma_{R,max}$ prediction using the laminar Stokes solution. This suggests the maximum streaks tilting angle is closely linked to the maximum spanwise wall velocity at around $y^+ = 10$.

Figures 4.28(a) and 4.28(b) show the correlation between \mathcal{DR} and the maximum streaks angle γ_{max} and the maximum streaks length l^+ , respectively. An opti-

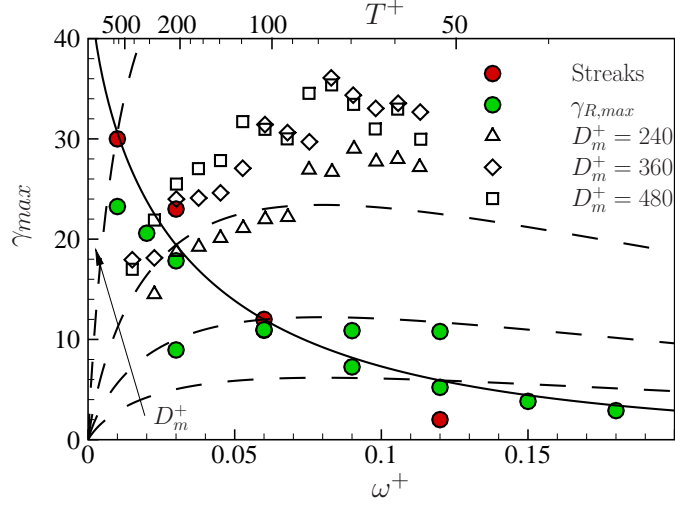


Figure 4.27: Streaks angles as a function of oscillation frequency (period), compared with (Ricco, 2004). Lines are $\gamma_{R,max}$ prediction using the laminar Stokes solution for W . The solid line is for $A_w^+ = 12$, and dashed lines are for $D_m^+ = 200, 400, 800$, and 2400.

mal γ_{max} is observed for the present data at fixed A_w^+ . The λ_2 structure also shows an optimal maximum tilting angle, but at a higher value. However, the experiment data from (Ricco, 2004) shows a monotonic increase of \mathcal{DR} as a function of γ_{max} up to $\gamma_{max} = 40^\circ$. This contrast is caused by the fact that majority of Ricco (2004)'s data are for fixed D_m^+ , as has been shown in figure 4.27. In figure 4.28(b), we identify the phase-wise maximum streak length using a threshold value of $u' = 0.01$ in the xz plane (at $y^+ = 10$) of the characteristic eddy fields, which is a somehow arbitrary choice. This is even more difficult for the optimal wall oscillation case, $\omega^+ = 0.06$ ($T^+ = 105$), where the streak formation process is strongly suppressed. Therefore, a 10% error bar for the streak length is included as a guide. Another dataset studied for the Lorentz force is directly taken from the pre-multiplied streamwise velocity spectra peaks (figure 5.24), and this process introduces a smaller arbitrary error. The streaks are further normalised by the streaks length of the no control case, l_0^+ , identified from each streak extraction method. With the aid from the experimental data by Ricco (2004), an optimal streaks length $l_{opt} \approx 0.5l_0$ can be seen. However, this argument only applies for the drag reduction cases, because for the drag increase cases, such as $\omega^+ = 0.01$ ($T^+ = 628$), they also show a streak length reduction.

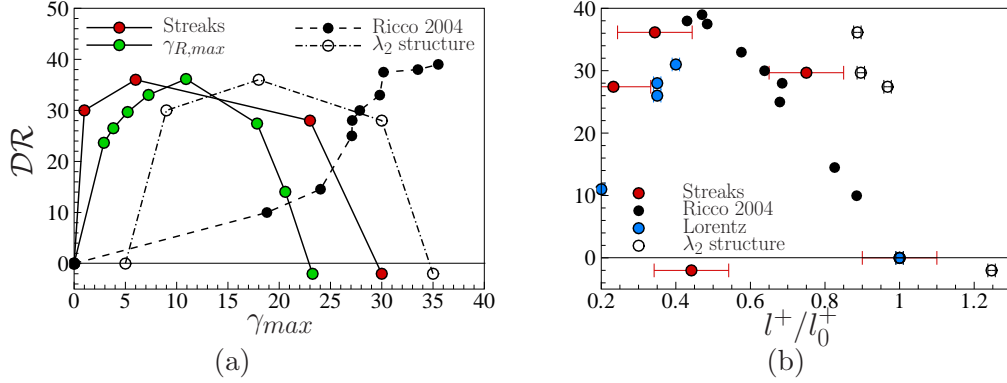


Figure 4.28: \mathcal{DR} as a function of (a) streaks angles γ ; and (b) normalised maximum streaks length l^+/l_0^+ .

4.3 Conclusions

Starting from the uni-direction wall movement, with particular focus on the transient process where an initial skin-friction drop happens, we investigated the turbulence response for $t^+ < 200$ using the ensemble averaged λ_2 structures and the turbulence statistics tools for the drag reduction mechanism exploration. Then the spanwise wall oscillation was studied at different oscillation frequencies, especially for $\omega^+ = 0.01, 0.03, 0.06$ and 0.12 ($T^+ = 628, 209, 105$ and 52). A vivid presentation of the near wall structure dynamics inside a spanwise oscillating Stokes layer is brought to surface, and this sheds light on the origin of the phase modulation of the turbulence statistics and the rich streaks behaviours. The following conclusions can be drawn from the study in this chapter:

- The positive and negative λ_2 structures respond to the initial spanwise wall motion in different ways, and they turn gradually in the spanwise direction to adjust the new flow. During this process, the near wall streaks are broken up, and the turbulent production cycle is weakened (Moin et al., 1990). Therefore, successively alternating spanwise wall motion can bring the flow into a lower C_f state. To achieve a sustained drag reduction by spanwise wall oscillation, half of the spanwise wall oscillation time scale needs to match the C_f decay time scale in the uni-direction wall motion, *i.e.*, $t^+ \approx O(80)$. This finding is in line with a serial of earlier works (Dhanak and Si, 1999; Quadrio and Ricco, 2004; Blesbois et al., 2013).
- Uni-direction wall motion is an extreme spanwise wall oscillation case with $\omega^+ = 0$ ($T^+ = \infty$), and can be used to predict the \mathcal{DR} asymptotic for spanwise

wall oscillation.

- In the quasi-steady spanwise oscillating Stokes layer, the positive and negative λ_2 structures have a cyclic dynamics, but with half an oscillation period shifted. During this process, the structures keep moving away from the wall, with their strength increasing initially, then decreasing till it is too weak to be identified.
- The phase modulation in the Reynolds shear stress and the skin-friction is closely linked to the identified λ_2 structure dynamics.
- The near wall streaks alternate the tilting angle during one oscillation cycle, but it is not in phase with the wall movement. The closest matching angle in phase is the Reynolds shear stress angle, γ_τ .
- Non-ideal sinusoidal temporal wave generated by the Lorentz force and the plasma actuators can be used for the drag reduction control.

Chapter 5

Drag Reduction by spanwise Lorentz Force

This chapter and the following chapter are two practical applications for skin-friction drag reduction control using two types of actuators: Lorentz force actuators in this chapter, and plasma actuators in the next chapter. The Lorentz force actuators use the electro-magnetic principle to generate a near wall body force, and use this body force to manipulate the flow, as sketched in figure 5.1. Therefore, the fluid needs to be electric conductive, such as sea water. The idea of using Lorentz body force is to replace the complex mechanical system which can ideally create spanwise wall oscillation or travelling waves of spanwise wall velocity (Auteri et al., 2010; Gouder et al., 2013; Gatti et al., 2015a).

Since the successful skin-friction control by spanwise oscillating Lorentz force (Berger et al., 2000), both spanwise and streamwise travelling wave by spanwise Lorentz force have been explored in a wide range of parameter space (Huang et al., 2010; Xie and Quadrio, 2013; Mamori et al., 2014). However, the control parameters were studied at different ranges for different travelling wave configurations, and the whole picture by spanwise Lorentz force is still missing. The aims of this chapter are three: 1) obtaining the whole drag reduction picture for different travelling wave controls by spanwise Lorentz force, with a particular emphasise on the oblique travelling wave; 2) demonstrating that there is no fundamental drag reduction mechanism difference among all these travelling wave controls by spanwise Lorentz force; 3) providing guides on the drag reduction control by plasma actuators in chapter 6.

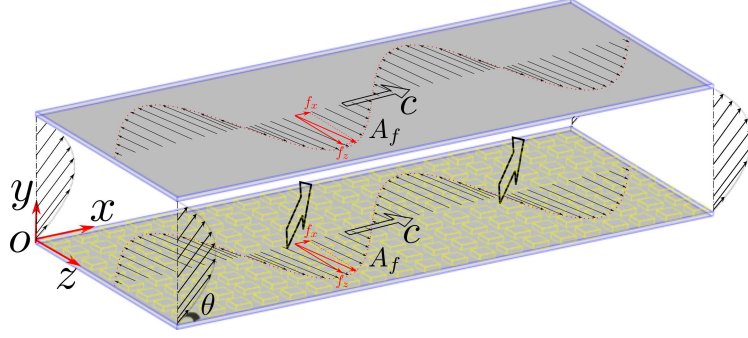


Figure 5.1: Schematics of skin friction control by the travelling wave of spanwise Lorentz force. The electro-magnetic tiles are represented by the small blocks on the wall. The mean flow has an angle of θ to the travelling wave direction.

5.1 Lorentz force model

By arranging electric and magnetic actuators alternatively in space under sea water (as shown in figure 5.1), an electric-magnetic body force can be generated. The governing equations are the Maxwell equations, shown as below.

$$\begin{aligned}
 \epsilon_{ijk} \frac{\partial E_k}{\partial x_j} &= -\frac{\partial B_i}{\partial t}, \\
 \epsilon_{ijk} \frac{\partial B_k}{\partial x_j} &= \mu_0 \sigma E_i, \\
 J_i &= \sigma(E_i + \epsilon_{ijk} u_j B_k), \\
 \frac{\partial B_i}{\partial x_i} &= 0, \\
 \frac{\partial J_i}{\partial x_i} &= 0, \\
 f_i &= \epsilon_{ijk} J_j B_k.
 \end{aligned} \tag{5.1}$$

Here, ϵ_{ijk} is the Levi-Civita symbol; f_i is the Lorentz force term, which appears in the right hand side of the N-S equations in equation (3.1); u_i is the fluid velocity; J_i is the current density; E_i is the electric field; B_i is the magnetic flux density; and μ_0 and σ are the magnetic permeability and the electrical conductivity of the fluid, respectively. It is clear to see that this is a two-way coupling system, with the electric-magnetic field acting on the fluid through the body force term $\epsilon_{ijk} J_j B_k$, and the fluid motion affecting the electric-magnetic field through the term $\epsilon_{ijk} u_j B_k$. However, Berger et al. (2000) has shown that for the drag reduction control under sea water using plasma actuators, $||\epsilon_{ijk} u_j B_k||$ is three order of magnitude smaller than $||E_i||$, therefore the electric magnetic field can be decoupled from the fluid

motion, resulting in a one-way coupling system only.

In the present study, only permanent magnet is considered, thus the above Maxwell equations can be further simplified by dropping the unsteady term for the magnetic flux, *i.e.*, $-\partial B_i/\partial t$. In this case the electric field E_i can be expressed by a potential function, $E_i = \partial\phi/\partial x_i$. The final form of the Maxwell equations to solve in the present application is as below.

$$\begin{aligned}
\frac{\partial^2 \phi}{\partial x_i^2} &= 0, \\
J_i &= \sigma \frac{\partial \phi}{\partial x_i}, \\
\frac{\partial J_i}{\partial x_i} &= 0, \\
\frac{\partial^2 B_i}{\partial x_j^2} &= 0, \\
\frac{\partial B_i}{\partial x_i} &= 0, \\
f_i &= \epsilon_{ijk} J_j B_k.
\end{aligned} \tag{5.2}$$

The derivation of equation (5.2) in a vector form has been given by Berger et al. (2000). By assuming that the boundaries for both the electric and the magnetic fields are sinusoidal, and the width of the electrode and magnetic tiles, a are the same but much smaller than the thickness of the fluid layer, an idealised Lorentz force expression can be obtained (see the appendix in (Berger et al., 2000)), shown as below.

$$f_z = A_f e^{-y/\Delta}, \tag{5.3}$$

where A_f is the non-dimensionalised force strength, *i.e.*, $A_f = J_0 B_0 h / \rho U_m^2$, where J_0 and B_0 are the current density and the magnetic flux on the electrode and the magnet surfaces, respectively; and Δ is the force penetration depth, *i.e.*, $\Delta = a/\pi$. To be noticed, the ideal Lorentz force only has a wall parallel component, and the wall normal component is zero. This ideal Lorentz expression has been widely used in the literature for drag reduction control study (Du et al., 2002; Huang et al., 2010; Mamori et al., 2014; Quadrio and Xie, 2015). Berger et al. (2000) also performed simulations with more realistic boundary conditions for the electric magnetic fields, and demonstrated that the effect on the skin-friction drag reduction is negligible. Therefore, the idealised Lorentz force model is employed in the present study, but in our case the wall parallel Lorentz force component is not necessary to be in z

direction, especially for the oblique travelling wave cases in section 5.4.

5.2 Wave configurations

Different wave configurations have been studied in the literature (see table 5.1 for a full list). In this section, four wave configurations are considered:

- Oblique oscillation – Lorentz force is applied with an orientation angle γ respect to the mean flow direction in x , and the force strength changes sinusoidally in time, as below,

$$\begin{aligned} f &= A_f e^{-y/\Delta} \sin(-\omega t), \\ f_x &= f \cos(\gamma), \quad f_z = -f \sin(\gamma), \end{aligned} \tag{5.4}$$

where ω is the oscillation frequency.

- Streamwise travelling wave – Lorentz force is applied in spanwise direction, and the force strength changes sinusoidally in x direction, as below,

$$f_z = A_f e^{-y/\Delta} \sin(-\kappa_x x), \tag{5.5}$$

where κ_x is the streamwise wavenumber.

- Spanwise travelling wave – Lorentz force is applied in spanwise direction, and the force strength changes sinusoidally in z direction, as below,

$$f_z = A_f e^{-y/\Delta} \sin(-\kappa_z z), \tag{5.6}$$

where κ_z is the spanwise wavenumber.

- Oblique travelling wave – Lorentz force is applied in the spanwise direction of the mean flow (not z direction). The force strength changes sinusoidally in the wave travelling direction (either x or z direction), as below,

$$\begin{aligned} f &= A_f e^{-y/\Delta} \sin(-\kappa \xi), \\ f_x &= f \sin(\alpha), \quad f_z = -f \cos(\alpha), \end{aligned} \tag{5.7}$$

where ξ is the wave travelling direction coordinate (either x or z); κ is the corresponding wavenumber; and α is the mean flow direction angle respect to x direction. The travelling wave angle $\theta = \alpha, 180^\circ - \alpha, 90^\circ + \alpha$ or $90^\circ - \alpha$ depending on the configuration.

Table 5.1: Travelling wave of Lorentz force studied in the literature.

Source	Re_τ	Wave form	A_f	Δ^+	T^+	λ^+
1	100, 200, 400	$f_z = A_f e^{-y/\Delta} \sin(\omega t)$	0.13, 0.25, 0.5, 1.0, 1.5 [‡]	5, 10, 20	25, 50, 75, 100, 125, 200, 500	-
2	150	$f_z = A_f e^{-y/\Delta} \sin(\omega t)$	1.3, 2, 4,	0.5, 1	25, 50,	210, 420, 840
		$f_z = A_f e^{-y/\Delta} \sin(\kappa_z z - \omega t)$	8, 20 [‡]	2, 3	100, 200	
3	177	$f_y = A_f e^{-y/\Delta} \sin(\kappa_x x - \omega t)$	2.3 [‡]	5, 10	$c = -2, -1,$	70 – 2000
		$f_x = A_f e^{-y/\Delta} \sin(\kappa_x x - \omega t)$			0, 1, 2	
4	180	$f_z = A_f e^{-y/\Delta} \sin(\kappa_x x - \omega t)$	2.3 [‡]	3.6	100	60, 140, 280, 380, 1130
5	180	$f_z = A_f e^{-y/\Delta} \sin(\kappa_x x + \kappa_z z - \omega t)$	1.2 [‡]	3.6	120	50 – 750

[†] 1: Berger et al. (2000); 2: Du et al. (2002); 3: Mamori and Fukagata (2011); 4: Huang et al. (2010); 5: Huang et al. (2014).

[‡] Converted value.

These four configurations are sketched in figure 5.2. For all the control cases, the mass flow rate is kept constant by dynamically adjusting the streamwise mean pressure gradient. For oblique travelling wave case, the mean flow has an angle α respect to x direction (figure 5.2(d1)), thus the mean pressure gradients in both x and z directions are adjusted simultaneously to maintain a constant mass flow rate, and their values at each time step are calculated based on the following force balance,

$$\begin{aligned} dP/dx &= -\frac{1}{h} \sqrt{\overline{\tau_{w,x}}^2 + \overline{\tau_{w,z}}^2} \cos \alpha, \\ dP/dz &= -\frac{1}{h} \sqrt{\overline{\tau_{w,x}}^2 + \overline{\tau_{w,z}}^2} \sin \alpha, \end{aligned} \quad (5.8)$$

where $\overline{\tau_{w,x}}$ and $\overline{\tau_{w,z}}$ are the xz plane averaged wall shear stresses in x and z directions, respectively.

5.3 Preliminary study

5.3.1 Effect of force parameters

The spanwise oscillating Lorentz force ($\gamma = 90^\circ$ in figure 5.2(a)) is first studied with the change of the Lorentz force parameters, *i.e.*, A_f , T^+ and Δ^+ . A baseline case is chosen at $A_f = 0.5$, $T^+ = 100$ and $\Delta^+ = 10$ according to the parameter study by Berger et al. (2000). These parameters are also within the popular parameter range explored in the literature (see table 5.1). Following Berger et al. (2000), the Lorentz force is only applied to the bottom wall, and the \mathcal{DR} is the skin friction reduction between the bottom and top walls. The Lorentz force strength A_f , oscillation period T^+ , and the Lorentz force penetration depth Δ^+ are varied to test the effect on the drag reduction. The comparison is also made with the data from Berger et al. (2000), as shown in figure 5.3. A good comparison can be observed, except the region where the Lorentz force strength A_f or the Lorentz force penetration depth Δ^+ is small. Overall, there is an optimal value for each control parameter when the other two parameters are fixed, and the chosen baseline case with $A_f = 0.5$, $T^+ = 100$ and $\Delta^+ = 10$ is a local maxima.

5.3.2 Oblique oscillation

The angle effect in the oblique oscillation case is studied for $A_f = 0.5$, $\omega^+ = 0.06$ ($T^+ = 105$). The C_f response and the long time \mathcal{DR} are shown in figure 5.4. At $\gamma = 0^\circ$, there is a large oscillation in the skin-friction time history due to the pumping effect created by the streamwise Lorentz force. The oscillation effect becomes smaller

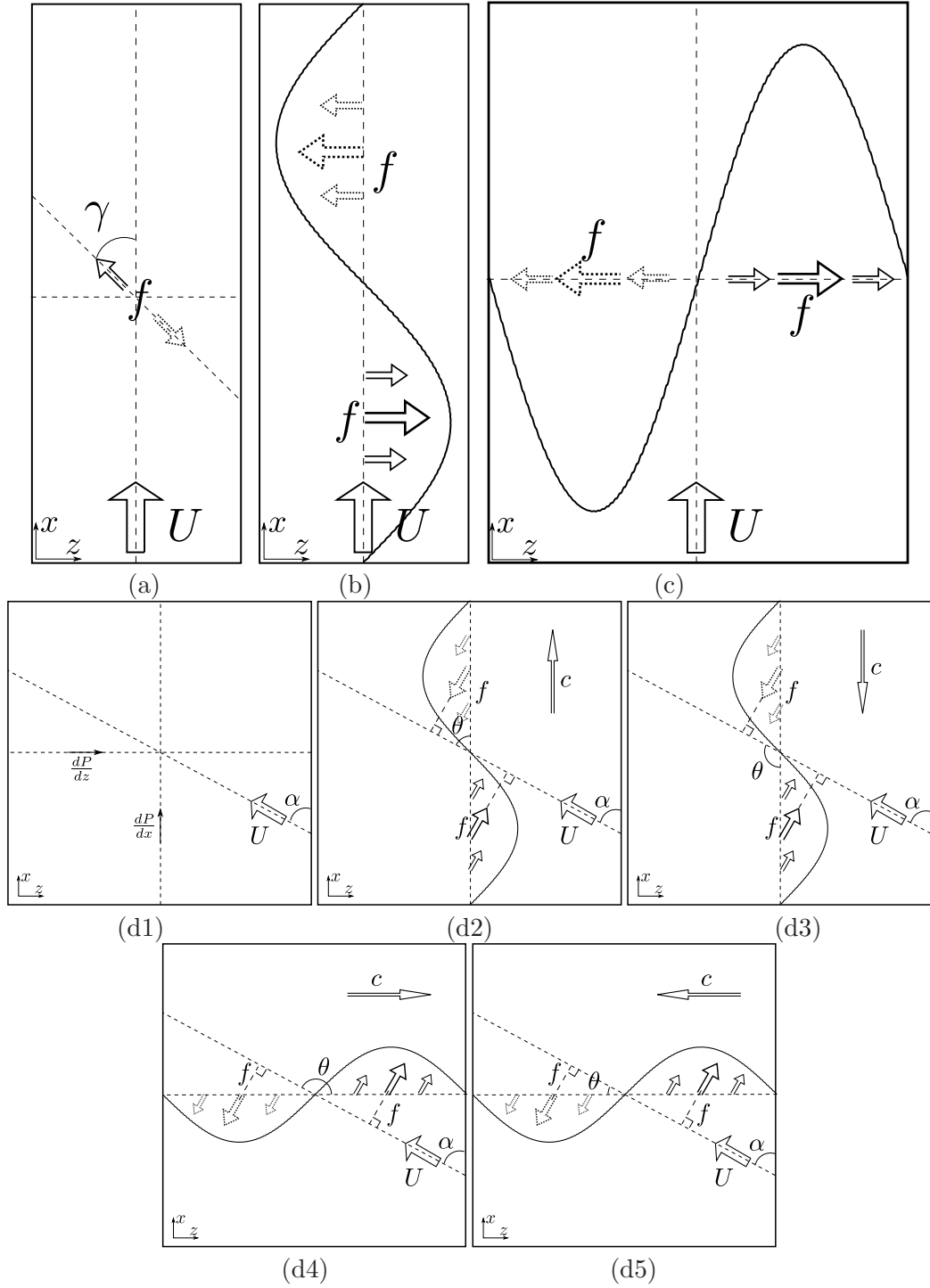


Figure 5.2: Wave configurations for: (a) oblique oscillation with an angle γ to the mean flow direction; (b) streamwise travelling wave; (c) spanwise travelling wave; and (d1-d5) oblique travelling waves.

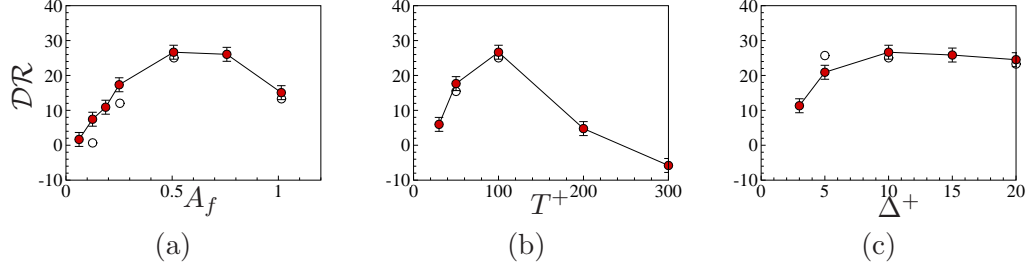


Figure 5.3: Effect on drag reduction \mathcal{DR} from (a) Lorentz force strength A_f ; (b) oscillation period T^+ ; and (c) Lorentz force penetration depth Δ^+ . Close symbols are the present data, and open symbols are from Berger et al. (2000).

as γ becomes larger. As expected, for the spanwise oscillating Lorentz force ($\gamma = 90^\circ$), the oscillation in C_f is the smallest. Drag reduction is only achieved for $\gamma > 45^\circ$, and the \mathcal{DR} value is almost constant at around $30 \pm 2\%$ for Lorentz force angle $\gamma \geq 60^\circ$. Zhou and Ball (2008) studied the effect of wall oscillation orientation, and their data at $A_w^+ = 12.48$, $\omega^+ = 0.063$ ($T^+ = 100$) is included in figure 5.4(b) for the comparison. As mentioned by the authors, there is a break-point at $\gamma = 60^\circ$ where \mathcal{DR} saturates above this angle. This is consistent with the present oscillating Lorentz force case, though for the present oscillating Lorentz force case \mathcal{DR} drops slightly at $\gamma = 90^\circ$. A big difference between these two cases appears at small γ , where $\mathcal{DR} \approx 10$ is still achievable for wall oscillation at $\gamma = 0^\circ$; while \mathcal{DR} is negative for $\gamma \leq 30^\circ$ in the oscillating Lorentz force case. Based on this observation, the Lorentz force is only applied in the spanwise direction ($\gamma = 90^\circ$) for the controls in the following sections.

5.3.3 Spatial transient response

The Lorentz force normally can only be applied to one portion of the wall. To test the effect of the force locality, the Lorentz force parameters of the baseline case ($A_f = 0.5$, $\Delta^+ = 10$, $T^+ = 100$) is applied to only the first half of the channel domain on both the bottom and the top walls. Periodic boundary conditions are applied in the streamwise direction, thus this flow is different from a true boundary layer flow simulation. To avoid the numerical instability due to the sharp change of the Lorentz force at the interface, a step function (Yudhistira and Skote, 2011) is applied with a window size of 0.5, as shown below,

$$S(x) = \begin{cases} 0, & \text{if } x \leq 0, \\ 1 / (1 + e^{1/(2x-1)+1/(2x)}), & \text{if } 0 < x < 0.5, \\ 0, & \text{if } x \geq 0.5. \end{cases} \quad (5.9)$$

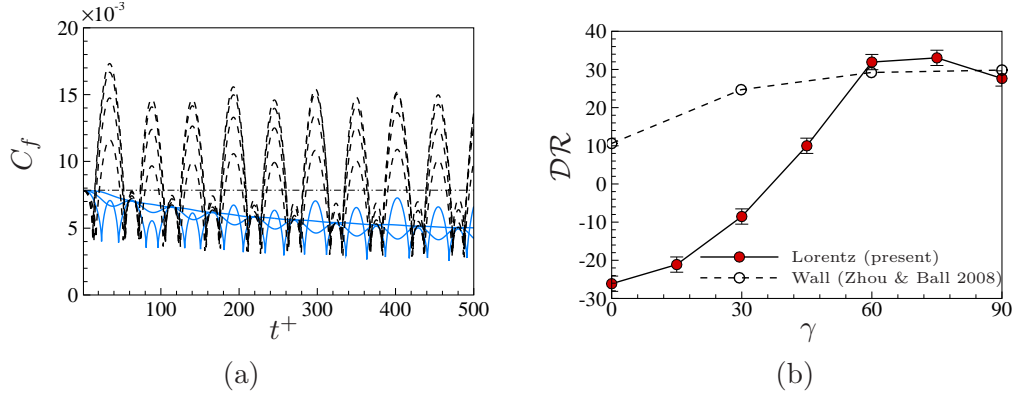


Figure 5.4: Effect of oscillating Lorentz force direction γ : (a) time history of the skin-friction C_f (dashed lines are for $\gamma \leq 45^\circ$, and solid lines are for $\gamma > 45^\circ$); (b) drag reduction values compared with wall oscillation cases (Zhou and Ball, 2008).

Figure 5.5 shows the instantaneous streamwise velocity contour at $y^+ \approx 5$ for three different channel lengths. Clearly, the high- and low-speed streaks are skewed in the controlled region, while they recover and align again in the streamwise direction in the second half of the channel, where the Lorentz force is off. At the interface between the control and the no control regions, the streaks behaviour is very similar to the experimental observation for spanwise wall oscillation (Choi et al., 1998) and spanwise oscillating Lorentz force (Pang et al., 2004).

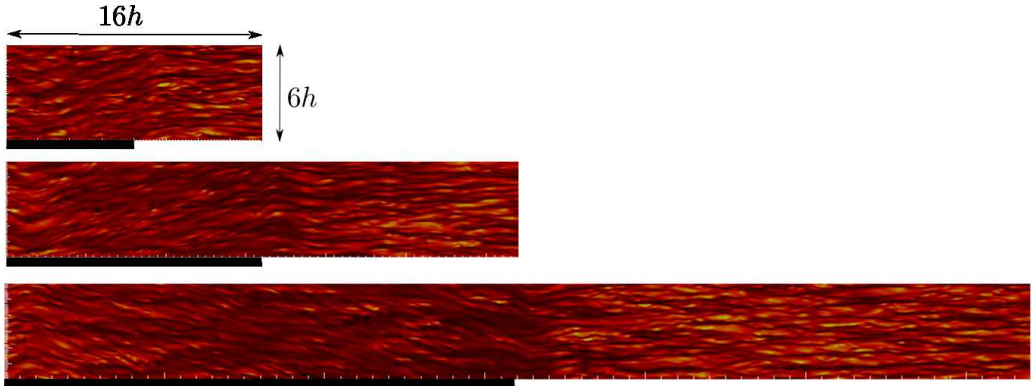


Figure 5.5: Near wall streaks at $y^+ \approx 5$ for test domain of $L_x = 16, 32$ and 64 . The oscillating Lorentz force ($A_f = 0.5$, $\Delta^+ = 10$, $T^+ = 100$) is applied in the first half of the domain length (indicated by black blocks).

The time, spanwise and top-bottom wall averaged skin-friction coefficient C_f is plotted in figure 5.6 as a function of the streamwise coordinate. When the Lorentz force is applied, the C_f starts to drop quickly. This transient process is as long as the case in the boundary layer (Choi et al., 1998; Ricco and Wu, 2004; Lee and Sung,

2005; Yudhistira and Skote, 2011; Lardeau and Leschziner, 2013). To make the C_f drop to the level of a full domain controlled case, the domain size must be very long, up to $L_x = 64$. By further increasing the domain size to $L_x = 128$, the transient C_f value can be even lower than the full domain controlled case, which is not the case in the turbulent boundary layer. This undershooting of C_f may be related to the periodic boundary condition effect. Once the flow enters the channel region without the Lorentz force, the C_f level starts to increase quickly. Interestingly, the increasing length seems to be domain size independent, and is fixed at around 15 for $L_x = 32, 64$ and 128 three cases.

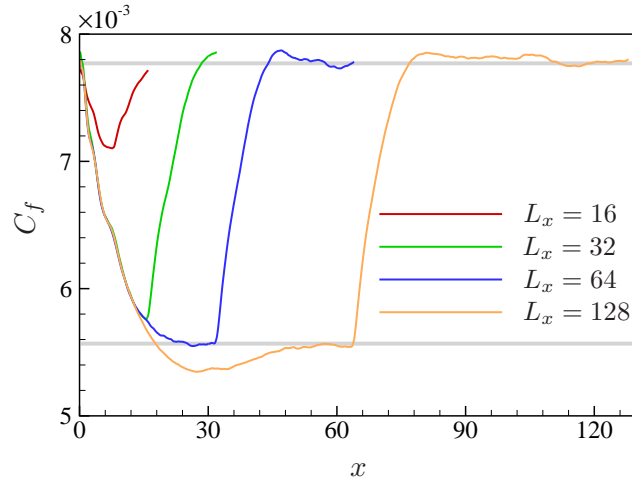


Figure 5.6: Skin-friction coefficient C_f distribution along streamwise direction for different channel lengths. Two horizontal lines indicate the C_f levels of the no control and the fully controlled cases, respectively.

The spatial transient behaviour is important in choosing the \mathcal{DR} measurement location for the boundary layer control in experiments. For example, Quadrio and Ricco (2003) estimated that this spatial transient length could be around $2000 \sim 4000$ in viscous lengths for spanwise wall oscillation, and pointed out that some published \mathcal{DR} measurements were too close to the leading edge of the oscillating section. Figure 5.7(a) compares the spatial response of the normalised C_f between our simulation results and the boundary layer measurements by Choi et al. (1998) and Ricco and Wu (2004). The experimental measurement by Ricco and Wu (2004) shows a long plateau after $x^+ \approx 3000$, which clearly suggests that the oscillating plate was long enough for C_f to settle down. Their C_f decay rate compares very well with our simulation result with $L_x \geq 32$, provided our simulations are not for true boundary layers. Choi et al. (1998)'s experimental data was more

scattering, and the C_f started to recover too early, which suggests the oscillating plate might not be long enough. This is also the case for the boundary layer control using spanwise oscillating Lorentz force by Lee and Sung (2005), where an even higher \mathcal{DR} should be expected if the control section was longer in their simulation.

The spatial response of C_f immediately after the trailing edge of the oscillating section is shown in figure 5.7(b). The recovery rate for $L_x \geq 32$ compares well with the experimental data by Ricco and Wu (2004), though the actual streamwise recovery length are different, $x^+ \approx 3000$ in our case, and $x^+ \approx 1500$ in (Ricco and Wu, 2004). It is worth mentioning that Lardeau and Leschziner (2013) showed a 5δ recovery length in their $Re_\tau = 520$ boundary layer simulation, which is close to our recovery length in wall units. The simulation by Lee and Sung (2005) shows a similar recovery rate to our $L_x = 16$ case, which again suggests that their control domain might be not long enough.

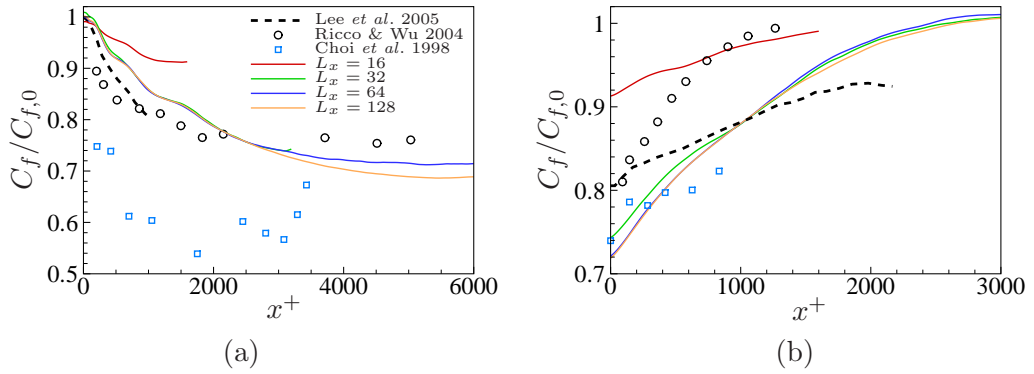


Figure 5.7: Spatial response of normalised Skin-friction coefficient $C_f/C_{f,0}$ after (a) the leading edge, and (b) the trailing edge of the oscillating section.

The \mathcal{DR} recovery is also checked from the instantaneous velocity field for $L_x = 32$ case, as shown in figure 5.8. At this instance ($t/T = 0.46$), the Lorentz force generates strong negative spanwise velocity in the controlled section ($x < 16$). However, this spanwise velocity does not go to zero immediately after the trailing edge. Instead, the temporal oscillation has been converted into a spatial oscillation in the downstream, which can be observed by the positive and negative w contour at $x > 16$. And this spanwise velocity keeps displacing the vortical structures relative to the near wall streaks (Ricco and Wu, 2004). A direct comparison of the vortical structures and the streaks orientation in yz planes is also shown in the graph: one is within the control region (at $x = 13$), and the other one is at the downstream of the trailing edge (at $x = 19$). The vortical structures at $y = 0.1$ ($y^+ = 20$) are twisted in spanwise direction in a similar fashion at these two x

locations. However, the near wall high- and low-speed streaks have clearly recovered at $x = 19$, and they are almost invisible at $x = 13$. Ricco (2004) visualised the near wall streaks and vortical structures using hydrogen bubble technique at $x^+ \approx 600$ downstream of the oscillating wall section, and argued that the high- and low-speed streaks were set to rest due to the no-slip wall condition, while the spanwise wall movement was transferred by viscous diffusion to convey the vortical structures at higher wall location, and this relative displacement between the streaks and vortical structures led to a slow \mathcal{DR} decay. This is generally the same situation for the present oscillating Lorentz force case.

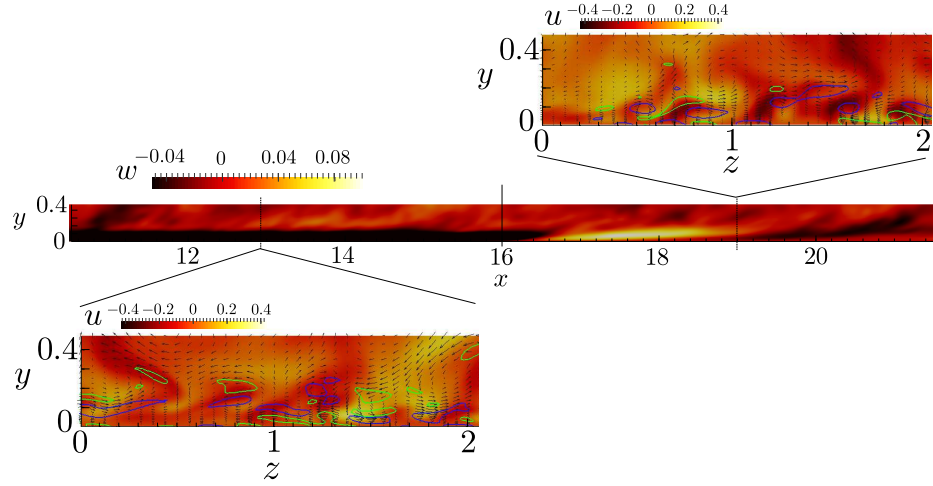


Figure 5.8: Instantaneous flow field visualisation around the trailing edge of an oscillating section ($x = 16$) for $L_x = 32$ case (only one portion of the domain is displayed). xy plane shows spanwise averaged w velocity contour; yz planes show streamwise velocity fluctuation u' contour, streamwise vorticity fluctuation ω'_x iso-lines (blue for $\omega'_x = 1.5$, and green for $\omega'_x = -1.5$), and $v' - w'$ velocity vectors.

5.4 Oblique travelling waves

The angle effect of the oblique travelling wave has been previously studied by Huang et al. (2014). However, in their study, the domain size (L_x, L_z) was fixed, and the total wavenumber κ ($\equiv \sqrt{\kappa_x^2 + \kappa_z^2}$) was adjusted by changing κ_x and κ_z , thus the total wavenumber κ was not a constant when the travelling wave angle θ ($\equiv \tan^{-1}(\kappa_z/\kappa_x)$) varied. Also, since there must be an integer number of waves in x and z directions, the total number of θ which could be studied (for a chosen domain size) was very limited. To avoid this issue, we fix the wave travelling direction in either x or z direction, and vary the mean flow direction to adjust the travelling wave angle θ ,

as shown in figure 5.2(d). We choose $L_x = L_z = 16$, thus with this configuration, the wavelength is always fixed, and a continuous change of the travelling wave angle θ is allowed. Moreover, the turbulence statistics can be sampled in the wave travelling direction and its perpendicular direction.

Four base flows are performed for the no control case (figure 5.2(d1)), and they have the angles of $\alpha = 0^\circ, 15^\circ, 30^\circ$ and 45° to x direction. For each base flow, the travelling wave can be applied in the positive x (figure 5.2(d2)), the negative x (figure 5.2(d3)), the positive z (figure 5.2(d4)) or the negative z (figure 5.2(d5)) direction, which corresponds to an oblique wave angle of $\alpha, 180^\circ - \alpha, 90^\circ + \alpha$ and $90^\circ - \alpha$. Therefore, the angle effect can be studied for a fixed wavelength in a range of $\theta = 0^\circ \sim 180^\circ$ with an interval of 15° (13 cases in total). To seek the possible maximum drag reduction, the wavenumber is chosen to be $\kappa^+ = 0.002$ ($\lambda^+ = 3142$) and the oscillation frequency $\omega^+ = 0.06$ ($T^+ = 105$), which passes the optimal travelling wave case BST ($\theta = 180^\circ$), as shown in table 5.2. When $\theta = 0^\circ$, it gives the FST case. And when $\theta = 90^\circ$, it is close to the SP case, since the spanwise domain is $L_z = 12$ for SP case, while it is $L_z = 16$ for the oblique travelling wave case. More details of BST, SP, BST and Oblique cases can be found in table 5.2. It has to be mentioned that the grid resolution in x direction has been improved to be the same as z direction, *i.e.*, $\Delta x^+ = \Delta z^+ = 2.5$ to compensate the effect caused by the new streak orientation in the present simulation set up.

Instantaneous snapshots for the velocity magnitude at $y^+ \approx 5$ are shown in figure 5.9 for the oblique travelling wave cases at $A_f = 0.5$, $\Delta^+ = 10$, $\kappa^+ = 0.002$ ($\lambda^+ = 3142$) and $\omega^+ = 0.06$ ($T^+ = 105$). The “ribbon” structure, which is caused by the travelling wave can be clearly seen as dark bands in the plots. As observed by Pang and Choi (2004) for the spanwise oscillating Lorentz force and by Huang et al. (2010) for the streamwise travelling wave case, the near wall streaks are strongly twisted in the direction parallel to the wave travelling direction. As expected, the twisting effect on the near wall streaks is the strongest for $\theta = 0^\circ$ and 180° , where the Lorentz force is perpendicular to the near wall streaks; and the twisting effect is hardly visible for $\theta = 90^\circ$, except at the interface where Lorentz force changes directions. This might be the reason that Du et al. (2002) thought the near wall streaks modulation was fundamentally different for spanwise travelling wave case. However, figure 5.9 clearly demonstrates the gradual change of the interaction between the “ribbon” structure and the near wall streaks from $\theta = 0^\circ$ to 180° . The nature of this interaction is similar among all the oblique travelling wave cases, and there is always a twisting effect of the near wall streaks.

The drag reduction obtained for all the 13 oblique travelling wave cases is

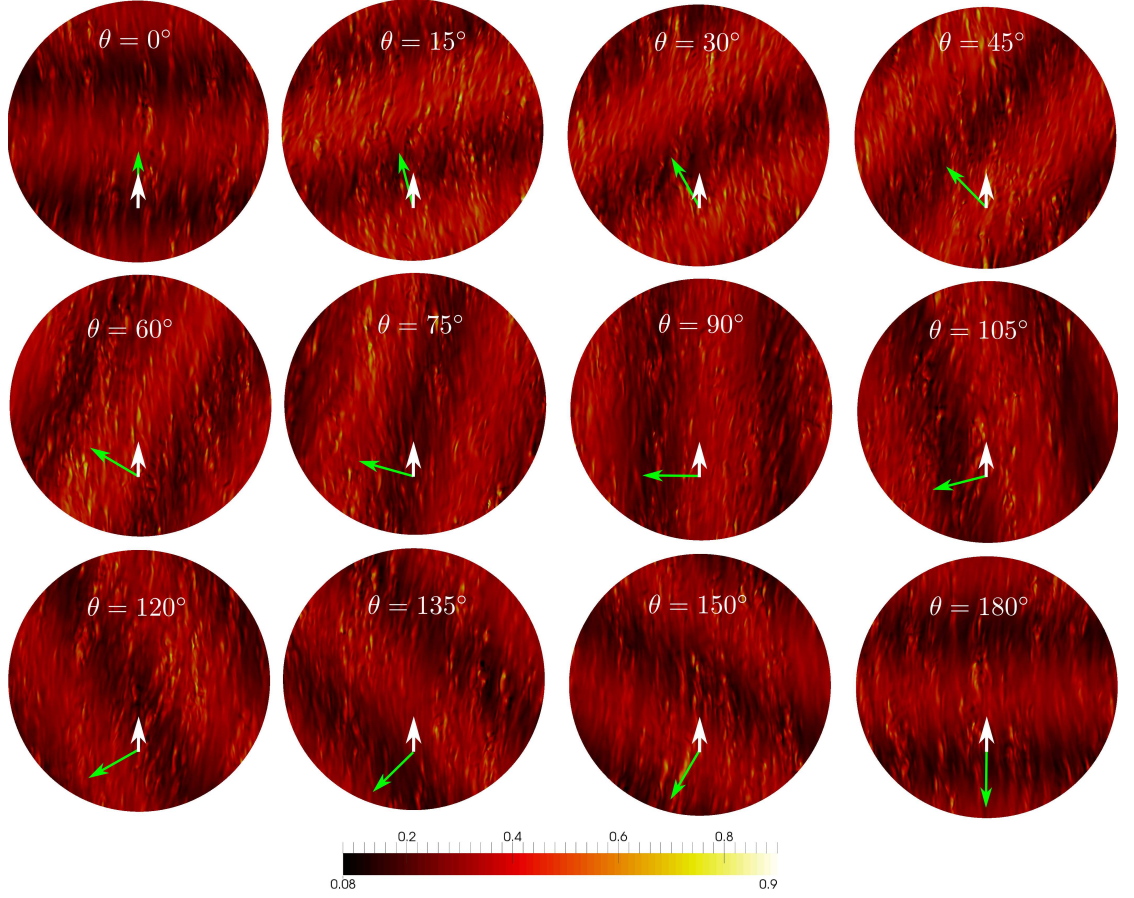


Figure 5.9: Instantaneous velocity magnitude $\sqrt{u^2 + v^2 + w^2}$ at $y^+ \approx 5$ for different travelling wave angles. On each snapshot, the white wide arrow indicates the main flow direction, and the green long arrow indicates the wave travelling direction. The view size is 16 in diameter.

shown in figure 5.10. The \mathcal{DR} prediction at $\theta = 0^\circ$, 90° and 180° compares well with that from FST, SP and BST cases. The maximum \mathcal{DR} value is achieved at $\theta = 180^\circ$. However, when $\theta > 90^\circ$, the \mathcal{DR} value is not sensitive to the wave angle θ , and the \mathcal{DR} variation is within a range of $\Delta\mathcal{DR} = 3$. A sharp increase of \mathcal{DR} is observed for $\theta < 90^\circ$, which has $\Delta\mathcal{DR} = 15$.

The turbulence statistics are sampled in both x and z directions. A coordinate transformation is used to transform the turbulence statistics into the streamwise and spanwise directions. The relationship between the velocities in the transformed coordinate system (u, v, w) and the original coordinate system (u_1, u_2, u_3) for the streamwise velocity, the streamwise velocity fluctuation and the streamwise turbu-

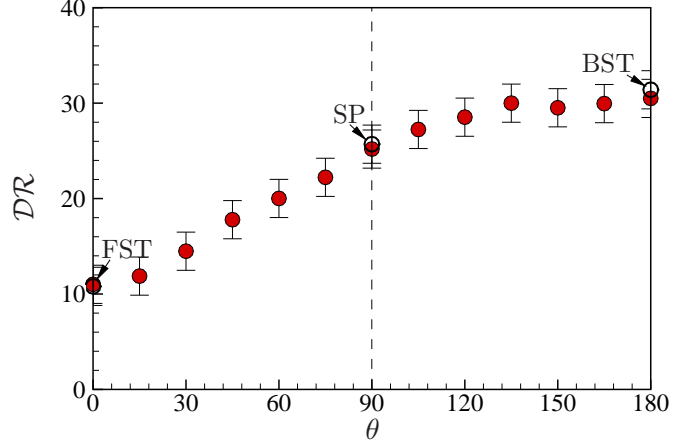


Figure 5.10: \mathcal{DR} against travelling wave angle θ for oblique travelling waves. Open circles are data from table 5.2 for FST, SP and BST cases.

lent shear stress is shown as below,

$$\begin{aligned}
 u &= u_1 \cos \theta - u_3 \sin \theta, \\
 \overline{u'^2} &= (\overline{u_1^2} - U_1^2) \cos^2 \theta + (\overline{u_3^2} - U_3^2) \sin^2 \theta - (\overline{u_1 u_3} - U_1 U_3) \sin(2\theta), \\
 \overline{u'v'} &= \overline{u_1 u_2} \cos \theta - \overline{u_2 u_3} \sin \theta.
 \end{aligned} \tag{5.10}$$

The transformed velocity r.m.s. $u_{i,rms}^+$ and the weighted streamwise turbulent shear stress $-(1-y)\overline{u'v'}$ are shown in figure 5.11. For all the 13 cases, the wall normal velocity fluctuation v_{rms}^+ and the spanwise velocity fluctuation w_{rms}^+ show a monotonic decrease as θ increases. However, the streamwise velocity fluctuation u_{rms}^+ shows an interesting phenomenon at the peak location: when θ increases from 0° to 90° , the peak slightly moves away from the wall, but the strength is dramatically weakened; when θ increases from 90° to 180° , the peak keeps moving away from the wall, but the strength slightly increases. This peak behaviour is closely linked to the near wall streaks and quasi-streamwise structures. Some evidence can be seen from the snapshots in figure 5.9, but more analysis will be described in the following sections. The weighted turbulent shear stress $-(1-y)\overline{u'v'}$ gives the contribution to the skin-friction from the turbulent fluctuation (equation (4.3)), and it shows a monotonic decrease, which is in agreement with the \mathcal{DR} plot in figure 5.10. Again, larger change of $-(1-y)\overline{u'_1 u'_2}$ appears for $\theta < 90^\circ$, while smaller change for $\theta > 90^\circ$.

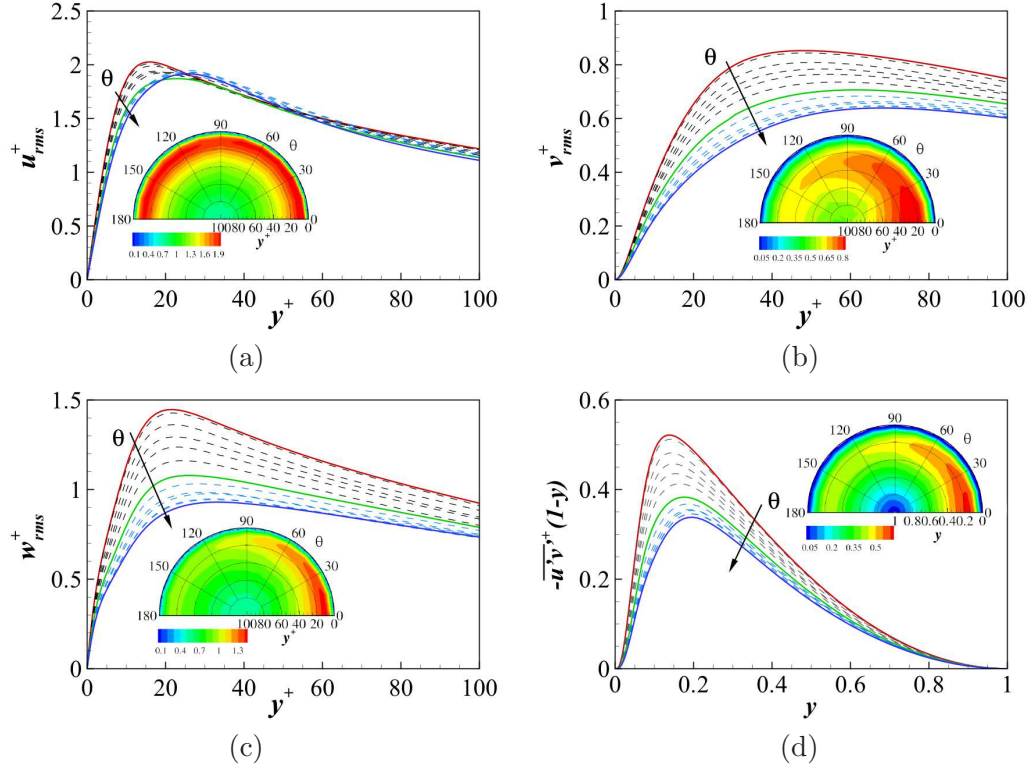


Figure 5.11: Turbulence statistics in transformed coordinate for: (a) u_{rms}^+ , (b) v_{rms}^+ , (c) w_{rms}^+ , and (d) $-(1-y)\overline{u'v'}$. The three solid lines represent $\theta = 0^\circ$, 90° and 180° , respectively. The inserted contour plots are the corresponding statistics in polar coordinate.

5.5 Streamwise and spanwise travelling waves

5.5.1 \mathcal{DR} maps

The drag reduction maps for both the streamwise and the spanwise travelling waves as a function of the oscillation frequency ω^+ and the wavenumber κ^+ are shown in figure 5.12, at fixed Lorentz force strength $A_f = 0.5$ and penetration depth $\Delta^+ = 10$. The horizontal axis is the oscillation frequency ω^+ (or period T^+), while the vertical axis represents the wavenumber κ^+ (or wavelength λ^+). A total number of 113 simulations are performed to create the \mathcal{DR} maps. The \mathcal{DR} map for the streamwise travelling wave (figure 5.12(a)) shows a great resemblance to the streamwise travelling wave induced by spanwise wall velocity (Hurst et al., 2014; Quadrio et al., 2009): a drag increase (\mathcal{DI}) region (light colour) accompanied by the drag reduction (\mathcal{DR}) regions (dark colour) at each side. The \mathcal{DI} region appears when the wave travels at a speed similar to the convection velocity \mathcal{U}_c^+ of the near

wall turbulence structure, which is typically around $\mathcal{U}_c^+ = 10$ (Kim and Hussain, 1993). However, several differences in the streamwise travelling wave \mathcal{DR} map between the spanwise Lorentz force and the spanwise wall motion (see figure 7.3 and figure 2 in (Quadrio et al., 2009)) can be observed:

- The \mathcal{DI} region in the spanwise wall motion has a wave speed $c^+ (\equiv \omega^+ / \kappa_x^+) = 12$, while it is $c^+ = 8$ in the spanwise Lorentz force case.
- The maximum drag reduction occurs in the backward streamwise travelling wave case with $\mathcal{DR} = 31 \pm 2$ at $\omega^+ = -0.06$ ($T^+ = 105$), $\kappa_x^+ = 0.002$ ($\lambda_x^+ = 3142$). However, in spanwise wall motion case, the optimal \mathcal{DR} case is within the forward travelling wave region with $\mathcal{DR} = 48 \pm 2$ at $\omega^+ = 0.02$ ($T^+ = 314$), $\kappa_x^+ = 0.008$ ($\lambda_x^+ = 785$).
- The \mathcal{DI} region is broader in the Lorentz force case, which means the control is less effective than the spanwise wall motion case.

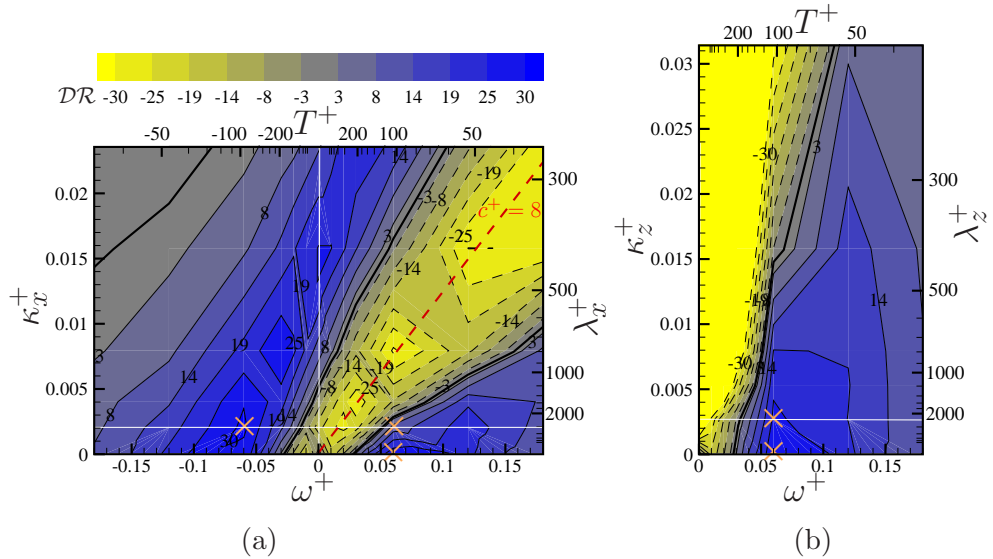


Figure 5.12: Drag reduction maps for (a) streamwise travelling wave and (b) spanwise travelling wave. The zero contour level is indicated by the black bold lines. Cross symbols mark OC, FST, SP and BST cases in table 5.2.

Figure 5.12(b) shows the \mathcal{DR} map for the spanwise travelling wave cases. It also has a \mathcal{DR} region and a \mathcal{DI} region. However, the shape is very different from the \mathcal{DR} map for the streamwise travelling wave. The \mathcal{DR} region and the \mathcal{DI} region are almost vertically separated. The optimal frequency ω_{opt}^+ shifts only slowly as κ_z^+ increases (it is almost fixed at $\omega^+ \approx 0.06$ ($T^+ \approx 104$) for small κ_z^+). All the

spanwise stationary wave cases ($\omega^+ = 0$) show a drag increase, and the \mathcal{DR} value is much larger than that in the streamwise travelling wave cases. Large drag reduction is associated with small spanwise wavenumber κ_z^+ , and this is consistent with the finding by Du et al. (2002). As has been pointed out by Xie and Quadrio (2013), spanwise oscillation case indeed results in the largest drag reduction compared to all the spanwise travelling wave cases at the same oscillation frequency.

From the drag reduction maps in figure 5.12, four typical cases are selected: the spanwise oscillation case (OC), forward streamwise travelling wave case (FST), spanwise travelling case (SP) and backward streamwise travelling wave case (BST). The four cases are indicated in figure 5.12 by cross symbols, and their control parameters are given in table 5.2. The selected BST is the case with the highest drag reduction among all the streamwise and spanwise travelling wave cases. The three travelling wave cases have roughly the same wavelength, and they are also the reference cases for the oblique travelling wave studied in section 5.4.

Table 5.2: Main case parameters with $A_f = 0.5$, $\Delta^+ = 10$.

Case	$L_x \times L_z$	$\Delta x^+ \times \Delta z^+$	ω^+	κ_x^+	κ_z^+	θ	\mathcal{DR}
OC	16×6	5.0×2.5	0.06	0	0	-	28 ± 2
FST	16×6	5.0×2.5	0.06	0.0020	0	0°	11 ± 2
SP	16×12	5.0×2.5	0.06	0	0.0026	90°	26 ± 2
BST	16×6	5.0×2.5	-0.06	0.0020	0	180°	31 ± 2
Oblique	16×16	2.5×2.5	± 0.06	$0.002 \setminus 0.0$	$0.0 \setminus 0.002$	-	-

The optimal oscillation frequency ω_{opt}^+ for the spanwise oscillating Lorentz force and the optimal streamwise wavenumber $\kappa_{x,opt}^+$ for the streamwise stationary wave are both changed from the spanwise wall motion cases. Quadrio et al. (2009) showed $\omega_{opt}^+ = 0.06$ ($T_{opt}^+ = 105$) for the spanwise wall oscillation case and $\kappa_{x,opt}^+ = 0.005$ ($\lambda_{x,opt}^+ = 1257$) for the streamwise stationary wave case. These two optimal values are linked by a convection velocity \mathcal{U}_c^+ . In the present spanwise Lorentz force case, there also appear to be an optimal oscillation frequency, ω_{opt}^+ , and an optimal streamwise wavenumber, $\kappa_{x,opt}^+$, as shown in figure 5.13. However, the optimal values are different from the case of spanwise wall motion, and they are very sensitive to the Lorentz force penetration depth, Δ^+ . As shown in figure 5.13, at $\Delta^+ = 10$, the optimal values are $\omega_{opt}^+ = 0.08$ ($T_{opt}^+ = 79$) and $\kappa_{x,opt}^+ = 0.014$ ($\lambda_{x,opt}^+ = 449$); at $\Delta^+ = 5$, these two optimal values are $\omega_{opt}^+ = 0.05$ ($T_{opt}^+ = 126$) and $\kappa_{x,opt}^+ = 0.01$ ($\lambda_{x,opt}^+ = 628$). By taking a look at the absolute \mathcal{DR} values for the spanwise oscillation cases and the streamwise stationary wave cases, surprisingly, it is found that for the spanwise oscillation case, the \mathcal{DR} value at ω_{opt}^+ is higher when $\Delta^+ =$

10, but for the streamwise stationary wave case, the \mathcal{DR} value at $\kappa_{x,opt}^+$ is higher when $\Delta^+ = 5$. This means that the exact shape of the \mathcal{DR} map can change with the penetration depth Δ^+ . Also, as observed from figure 4.13, \mathcal{DR} has different asymptotic behaviours depending on Δ^+ . However, due to the computational cost, no exploration is attempted for the effect of the Lorentz force penetration depth Δ^+ .

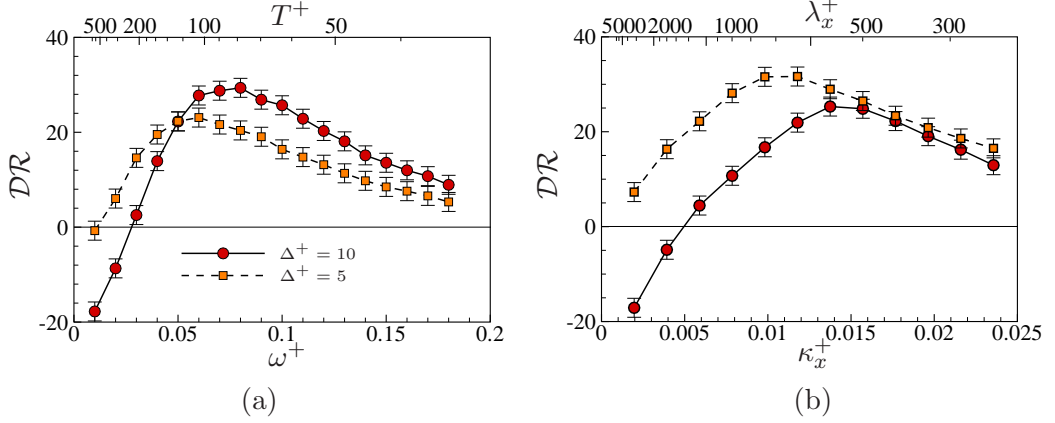


Figure 5.13: Drag reduction for (a) spanwise oscillation cases and (b) streamwise stationary wave cases at $A_f = 0.5$ with $\Delta^+ = 10$ and $\Delta^+ = 5$.

Berger et al. (2000) showed that the optimal wavenumber $\kappa_{x,opt}^+$ for the spatially oscillating Lorentz force was linked to the optimal oscillation frequency ω_{opt}^+ of the temporal oscillating Lorentz force at the range of $\omega^+ = 0.05 \sim 0.25$ ($T^+ = 25 \sim 125$) by a constant convection velocity $\mathcal{U}_c^+ = 10$. The comparison between the spatially oscillating Lorentz force and the temporal oscillating Lorentz force for the present data is shown in figure 5.14. A convection velocity of $\mathcal{U}_c^+ = 5$ is used for the convection. In a broad range of $\omega^+ = 0.05 \sim 0.2$, the \mathcal{DR} trends are similar. A more general way is to extend the time scale \mathcal{T}^+ proposed by Quadrio et al. (2009) for the streamwise travelling of spanwise wall velocity to the following form, with the travelling wave angle considered,

$$\mathcal{T}^+ = \frac{\lambda^+}{|\mathcal{U}_c^+ \cos(\theta) - c^+|}. \quad (5.11)$$

The oscillation frequencies for the forward streamwise travelling wave, spanwise travelling wave, backward streamwise travelling wave at $\kappa^+ \approx 0.002$ ($\lambda^+ \approx 3142$) (as shown by the white solid lines in figure 5.12), and all the 13 oblique travelling wave cases (from figure 5.10) are converted using equation (5.11) with $\mathcal{U}_c^+ = 8$. The data are shown in figure 5.14 for the comparison with the temporal oscillation

case. All the curves for the travelling waves almost collapse with the one for the temporal oscillation case. Overall, figure 5.14 suggests that all the travelling waves at $\kappa^+ \approx 0.002$ ($\lambda^+ \approx 3142$) can be analogue to the temporal oscillation case, and all of them show an optimal converted optimal oscillation frequency at $\omega_{opt}^+ = 0.05 \sim 0.1$. The good agreement between the converted oblique travelling wave case and the temporal oscillation case strongly supports that the interaction between the “ribbon” structure in the travelling wave case (Du and Karniadakis, 2000) and the near wall streaks is similar to the case in temporal oscillation case, where the interaction comes from the homogeneous Lorentz force. In the following sections, the similarity in the turbulence statistics and the structure dynamics will be further explored.

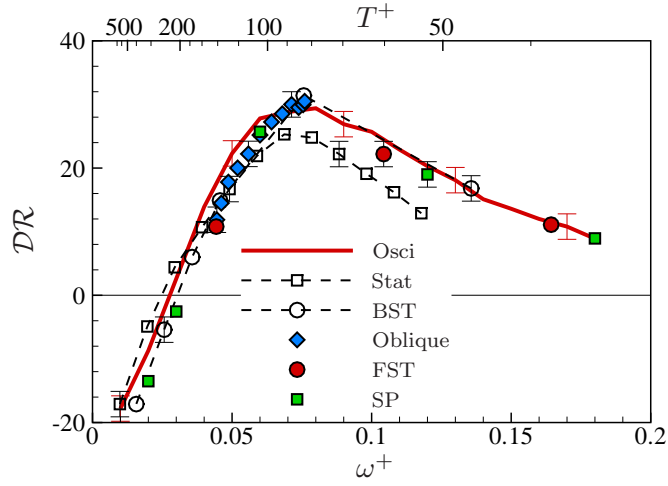


Figure 5.14: \mathcal{DR} comparison for travelling wave cases with the oscillation frequency converted using equation (5.11), where $\mathcal{U}_c^+ = 5$ is used for streamwise stationary wave (Stat), and $\mathcal{U}_c^+ = 8$ for all the others. Stationary, forward streamwise travelling wave, spanwise travelling wave and backward streamwise travelling wave are indicated by the while lines in figure 5.12, and the oblique travelling wave is from figure 5.10.

5.5.2 Power budget

Following Ricco et al. (2012), the kinetic energy balance in the controlled channel unit is given as below,

$$\begin{aligned}\mathcal{E}_P + \mathcal{E}_f &= \mathcal{D}_U + \mathcal{D}_W + \mathcal{D}_{\mathcal{T}}, \\ \mathcal{E}_P &= \left[U_m \frac{\partial \tilde{P}}{\partial x} \right]_g, \quad \mathcal{E}_f = [\widetilde{fw}]_g, \\ \mathcal{D}_U &= \left[\left(\frac{\partial \tilde{U}}{\partial y} \right)^2 \right]_g, \quad \mathcal{D}_W = \left[\left(\frac{\partial \tilde{W}}{\partial y} \right)^2 \right]_g, \quad \mathcal{D}_{\mathcal{T}} = \left[\widetilde{\frac{\partial u_i}{\partial x_j} \frac{\partial u_i}{\partial x_j}} \right]_g,\end{aligned}\tag{5.12}$$

where $\tilde{\cdot}$ indicates phase average as shown in equation (4.4), and $[\cdot]_g$ is defined as,

$$[\cdot]_g = \frac{1}{TV} \int_0^T \int_V \cdot dV dt = \frac{1}{2TL_x L_z} \int_0^T \int_0^2 \int_0^{L_x} \int_0^{L_z} \cdot dx dz dy dt.$$

\mathcal{E}_P is the pumping power through the streamwise pressure gradient, \mathcal{E}_f is the power input through the spanwise Lorentz body force, \mathcal{D}_U , \mathcal{D}_W and $\mathcal{D}_{\mathcal{T}}$ are the dissipation rates in the streamwise mean flow, the spanwise mean flow and the turbulent fluctuations, respectively. Therefore, the fluid power input due to the Lorentz force can be either calculated from \mathcal{E}_f directly or from its balance terms in equation (5.12). However, f and its generated w are not always in phase, thus the fluid is less efficient in extracting power from the Lorentz body force. This process is demonstrated for a laminar case at $\omega^+ = 0.06$ ($T^+ = 105$) in figure 5.15(a). In this case, \mathcal{E}_f is in balance with \mathcal{D}_W . However, $\frac{1}{V} \int_V \widetilde{fw} dV$ is negative in some phase, corresponding to the power output from the fluid to the Lorentz force actuators. However, this energy recycling mechanism does not exist for our one-way coupled plasma actuator model, and the Lorentz force actuator has to consume power to do the negative fluid work. Therefore, we define the minimum power spent (relative to the pumping power) from our Lorentz force actuators as,

$$P_{sp} = [\widetilde{fw}]_g / \mathcal{E}_P \times 100 (\%),\tag{5.13}$$

and correspondingly the relative net energy saving is defined as,

$$P_{net} = \mathcal{DR} - P_{sp}.\tag{5.14}$$

Here the minimum power spent is in the sense that we do not consider any electric power lost due to the electric efficiency of the actuators. Figure 5.15 shows that

$[\widetilde{fw}]_g / \mathcal{E}_P$ is always larger than $[\mathcal{E}_f]_g / \mathcal{E}_P$ for a wide range of oscillation frequencies.

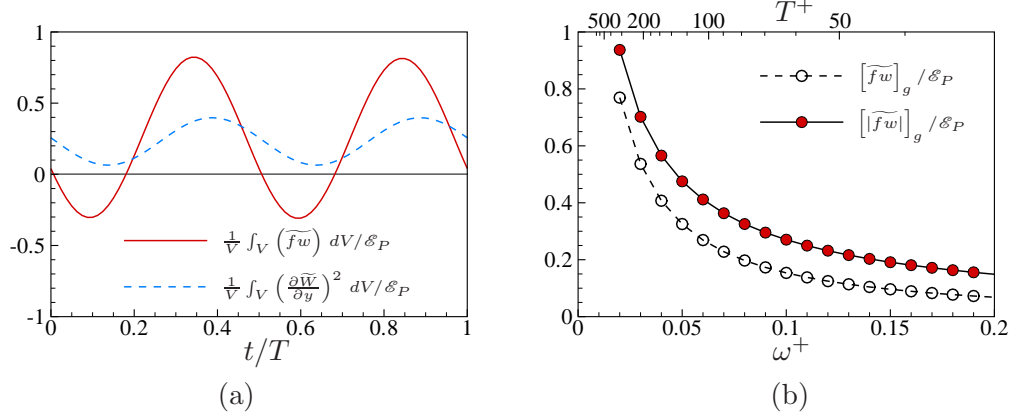


Figure 5.15: Power calculation for the laminar case in figure 5.18: (a) power input and dissipation variation during one period ($\omega^+ = 0.06$, ($T^+ = 105$)); (b) power input against different frequencies.

The power spent maps for the streamwise and spanwise travelling waves are shown in figure 5.16. The highest power spent roughly coincides with the \mathcal{DI} regions. The minimum P_{sp} are located furthest away from the origin, and with a value of around 20 for both the streamwise and the spanwise travelling waves, and the corresponding P_{sp} minimum are at $(\kappa_x^+, \omega^+) = (0.024, -0.18)$ (or $(\lambda_x^+, T^+) = (260, -35)$) and $(\kappa_z^+, \omega^+) = (0.031, 0.18)$ (or $(\lambda_z^+, T^+) = (200, -35)$), respectively.

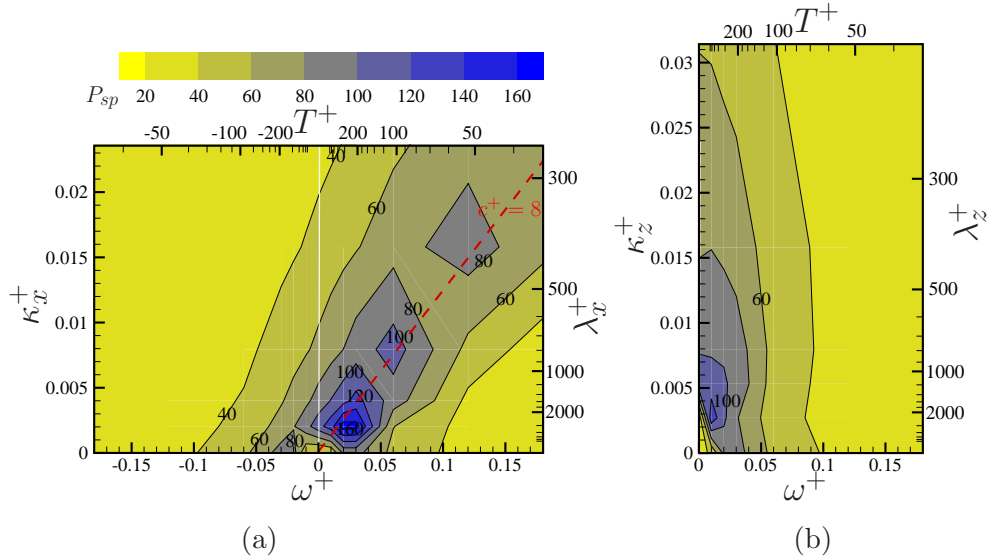


Figure 5.16: Power spent (P_{sp}) maps for (a) streamwise travelling wave and (b) spanwise travelling wave.

The net energy saving is shown in figure 5.17. The most notable feature on the maps is that no positive P_{net} is achieved. The best performance case for the streamwise travelling wave is at $(\kappa_x^+, \omega^+) = (0.002, 0.12)$ (or $(\lambda_x^+, T^+) = (3140, 50)$) with $P_{net} \approx -10$, and for the spanwise travelling wave case, it is at $(\kappa_z^+, \omega^+) = (0.005, 0.12)$ (or $(\lambda_z^+, T^+) = (1260, 50)$) with $P_{net} \approx -9$.

For a real Lorentz force actuator, the power supply is provided by electricity, and the electricity power used can be expressed as $P_e = V_0 J_0 A_e$, where V_0 is the voltage drop and A_e is the wetted surface area of the electrodes. By substituting $A_f = J_0 B_0 h / \rho U_m^2$ into the above expression, the final estimated electricity consumption (non-dimensionalised by the pumping power \mathcal{E}_P) can be obtained as below,

$$P_e = \frac{A_e \rho U_m^2}{B_0 L_x L_z h \mathcal{E}_P} A_f V_0. \quad (5.15)$$

A_f can be adjusted through either changing the current density J_0 or changing the permanent magnet flux B_0 . Roughly, $P_e \sim Const.$ for purely changing B_0 ; and $P_e \sim A_f^2$ for purely changing V_0 . To achieve $A_f = 0.2$, Berger et al. (2000) estimated $P_e \sim 600$ (please notice that their pumping power was expressed in $\tau_w u_\tau$ form). For the best scenario we take $P_e \approx 600$ for $A_f = 0.5$ used in the present study. Considering that the general power input is around the same order as \mathcal{E}_P (see figure 5.16), the efficiency for the Lorentz force actuators to convert the electric power to the fluid power is $\eta \sim 1/600 \sim O(10^{-3})$. To achieve a net energy saving, $P_e < 1$ is required, thus it is more challenging to achieve a net energy using Lorentz force actuators.

5.5.3 Lorentz force induced Stokes layer

The spanwise mean velocity profiles for the spanwise oscillating Lorentz force are shown in figure 5.18(a), and are compared with the profiles generated by the spanwise oscillating wall and pressure gradient. The Stokes layer due to the spanwise Lorentz force is termed as the Lorentz force Generated Stokes Layer (LGSL) in the present study. The governing equation for the laminar LGSL is given as below,

$$\begin{aligned} \frac{\partial W^+}{\partial t^+} &= \frac{\partial^2 W^+}{\partial y^{+2}} + A_f^+ e^{-y^+/\Delta^+} \sin(-\omega^+ t^+), \\ B.C. : \quad W^+|_{y^+=0} &= 0, \quad W^+|_{y^+=\infty} = 0. \end{aligned} \quad (5.16)$$

The analytical solution is given in appendix E, and is compared with the turbulent spanwise mean velocity profiles at 8 equally separated phases. They are similar

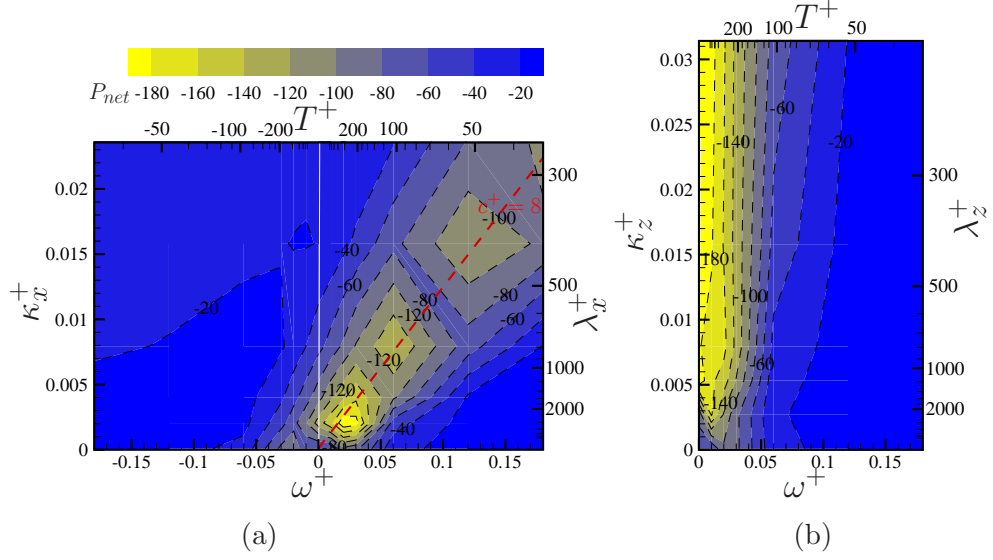


Figure 5.17: Net energy saving (P_{net}) maps for (a) streamwise travelling wave and (b) spanwise travelling wave.

to each other close to the wall, while they deviate from each other further away from the wall. The discrepancy is caused by the additional Reynolds stress term $\partial \widetilde{v'w'}/\partial y$ as shown in figure 5.18(b), and this point has been discussed in figure 4.16 for spanwise wall oscillation. Due to the no-slip wall boundary, the maximum spanwise mean velocity appears around $y^+ \approx \Delta^+$. This gives the obvious difference of the spanwise mean velocity profiles between OC case and either the spanwise wall oscillation case or spanwise oscillating crossing flow case (Jung et al., 1992). It was demonstrated by Jung et al. (1992) that oscillating spanwise crossing flow (equivalent to spanwise oscillating pressure gradient) had a similar \mathcal{DR} effect as spanwise wall oscillation. There are two ways to explain this point. First, we investigate the momentum equations for u and w in the spanwise wall oscillation case, shown as below,

$$\begin{aligned} \frac{\partial u}{\partial t} + u \frac{\partial u}{\partial x} + v \frac{\partial u}{\partial y} + w \frac{\partial u}{\partial z} &= -\frac{\partial p}{\partial x} + \frac{1}{Re} \left(\frac{\partial^2 u}{\partial x^2} + \frac{\partial^2 u}{\partial y^2} + \frac{\partial^2 u}{\partial z^2} \right), \\ \frac{\partial w}{\partial t} + u \frac{\partial w}{\partial x} + v \frac{\partial w}{\partial y} + w \frac{\partial w}{\partial z} &= \frac{1}{Re} \left(\frac{\partial^2 w}{\partial x^2} + \frac{\partial^2 w}{\partial y^2} + \frac{\partial^2 w}{\partial z^2} \right), \\ B.C. : u|_{y=0} &= 0, \quad w|_{y=0} = A_w \sin(-\omega t). \end{aligned}$$

Following the approach by Sendstad and Moin (1992) (pp. 20), a transformation for w is used, and the new spanwise velocity is defined as $\tilde{w} = w - A_w \sin(-\omega t)$.

Plug the transformation into the above equations, we can have,

$$\begin{aligned}\frac{\partial u}{\partial t} + u\frac{\partial u}{\partial x} + v\frac{\partial u}{\partial y} + \tilde{w}\frac{\partial u}{\partial z} &= \left(-\frac{\partial p}{\partial x} - A_w \sin(\omega t)\frac{\partial u}{\partial z}\right) + \frac{1}{Re} \left(\frac{\partial^2 u}{\partial x^2} + \frac{\partial^2 u}{\partial y^2} + \frac{\partial^2 u}{\partial z^2}\right), \\ \frac{\partial \tilde{w}}{\partial t} + u\frac{\partial \tilde{w}}{\partial x} + v\frac{\partial \tilde{w}}{\partial y} + \tilde{w}\frac{\partial \tilde{w}}{\partial z} &= \left(A_w \omega \cos(-\omega t) - A_w \sin(\omega t)\frac{\partial \tilde{w}}{\partial z}\right) \\ &\quad + \frac{1}{Re} \left(\frac{\partial^2 \tilde{w}}{\partial x^2} + \frac{\partial^2 \tilde{w}}{\partial y^2} + \frac{\partial^2 \tilde{w}}{\partial z^2}\right),\end{aligned}$$

$$B.C. : u|_{y=0} = 0, \quad \tilde{w}|_{y=0} = 0.$$

If we ignore the small term $-A_w \sin(\omega t)\frac{\partial u}{\partial z}$ (compared to $-\frac{\partial p}{\partial x}$, since $\frac{\partial u}{\partial z}$ is small) and $A_w \sin(\omega t)\frac{\partial \tilde{w}}{\partial z}$ (compared to $A_w \omega \cos(-\omega t)$, since $\frac{\partial \tilde{w}}{\partial z}$ is small), the transformed equations become identical to the governing equations for a spanwise oscillating pressure gradient problem, with $\frac{\partial p}{\partial z} = -A_w \omega \cos(-\omega t)$. Second, it is widely accepted that in spanwise wall oscillation case the Stokes layer displaces the near wall streaks respect to the vortical structures, resulting in the drag reduction (Akhavan et al., 1993; Laadhari et al., 1994; Baron and Quadrio, 1996). For the spanwise oscillating pressure gradient case, as pointed out by Ricco (2004), it is the vortical structures oscillating transversally over the near wall streaks that causes the drag reduction. But in general, both cases decorrelate the spatial arrangement between the near wall streaks and the vortical structures.

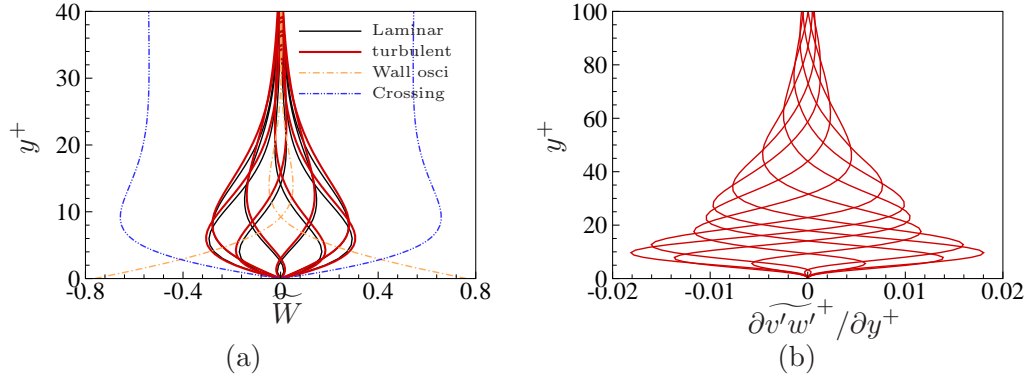


Figure 5.18: (a) Spanwise mean velocity profiles for OC case compared with the laminar solution (equation (5.16)), spanwise wall oscillation, and spanwise crossing flow; (b) $\partial v'w'⁺/\partial y⁺$ profiles for spanwise oscillating Lorentz force.

Unlike OC case, whose spanwise mean velocity profile varies in time, for FST, SP and BST cases, these profiles vary in space as well. The spanwise mean velocity profiles for FST, SP and BST cases are compared with the OC case in figure 5.19, with only the profiles at two phases shown. Again, within the viscous

sublayer ($y^+ < 5$), the spanwise mean velocity profiles are very similar, but they are different further away from the wall. For SP case, the Lorentz force travels in the positive spanwise direction, thus it induces a positive net mass flow near the wall, while a negative mass flow away from the wall ($W = -0.05$ at the core region), as also observed by Xie and Quadrio (2013). The thickness of the LGSL δ^+ can be defined as a wall distance where the spanwise mean velocity decreases to e^{-1} of the maximum spanwise mean velocity as in the spanwise wall oscillation case. For spanwise travelling wave, the induced spanwise mean velocity is removed first before determining δ^+ . This gives $\delta^+ = 19, 25, 19$ and 18 for the OC, FST, SP and BST cases, respectively.

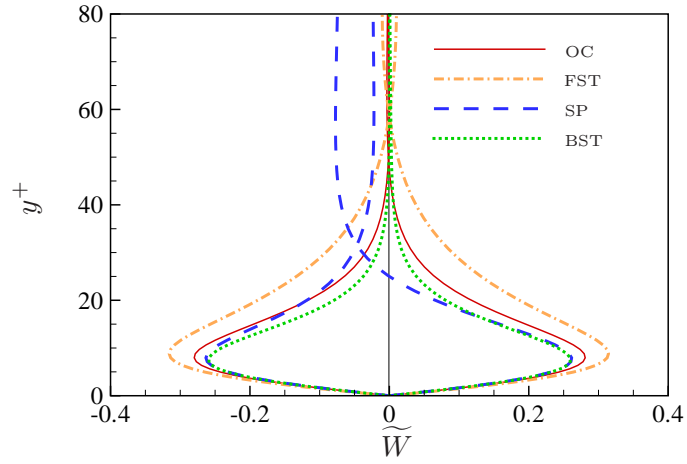


Figure 5.19: Spanwise mean velocity profiles for travelling wave cases.

To further check the correlation between \mathcal{DR} and δ^+ , the LGSL thickness is calculated for all the streamwise and spanwise travelling wave cases, and is shown in figure 5.20. The two δ^+ maps show a similar pattern as the \mathcal{DR} maps. Generally in the \mathcal{DI} region, δ^+ is much larger. The optimal \mathcal{DR} region corresponds to $\delta^+ \approx 18$. The correlation is further presented in a 1D format as shown figure 5.21, similar to Quadrio and Ricco (2011) for generalised Stokes layer study. Cases with too large δ^+ or \mathcal{DI} values are excluded for a clearer view. The data here is scattering, but it suggests that: 1) δ^+ can hardly go below $\delta^+ = 10$, which is the penetration depth Δ^+ of the Lorentz body force; 2) there is an optimal thickness of $\delta_{opt}^+ \approx 17.5$. Streamwise travelling wave with small \mathcal{T}^+ tends to follow the fitting line given by Quadrio and Ricco (2011) (shifted by $\Delta\delta^+ = 10$), but the linear correlation in this regime for the spanwise travelling wave is poorer. Since the current dataset is small, it is not clear whether a similar minimum LGSL thickness exists as the streamwise

travelling wave of spanwise wall velocity. For the four studied cases, *i.e.*, OC, FST, SP and BST, they are all located above δ^+_{opt} , and their \mathcal{DR} values roughly correlate with their LGSL thickness linearly.

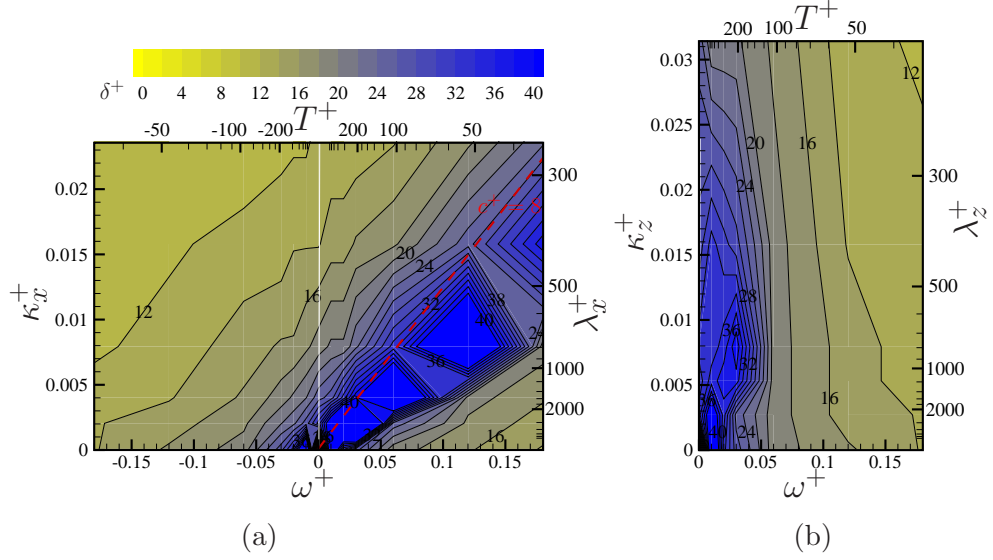


Figure 5.20: δ^+ maps for: (a) streamwise travelling wave; and (b) spanwise travelling wave.

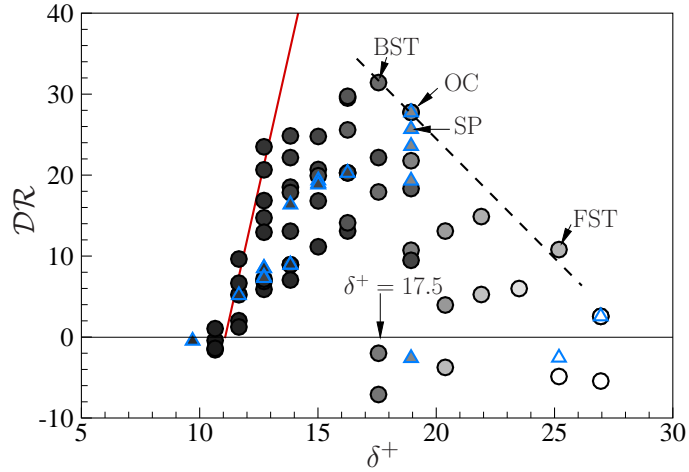


Figure 5.21: \mathcal{DR} against δ^+ for both streamwise (circles) and spanwise (triangles) travelling waves. Red solid line is from (Quadrio and Ricco, 2011), shifted by $\Delta\delta^+ = 10$. Symbols are coloured by time scale \mathcal{T}^+ (equation (5.11)), with dark colour indicating lower value.

5.5.4 Statistics and spectra

The turbulent velocity and vorticity fluctuations for OC, FST, SP and BST are shown in figure 5.22. For the three travelling wave cases, $u_{i,rms}^+$ behaviours are the same as the oblique travelling wave study shown in figure 5.11. The statistics modulation for the travelling wave cases is similar to the oscillation case. As can be seen, over the entire channel, u_{rms}^+ decreases for all the four drag reduction cases, especially for the near wall peak, which has a maximum decrease of around 30% for the OC case. The near wall u_{rms}^+ peak appears at $y^+ = 14$ for the no control case (Kim et al., 1987), while it moves to $y^+ = 16, 20, 24$ and 28 for the OC, FST, SP and BST cases, respectively. The peak of v_{rms}^+ monotonically decreases, which is roughly proportional to the \mathcal{DR} value. The peak values modulation on w_{rms}^+ is quite different for FST case, where 30% increase in the w_{rms}^+ peak value is observed despite that FST case gives around 10% drag reduction. For the vorticity plots, $\omega_{y,rms}^+$ is normally used to measure the strength of the near wall streaks (Le et al., 2000). As we can see, $\omega_{y,rms}^+$ decreases for all the control cases (figure 5.22(e)), which is the same as v_{rms}^+ plot. Surprisingly, $\omega_{x,rms}^+$ does not decrease for all cases (figure 5.22(d)). For example, $\omega_{x,rms}^+$ increases in the region of $4 < y^+ < 14$ for OC and SP cases, while $\omega_{x,rms}^+$ increases within the whole channel height for FST case. This is reminiscent of the drag reduction mechanism given by Du et al. (2002) that the appropriate enhancement of the streamwise vortices leading to the weakening of the streak intensity. Considering that all four travelling wave cases give drag reduction, the drag reduction correlates better with the wall normal fluctuations, *i.e.*, v_{rms}^+ and $\omega_{y,rms}^+$ (Chung and Talha, 2011). Among all the three velocity fluctuation statistics, the SP case is very similar to the OC case. Since the travelling wavelength $\lambda_z^+ \approx 2400$ ($\kappa_z^+ = 0.0026$) for SP is large, the near wall structure can not sense the difference between the spatial Lorentz force and the homogeneous temporal one.

Figure 5.23 shows the vorticity fluctuation profiles for FST scaled by the no control case wall units and the control case wall units, respectively. This is compared with the constant pressure gradient control case for streamwise travelling wave of spanwise wall velocity from (Quadrio and Ricco, 2011). In their case, the wall units are fixed, which gives a clear inner scaling. Zhou and Ball (2008) have made an intensive comparison of the turbulent statistics for spanwise wall oscillation between constant mass flow rate (CFR) and constant pressure gradient (CPG) controls. Our CFR data under two different scaling are very similar, with just an upward shift when a smaller u_τ associated with the control case is used. There is a big difference in the near wall vorticity modulation under CFR and CPG, especially for $\omega_{y,rms}^+$ and $\omega_{z,rms}^+$. But both FST and the travelling wave case by Quadrio and Ricco (2011)

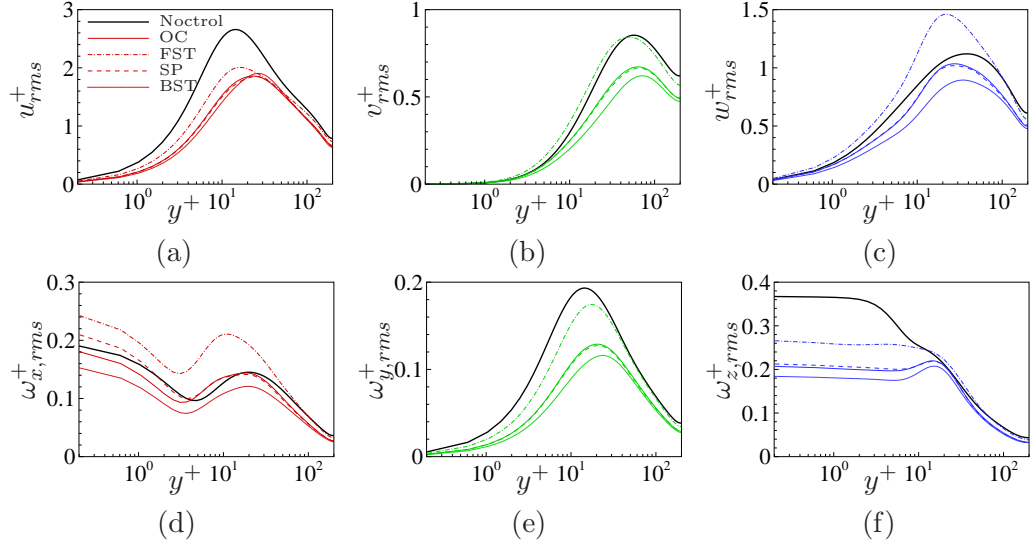


Figure 5.22: R.m.s. of the velocity and vorticity fluctuations comparison among no control, OC, FST, SP and BST cases for (a) u_{rms}^+ , (b) v_{rms}^+ , (c) w_{rms}^+ , (d) $\omega_{x,rms}^+$, (e) $\omega_{y,rms}^+$, and (f) $\omega_{z,rms}^+$.

show a significant increase of $\omega_{x,rms}^+$ up to $y^+ \approx 50$. As pointed out by Quadrio and Ricco (2011), this is quite surprising, because these two cases have a large amount of drag reduction ($\mathcal{DR} = 11 \pm 2$ for FST and $\mathcal{DR} = 45$ for (Quadrio and Ricco, 2011)). Clearly, it suggests that the \mathcal{DR} by the travelling waves is not directly linked to the weakening of the near wall quasi-streamwise vortices (such as for ribblet case (Choi et al., 1993)), but to decrease the spatial correlation between the quasi-streamwise vortices and the streaks (Baron and Quadrio, 1996). This non-monotonous change of $\omega_{x,rms}^+$ is also reflected in the spanwise wall oscillation cases (see figure 4.14(f)).

The energy change in the streamwise velocity fluctuation is checked by the two-dimensional pre-multiplied streamwise velocity spectrum $k_x k_z E_{uu}$ at $y^+ = 10$, as shown in figure 5.24. At this location, the near wall streaks in no control case are shown by an energy peak site of a streamwise length scale $\lambda_x^+ \approx 1000$ and a spanwise length scale $\lambda_z^+ \approx 100$. When the flow is controlled by spanwise Lorentz force, there is a significant reduction in the streamwise length scale of the near wall streaks, with $\lambda_x^+ \approx 350$ for OC and SP cases, $\lambda_x^+ \approx 200$ for FST case, and $\lambda_x^+ \approx 400$ for BST case, as indicated by the arrow in the 1D pre-multiplied streamwise spectra. However, the length scale change in the spanwise direction λ_z^+ (as indicated by the arrows) is not obvious. This again suggests that the near wall streaks are broken-up by the travelling waves, resulting in a significant amount of energy reduction in the large scales $\lambda_x^+ > 1000$, which is also evident from the instantaneous streaks plot in

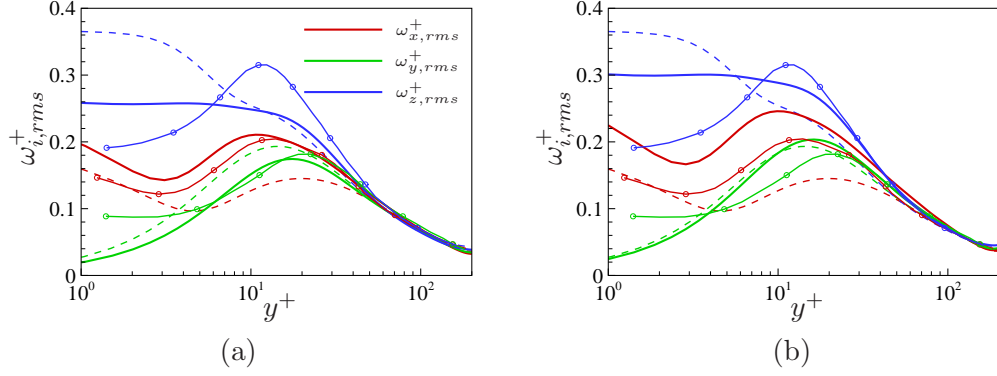


Figure 5.23: R.m.s. of vorticity fluctuations for FST (bold solid lines) scaled by: (a) the no control wall units, and (b) the control wall units, compared with streamwise travelling wave of spanwise wall velocity at $A_w^+ = 12$, $\omega^+ = 0.045$, $\kappa_x^+ = 0.012$ (Quadrio and Ricco, 2011) (solid lines with circles). Dashed lines are for the no control case.

figure 5.9.

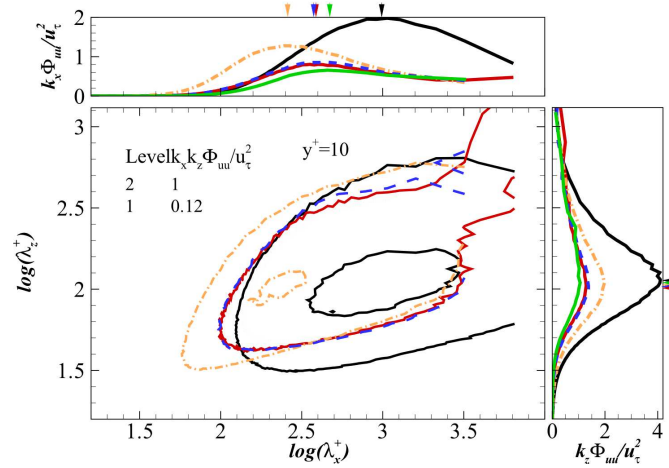


Figure 5.24: 2D and 1D pre-multiplied streamwise velocity spectra $k_x k_z E_{uu}$ at $y^+ = 10$ for no control case (black solid line) and control cases (see figure 5.19 for the line key). 7% and 60% of the no control case peak value are shown by contour lines in the 2D plot for each spectrum.

The one-dimensional pre-multiplied spectra for the streamwise velocity over the channel are shown in figures 5.25(a)-5.25(d) for the OC, FST, SP and BST cases compared with the no control case. It is clear to see the peak location of the streamwise velocity fluctuation in the wall normal direction for all the four travelling wave cases. Again, this energy peak site moves further away from the wall for all the control cases. To emphasise the energy in the LGSL, $k_z E_{ww}$ is

shown for SP case, while $k_x E_{ww}$ is shown for the other control cases. The energy contained in the LGSL as shown in figure 5.19 has the scale of the domain size and keeps energetic in the whole LGSL. For OC case, there is no energy in the LGSL due to the force homogeneity in space, thus this part of energy is contained in the phase mean component. A complicated interaction exists between the LGSL and the most energetic spanwise velocity structure, which has a length scale of $\lambda_x^+ \approx 300$ and $\lambda_z^+ \approx 200$. The LGSL does not obviously change the scale of the spanwise velocity structure, but mainly changes the containing energy. This modification seems to be closely related to the thickness of the LGSL. For the FST case, the LGSL is the thickest, and the spanwise velocity structure is amplified. But for OC, SP and BST cases, this part of energy is reduced. This observation is consistent with the w_{rms}^+ plot in figure 5.22(c).

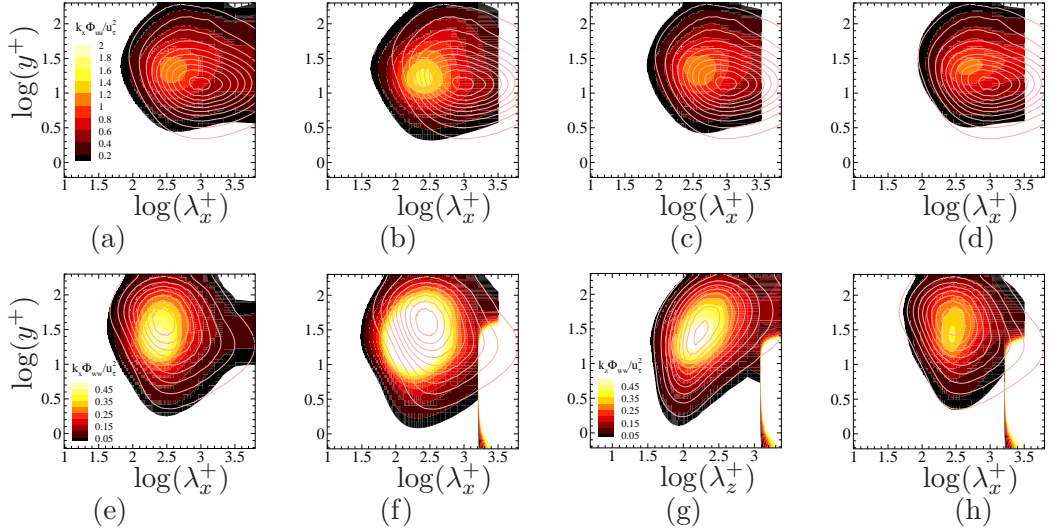


Figure 5.25: One-dimensional pre-multiplied spectra over the half channel height for OC case ((a)(e)); FST case ((b)(f)); SP case ((c)(g)) and BST case ((d)(h)). The spectrum for no control case is shown by contour lines, while the control cases are shown by shaded contour. (a)-(d) are spectra of $k_x E_{uu}$; (e)(f)(h) are spectra of $k_x E_{ww}$ and (g) is the spectrum of $k_z E_{ww}$. The same contour levels are used for the same variable.

5.5.5 λ_2 structures

The above analysis shows a significant similarity in the skin-friction control between Lorentz force and spanwise wall motion. In this section, the dynamics of the λ_2 structures and the streaks is further investigated to show the similarity between the travelling waves and the temporal oscillation by spanwise Lorentz force.

Same as spanwise wall motion, instantaneous flow fields of the OC case ($\omega^+ = 0.06$, $T^+ = 105$) are saved at 16 equally separated phases for 10 periods after the transient period. The conditional averaged positive λ_2 structures at each phase are shown in figure 5.26 for $\Delta^+ = 10$. The drag reduction values for this case is $\mathcal{DR} = 28 \pm 2$ (see table 5.2). As has been understood from figure 4.19, the negative structure dynamics is half a period phase shift from the positive one, therefore it is not shown. The positive λ_2 structure changes the tilting angle periodically in the xz plane, and the centre position moves away from the wall towards the outer region of the flow in wall normal direction. At the beginning of the period, the positive structure is most negatively tilted in the xz plane, and it is closest to the wall. As the spanwise Lorentz force goes to the negative spanwise direction (left), the positive structure starts to rotate in clockwise direction in the xz plane until the tilting angle is positive in the end of the oscillation period. In the mean time, the positive structure keeps moving away from the wall and its strength increases in the first half period and decreases in the second half period. This is similar to what has been observed in the spanwise wall oscillation case (see figure 4.19). It is interesting to notice that at phase $\phi = 15\pi/8$, two positive λ_2 structures are identified simultaneously: a strong structure close to the wall; and a weak structure further away from the wall. This is consistent with figure 4.21, where an additional condition was used to split the lower structure from the upper one.

Similar analysis for the characteristic eddies (as for the spanwise wall oscillation case) is conducted, and the result is shown in figure 5.27. The high-speed streak is $\lambda_x^+ \approx 500$ in length from a xz plane view (not shown), much shorter than that in the no control case (figure 3.8) (Choi et al., 1998; Ricco, 2004). Recalling that the thickness of the LGSL is $\delta^+ = 20$ for OC case (figure 5.19), the high- and low-speed streaks are significantly twisted in this layer; while they are almost un-modulated outside of this region (Baron and Quadrio, 1996). A comparison with figure 5.26 suggests that the streaks twisting angle generally matches the angle of the stronger λ_2 structure. However, due to the two-fold twisting, for example at phase $\phi = \pi/2$ and $3\pi/2$, multiple streaks angle are observed from different heights of the wall.

Overall, the ensemble averaged λ_2 structures and streaks analysis shows the similar structure dynamics in a spanwise oscillating flow induced by spanwise Lorentz force and by spanwise wall velocity. To verify the λ_2 structure behaviours in FST, SP and BST cases, the positive and negative λ_2 structures are conditioned in the positive and negative Lorentz force regions separately. The conditioned λ_2 structures are shown in figure 5.28. Since one wavelength is only divided into two parts, the resolution is much lower than the conditioned structures in OC case shown

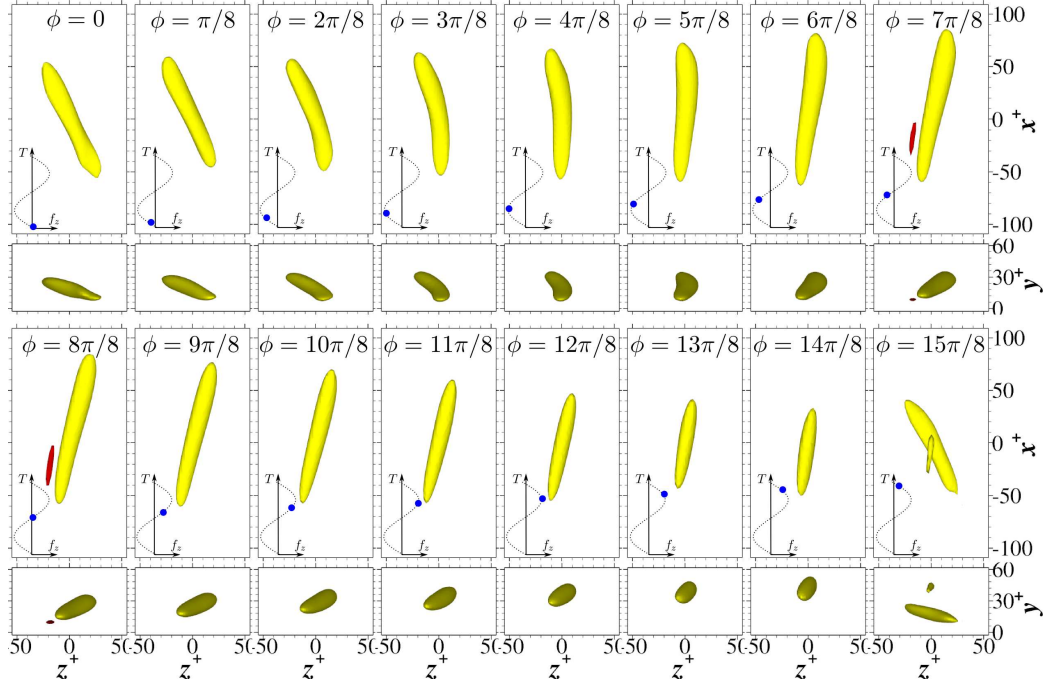


Figure 5.26: Conditional averaged positive λ_2 structure at 16 equally separated phases of one oscillation period for OC case. The structures are visualised by $\lambda_2^+ = -0.01$.

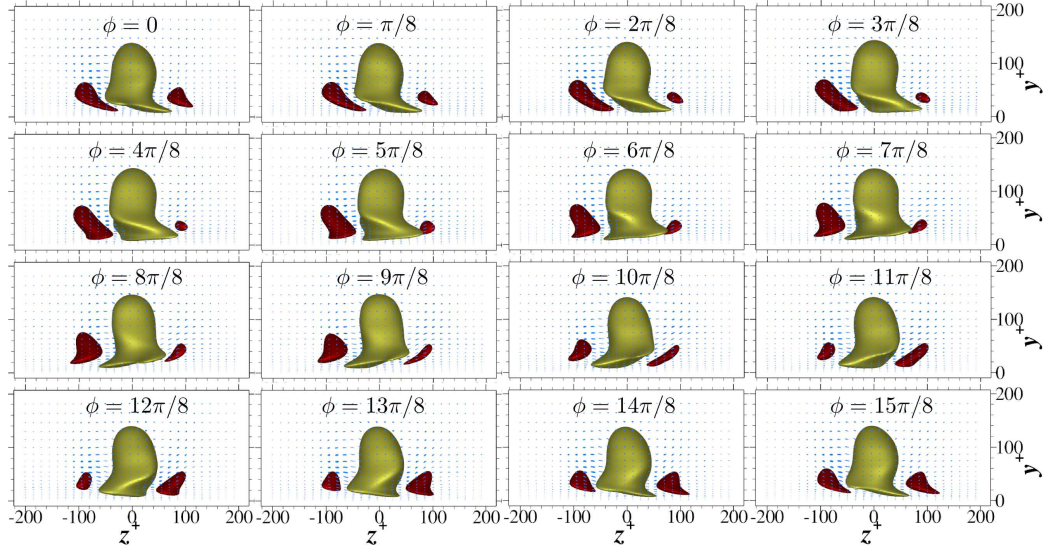


Figure 5.27: End view of the characteristic eddy at 16 equally separated phases of one oscillation period for the OC case. The high- and low-speed streaks are visualised by $u' = \pm 0.35$, respectively.

in figure 5.26. To make the comparison more straightforward, the λ_2 structures are also conditioned in the positive and negative Lorentz force regions only for the OC case, and is shown in figure 5.28(a). The structure behaviours in the positive and negative Lorentz force regions for the travelling wave cases resemble the OC case significantly. The positive and negative structures reside at two very different wall normal locations: the upper structures are at $y^+ \approx 25$, while the lower structures are at $y^+ \approx 14$. In the positive force region, the negative λ_2 structure is lower and turns in clockwise direction; while the opposite situation happens for the positive structure in the negative force region. When visualised with the same λ_2 criteria, differences in the structure strength, tilting angle can be observed among the FST, SP and BST cases.

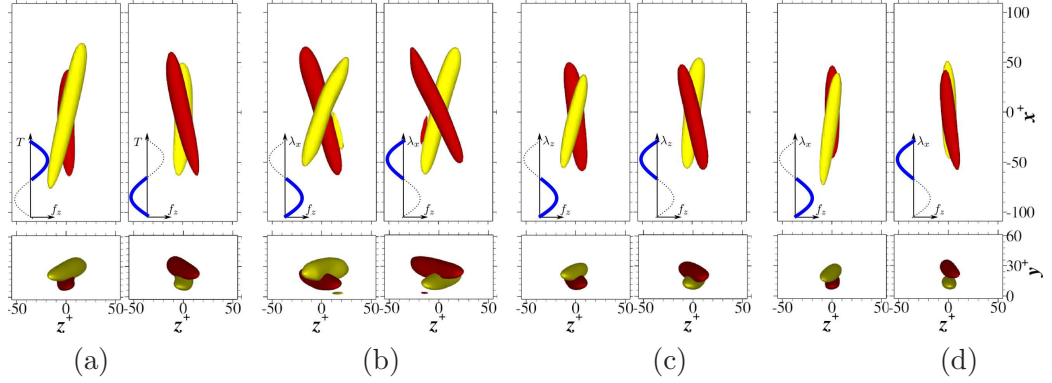


Figure 5.28: Conditional averaged positive and negative λ_2 structures in the positive and negative Lorentz force regions for (a) OC case; (b) FST case, (c) SP case, and (d) BST case. The structures are visualised by $\lambda_2^+ = -0.01$.

The tilting angle and the strength (evaluated using the minimum value of the λ_2 field) are measured and plotted in figure 5.29 against the drag reduction. The tilting angles of both the upper and lower structures correlate well with \mathcal{DR} , which shows a slope of -0.67 . This is reminiscent of the ensemble averaged λ_2 structures in spanwise oscillation cases with different frequencies, where the lowest frequency, $\omega^+ = 0.01$ ($T^+ = 628$) creates largest structure tilting angle, and drag increase (figure D.1). Due to the fact that the lower structure is more strongly convected by the Lorentz force, and its tilting angle can vary from a positive value to a negative one, or vice versa (see figures 5.26), which results in the overall averaged tilting angle for the lower structure smaller than that for the upper one. This is suggested in figure 5.29. When the strength is measured by the minimum of the λ_2 field, the upper structure is always weaker than the lower one, which is consistent with the continuous structure dynamics in the OC case shown in figure 5.26. The strength

variation of the upper structure is negligible among all the four control cases. A big strength variation is observed for the lower structure, and this strength variation shows a good correlation with \mathcal{DR} value. This suggests the strong link between the drag reduction and the asymmetry between the positive and the negative quasi-streamwise vortices.

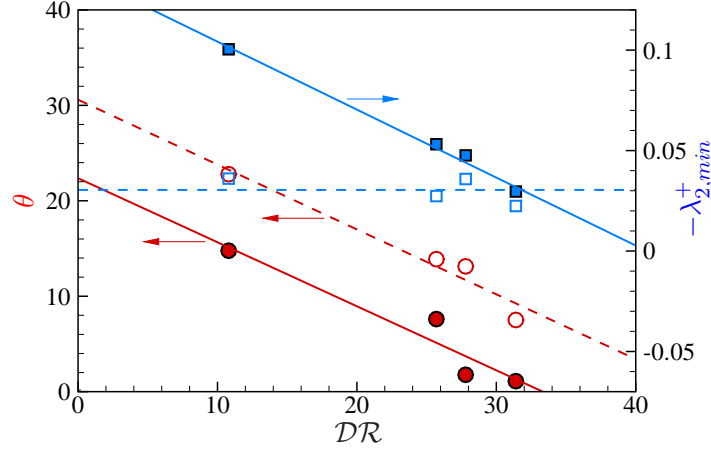


Figure 5.29: Correlation between \mathcal{DR} with the structure tilting angles (circles) and structure strength (squares) for the upper and lower structures shown in figure 5.28. Open symbols are for the upper structures, and closed symbols are for the lower structures.

The near wall streaks are generated by the streamwise aligned positive and negative quasi-streamwise vortices (Jeong et al., 1997). The tail of the positive (negative) structure is overlaid with the head of the negative (positive) structure (see figure 2.2). However, in the OC, FST, SP and BST cases, this symmetry is broken-up. The positive and the negative structures do not stay at the same wall distance and their large tilting angles make this connection more difficult. This leads to the break up of the near wall high- and low-speed streaks, decreasing the energy in the large streamwise length scales.

5.6 Conclusions

A systematic study of the streamwise, spanwise and oblique travelling waves by spanwise Lorentz force was conducted, with a maximum of about 30% drag reduction achieved at the explored Lorentz force strength $A_f = 0.5$ and penetration depth $\Delta^+ = 10$. The simulation was designed to align the mean flow with an angle to x direction, so that the effect of the travelling wave angle at a fixed wavelength could

be studied. The most effective drag reduction waveform was found to be backward streamwise travelling wave, $\theta = 180^\circ$.

The interaction between the travelling wave (“ribbon” structure) and the near wall streaks was found to be the same as in the spanwise oscillating Lorentz force case. Detailed structure dynamics was presented by the ensemble averaged λ_2 structure and the characteristic eddy. It was shown that spanwise Lorentz force created asymmetry between the positive and the negative near wall λ_2 structures, and this broke the λ_2 structure train in the buffer layer, weakened the formation of the long high- and low-speed streaks, resulting in drag reduction, which was essentially the same as the transient drag reduction mechanism discussed for uni-direction wall motion in section 4.1. The similarity between the travelling wave and the spanwise oscillating Lorentz force was also revealed in the turbulence statistics and spectra. A time scale $\mathcal{T}^+ = \lambda^+ / (\mathcal{U}_c^+ \cos(\theta) - c^+)$ was found to link the drag reduction effectiveness of the travelling waves with the spanwise oscillating Lorentz force well at low control wavenumber.

The presented results strongly suggests that the skin-friction drag reduction control by spanwise wall oscillation can be replaced by spanwise body force with the travelling wave form in any angle to the mean flow direction. This provides the guide for the work in the next chapter.

Chapter 6

Drag Reduction by DBD Plasma Actuators

Following the previous chapter on drag reduction using Lorentz force actuators, this chapter studies another type of actuator, *i.e.*, DBD (dielectric barrier discharge) plasma actuator (Roth, 2003). DBD plasma actuators mainly work for air, and they do not require the fluid to be electro conductive. Moreover, plasma actuators are light, easy to be implemented, and have high response frequency. These advantages make them a perfect candidate for the flow control applications of aircrafts and land transport vehicles. Currently, there is a large amount of flow control applications using DBD plasma actuators (Wang et al., 2013), but only a very limited number of works were done on skin-friction drag reduction control by DBD plasma actuators (Choi et al., 2011; Elam, 2012). A typical skin-friction control set up by DBD plasma actuators is shown in figure 6.1. The aim of this chapter is to explore the possible DBD plasma actuator configurations for achieving skin-friction drag reduction, and for understanding the effect of the control parameters. It provides some guidance on how to design the DBD plasma actuator device for the skin-friction drag reduction control.

6.1 Plasma actuator model and its validation

A DBD plasma actuator consists of two electrodes, with one exposed in air, and the other one embedded in dielectric material. When a high AC (alternating current) voltage is applied to the electrodes, the air in the vicinity of the electrodes is ionised, and the ions and neutral gas particles strongly collide with each other to exchange momentum and energy. Moreover, this process is not symmetric in the positive and

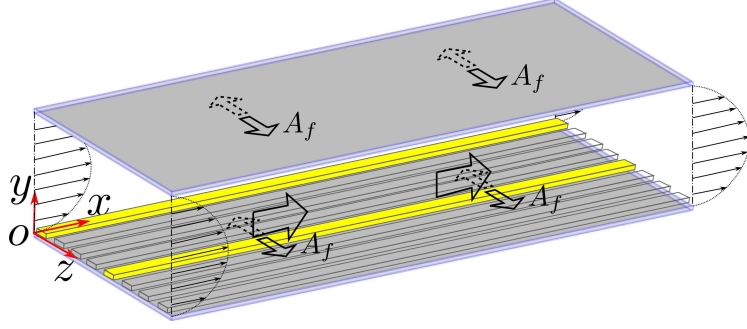


Figure 6.1: Schematics of skin-friction control by plasma actuators. The plasma actuators are represented by streamwise elongated strips on the wall. Coloured actuators are activated, while the others are not.

the negative electric cycle, thus creating a net force, which is very useful for flow control applications (Moreau, 2007). The discharge dynamics of the DBD plasma actuators is governed by the following equations (Unfer, 2013),

$$\begin{aligned} \frac{\partial N_e}{\partial t} + \nabla \cdot \mathbf{\Gamma}_e &= \left(\sum_i \alpha_i - \sum_j \eta_j \right) N_e N_o - \sum_i r_{e,p_i} N_e N_{p_i}, \\ \frac{\partial N_{p_i}}{\partial t} + \nabla \cdot \mathbf{\Gamma}_{p_i} &= \alpha_i N_e N_o - r_{e,p_i} N_e N_{p_i} - \sum_j r_{p_i,n_j} N_{p_i} N_{n_j}, \end{aligned} \quad (6.1)$$

$$\begin{aligned} \frac{\partial N_{n_j}}{\partial t} + \nabla \cdot \mathbf{\Gamma}_{n_j} &= \eta_j N_e N_o - \sum_i r_{p_i,n_j} N_{p_i} N_{n_j}, \\ \mathbf{\Gamma}_k &= \mu_k \mathbf{E} N_k - D_k \nabla N_k + \mathbf{u} N_k, \quad (k = e, p_i, n_j), \end{aligned} \quad (6.2)$$

$$\nabla \cdot (\epsilon \mathbf{E}) = e \left(\sum_i N_{p_i} - \sum_j N_{n_j} - N_e \right) + \sigma \delta_s, \quad (6.3)$$

$$\frac{\partial N_e \epsilon_e}{\partial t} + \nabla \cdot \mathbf{\Gamma}_{N_e \epsilon_e} = -e \mathbf{\Gamma}_e \cdot \mathbf{E} - e N_e \Theta. \quad (6.4)$$

Equation (6.1) is the continuity equations. Subscripts e , p_i , n_j and o indicate electrons, positive ions for the i^{th} species, negative ions for the j^{th} species, and neutral gas particles, respectively. For air, it can be approximated as the mixture of two species, *i.e.*, 77% N_2 and 23% O_2 . N is the particles number density; α , η and r are the ionization, attachment and recombination coefficients, respectively. The flux $\mathbf{\Gamma}$ is given in equation (6.2), with μ , D being the species mobility and diffusion coefficients, respectively. \mathbf{u} is the neutral gas velocity. The electric field generated by the plasma discharge can be obtained by solving the Poisson equation (6.3), where σ is the surface charge density, and δ_s is the delta function (equal to

one at the gas/dielectric interface and zero elsewhere). The energy balance is given in equation (6.4), with ϵ_e being the mean electron energy, and Θ being the sum of the electron energy loss in all elementary processes. The first heat sink terms on the right hand side, $-e\mathbf{\Gamma}_e \cdot \mathbf{E}$ is due to Joule heating, which transfers energy to the neutral gas. In the mean time, DBD plasma actuators generate an electric hydrodynamics force, which is evaluated in equation (6.5). This is a momentum source to the neutral gas, and also the most attractive feature for the present flow control application.

$$\mathbf{f} = e \left(\sum_i N_{p_i} - \sum_j N_{n_j} - N_e \right) \mathbf{E} - \nabla \left(N_e k_B T_e + \sum_i N_{p_i} k_B T_{p_i} + \sum_j N_{n_j} k_B T_{n_j} \right). \quad (6.5)$$

It is clear that the above equations are strongly coupled with the Navier-Stokes equations in flow control applications: 1) plasma discharge provides momentum and heat source into the Navier-Stokes equations, through $\mathbf{f}t$ and $-e\mathbf{\Gamma}_e \cdot \mathbf{E}$, respectively; 2) the bulk flow of the neutral gas enhances the drift of the electrons and the ions through $\nabla \cdot (\mathbf{u}n_k)$, and affects the chemical reaction through the density change N_o . The DBD plasma actuator used for the present flow control applications is non-thermal, and majority of the electrical energy goes into the production of the energetic electrons, instead of heating the surrounding gas (Moreau, 2007). The experimental work by Jukes et al. (2006a) showed that a same type of DBD actuator only had a maximum temperature rise of $2 \pm 0.1^\circ\text{C}$. The modelling result by Unfer and Boeuf (2010) showed that when the DBD plasma actuator was driven by a sinusoidal wave voltage, it acted as a momentum source; when driven by nanosecond pulses, it acted as an aeroacoustic actuator generating micro shock waves and also significant amount of heating. The DBD plasma actuators in the present flow control are operated at the radio frequency (Choi et al., 2011), thus the heating effect is weak, and the compressibility due to the gas heating is negligible. Since the control application is in the low Mach number regime, the incompressible Navier-Stokes equations are used for the whole domain without solving the energy equation. This approach was also used by Belson et al. (2012). Therefore, N_o is constant, and the bulk flow can only affect the plasma through the term $\nabla \cdot (\mathbf{u}n_k)$. When the characteristic time scale of the fluid flow is much larger than that in the plasma dynamics, such as the current application with DBD plasma actuators operated at the radio frequency, $\nabla \cdot (\mathbf{u}n_k)$ can be neglected (Abdollahzadeh et al., 2016). Therefore, the system can be treated as one-way coupled, with the bulk fluid flow not affecting the

plasma dynamics, but only the plasma contributing momentum source to the bulk flow. Such a one-way coupling system for the flow control with plasma actuators is widely used in the literature (Suzen et al., 2005; Orlov and Corke, 2006; Maden et al., 2013).

The effect of the momentum contribution from the plasma actuators is illustrated in figure 6.2. There are different ways to obtain the electro hydrodynamics force generated by DBD plasma actuators (Shyy et al., 2002; Suzen et al., 2005; Orlov and Corke, 2006; Maden et al., 2013). One recently proposed plasma body force estimation is based on the PIV (particle image velocimetry) data (Kotsonis et al., 2011). Different assumptions were given by different authors to evaluate the plasma body force, due to the unavailability of the pressure field, as summarised in table 2.2. Once the plasma body force is evaluated, this force can be directly used for the flow control simulations, or the body force can be parametrised first, as done by Maden et al. (2013). Since the present study focuses on the plasma actuator configuration for the skin-friction drag reduction, and a series of parameter studies is going to be explored, the plasma body force model should be simple but also with an acceptable accuracy. Thus the model proposed in this study is a balance between the model by Shyy et al. (2002), where the plasma body force distribution was assumed to be linear, and by Maden et al. (2013), where 9 parameters were used for the least square fitting of the PIV based body force.

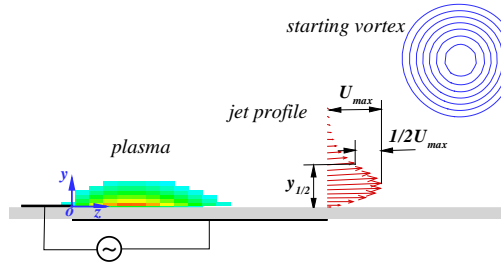


Figure 6.2: Schematics of a DBD plasma actuator viewed from a cross section, showing the body force distribution, the jet profile and the starting vortex.

A long time-averaged high resolution PIV data for the DBD plasma actuator which is similar to the DBD-VG1 studied by Jukes and Choi (2013), is used for the model validation (see figure 6.4(a)). The width of the upper and lower electrodes are $L_u = 2.5$ mm and $L_l = 15$ mm (figure 6.2). The plasma body force is reconstructed using Wilke (2009) model and Albrecht et al. (2011) model, and shown in figures 6.3(a) and 6.3(b), respectively. The horizontal force distributions for f_z from the two models have a very similar pattern: the force concentrates at the left edge of the

lower electrode, with a maximum of 5.2 kN/m^2 at around $z = 1 \text{ mm}$, and the force sharply decreases to zero in the wall normal direction. This is consistent with the plasma force distribution shown by Kotsonis et al. (2011), Maden et al. (2013) and Dörr and Klokner (2015). From Wilke (2009) model, the vertical force component f_y is also shown, and clearly the vertical force component f_y is much smaller than the horizontal one f_z .

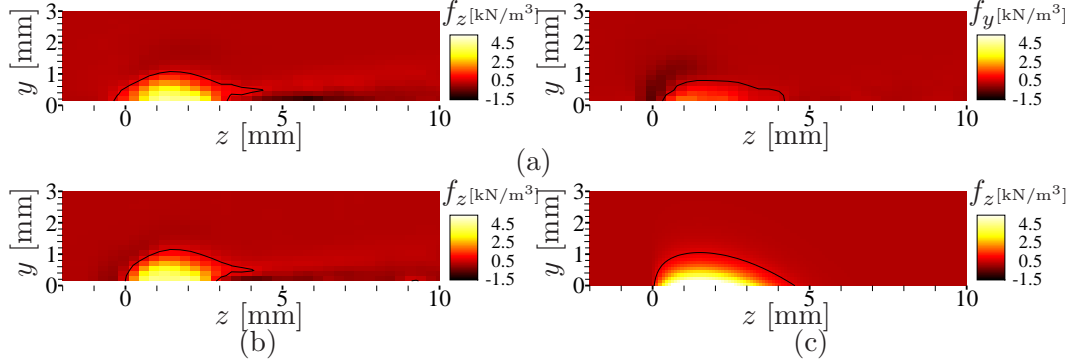


Figure 6.3: Plasma body force distribution of a single DBD plasma actuator for: (a) f_z and f_y from Wilke (2009) model, (b) f_z from Albrecht et al. (2011) model, and (c) f_z from equation (6.7). Solid lines are 10% iso-contour of the corresponding field maximum.

Based on the observation from figure 6.3, we ignore the vertical force component f_y , and assume that the horizontal force component f_z is Rayleigh distributed in the horizontal direction and exponentially distributed in the wall normal direction, *i.e.*,

$$\begin{cases} f_z(y) &= \lambda e^{-\lambda y}, (y \geq 0), \\ f_z(z) &= \frac{z}{\sigma^2} e^{-z^2/2\sigma^2}, (z \geq 0), \end{cases} \quad (6.6)$$

where λ and σ are the control parameters. The final form of the formulated plasma body force f_z distribution is,

$$f_z(y, z) = I f_z(y) f_z(z) = A_f \frac{\sqrt{e} z}{\sigma} e^{-z^2/2\sigma^2 - \lambda y}, (y \geq 0, z \geq 0), \quad (6.7)$$

where I is the total volume force, $A_f (= \frac{I\lambda}{\sqrt{e}\sigma})$ is the maximum force located at $(\sigma, 0)$. Similar to the expression for Lorentz force (Du and Karniadakis, 2000), the penetration depth is defined as $\Delta = 1/\lambda$.

The formulated body force with control parameters: $A_f = 9.4 \text{ kN/m}^3$, $\sigma = 1.5 \text{ mm}$ and $\lambda = 2.8 \text{ mm}^{-1}$ is shown in figure 6.3(c). Here λ and σ are

chosen to match the shape of the force region in figures 6.3(a) and 6.3(b), and the maximum force A_f is tuned to match the averaged force strength. As can be seen, the formulated plasma body force shows a good approximation of the plasma body force distribution. This model gives a better description of the plasma body force than the linear model proposed by Shyy et al. (2002), but less control parameters than the one proposed by Maden et al. (2013), who used 9 parameters for a least square fitting. In the present study, we are not trying to link the plasma body force with the applied voltage and frequency (Abdollahzadeh et al., 2014). The unsteadiness of the plasma body force in the positive and the negative going AC electric cycle is not taken into consideration neither due to the computational cost (Benard et al., 2013).

The simulated velocity field using the formulated plasma body force (figure 6.3(c)) is compared with the PIV data in figure 6.4, after the flow around the DBD plasma actuator becomes steady. A similar flow pattern between the simulation results with the present empirical model and the PIV measured data is observed, except that the maximum velocity value is slightly underestimated in the simulation. The jet profiles at four downstream locations, *i.e.*, $z/L_l = 0.27, 0.53, 0.8$ and 1.07 are compared between the PIV data and the simulation results from the empirical model, Wilke (2009) model and Albrecht et al. (2011) model. As can be seen, the jet velocity profiles using the empirical model match the PIV data at all locations; while the profiles of both Wilke (2009) and Albrecht et al. (2011) models deviate from the PIV data dramatically for $z/L_l \leq 0.53$ due to the effect of the negative plasma body force tail (figures 6.3(a) and 6.3(b)). In the present skin-friction control application, the most important effect of the plasma actuator is these induced jet velocity profiles (Jukes and Choi, 2013).

The DBD plasma actuator also induces a primary starting vortex (figure 6.2) travelling downstream and a secondary vortex close to the wall due to the no slip boundary (Whalley and Choi, 2012). A plasma body force strength of $A_f = 0.26$ kN/m³ is chosen to match the momentum changing rate in Case A of the experimental data by Whalley and Choi (2012). $\sigma = 1.8$ mm and $\lambda = 1.6$ mm⁻¹ are chosen as an approximation of the plasma body force region. A more detailed explanation about the simulation parameter selection is given in appendix F. The vorticity contour and velocity vector at $t^* = 1620, 2700$ and 3780 (* indicates that the variables are non-dimensionalised by the maximum jet velocity W_{max} before reaching a steady state, and ν/W_{max}) are compared in figure 6.5 between the PIV measured result (Whalley and Choi, 2012) and the simulation result. In the simulation, the strongest circulation region is close to the origin where the body force is the strongest, while

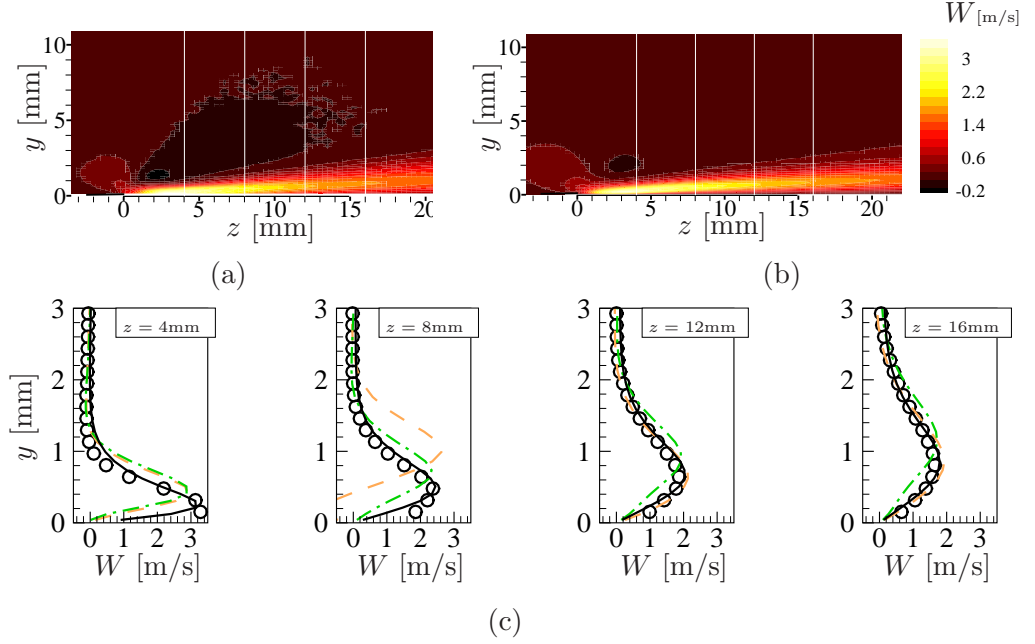


Figure 6.4: Horizontal velocity contour u between (a) PIV experimental result and (b) simulation result using the present empirical model. The profiles at 4 different vertical sections are shown in (c) for comparison between PIV result (circles), and the simulation results using the empirical model (solid lines), Wilke (2009) model (dash lines) and Albrecht et al. (2011) model (dash-dot lines).

this information is not available from the PIV data due to the limitation in the measurement. There is a good agreement in the starting vortex size, but the simulated starting vortex tends to travel slower than the PIV data. This difference is acceptable considering that no PIV derived body force can be used to fit the control parameters in equation (6.7).

6.2 Multiple actuators

The starting vortices by the plasma actuators play an important role in the flow evolution. Jukes and Choi (2013) studied how the three-dimensional starting vortex induced by plasma actuators was folded in a laminar boundary layer and compared it with the conventional vane-type vortex generator for the flow separation control application. For the skin-friction control, besides the folding effect of the starting vortices, another important factor is the interaction between two neighbour starting vortices. These two effects are studied in a laminar channel flow at $Re = 3150$. Based on the works on Lorentz force actuators in chapter 5, the geometry and strength of the plasma actuators are fixed at $A_f = 1$, $\sigma = 0.07$ (non-dimensionalised by h) and

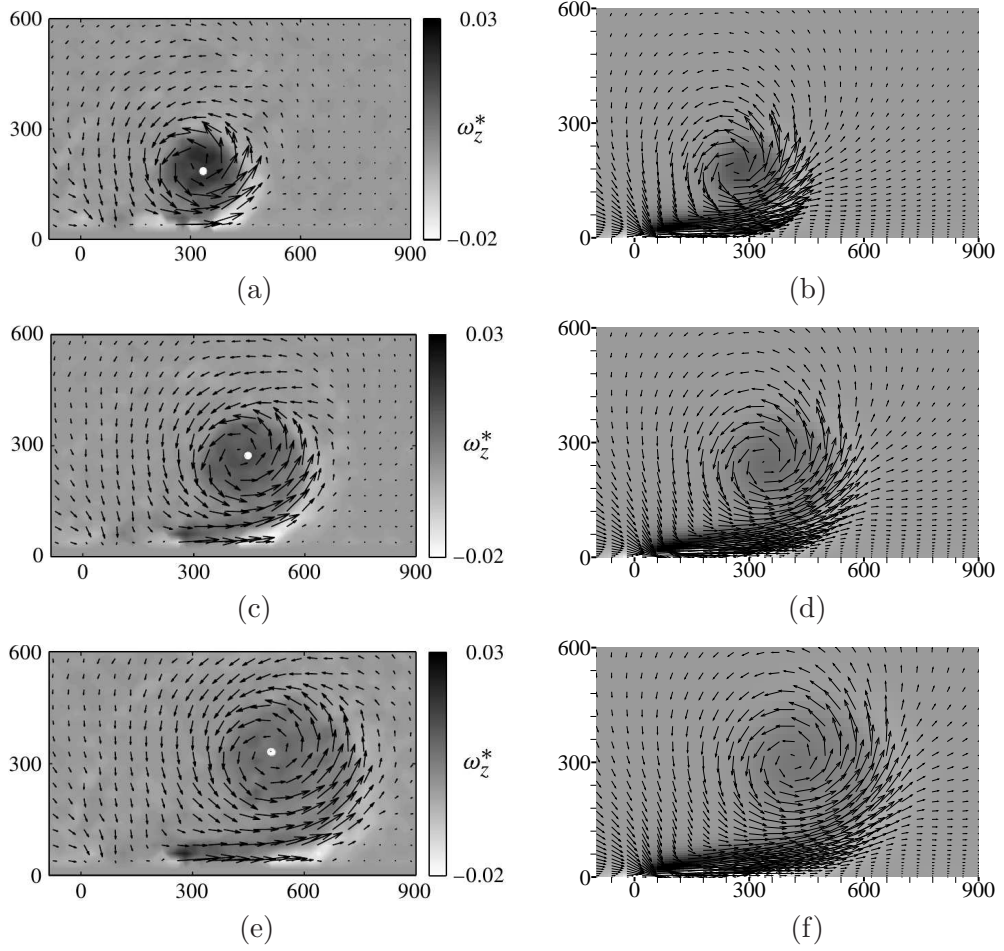


Figure 6.5: Vorticity field (contour) and velocity vectors for the starting vortex at (a)(b) $t^* = 1620$; (c)(d) $t^* = 2700$; and (e)(f) $t^* = 3780$. (a)(c)(e) are PIV data taken from (Whalley and Choi, 2012) and (b)(d)(f) are simulation result. The same contour levels are used everywhere.

$\lambda = 45$ ($\Delta^+ = 4.5$). For the study in this section, the plasma actuators are aligned in the streamwise direction, and only cover a range of $[1/3L_x, 2/3L_x]$ ($L_x = 32$) in the streamwise direction. The inflow of the channel is a parabolic velocity profile, and the outlet is a convection boundary with the convection velocity equal to the local mean velocity.

Figure 6.6(a) shows a close view of the starting vortex at the leading edge of a single DBD plasma actuator. The vortex-formation mechanism in a shear layer has been nicely explained by Jukes and Choi (2013), and this can be visualised by the two streamlines released from $y = 0.2$ (blue) and $y = 0.1$ (red). When the spanwise distance between two adjacent DBD plasma actuators is reduced to

$s = 0.5$, as shown in figure 6.6(b), there is a strong interaction between the two neighbour vortices. At the leading edge of the actuators, it forms complicated ‘W’ shaped vortices. The entrainment of the adjacent actuators inhibits the lift-up of the single starting vortex in figure 6.6(a). The upward and downward velocity by the starting vortices is much weaker, which can be observed from the streamwise velocity contour lines.

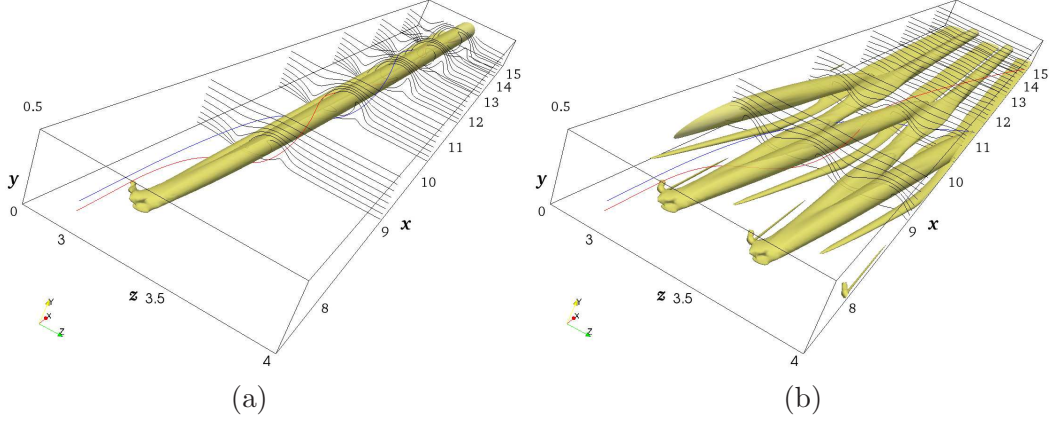


Figure 6.6: Starting vortices at the leading edge of the plasma actuators with different actuator gaps: (a) $s = 3$ and (b) $s = 0.5$. The vortex is shown by iso-surface of $\lambda_2 = -0.001$. Black contour lines show the streamwise velocity at several downstream locations. The blue and red lines show the streamlines starting from $y = 0.2$ and $y = 0.1$ respectively. Only one portion of the domain is shown.

The cores of the starting vortices are identified by the local minima of the λ_2 field in each yz plane, and the trajectory of the core is plotted against the streamwise location x in figure 6.7 to show the spatial evolution of the starting vortices. Jukes and Choi (2013) showed that the starting vortices for their DBD-VG1 and DBD-VG2 had a similar scaling at the initial stage, *i.e.*, $y \sim x^{2/3}$ and $z \sim x^{2/3}$. This is roughly matched for the present starting vortex with $s = 3$, despite that the actuators are within very different streamwise shear layer. However, the evolution of the vortex core trajectory is significantly modified for $s = 0.5$. The starting vortex tends to move faster in both wall normal and spanwise directions, when the effect from the neighbour starting vortex becomes important. Especially when the starting vortex moves to above the neighbour actuator at $x = 3$, it suddenly drops to a much lower wall normal location due to the strong entrainment from the neighbour actuator, which is clearly shown in figure 6.6(b).

The effect of the spanwise actuator gap s can be more clearly seen in figure 6.8 for the transition to turbulence in a periodic channel. Here, seven different gaps

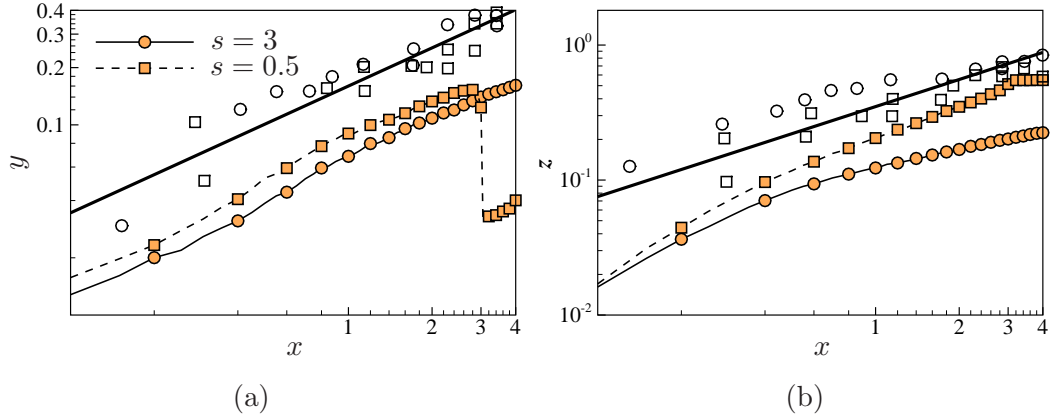


Figure 6.7: Spatial evolution of the starting vortex core in (a) wall normal direction and (b) spanwise direction for spanwise actuator gap $s = 3$ (closed circles) and $s = 0.5$ (closed squares). The open circles and open squares are the data for DBD-VG1 and DBD-VG2 studied by Jukes and Choi (2013) in a laminar boundary layer, and the given scaling $y \sim x^{2/3}$ and $z \sim x^{2/3}$ are shown by the solid line in each plot.

$s = 0.5, 0.6, 0.75, 1, 1.5, 2, 3$ are considered. For $s \geq 1$, the flow ends at the turbulent state; while for $s \leq 0.75$ the flow stays at the laminar state. Interestingly, an “increase-increase” stage and an “increase-decrease” stage for each C_f trajectory curve are observed. The initial C_f increasing rate is inversely proportional to the spanwise actuator gap s , because smaller s means more starting vortices are created to generate stronger upward and downward fluid motion. If the interaction of the neighbour starting vortices is weak ($s \geq 1$), the flow transits to turbulence quickly due to the strong disturbance growth from each individual vortex roller; while if this interaction is strong ($s \leq 0.75$), the behaviour of the single starting vortex can be inhibited (figure 6.6(b)), resulting in the return of the flow to the laminar state. Therefore, in order to reduce the skin-friction using DBD plasma actuators, the spanwise actuator gap s should be kept as small as possible to weaken the starting vortices. This will be confirmed in the following sections.

6.3 Travelling wave configurations

In this section, the aim is to generate transverse motion (Karniadakis and Choi, 2003) using plasma actuators, thus the plasma actuators strips are aligned in stream-wise direction to generate spanwise body force. Choi et al. (2011) studied the span-wise travelling wave and spanwise oscillation generated by DBD plasma actuators. Their plasma actuators configuration and the control signal in time are shown in

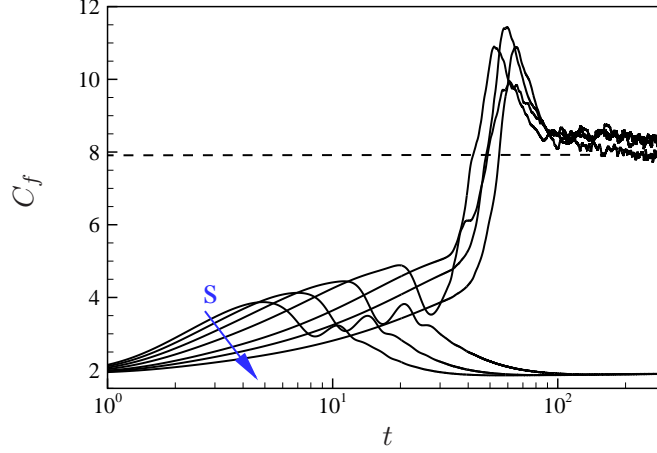


Figure 6.8: Time history of the skin-friction coefficient C_f for different spanwise actuator gaps in a periodic channel. The arrow indicates the increasing direction of the actuator gap, *i.e.*, $s = 0.5, 0.6, 0.75, 1, 1.5, 2, 3$. The dash-dot line shows the skin-friction level at corresponding turbulent state.

figure 6.9. For spanwise travelling wave (figure 6.9(a)), the DBD plasma actuators are divided into four different groups, and each group is only activated for 1/4 of the cycle. The actuated plasma actuators are always 1/4 period delayed than the previous one, so that the plasma actuators in different groups are not activated at the same time. For the spanwise oscillation configuration (figure 6.9(b)), all the plasma actuators are synchronised, with the plasma body force into the positive z direction in the first half oscillation period, and into the negative z direction in the second half period. To increase the lifespan of the plasma actuators (heat accumulation), in practice these DBD plasma actuators are operated with a duty cycle $\mathcal{D} < 1$, as sketched by figure 6.10(a) (Jukes et al., 2006b). Here, the duty cycle \mathcal{D} is defined as below,

$$\mathcal{D} = \frac{T_{on}}{T_{on} + T_{off}}, \quad (6.8)$$

where T_{on} and T_{off} are the time duration that the plasma actuator is on and off, respectively.

The plasma body force is synchronised with the applied voltage variation. Figure 6.10 shows the time signal for the voltage and the generated plasma body force. Accurate modelling and experimental measurement for the DBD plasma actuators have shown the unsteadiness of the generated plasma body force (Likhanskii et al., 2008; Debien et al., 2012). However, the variation of the body force is at the

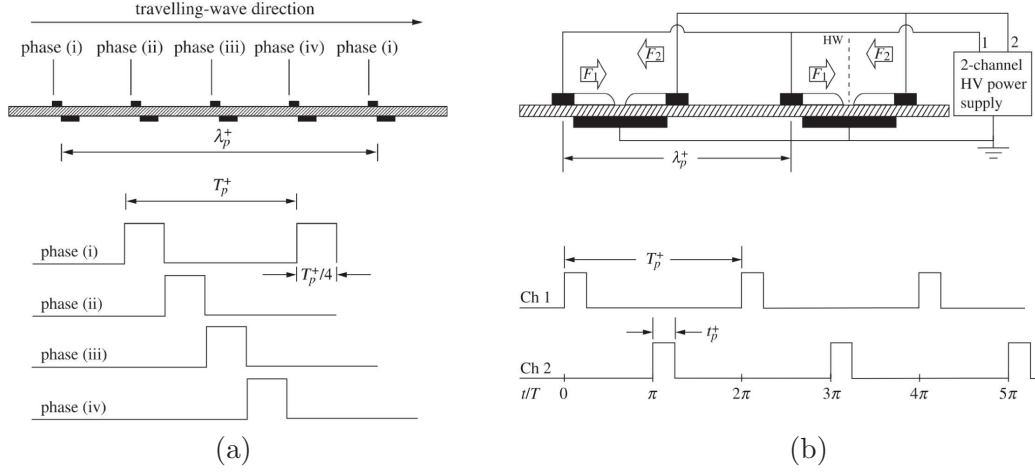


Figure 6.9: DBD plasma actuators configurations for (a) spanwise travelling wave; and (b) spanwise oscillation, taken from Choi et al. (2011).

time scale of $1/f$, which is much smaller than the oscillation period T in the flow control at low Reynolds numbers. For examples, the typical parameter used by Choi et al. (2011) for a $Re_\tau = 475$ turbulent boundary layer control with plasma actuators are: peak to peak voltage magnitude $V_{p-p} = 6.8$ kV, electric frequency $f = 19$ kHz ($1/f \approx 0.05$ ms), oscillation period $T^+ = 40$ ($T \approx 95$ ms), thus one oscillation period contains around 1800 electric cycles. For the present channel flow simulation at $Re_\tau = 200$, the physical time for $T^+ = 40$ would be doubled. Therefore, it is reasonable to assume that the plasma body force is steady during one oscillation period in a macro scale sense. It also has to be mentioned that the flow simulation time step is $\Delta t^+ = 0.2$ ($\Delta t \approx 0.5$ ms converted by the above experimental data), which is one order of magnitude larger than the electric cycle period. Therefore, the unsteadiness of the plasma body force can not be resolved in the present simulation due to the simulation cost. To resolve the unsteadiness, at least two-order of magnitude smaller time step is needed. However, for the flight Reynolds number simulation, $T^+ = 100$ is ~ 0.1 ms (see appendix A), thus resolving the unsteadiness of the plasma body force in this situation becomes crucial. The plasma flow control simulations performed in this chapter are all below $Re_\tau = 400$, thus a steady plasma body force approximation at the electric cycle time scale is used through out. Though ideally the magnitude of the applied voltage can vary in some sinusoidal fashion, so that it can give a plasma body force in the form of $f = \sin(\omega t)$ (Elam, 2012). However, this is a non-standard way to operate DBD plasma actuators (Choi et al., 2011), thus this waveform is not considered in this study.

To test the effect caused by the sudden change of the plasma body force,

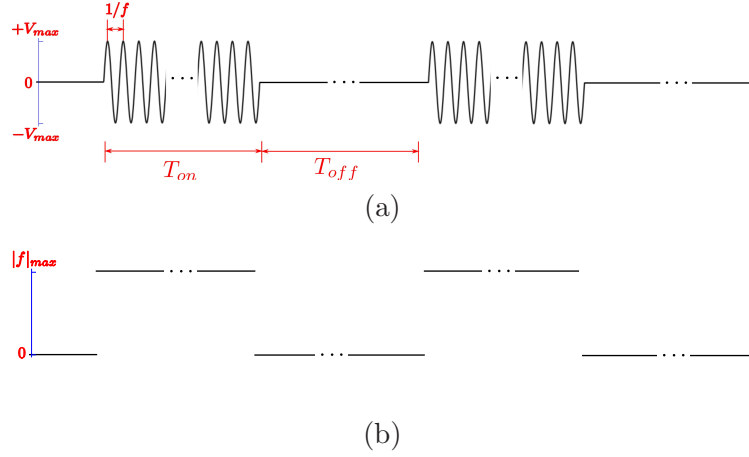


Figure 6.10: Time variation for: (a) voltage; and (b) plasma body force. f is the AC frequency, T_{on} is the plasma-on duration time, and T_{off} is the plasma-off duration time.

another two step functions are considered, *i.e.*, a linear function, and a smooth function as in equation (5.9). The window size for the plasma body force to change from the maximum (minimum) to the minimum (maximum) is assumed to be around 5% of the oscillation period, and the test simulations are run for Jukes et al. (2006b)'s spanwise oscillation case at $A_f = 1.0$, $s^+ = 20$ (or $\lambda_p^+ = 20$ as in figure 6.9) and $\omega^+ = 0.06$ ($T^+ = 105$). A probe is placed at $y^+ \approx 2$ inside the plasma force region to record the force strength and the spanwise velocity, and the results are shown in figure 6.11(a). The step function employed does not affect the wave shape for the induced spanwise velocity strongly. The effect on the steady level of the skin-friction is also negligible, as shown in 6.11(b). Therefore, in the following study, only a sudden change of the plasma body force is considered.

The effect of the duty cycle \mathcal{D} on \mathcal{DR} is studied for the spanwise oscillation case at $A_f = 1.0$, $s^+ = 20$ (or $\lambda_p^+ = 20$) and $\omega^+ = 0.06$ ($T^+ = 105$), shown in figure 6.12. Together given are the experimental data at $T^+ = 16$, 36, and 104 ($T_{off}^+ = 2$ for all three cases) from (Jukes et al., 2006b). The present simulation data is not expected to quantitatively match the experimental data, because the plasma strength is not tuned for this case, and the \mathcal{DR} uncertainty in this type of experimental measurement can be quite high. Therefore, only a qualitative comparison is made here. The maximum drag reduction is achieved at $\mathcal{D} = 100\%$, and \mathcal{DR} almost monotonously decreases as the duty cycle \mathcal{D} decreases, which is also suggested by the three experimental points. Therefore, in the following part, the drag reduction map is given for the maximum duty cycle $\mathcal{D} = 100\%$ only, which corresponds to the highest drag reduction achievable. It is interesting to mention that Cimarelli et al.

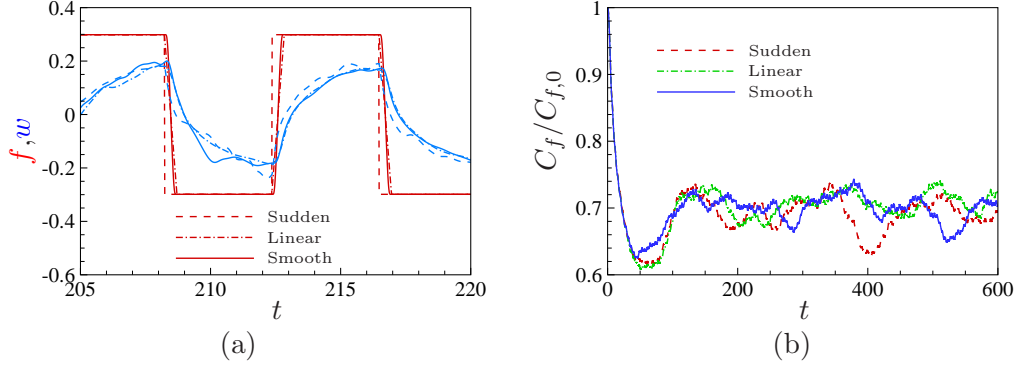


Figure 6.11: Comparing simulation results with three different step functions: (a) plasma body force and spanwise velocity variation at $y^+ \approx 2$; (b) time history of the normalised skin-friction.

(2013) studied different temporal waveforms for spanwise wall oscillation, and their square waveforms (b) and (c) were very similar to the plasma body force waveform studied here: one with a duty cycle $\mathcal{D} = 100\%$. and the other one with $\mathcal{D} < 100\%$. Square waveform with $\mathcal{D} = 100\%$ gave the best \mathcal{DR} performance among all the 5 waveforms reported, though \mathcal{DR} performance for the square waveform (c) was not given by the authors.

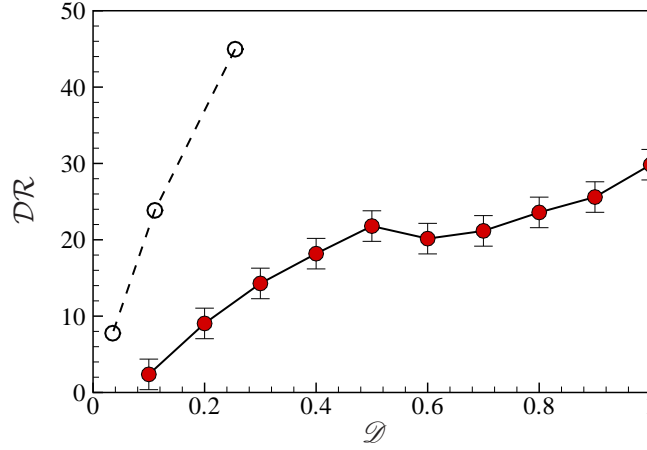


Figure 6.12: Effect of duty cycle \mathcal{D} for spanwise oscillation at $A_f = 0.5$, $s^+ = 20$, $\omega^+ = 0.06$ ($T^+ = 105$). Open circles are from (Jukes et al., 2006b) at constant $T_{off}^+ = 2$.

As demonstrated in section 6.2 for the laminar channel, the plasma actuator gap needs to be small to eliminate the effect from the starting vortices. Jukes et al. (2006b) and Elam (2012) also showed that drag reduction could be only achieved

for $s^+ \leq 20$. Therefore, for the travelling wave case at a fixed plasma actuator gap, the maximum drag reduction appears if the plasma body force varies continuously in the spanwise direction. In practice, this requires that the plasma actuators to be arranged as close as possible to have a good wave approximation. Numerically, this travelling wave configuration can be easily achieved using the following formula for the time and space dependent plasma body force $F_z(y, z)$,

$$F_z(y, z) = \sum_{k=1}^n H[g_1(t)] f_z(y, z') + \sum_{k=1}^n H[g_2(t)] f_z(y, -z'), \quad (6.9)$$

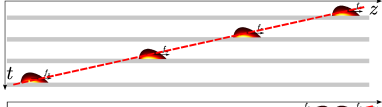
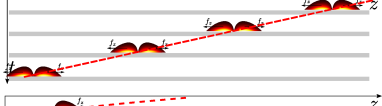
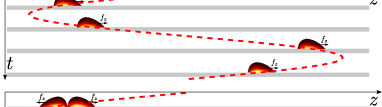
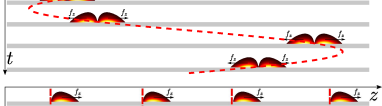
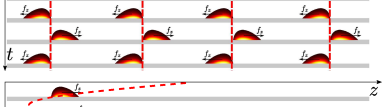
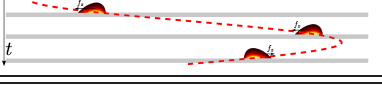
$$z' = z - \frac{k-1}{n} L_z - C(t)t,$$

where n is the total number of actuators placed on the channel wall, f_z is given in equation (6.7), and $H(t)$ is the Heaviside step function,

$$H(t) = \begin{cases} 1, & t \geq 0, \\ 0, & t < 0. \end{cases} \quad (6.10)$$

$C(t)$, $g_1(t)$ and $g_2(t)$ are time dependent control functions given in table 6.1 for each configuration separately. Due to the continuity in the travelling wave speed, the above plasma body force achieves the best drag reduction possible in experiment. In the present study, six configurations are considered: two are spanwise travelling wave cases (ST1, ST2) and four are spanwise oscillation cases (SO1, SO2, SO3, SO4). The distribution of the plasma force is shown in $z - t$ spatial-temporal space (table 6.1) to schematically show the wave forms. ST1 and SO3 are the spanwise travelling wave and spanwise oscillation cases studied by Whalley and Choi (2014) and Jukes et al. (2006b), respectively. ST2 is the case inspired by the spanwise travelling wave of spanwise Lorentz force (Du and Karniadakis, 2000), where the mean force in the spanwise direction is zero. However, compared to Lorentz force, the plasma body force is discrete, and contains different harmonics frequencies. The Fourier spectrum of the spanwise arranged DBD plasma actuator force with $s^+ = 100$ is shown in figure 6.13, together with the mean and first two most energetic Fourier modes, *i.e.*, k_0 , k_1 and k_2 . As expected, the energy is distributed among the length scale of $\lambda_z^+ = s^+$ and its harmonics. SO4 is a new configuration combining the spanwise oscillation and the spanwise travelling wave, which is termed as a “local travelling and global oscillation” configuration.

Table 6.1: Configurations for spanwise travelling wave (ST) and spanwise oscillation (SO) by DBD plasma actuators.

Waves	Sketch	$C(t)$	$g_1(t)$	$g_2(t)$
ST1		c_0	1	-1
ST2		c_0	1	1
SO1		$c_0 \cos(\omega t)$	1	-1
SO2		$c_0 \cos(\omega t)$	1	1
SO3		0	$\cos(\omega t)$	$-\cos(\omega t)$
SO4		$c_0 \cos(\omega t)$	$\cos(\omega t)$	$-\cos(\omega t)$

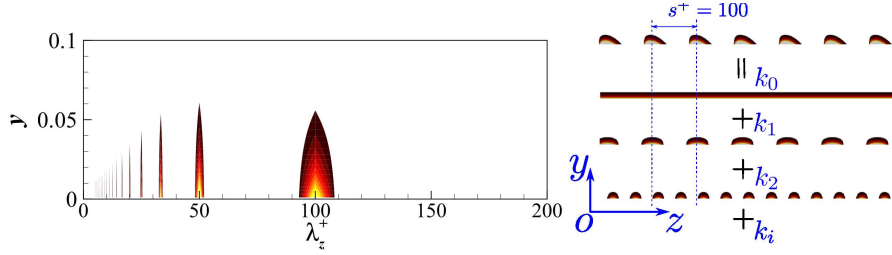


Figure 6.13: Spectrum and the first two most energetic Fourier modes for spanwise arranged DBD plasma actuator force with actuator gap $s^+ = 100$. Low level contours are clipped to give a clearer view.

6.4 Drag reduction maps

With the parameters in the plasma body force distribution fixed at $A_f = 1$, $\sigma = 0.07$ and $\lambda = 45$ ($\Delta^+ = 4.5$), the effect of wave speed c^+ , oscillation frequency ω^+ and actuator gap s^+ are explored. For each configuration, 25 simulations are performed, with s^+ ranging in $[25, 50, 100, 200, 400]$, c^+ ranging in $[0, 1, 2, 4, 8]$ and ω^+ ranging in $[0.01, 0.02, 0.03, 0.06, 0.12]$ (or T^+ ranging in $[628, 314, 209, 105, 52]$). The DBD plasma actuators are arranged on the top and bottom walls of the channel with the same phase in movement and the same force direction. The baseline no control case is CH200. The mass flow rate is kept constant by dynamically adjusting the

streamwise mean pressure gradient for all the control cases. \mathcal{DR} value is evaluated using equation (3.31).

Figure 6.14 shows the drag reduction maps for ST1, SO1, ST2, SO2, SO3 and SO4 configurations. A negligible drag reduction is observed for the high speed travelling wave of ST2, but no drag reduction is observed for SO2 in the whole $\omega^+ - s^+$ space. A significant amount of drag reduction is achieved for ST1, SO1, SO3 and SO4, which are $19 \pm 2\%$, $19 \pm 2\%$, $34 \pm 2\%$ and $35 \pm 2\%$ at the optimal point, respectively.

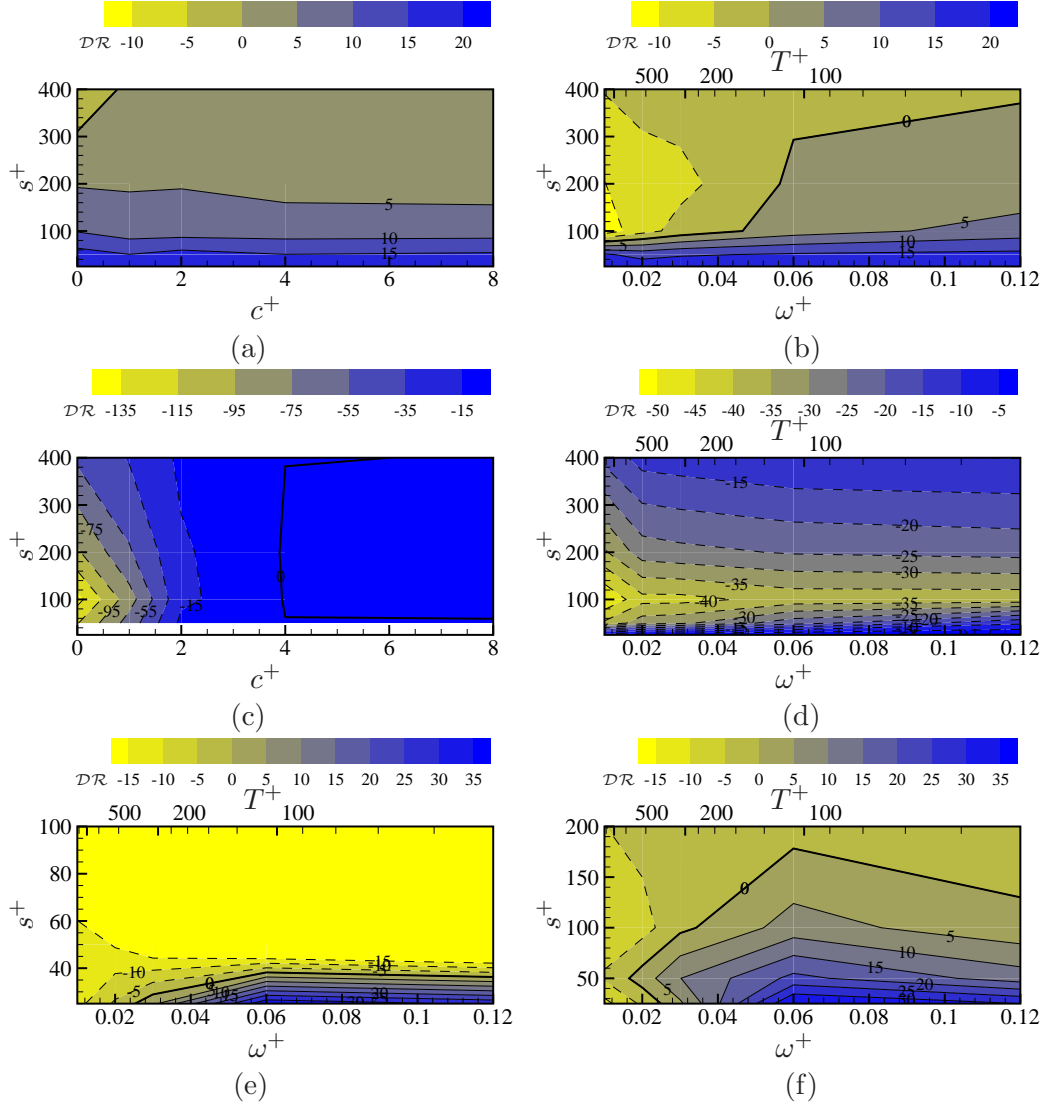


Figure 6.14: Drag reduction maps for (a) ST1; (b) SO1; (c) ST2; (d) SO2; (e) SO3 and (f) SO4.

Comparing ST1 and SO1, the two \mathcal{DR} maps are rather similar, especially in the region with small actuator gap s^+ . To be noticed, for SO1, the volume averaged C_f has large oscillation in time, especially for large gap s^+ , resulting in larger uncertainty in the \mathcal{DR} values compared to ST1. At a fixed actuator gap s^+ , ST1 and SO1 give the same \mathcal{DR} value, and this value is equal to that at $c^+ = 0$ (or $\omega^+ = 0$). To explain this, simulations with the mean and the most energetic Fourier modes of the plasma body force (shown in figure 6.13) are performed separately for $s^+ = 100$ and 50, and the time history of the skin-friction coefficient C_f is shown in figure 6.15. As can be seen, for both cases with $s^+ = 100$ and 50, the overall skin-friction coefficient C_f follows that of the most energetic Fourier mode initially after the actuators are switched on; then it drops to follow the C_f trajectory of the mean mode. The long-term C_f level is dominated by the mean mode. Again, this confirms that the important factor for the drag reduction by plasma actuators is the mean force component, rather than the individual actuator force, as found in section 6.2. Du et al. (2002) found that for the spanwise travelling wave by spanwise Lorentz force, larger \mathcal{DR} appeared at larger spanwise wavelength λ_z^+ . This agrees with the drag increase obtained for the most energetic Fourier mode (green lines in figure 6.15), which has the spanwise wavelength much smaller than the spanwise wavelength $\lambda_z^+ = 840$ explored by Du et al. (2002). The mean force component for ST2 and SO2 are both zero, and all the plasma forces are distributed among the small spanwise wavelengths, thus only a drag increase is observed for these two configurations.

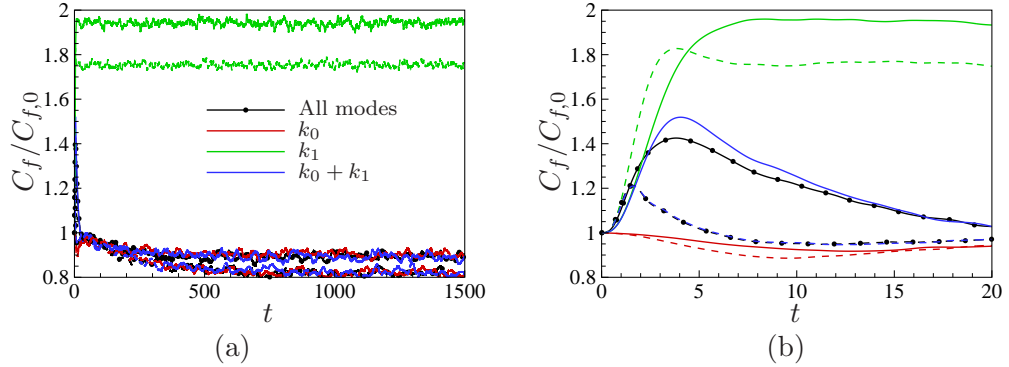


Figure 6.15: Time history of skin-friction coefficient C_f for ST1 at $c^+ = 0$ with $s^+ = 100$ (solid lines) and $s^+ = 50$ (dashed lines): (a) long time history; and (b) initial stage response.

The \mathcal{DR} maps for SO3 and SO4 at small spanwise plasma actuator gap s^+ are similar, both have around $35 \pm 2\%$ drag reduction at $\omega^+ = 0.06$ ($T^+ = 105$).

However, the drag reduction deteriorates dramatically for SO3 as the actuator gap increases. When $s^+ > 40$, no drag reduction is observed for SO3; while around $5 \pm 2\%$ drag reduction is still achievable for SO4 up to $s^+ = 100$. This is a big improvement to SO3 by Jukes et al. (2006b) and Elam (2012). The quick \mathcal{DR} deterioration for SO3 is due to the starting vortices generated by the plasma actuators, which can be viewed from the particle visualisation in the quiescent air (figure 6.16(a)) and the streamwise mean vorticity component in a turbulent field (figure 6.16(b)). The particles are released at $y^+ \approx 10$ in a quiescent air for two plasma actuator gaps, *i.e.*, $s^+ = 25$ and 50 at four equally separated phases of one oscillation period. The plasma actuators generated Stokes layer (PGSL) is very uniform in the spanwise direction at $s^+ = 25$. However, at $s^+ = 50$, the non-uniformity dominates the PGSL, and large size local starting vortices are generated, which is similar to the smoke visualisation by Jukes et al. (2006b) (figure 2.5). These starting vortices by the plasma actuators generate strong downward and upward fluid motions, corresponding to strong streamwise mean vorticity in the controlled turbulent field (figure 6.16(b)), resulting in higher skin-friction. At $s^+ = 25$ and 50 , the \mathcal{DR} value against the oscillation frequency ω^+ is shown in figure 6.17 for SO3 and SO4, with the comparison of the spanwise wall oscillation (figure 4.17(b)) and the spanwise oscillating Lorentz force (figure 5.13(a)). Clearly, at $s^+ = 25$, the \mathcal{DR} curves between SO3 and SO4 are undistinguishable; while at $s^+ = 50$, all the \mathcal{DR} values are negative for SO3, and \mathcal{DR} deteriorates by around 35% for SO4. The dramatic change of \mathcal{DR} for SO3 was also shown by the experimental data, where negative \mathcal{DR} appeared at $s^+ = 30$ (Jukes et al., 2006b). All the spanwise oscillation cases (including wall motion and Lorentz force) show the same feature, that the imposed spanwise mean strain by wall motion or body force interacts with the flow most at an oscillation frequency of $\omega^+ \approx 0.06$ (or $T^+ \approx 100$). Jukes et al. (2006b) conjectured that the plasma actuator induced streamwise vortices disrupted or cancelled the quasi-streamwise vortices in a natural boundary layer, and this caused the drag reduction. However, \mathcal{DR} only appears at small plasma actuator gap ($s^+ < 30$ according to their experimental data), in which situation the plasma induced streamwise vortices are significantly merged to form strong uniform spanwise motions as in the spanwise wall oscillation and Lorentz force cases, thus the plasma induced streamwise vortices play a less important role in the drag reduction.

For ST1, SO1 and SO4, the power spent P_{sp} and the net energy saving P_{net} are computed using the same formula as in the Lorentz force case (see equation (5.13)). The maps of P_{sp} and P_{net} are shown for ST1, SO1 and SO4 in figures 6.18 and 6.19, respectively. As expected, the case with a smaller plasma actuator gap

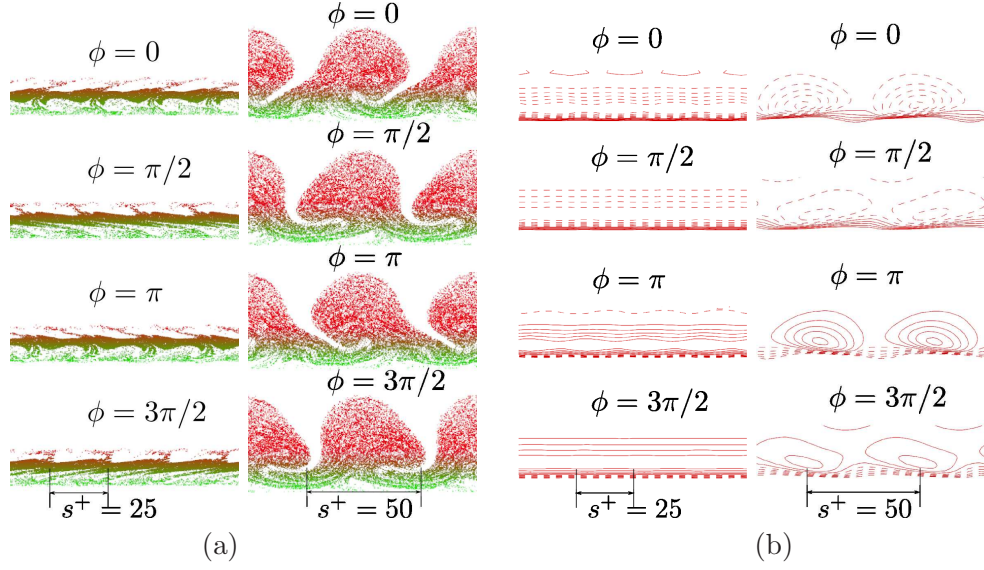


Figure 6.16: Vortical structures in SO3 case at $\phi = 0, \pi/2, \pi, 3\pi/2$ for different actuator gaps: $s^+ = 25$ and $s^+ = 50$, visualised by (a) particles released at $y^+ \approx 10$ in quiescent air (particles are coloured by wall distance), and (b) streamwise mean vorticity in an actuated turbulent field.

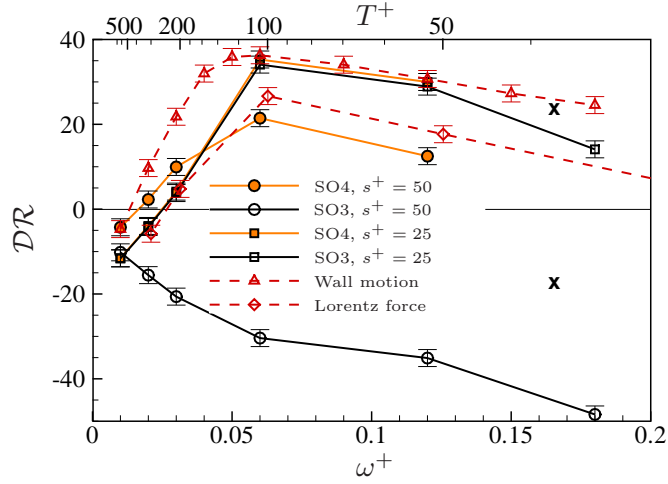


Figure 6.17: Drag reduction \mathcal{DR} against the oscillation frequency ω^+ for SO3, SO4, spanwise wall oscillation from figure 4.17(b), spanwise oscillating Lorentz force with $\Delta^+ = 10$ from figure 5.13(a). The two cross symbols are for $s^+ = 20$ and $s^+ = 30$ from Jukes et al. (2006b).

has higher energy spent. For ST1 and SO1, the energy spent is almost independent from the travelling wave speed c^+ and the oscillation frequency ω^+ , same as their \mathcal{DR} maps in figure 6.14. The control energy input is smaller for SO4, because the overall induced spanwise flow is smaller (see figure 6.30).

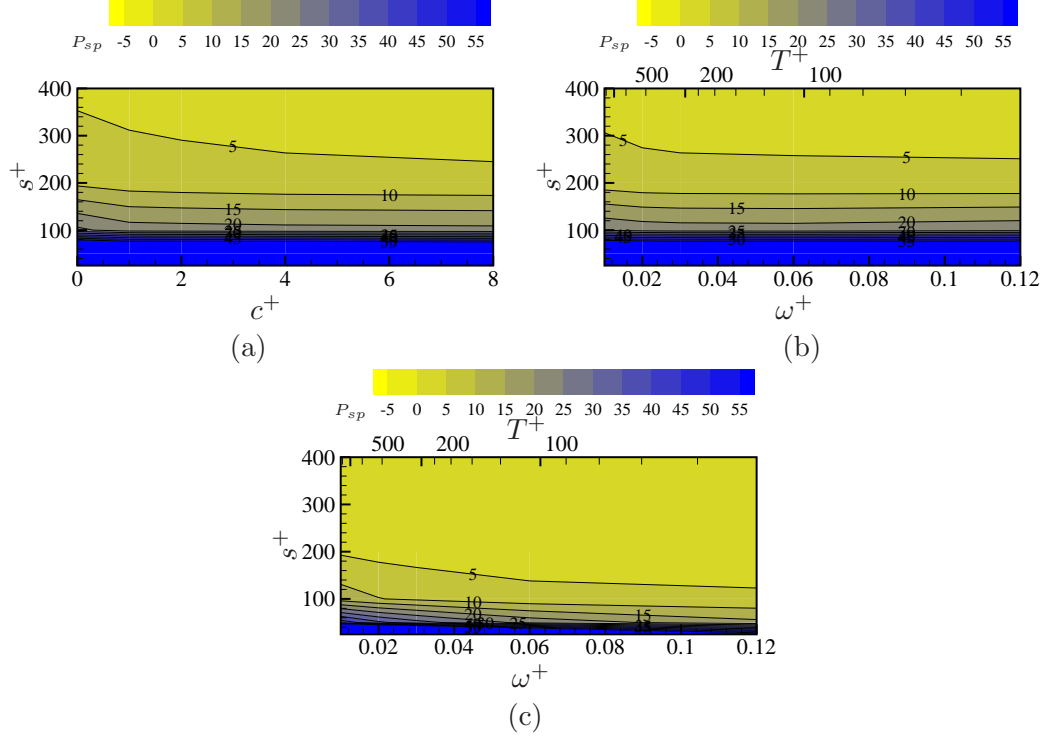


Figure 6.18: Power spent (P_{sp}) maps for (a) ST1; (b) SO1; and (c) SO4.

As shown in figure 6.19, almost no net energy saving is observed for all the three configurations, ST1, SO1 and SO4, within the parameter space explored. The best performance cases are ($c^+ = 2, s^+ = 400$) with $P_{net} = 0.4$ for ST1, ($\omega^+ = 0.12, s^+ = 400$) (or ($T^+ = 52, s^+ = 400$)) with $P_{net} = -2$ for SO1, and ($\omega^+ = 0.06, s^+ = 100$) (or ($T^+ = 105, s^+ = 100$)) with $P_{net} = 0.5$ for SO4. The less than 1% P_{sp} is within the uncertainty of the present simulations. However, a large portion of the P_{sp} maps is within $P_{sp} > -5$, thus by carefully choosing the control parameters, it is still likely to win a net energy saving (at least for $Re_\tau = 200$ explored.)

The original idea to use plasma actuators for the skin-friction control is to implement spanwise wall oscillation in a more practical way. The discrete plasma body force makes the \mathcal{DR} control less effective than the uniform spanwise wall oscillation or Lorentz force oscillation, as has been seen from figure 6.17. However, the discrete body force also reduces the amount of energy consumption, and it may be more favoured than uniform Lorentz force for a positive P_{sp} . This can be seen in figure 6.20, where the change of \mathcal{DR} against P_{sp} for SO4 at $\omega^+ = 0.06$ ($T^+ = 105$) is shown. At small s^+ , SO4 has a similar \mathcal{DR} performance as the spanwise wall oscillation and spanwise oscillating Lorentz force, but located in $\mathcal{DR} < P_{sp}$ region.

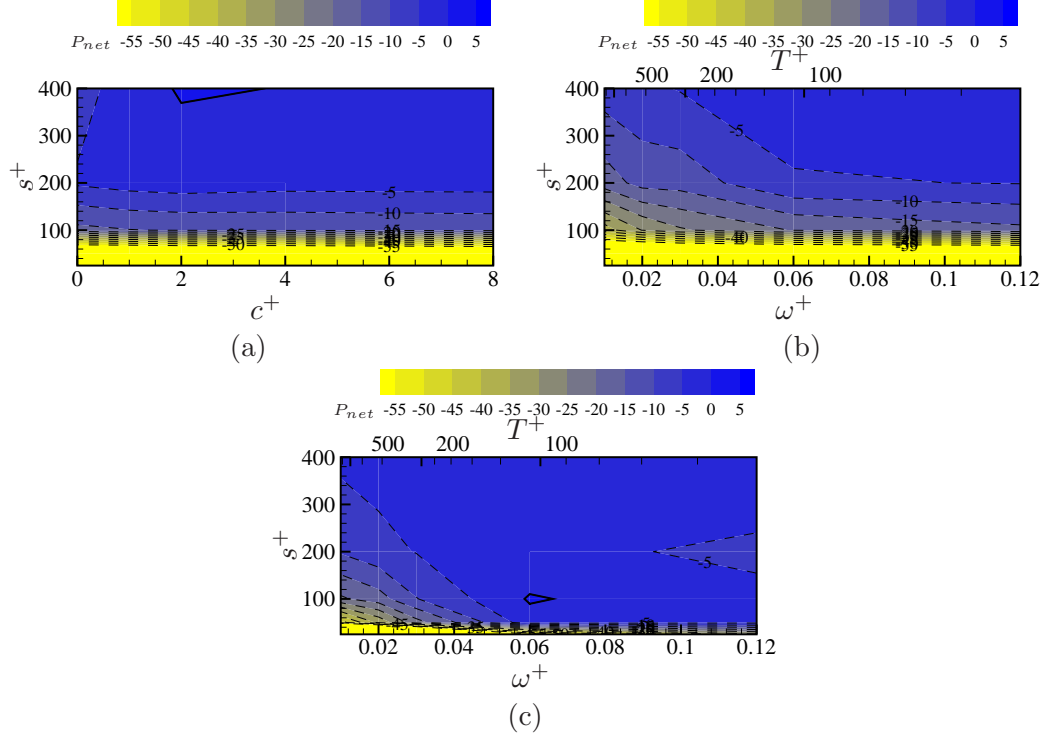


Figure 6.19: Net energy saving, P_{net} maps for (a) ST1; (b) SO1; and (c) SO4.

As s^+ increases, the P_{sp} decrease overcomes \mathcal{DR} deterioration, and the control point approaches $\mathcal{DR} = P_{sp}$ line quickly. Recently, Mishra and Skote (2015) used only half of the spatial waves cycle to reduce the power consumption, and their PS2 and PS3 achieved positive P_{sp} at $A_w^+ \approx 12$. At this wall velocity amplitude, the spanwise wall oscillation has $P_{sp} = -4$ (Baron and Quadrio, 1996). Similarly, Cimarelli et al. (2013) explored different temporal oscillation waves, and showed that the largest P_{sp} was achieved for a sharp pulse wave with a large fraction of the period quenched (their wave (f)).

The power supply for a real plasma actuator comes from electricity, and this power consumption can be calculated through,

$$P_{elec} = \frac{1}{T} \int_0^T V I dt, \quad (6.11)$$

where V and I are the instantaneous voltage and current from the main power supply, T is the plasma force oscillation period. Jukes et al. (2006b) measured $P_{elec} = 100\text{W}$ in their experiment for a similar plasma control configuration with $s^+ = 20$, and the estimated efficiency $\eta = \mathcal{E}_f L_x L_z / P_{elec}$ from the electric power to the fluid power is $\eta \sim 10^{-3}$ (Moreau, 2007). Considering the plasma actuator

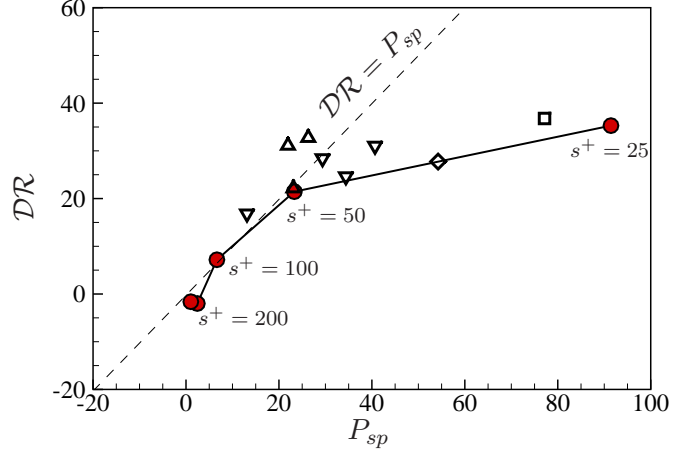


Figure 6.20: \mathcal{DR} against P_{sp} at $\omega^+ \approx 0.06$ ($T^+ \approx 105$) comparison among different waveforms: SO4 (circles); spanwise wall oscillation from (Baron and Quadrio, 1996) (square); spanwise oscillating Lorentz force (diamond); half spatial waves from (Mishra and Skote, 2015) (upper triangles, $A_w^+ \approx 12$); arbitrary temporal waves from (Cimarelli et al., 2013) (lower triangles, $A_w^+ = 9$).

loses part of its electric power in heating the dielectric material, its efficiency is even lower than the Lorentz force actuators. Table 6.2 shows the estimated real power consumption in the wind and water tunnels for different devices. With only the fluid power consumption considered, all the devices, including spanwise wall oscillation, rotating disks (Ricco and Hahn, 2013), Lorentz actuators and plasma actuators are compatible. However, the efficiency for Lorentz force and plasma actuator are several order of magnitude lower than the other two, which makes them not favoured by the \mathcal{DR} control at all.

6.5 Turbulence statistics

The turbulence statistics are analysed for two typical drag reduction control cases: ST1 with $c^+ = 0$ and SO4 with $\omega^+ = 0.06$ ($T^+ = 105$). The streamwise mean velocity profiles at two different spanwise locations between two adjacent actuators, *i.e.*, $z/s = 0$ and 0.5 , are shown in figure 6.21 for ST1 with a large actuator gap of $s^+ = 400$. As can be seen, there is a large variation of the mean velocity profile in the spanwise direction. Choi et al. (2011) reported that the streamwise mean velocity profile was modified up to $y^+ = 100$ for the travelling wave case due to the starting vortex, with a mean velocity increase in the near wall region and a reduction in the region of $y^+ = 25 \sim 100$ (shown in figure 6.21 by open circles). This feature

Table 6.2: Energy budget estimation for control [†] in wind and water tunnels.

Wind tunnel	Re_m	Re_τ	h^* (mm)	U_m^* (m/s)	u_τ^* (m/s)	ρ kg/m ³	$\nu^* \times 10^6$ (m ² /s)	ν^*/u_τ^* (mm)	ν^*/u_τ^{*2} (ms)	$2\tau_w^* U_m^*$ mW/m ²
	3150	200	40	1.18	0.075	1.3	15	0.2	2.7	17.6
		A_w^* m/s	A_f^* mN/kg	T^* ms	S^* [‡] mm	P_{saved}^* mW/m ²	P_{spent}^* mw/m ²	η		
	Wall oscillation	0.9	-	250	-	6	14	$O(0.1)$		
	Rotating disks	0.5	-	1000	150	3	1.5	$O(0.1)$		
	Plasma actuators	-	35	250	5	4	4	$O(10^{-3})$		
Water tunnel	Re_m	Re_τ	h^* (mm)	U_m^* (m/s)	u_τ^* (m/s)	ρ kg/m ³	$\nu^* \times 10^6$ (m ² /s)	ν^*/u_τ^* (mm)	ν^*/u_τ^{*2} (ms)	$2\tau_w^* U_m^*$ mW/m ²
	3150	200	20	0.16	0.01	1.03×10^3	10	0.1	10	32.4
		A_w^* m/s	A_f^* mN/kg	T^* ms	S^* [‡] mm	P_{saved}^* mW/m ²	P_{spent}^* mw/m ²	η		
	Wall oscillation	0.12	-	1	-	12	25	$O(0.1)$		
	Rotating disks	0.07	-	4000	80	6	3	$O(0.1)$		
	Lorentz actuators	-	620	1	3	9	18	$O(10^{-3})$		

[†] - typical control cases are: $A_w^+ = 12$, $T^+ = 100$ for spanwise wall oscillation; $D^+ = 820$, $W^+ = 6.7$, $T^+ = 386$ for rotating disks (Ricco and Hahn, 2013); $A_f = 0.5$, $T^+ = 100$ for Lorentz force actuators; and $A_f = 1.0$, $T^+ = 100$ for plasma actuators;

[‡] - diameter for rotating disk; width for Lorentz actuator magnet and electrode; width for plasma actuator embedded electrode.

is also observed for the present ST1 case with a large actuator gap, $s^+ = 400$. Since the downward velocity is the strongest just above the DBD plasma actuators, the modification in the logarithmic region is the strongest at $z/s = 0$. However, as the actuator gap is decreased to $s^+ = 50$, the spanwise variation of the mean velocity profiles is very small, and the modulation in the logarithmic region by the plasma actuators is less obvious, which can be seen from the two-dimensional streamwise velocity contour in figure 6.22 with three different actuator gaps, *i.e.*, $s^+ = 400$, 100 and 50.

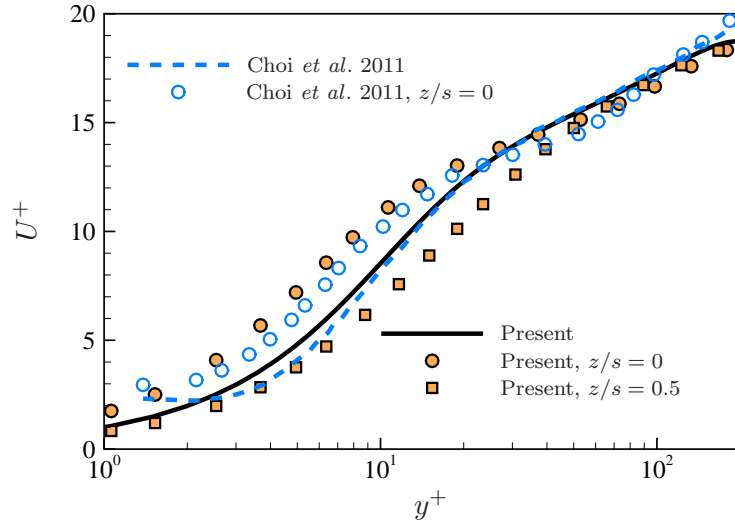


Figure 6.21: Streamwise mean velocity profiles comparison between present work for ST1 with $s^+ = 400$ and experimental data from Choi et al. (2011) for spanwise travelling wave with $s^+ = 500$.

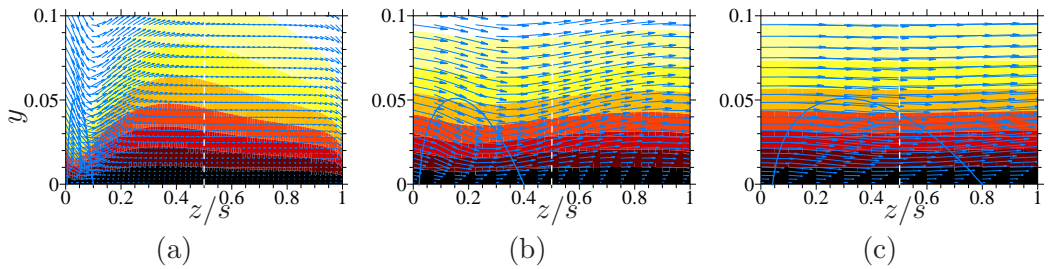


Figure 6.22: Two-dimensional streamwise velocity contour between two adjacent plasma actuators for ST1 with (a) $s^+ = 400$, (b) $s^+ = 100$, and (c) $s^+ = 50$. In-plane vectors are for spanwise and wall normal velocities. Contour lines are for 10% maximum level of the plasma body force distribution. Same contour levels are used for all the plots.

The following statistics focuses on ST1 and SO4 cases with a plasma actuator gap of $s^+ = 50$. The mean velocity profile change is shown in figure 6.23(a), together with the spanwise wall oscillation case with $A_w^+ = 12$, $\omega^+ = 0.06$ ($T^+ = 105$) (figure 4.14(a)). The overall averaged mean velocity profiles show a very similar modulation to the spanwise wall oscillation. When non-dimensionalised in the no control wall units, the velocity gradient is significantly reduced, while the logarithmic region almost remains unchanged. The streamwise velocity fluctuation u_{rms}^+ and turbulent shear stress profiles $-\overline{u'v'}^+$ are shown in figure 6.23(b) for the comparison among no control case, ST1, SO4 and spanwise wall oscillation cases. Both quantities show a decrease of the peak values and an increase of the peak location. These are consistent with the drag reduction observed.

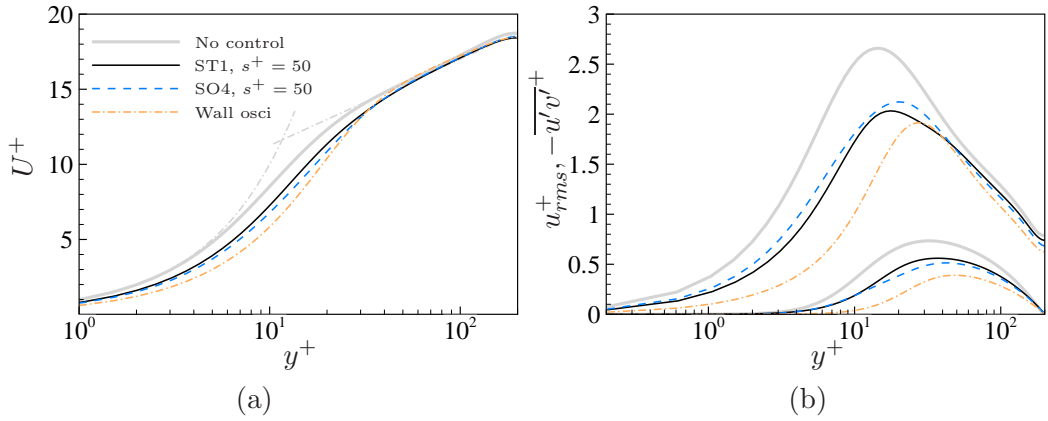


Figure 6.23: Comparison between no control and control cases for (a) streamwise mean velocity profiles, and (b) streamwise velocity fluctuation u_{rms}^+ and turbulent shear stress $-\overline{u'v'}^+$. In (a), law of wall is shown by grey dash-dot lines with $U^+ = 1/0.4 \ln y^+ + 5.5$.

The two-dimensional pre-multiplied co-spectra $k_x k_z \Phi_{uv}$ are shown in figure 6.24 for three wall normal locations, *i.e.*, $y^+ = 5, 10$ and 20 . At all three locations, the streamwise length scale λ_x^+ becomes shorter for both ST1 and SO4. No big change appears for the spanwise length scale λ_z^+ for SO4, but the most energetic λ_z^+ becomes much larger for ST1, which can be clearly seen by the anti-clockwise rotating of the contour plot. Since the plasma body force concentrates closer to the wall, the modification on the co-spectra level is larger as the xz plane moves from $y^+ = 20$ to $y^+ = 5$. This length scale change can be more clearly observed from the one-dimensional co-spectra $k_x \Phi_{uv}$ and $k_z \Phi_{uv}$ in figure 6.25. Due to the discrete nature of the plasma actuators (shown in figure 6.13), the spikes at $\lambda_z^+ = 50$ for ST1 and SO4 are clear at $y^+ = 5$ (much stronger for SO4 case). This partially causes the

deterioration of \mathcal{DR} using plasma body force compared to the continuous Lorentz force (see figure 6.17).

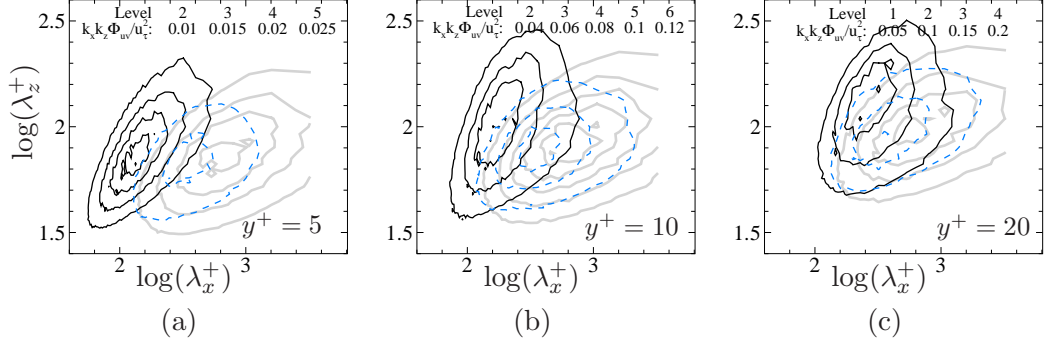


Figure 6.24: 2D pre-multiplied spectra $k_x k_z \Phi_{uv}$ for no control case, ST1 and SO4 at (a) $y^+ = 5$; (b) $y^+ = 10$ and (c) $y^+ = 20$. For line code, see figure 6.23.

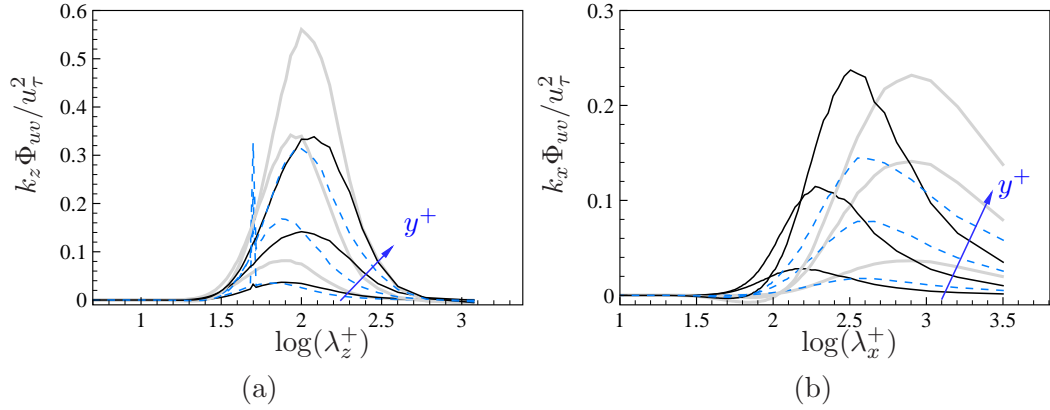


Figure 6.25: Pre-multiplied 1D energy spectra (a) $k_z \Phi_{uv}$ and (b) $k_x \Phi_{uv}$ at $y^+ = 5, 10$ and 20 (indicated by the arrow). For line code, see figure 6.23.

To further understand the structure modulation by the plasma body force, the correlation structures R_{uu} , R_{vv} and R_{uv} are calculated. Here, the R_{uu} structure can be interpolated as the near wall streaks; while the R_{vv} structure can be interpolated as the quasi-streamwise vortices. In figure 6.26, the correlation structures for ST1 are shown for $y^+ = 5, 10$ and 20 . Compared to the no control case, where these structures are perfectly aligned in the streamwise direction, the correlation structures for ST1 are significantly tilted into one direction due to the spanwise plasma body force. As can be seen, R_{uv} correlation structure is not symmetric in the flow, and the asymmetry becomes more obvious at $y^+ = 5$. The tilting angles of the top half of the structures are identified, and it is found that R_{uu} , R_{vv} and R_{uv} correlation structures have different preferential orientation angles. As expected, the R_{uv}

structure always has a tilting angle between those of the R_{uu} and R_{vv} structures.

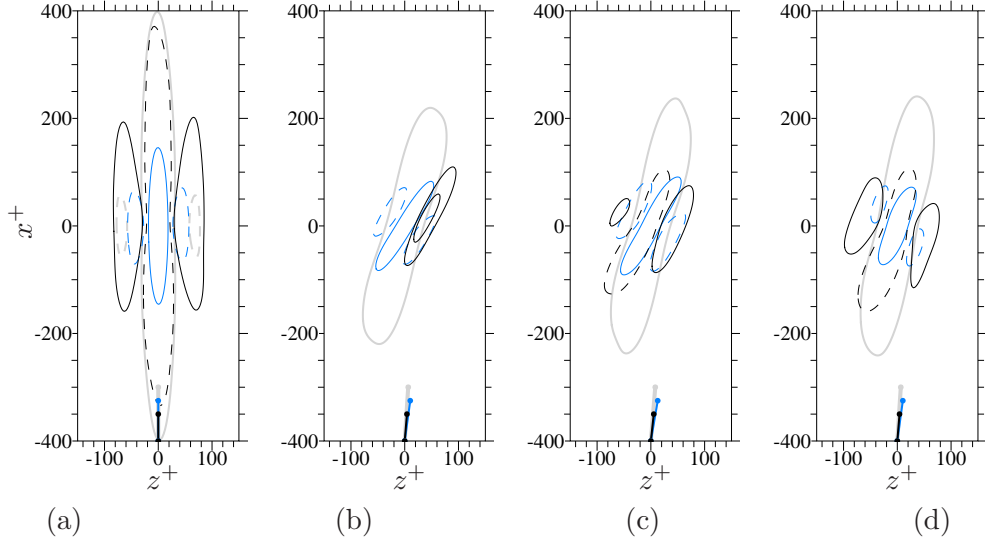


Figure 6.26: Correlation R_{uu} (grey bold lines), R_{vv} (blue thin lines) and R_{uv} (black thin lines) for (a) no control case at $y^+ = 20$, and ST1 at (b) $y^+ = 5$; (c) $y^+ = 10$ and (d) $y^+ = 20$. An arbitrary contour level is shown to outline the correlation structures. The tilting angles are indicated by the lines at the bottom.

The R_{uu} , R_{vv} and R_{uv} correlation structures for SO4 in the first half period, *i.e.*, $\phi = 0, 3\pi/8, 5\pi/8$ and $7\pi/8$ are shown in figure 6.27. Due to the periodicity of the flow, the second half period is the mirror image about $z^+ = 0$ of the first half (as the ensemble averaged λ_2 structures in figure 4.19). Again, for SO4 the R_{uu} , R_{vv} and R_{uv} correlation structures have different preferential tilting angles at each phase. The tilting angle variation during the whole oscillation period is shown in figure 6.28. The R_{uv} structure is always tiled in the middle of the other two. When the three structures are in phase, it gives the highest skin-friction value during the oscillation period, though a slight phase leading of C_f peak can still be seen. This result is reminiscent of the ensemble averaged λ_2 structure dynamics in figure 4.23 for the spanwise wall oscillation. The reason for not applying the ensemble averaged λ_2 structure analysis for SO4 case is that, the starting vortices generated by the plasma actuators contaminate the near wall quasi-streamwise vortices field, and the proposed coherent structure identification in section 3.2 can not distinguish these two types of vortices clearly.

The above results about the correlation structure analysis support the model proposed by Baron and Quadrio (1996) for the drag reduction in spanwise wall oscillation case. In their model, the spanwise strain convects the R_{uu} structure

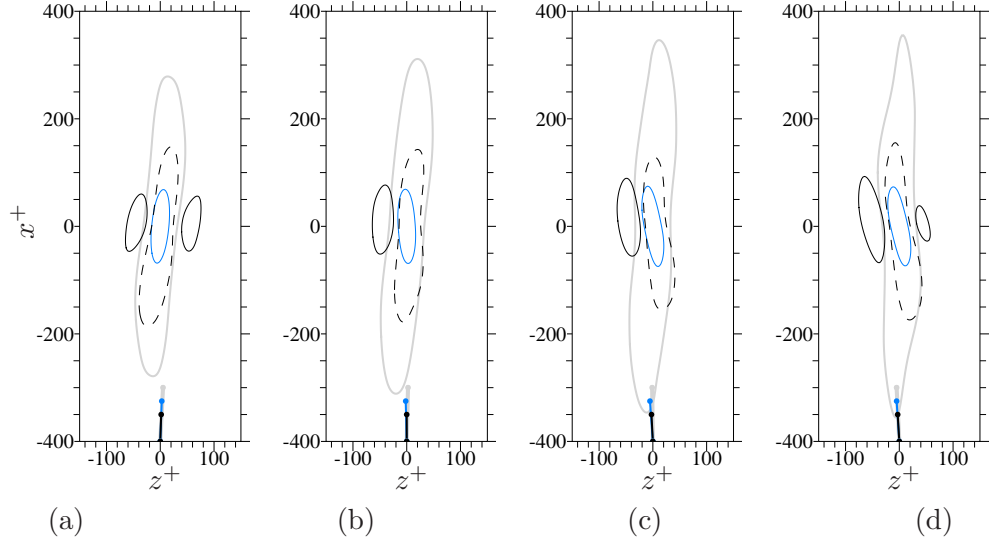


Figure 6.27: Correlation R_{uu} , R_{vv} and R_{uv} for SO4 at $y^+ = 20$ with phase (a) $\phi = 0$, (b) $\phi = 3\pi/8$, (c) $\phi = 5\pi/8$, and (d) $\phi = 7\pi/8$.

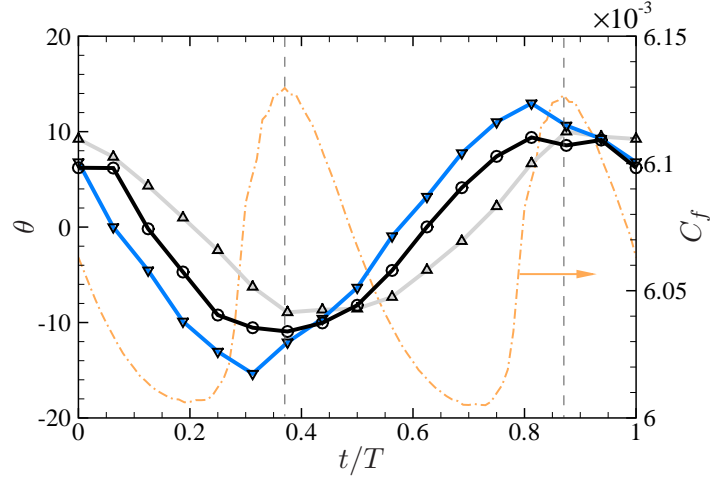


Figure 6.28: Structure angles for R_{uu} (line with upper triangles), R_{vv} (line with lower triangles), R_{uv} (line with circles) and skin-friction coefficient C_f (dash-dot line) variation during one oscillation period for SO4.

(near wall streaks) and the R_{vv} structure (quasi-streamwise vortices) in the spanwise direction with different speeds, resulting in the decorrelation of the Reynolds shear stress $\overline{u'v'}$.

6.6 Effect of flow symmetry

The flow symmetry in the top half and the bottom half of the channel is an important factor for ST1. For the symmetry effect study of ST1, a steady Lorentz force (equation (5.3)) is considered, which corresponds to a uniform plasma body force distribution in the spanwise direction. The force strength is fixed at $A_f = 0.5$, and the force penetration depth Δ^+ varies. Three situations are considered: (1) the body forces on the top and bottom half channels are in the same direction; (2) the body force is only applied to the bottom half channel; and (3) the body forces on the top and bottom half channels are in the opposite directions. Figure 6.29 shows the drag reduction dependency on the body force penetration depth Δ^+ for all the three situations. Unlike the uni-direction wall movement case (figure 4.8), which can only have a drag increase no matter the top and bottom walls move in the same or opposite directions, the body force surprisingly achieves a drag reduction at certain body force penetration depth Δ^+ , with the optimal drag reduction appearing at $\Delta^+ = 5$, which is very close to the plasma body force penetration explored in this chapter ($\Delta^+ = 4.5$). The drag reduction values for the three situations are very different at the same body force penetration depth, with situation (1) giving the best performance, while situation (3) giving the worst performance, and situation (2) in between. For instance, at $\Delta^+ = 5$, $\mathcal{DR} = 16 \pm 2$ is achieved for situation (1); $\mathcal{DR} = 7 \pm 2$ for situation (2); and $\mathcal{DR} = -7 \pm 2$ for situation (3).

The force symmetry effect is almost negligible for the unsteady body force cases. The spanwise mean velocity profiles for the steady force with different penetration depths Δ^+ are shown in figure 6.30, together with the profiles for SO4 with $s^+ = 50$. For SO4, the body force on one side of the wall can hardly affect the flow on the other side, because the spanwise mean velocity is almost zero for $y^+ > 30$. However, for the steady body force cases, the channel centreline spanwise velocities are significantly different when the top and bottom plasma actuators actuate in the same or opposite directions. This further affects the spanwise mean velocity profile in the near wall region.

The effect of the flow symmetry about the channel centre confirms the drag reduction model by Baron and Quadrio (1996), *i.e.*, only a certain spanwise mean strain can effectively decorrelate the near wall streaks and the quasi-streamwise vortices. However, what kind of spanwise mean velocity profile is most effective, remains to be an open question. For ST1 in a turbulent boundary layer, it is similar to situation (2) in a channel, where certain amount of drag reduction is still achievable, but less effective than in the channel. In this sense, SO4 is the case most

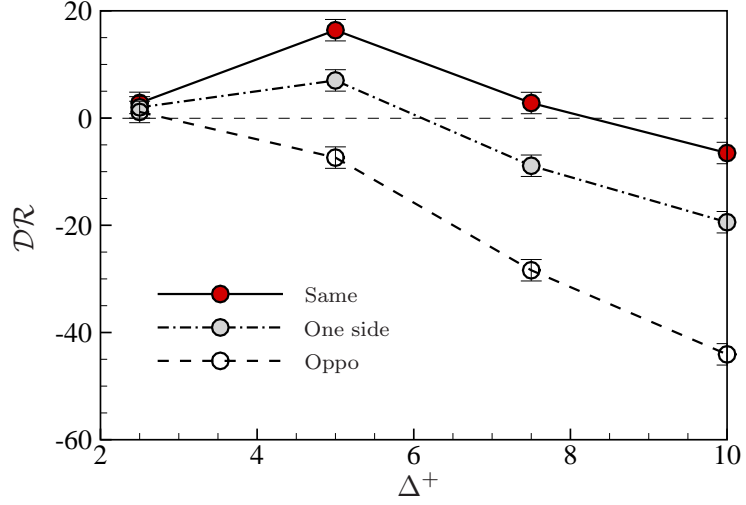


Figure 6.29: Drag reduction dependency on the body force penetration depth Δ^+ , when plasma body force on the top and bottom walls are in the same direction (solid lines), opposite directions (dash lines), or the body force is only applied to the bottom half channel (dash-dot lines).

likely to achieve drag reduction for the turbulent boundary layer control.

6.7 The application

In real situation, the DBD plasma actuators can only actuate at certain fixed wall locations. This is considered for SO4 case with $\omega^+ = 0.06$ ($T^+ = 105$), $s^+ = 50$. Figure 6.31(a) shows the schematics of the operation mode. Two groups of DBD plasma actuators are arranged on the wall, with the actuator gap between two activated plasma actuators to be $s^+ = 50$ (the gap between two adjacent plasma actuators is $s^+/2$). During one oscillation period T , the plasma actuators can have four “ON” modes, as shown on the left of figure 6.31(a); while the “ON-OFF” time signal sequence is shown on the right of figure 6.31(a). The burst ratio \mathcal{B} of the plasma actuators is defined as,

$$\mathcal{B} = T_{on}/T,$$

where T_{on} is the time duration for each “on” operating mode. Similarly, T_{off} is for “off” mode. For simplicity, T_{off} is set to be the same as T_{on} . Simulations with different burst ratios \mathcal{B} are run, and the time history for the skin-friction coefficient C_f is shown in figure 6.31(b). As can be seen, when $\mathcal{B} < 2\%$, the C_f trajectory is similar to SO4 case; while when \mathcal{B} becomes larger, the C_f trajectory gets closer to

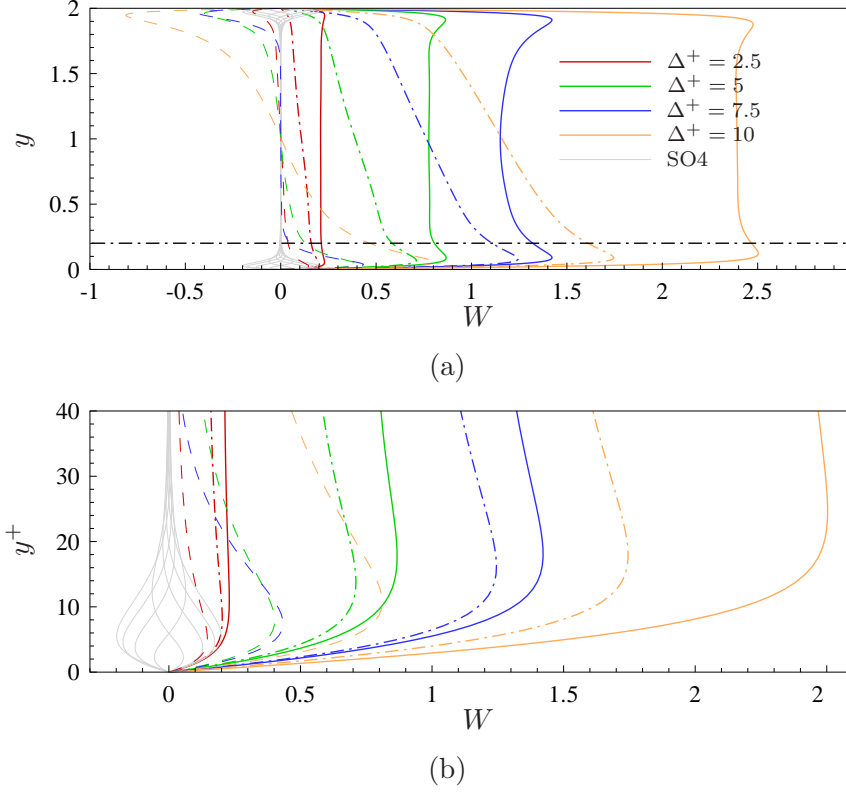


Figure 6.30: The spanwise mean velocity profiles for steady body force cases with different body force penetration depths Δ^+ and SO4 with $s^+ = 50$: (a) over the whole channel; and (b) in the near wall region, $y^+ < 40$.

SO3 case, which has a burst ratio of $\mathcal{B} = 50\%$. This suggests that a small burst ratio operation mode can achieve a similar effect to the continuous travelling wave speed in SO4 case. The advantage of SO4 is that it avoids the arc discharge between two adjacent active plasma actuators by introducing a large actuator gap, but allows a local travelling wave to inhibit the starting vortices.

Figure 6.32 shows a concept of implementing the plasma actuators device onto a car body for the drag reduction using the SO4 configuration. The plasma actuators are put on the car surfaces, aligning in the streamwise direction. The actuators are divided into groups (3 groups in the demonstration) according to the selected actuator gap s^+ . According to the \mathcal{DR} map in figure 6.14(f), the gap s^+ should be as small as possible within the manufacturing and operating restriction. The computer controls the electric bridge to create the local travelling global oscillation sequence: 1) 1 – a, 2) 2 – b, 3) 3 – c, 4) 3 – a, 5) 2 – c and 6) 1 – b; and keep each state for a time period of $TB = T \times \mathcal{B}$. Since the burst ratio

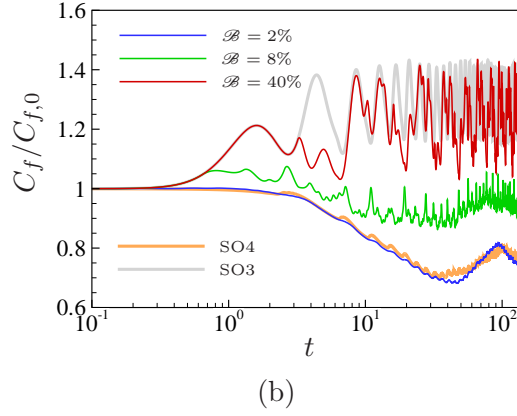
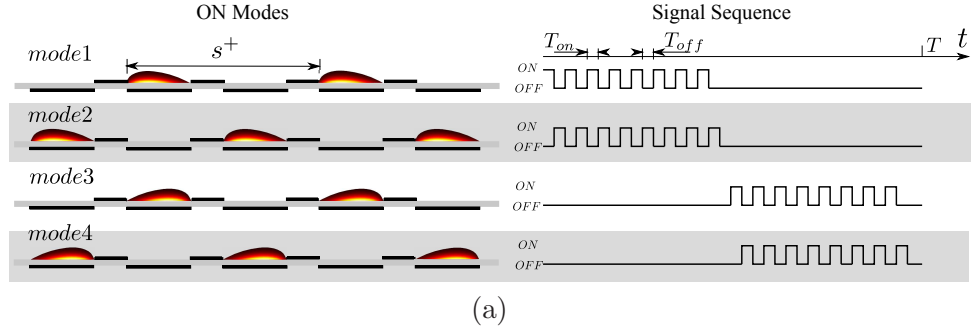


Figure 6.31: (a) Schematics of operation mode with two groups of DBD plasma actuators; (b) time history of skin-friction coefficient C_f for different burst ratio of plasma actuators.

\mathcal{B} needs to be small for a better performance (figure 6.31(b)), the switching process should be fast.

Though the idea to implement DBD plasma actuators is practical, the net energy saving is a big challenge. As has been shown in figure 6.19, there is no net energy saving for all the plasma actuator configurations considered in this study. With the consideration of the electricity efficiency of the plasma actuators, the total power spent will be even larger, and the likelihood to get a net energy saving is even smaller. From this point of view, the value of implementing plasma actuator will be lost. However, two possible solutions can still be expected: 1) a better plasma actuator configuration; 2) the pressure-drag reduction together with the skin-friction drag reduction to achieve an overall net energy saving. For the second point, it has been demonstrated that DBD plasma actuators can be used to replace the conventional vortex generators (VGs) for the flow separation control (Jukes et al., 2012), and to largely reduce the drag coefficient. The DBD-VGs are also aligned in the flow direction as in SO4 case. Therefore, on a curved air-foil surface with weak flow separation, the DBD plasma actuators used for the skin-friction

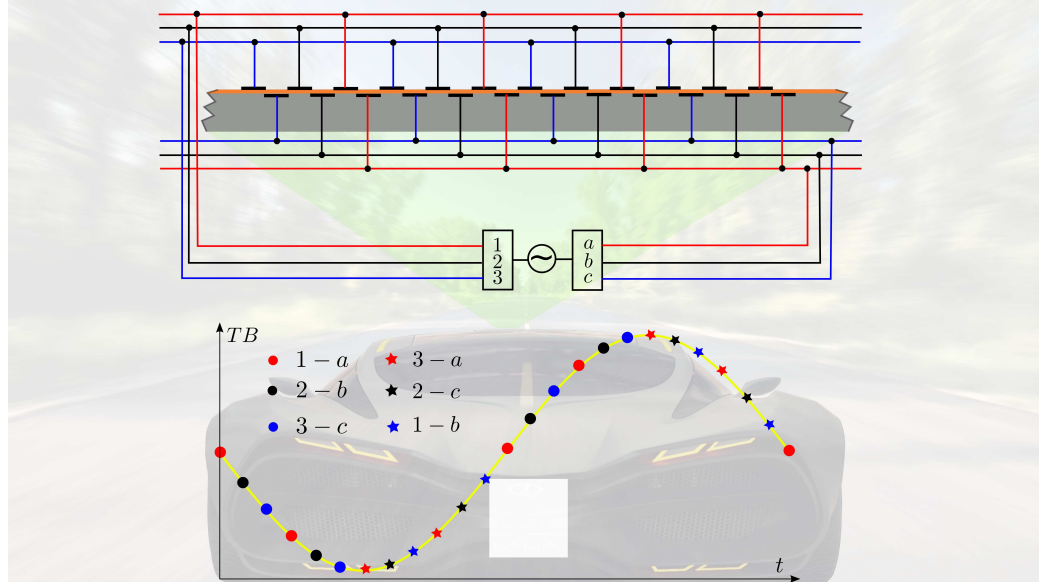


Figure 6.32: A concept of implementing DBD plasma actuators on a car body for skin-friction reduction purpose using SO4 configuration.

drag reduction may also be helpful to delay flow separation in the downstream. And this can enhance the energy saving performance of the DBD plasma actuators, and possibly gives a net energy saving.

6.8 Conclusion

Skin-friction drag reduction by DBD plasma actuators was studied in this chapter using a simple empirical DBD plasma actuator model. The plasma body force was assumed to be Rayleigh in the horizontal direction and exponential in the wall normal direction. The jet velocity profiles and the starting vortex movement were compared well with the experimental data. Even though the present empirical model had a strong simplification, it captured the main characteristics of the DBD plasma actuators well.

When the actuator gap was large, the starting vortices played the role of the quasi-streamwise vortices in a natural turbulent boundary layer flow, and quickly triggered the flow to become turbulent. However, when the actuator gap was small, the entrainment from the neighbour actuator prohibited the lift up of the starting vortices, and significantly weakened the individual streamwise rolling effect.

Six configurations were explored to generate the spanwise travelling wave and the spanwise oscillation. For the spanwise travelling wave by DBD plasma

actuators as explored by Whalley and Choi (2014), ST1 was successful in the drag reduction. The drag reduction was determined by the mean force component, thus \mathcal{DR} was not sensitive to the travelling wave speed c^+ for ST1 nor the oscillation frequency ω^+ for SO1. Moreover, due to the nature of the small wavelength and the zero mean force associated with the plasma actuators, ST2 and SO2 did not achieve any drag reduction. For the spanwise oscillation configuration (SO3) as explored by Jukes et al. (2006b), drag reduction was only observed for a small plasma actuator gap $s^+ \leq 25$. Instead, a local travelling, global oscillation configuration (SO4) was found to be successful in reducing skin-friction for a much larger plasma actuator gap ($s^+ = 150$), and it gave a maximum of $35 \pm 2\%$ drag reduction at $s^+ = 25$.

The turbulence statistics for SO4 was found to be very similar to the spanwise wall oscillation case. The Reynolds shear stress structure $u'v'$ became shorter in the streamwise direction due to the breaking up of the near wall streaks. The correlation structures for R_{uu} , R_{vv} and R_{uv} had different preferential tilting angles, which resulted in the decorrelation of the Reynolds shear stress $\overline{u'v'}^+$.

The present work demonstrated a practical way to implement the spanwise wall oscillation for the turbulent skin-friction drag reduction using DBD plasma actuators, but the net energy saving is a challenge to be solved in the future.

Chapter 7

Influence of the VLSMs at High Reynolds Numbers

We begin this chapter by extending the previously studied three spanwise motion control strategies, *i.e.*, spanwise wall oscillation, spanwise Lorentz force, and spanwise plasma actuators, to higher Reynolds numbers. The normalised skin-friction at the beginning of the control is shown in figure 7.1(a). Two features can be seen: 1) spanwise wall oscillation is more efficient than spanwise Lorentz force, and spanwise Lorentz force is more efficient than spanwise plasma force at the same Reynolds number for drag reduction (at least for the tested control parameters); 2) for the same type of control, the new equilibrium skin-friction level is higher at higher Reynolds number, indicating the \mathcal{DR} deterioration. The \mathcal{DR} deterioration can be better observed in figure 7.1(b). For all the three controls, the scaling is worse than the commonly accepted one $\mathcal{DR} \sim Re_\tau^{-0.2}$ (Touber and Leschziner, 2012) for the Reynolds number range tested.

This is a phenomenon which has been observed for a long time since Berger et al. (2000), Choi et al. (2002), Iwamoto et al. (2002) for a variety of near wall flow controls. However, the reason for the \mathcal{DR} deterioration remains unclear. The purpose to study the Reynolds number effect is to answer whether skin-friction drag reduction is still possible at the flight Reynolds number, $Re_\tau \sim O(10^4)$ (Ricco and Hahn, 2013; Deck et al., 2014) (see also appendix A for the estimation). Choi et al. (2002) gave a power law scaling, *i.e.*, $\mathcal{DR} \sim Re_\tau^{-\alpha}$, suggesting that \mathcal{DR} at high Reynolds numbers was negligible. However, the analysis results from the linearised N-S equations (Duque-Daza et al., 2012; Belan and Quadrio, 2013) and the scaling argument suggest an asymptotic \mathcal{DR} value at high Reynolds numbers (Quadrio and Gatti, 2015; Skote et al., 2015). In the present study and the study by Hurst

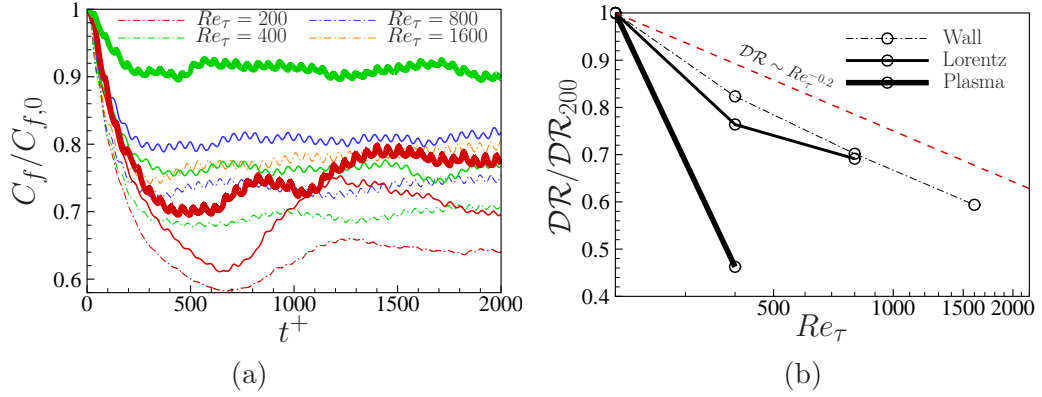


Figure 7.1: DR deterioration at high Reynolds numbers for spanwise wall oscillation (dash-dot lines, $A_w^+ = 12$, $\omega^+ = 0.06$ ($T^+ = 105$)), spanwise oscillating Lorentz force case (thin solid lines, $A_f = 0.5$, $\omega^+ = 0.06$ ($T^+ = 105$)), and plasma actuators SO4 (bold solid lines, $A_f = 1.0$, $\omega^+ = 0.06$ ($T^+ = 105$), $s^+ = 50$) for: (a) normalised skin-friction; and (b) Reynolds number scaling.

(2013), the large domain DNSs for the streamwise travelling wave of spanwise wall velocity were performed at $Re_\tau = 1600$, which is still one order of magnitude lower than the flight Reynolds number. However, recent findings suggest that the DR deterioration is linked to the outer structures as the Reynolds number increases (Touber and Leschziner, 2012; Deng et al., 2015), as sketched in figure 7.2. At the present high Reynolds numbers, $Re_\tau = 800$ and $Re_\tau = 1600$, the near wall small scales and the outer large scales are clearly separated, thus the influence of the VLSMs can be explored in more details. Particularly, for the streamwise travelling wave at $Re_\tau = 800$, a wide range of control parameters were studied, which can offer a clearer view of the DR picture, though not a whole picture yet. This chapter will focus on the streamwise travelling wave of spanwise wall velocity only, but similar results should also be expected for the high Reynolds number skin-friction control by Lorentz and plasma body forces.

7.1 Reynolds number effect

The streamwise travelling wave of spanwise wall velocity was extensively studied by Hurst (2013). The wall motion in this control is described in the formula as below,

$$W_w = A_w \sin(\kappa_x x - \omega t), \quad (7.1)$$

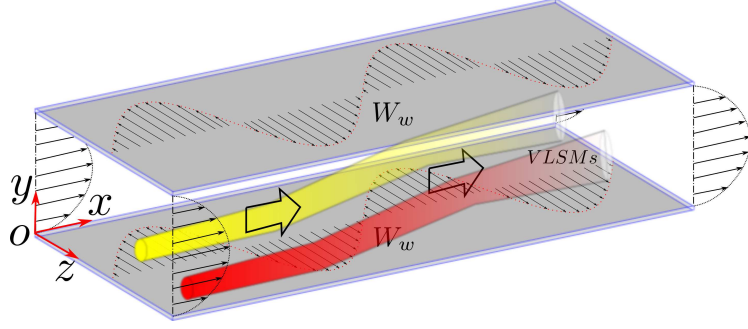


Figure 7.2: Schematics of skin-friction control by streamwise travelling wave of spanwise wall velocity at high Reynolds numbers.

where W_w is the spanwise wall velocity; A_w is the amplitude of the spanwise wall velocity; κ_x is the streamwise wavenumber; and ω is the oscillation frequency. The control parameters are fixed in wall units of the no control case, *i.e.*, $A_w^+ = 12$, $\kappa_x^+ = 0, 0.002, 0.004, 0.008, 0.012, 0.016$ and $\omega^+ = 0, 0.01, 0.02, 0.03, 0.06, 0.09, 0.12, 0.15, 0.18$. For $Re_\tau = 800$, there are 54 cases in total; and for $Re_\tau = 1600$, three control cases are considered, *i.e.*, oscillation case ($\omega^+ = 0.06, \kappa_x^+ = 0$), stationary wave case ($\omega^+ = 0, \kappa_x^+ = 0.008$) and streamwise travelling wave case ($\kappa_x^+ = 0.016, \omega^+ = 0.04$), which are the estimated optimal control cases for each type of the spanwise wall velocity based on the data at lower Reynolds numbers.

The drag reduction map at $Re_\tau = 800$ is shown in figure 7.3. The other two \mathcal{DR} maps at lower Reynolds numbers, *i.e.*, $Re_\tau = 200$ and 400 can be found in (Hurst et al., 2014). On the horizontal axis, ω^+ (or T^+) is the oscillation frequency (or period); on the vertical axis, κ_x^+ (or λ_x^+) is the streamwise wavenumber (or wavelength). The cone region along the diagonal line in the \mathcal{DR} map (bright contour) is a drag increase region, which has a wave travelling speed of $c^+ (\equiv \omega^+ / \kappa_x^+) \approx 10$, same as the convection velocity, \mathcal{U}_c^+ of the near wall structures (Kim and Hussein, 1993). Quadrio et al. (2009) offered an explanation about the drag increase in the cone region: when the streamwise wave travels at the same velocity as the near wall structures, the structures can extract energy from the wall motion and be amplified. When the relative speed between the streamwise travelling wave and the near wall structures ($\mathcal{U}_c^+ - c^+$) is large, the near wall structures can be attenuated, which is indicated by the blue coloured region, with the maximum drag reduction ($\mathcal{DR}_{max} = 40 \pm 2$, indicated by a cross symbol in the \mathcal{DR} map) appearing at $\omega^+ = 0.03, \kappa_x^+ = 0.014$ within $c^+ < 10$ region.

The horizontal axis corresponds to $\kappa_x^+ = 0$, which is for spanwise wall oscillation cases studied in chapter 4, and the vertical axis corresponds to $\omega^+ = 0$,

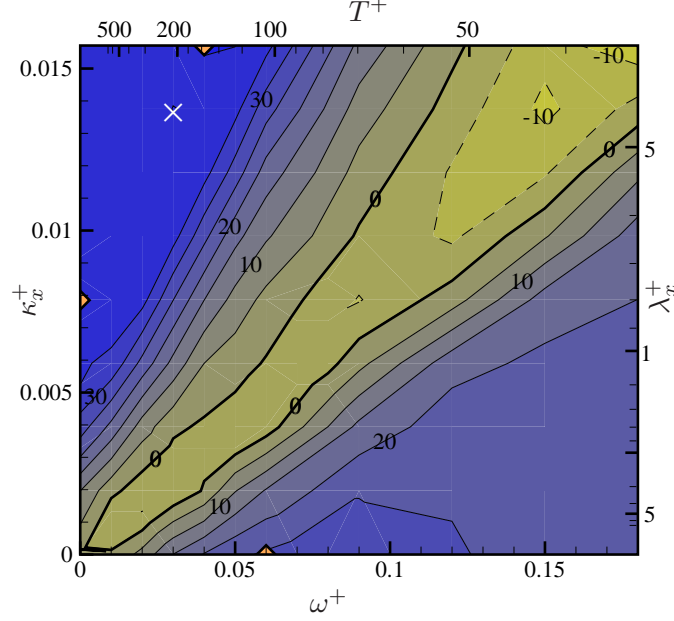


Figure 7.3: Drag reduction map at $Re_\tau = 800$. Interval level is 5. The three triangle symbols indicate the control cases at $Re_\tau = 1600$. The optimal \mathcal{DR} point at $Re_\tau = 800$ is indicated by a cross symbol.

which is for stationary wave cases. The drag reduction at four Reynolds numbers, *i.e.*, $Re_\tau = 200, 400, 800$ and 1600 are plotted for oscillation cases, stationary wave cases, streamwise travelling wave cases passing through $\kappa_x^+ = 0.016$ and streamwise travelling wave cases passing through $\omega^+ = 0.03$ (for $Re_\tau = 1600$ case, $\omega^+ = 0.04$) in figure 7.4. The drag reduction deterioration can be clearly seen for all the four plots as the Reynolds number increases from $Re_\tau = 200$ to 1600 . For instance, the \mathcal{DR} value drops from 37 ± 2 at $Re_\tau = 200$ to 22 ± 2 at $Re_\tau = 1600$ for oscillation cases at $\omega^+ = 0.06$; from 46 ± 2 at $Re_\tau = 200$ to 33 ± 2 at $Re_\tau = 1600$ for stationary wave cases at $\kappa_x^+ = 0.008$; from 45 ± 2 at $Re_\tau = 200$, $\omega^+ = 0.03$, $\kappa_x^+ = 0.016$ to 37 ± 2 at $Re_\tau = 1600$, $\omega^+ = 0.04$, $\kappa_x^+ = 0.016$ for streamwise travelling wave cases. A phenomenon observed by Hurst et al. (2014) was that the optimal control parameter is not fixed in wall units, which is very obvious for the oscillation cases (figure 7.4(a)) and stationary wave cases (figure 7.4(b)). With the optimal oscillation frequency ω_{opt}^+ indicated by arrows, ω_{opt}^+ shifts from 0.06 at $Re_\tau = 200$ to 0.07 at $Re_\tau = 400$ and to 0.08 at $Re_\tau = 800$. Similarly, the optimal wavenumber $\kappa_{x,opt}^+$ shifts from 0.006 at $Re_\tau = 200$ to 0.008 at $Re_\tau = 400$ and to 0.01 at $Re_\tau = 800$, although the peaks are broader. For the streamwise travelling wave cases, the optimal oscillation frequency at a fixed wavenumber, or the optimal wavenumber at a fixed oscillation

frequency is also shifting as shown in figures 7.4(c) and 7.4(d).

In summary, the main interests in this chapter are the two Reynolds number effects as observed by Hurst et al. (2014): 1) the \mathcal{DR} deteriorates as the Reynolds number increases; 2) the optimal oscillation frequency (and wavenumber) shifts towards a higher value for the spanwise wall oscillation (and stationary wave) as the Reynolds number increases.

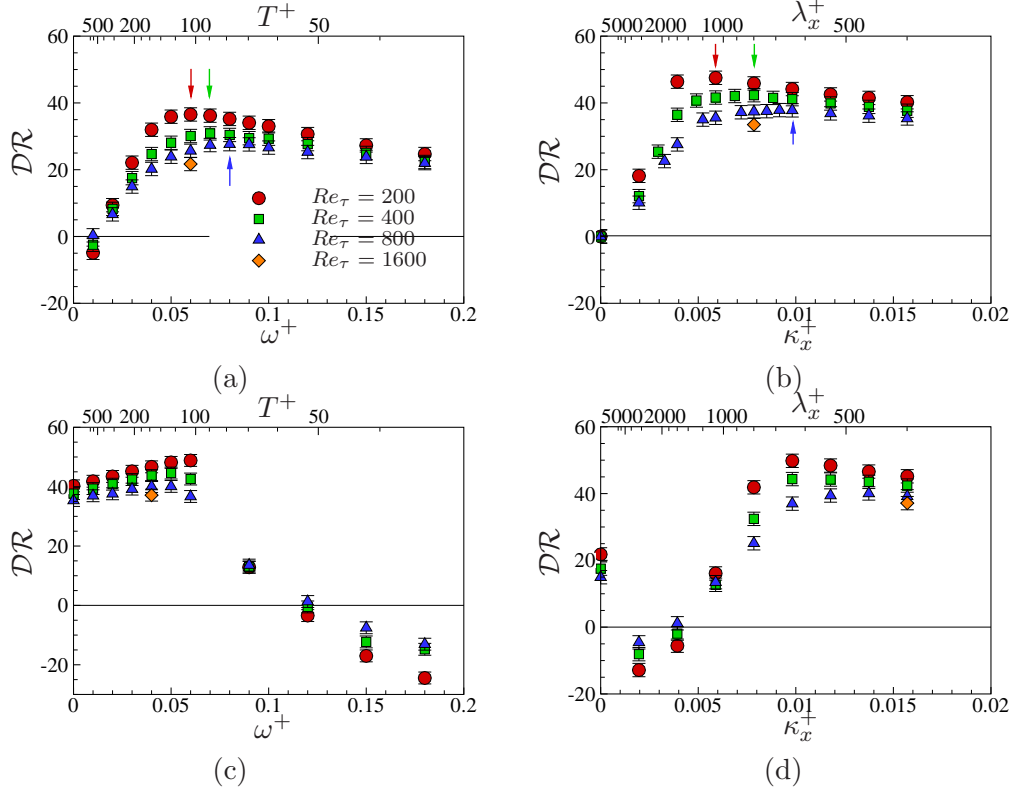


Figure 7.4: Drag reduction at four Reynolds numbers for (a) wall oscillation cases, (b) stationary wave cases, (c) streamwise travelling wave cases passing through $\kappa_x^+ = 0.016$, and (d) streamwise travelling wave cases passing through $\omega^+ = 0.03$ (for $Re_\tau = 1600$ case, $\omega^+ = 0.04$). (a)(b)(c) are adapted from Hurst et al. (2014). The arrows in (a)(b) indicate the optimal control parameters at corresponding Reynolds numbers.

7.2 Some further observations from the literature

7.2.1 VLMS definition and visualisation

The VLMSs are scaled in global units (del Álamo et al., 2006; Pujals et al., 2009), thus a convenient way to define the VLMSs is in the Fourier space. The difficulty

lies in the exact length scale to choose as a cut-off line. In the present study, the VLSMs are defined as,

$$\text{VLSMs: } \lambda_x > 3, \lambda_z > 0.5. \quad (7.2)$$

Due to the limitation of the highest Reynolds number achievable, the large scale motions (LSMs) (Adrian et al., 2000) are not distinguished from the VLSMs. $\lambda_x > 3$ and $\lambda_z > 0.5$ are the common Fourier filter sizes used in the literature (Bernardini and Pirozzoli, 2011; Wu et al., 2012). Both the length and the width of the VLSMs are constrained in the present study, this can remove the high wavenumber noise in the VLSMs, thus making the later study of the conditional sampling under the positive and the negative VLSMs regions easier. The VLSMs extracted from the Fourier filter in equation (7.2) is given in appendix G, with the comparison with the Hilbert-Huang empirical decomposition employed by Agostini and Leschziner (2014) for the VLSMs study. It shows that the present definition captures the VLSMs well.

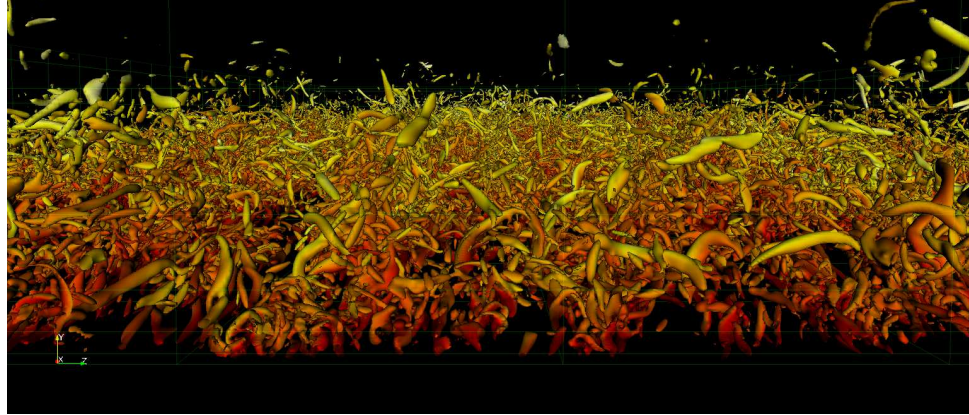
Based on the VLSMs definition in equation (7.2), for any turbulent flow property ϕ , the stochastic component ϕ' after the triple decomposition (equation (4.4)), can be used to decompose the flow into the small scales contribution, ϕ'_S and the large scales contribution, ϕ'_L . The root mean square (r.m.s.) values of ϕ' , ϕ'_L and ϕ'_S are defined as $\phi_{rms} = \sqrt{\overline{\phi'^2}}$, $\phi_{L,rms} = \sqrt{\overline{\phi'^2_L}}$ and $\phi_{S,rms} = \sqrt{\overline{\phi'^2_S}}$. Analogously to the definition of \mathcal{DR} , a relative reduction for the flow property ϕ caused by the streamwise travelling wave compared to the no control case, is defined as below,

$$\mathcal{R}(\phi) = \frac{\overline{\phi_0} - \overline{\phi}}{\overline{\phi_0}} \times 100(\%), \quad (7.3)$$

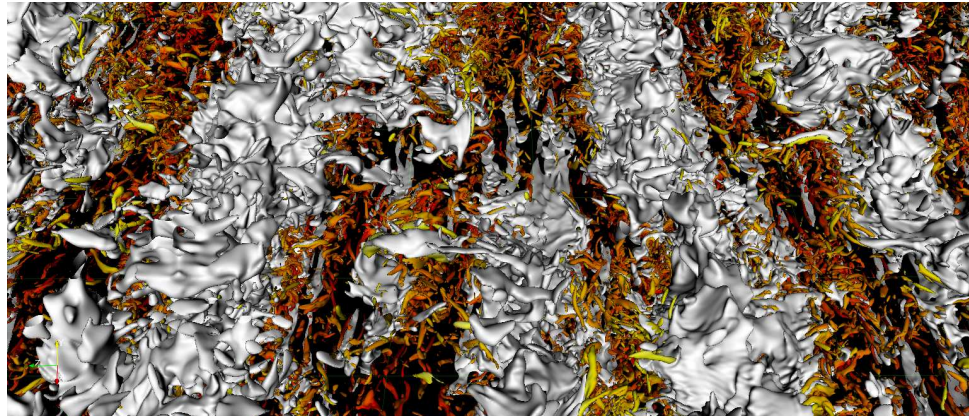
where ϕ_0 is the flow property of the no control case.

Figure 7.5 shows the visualisation of the quasi-streamwise vortices in the buffer layer and the VLSMs in the outer region. These two types of structure are scaled in the inner and the outer units of the channel flow respectively, and are associated with the inner and the outer peaks of the two-dimensional pre-multiplied streamwise velocity spectra (figure 3.15) (Hoyas and Jiménez, 2006). The VLSMs are correlated over the whole half channel height and have strong footprints in the near wall region (Bernardini et al., 2014).

Figure 7.6 visualises the streaks pattern for CH800 no control case at 8 different wall normal locations, *i.e.*, $y^+ = 5, 15, 30, 60, 150, 245, 400$ and 560 . The small streaks can be clearly identified up to $y^+ = 30$. As the xz cutting plane moves away from the wall, the streaks become longer and wider. The small high-



(a)



(b)

Figure 7.5: A 3D graphic view of (a) the near wall small scale structures (visualised by $\lambda_2^+ = -0.01$) and (b) the outer region VLSMs (white colour, visualised by streamwise velocity fluctuation $u' = 0.1$) for CH800L.

and low-speed streaks are not clear enough to be identified, but the large scale high- and low-speed streaks (super streaks) start to dominate the flow field. The VLSMs are picked up by a low-pass filter ($\lambda_x = 3$, $\lambda_z = 0.5$) in the Fourier space, and are indicated by the contour lines in figure 7.6. The VLSMs contain the largest energy in the outer region, and leave strong footprints in the near wall region.

The two types of scales can be clearly separated using the characteristic eddy defined by Moin and Moser (1989), which are shown in figure 7.7. The characteristic eddy is the first wall normal POD mode of all the spanwise wavenumbers, k_z . The mathematical formulation was given in section 3.3. At $Re_\tau = 800$, the scale separation between the outer VLSMs and the near wall small scale structures is clear. The VLSMs are shown as super streaks in figure 7.7(a). At the upper bound of the logarithmic region, $y = 0.2$, the separation between the positive and the negative

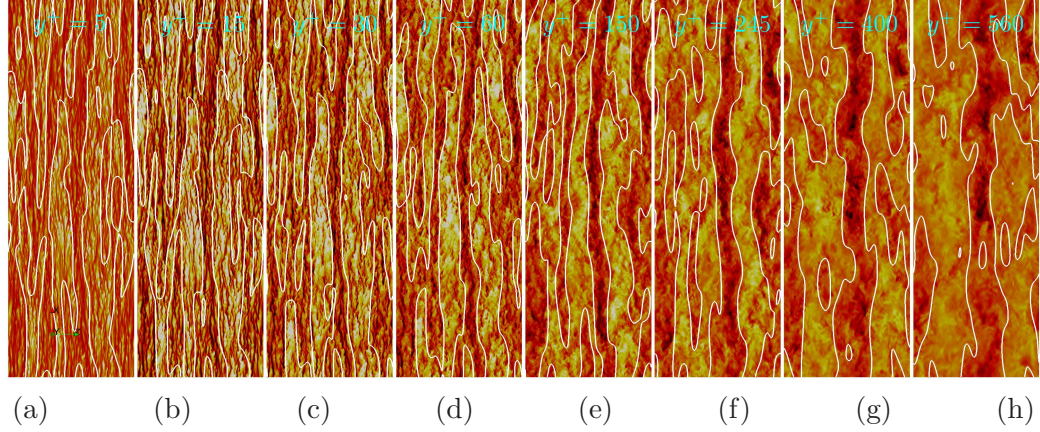


Figure 7.6: Instantaneous streamwise velocity fluctuation contour at 8 different wall normal locations, *i.e.*, $y^+ = 5, 15, 30, 60, 150, 245, 400$ and 560 . Contour lines indicate the zero level of the VLSMs. Flow goes from bottom to top. View size is 12×4 .

super streaks in the spanwise direction is $\lambda_z \approx 0.5$, but λ_z clearly increases with the wall distance, which supports the attached eddy model by Townsend (1961). The classic near wall streaks in the red box is zoomed in and shown in figure 7.7(b). As expected, the positive and negative streaks have a spanwise separation of $\lambda_z^+ \approx 50$ (Kim et al., 1987).

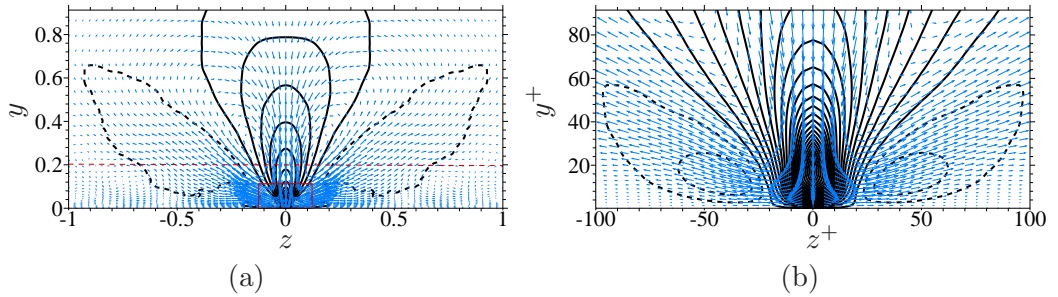


Figure 7.7: The characteristic eddy in yz plane for (a) super streaks in the outer region and (b) classic streaks in the near wall region (zoomed-in view of the box in (a)). Negative contour lines are dashed.

The footprints of the VLSMs in the wall shear stress are shown in figure 7.8 for the no control, oscillation, stationary and streamwise travelling wave cases at $Re_\tau = 1600$, where the two different scales in the wall shear stress are very clear. The positive fluctuation is much stronger than the negative one as evidenced by the highly skewed probability density distribution of the wall shear stress (Örlü and Schlatter, 2011). The footprints of the VLSMs are more clearly presented for the

three control cases due to the attenuation of the near wall streaks. The near wall streaks are very non-uniformly distributed: in some patches of the VLSMs, the near wall streaks remain strong; while in some other patches of the VLSMs, they are completely attenuated. This effect will be further studied in the following sections.

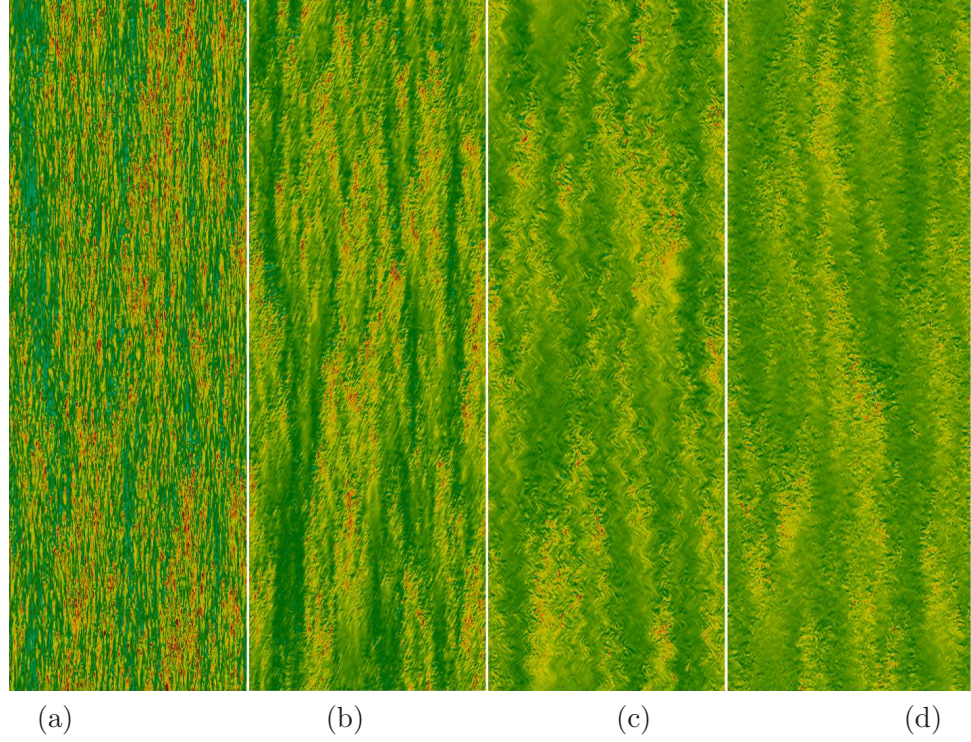


Figure 7.8: Wall shear stress fluctuation for (a) no control case, (b) oscillation case ($\omega^+ = 0.06$), (c) stationary wave case ($\kappa_x^+ = 0.008$), and (d) streamwise travelling wave case ($\kappa_x^+ = 0.016, \omega^+ = 0.06$) at $Re_\tau = 1600$. For all cases, flow goes from bottom to top. Contour levels are $[-0.05, 0.05]$.

7.2.2 Wavenumber and convection velocity modulation

It has been observed that the frequency of the small scales are modulated by the large scales in experiments (Ganapathisubramani et al., 2012; Guala et al., 2011; Baars et al., 2015). Due to the complexity of the convection velocity (del Álamo and Jiménez, 2009), there is no direct evidence about the length scale modulation of the small scales yet. To answer this question, a conditioning procedure is proposed for the present DNS data, with the focus only on the wall shear stress:

- 1) Decompose the original wall shear stress fluctuation into the small ($\tau'_{w,S}$) and the large scales ($\tau'_{w,L}$) based on equation (7.2).
- 2) Identify the positive and the negative VLSMs regions in the large scale fields as

described using the criteria of $\tau'_{w,L} > 0$ and $\tau'_{w,L} < 0$.

- 3) Assign $\tau'_{w,S}$ to be 0 under the positive (negative) VLSMs regions. The instantaneous view of the conditioning window is shown in figure 7.9(a).
- 4) Calculate the 1D pre-multiplied spectrum, $k_x \Phi_{\tau'_w \tau'_w}$ and the wavenumber-frequency spectrum, $\Phi_{\tau'_w \tau'_w}(k_x, \omega)$ for the modified small scale field, $\tau'_{w,S}$.

The conditioned 1D pre-multiplied spectrum, $k_x \Phi_{\tau'_w \tau'_w}$ is shown in figure 7.9(b) for two Reynolds numbers, *i.e.*, $Re_\tau = 800$ and 1600. No control wall units are used for the non-dimensionalisation. To check the reliability of the conditioning procedure, the spectra under the positive and the negative VLSMs regions are summarised and compared with the one without the conditioning. Only a small difference is observed between the two curves, which suggests that the condition procedure is reliable to quantify the modulation effect of the small scales from the VLSMs. The amplitude and the wavenumber modulation effects are revealed in figure 7.9(b). Along the whole wavelength, the fluctuation energy contained in the small scales under the positive VLSMs regions are higher than that under the negative VLSMs regions. The dominant peak locations are different under the positive VLSMs regions ($\lambda_x^+ \approx 650$) and the negative VLSMs regions ($\lambda_x^+ \approx 750$). This suggests that the small scales under the positive VLSMs regions are stronger but shorter than those under the negative VLSMs regions.

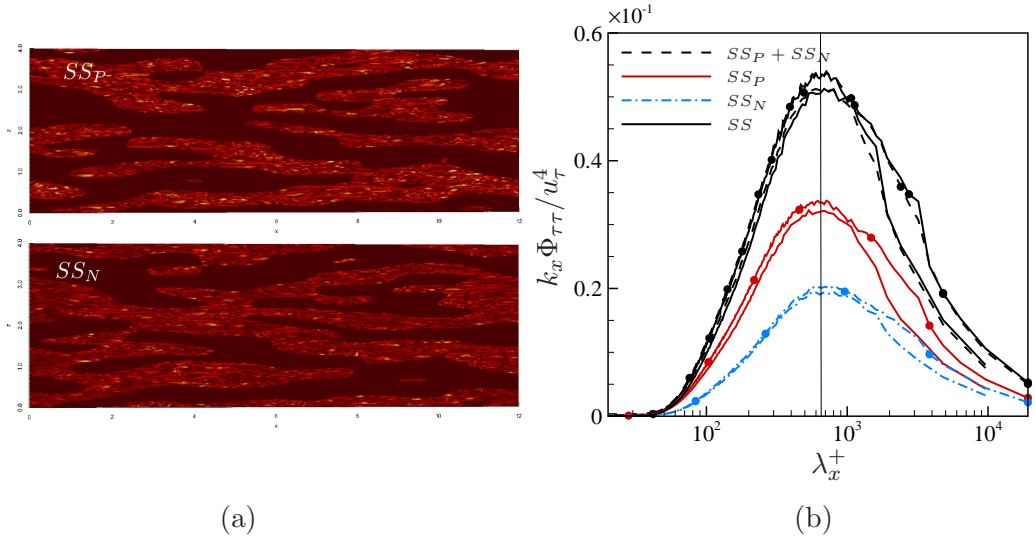


Figure 7.9: (a) Instantaneous view of the small scales under positive (SS_P) and negative (SS_N) VLSMs regions at $Re_\tau = 800$. (b) The 1D pre-multiplied spectra for SS_P and SS_N VLSMs regions. Lines with (without) symbols are for $Re_\tau = 1600$ (800).

The above procedure is also applied to the convection velocity, \mathcal{U}_c . The con-

ditioned convection velocity is shown in figure 7.10 from the wavenumber-frequency spectrum. The wavelength dependent convection velocity for the wall shear stress fluctuation is calculated using the following relationship (Jeon et al., 1999),

$$\mathcal{U}_c(k_x) = -\frac{\omega_c}{\kappa_x}, \quad \left. \frac{\partial \Phi(k_x, \omega)}{\partial \omega} \right|_{\omega=\omega_c} = 0. \quad (7.4)$$

The trajectories of ω_c are plotted with lines in figure 7.10 for both $Re_\tau = 800$ and 1600. Over the whole range shown, *i.e.*, $0 < k_x < 30$, the convection velocities for the small scales under the positive VLSMs regions are all higher than those under the negative VLSMs regions. At the dominant length scale, $\lambda_x^+ \approx 1000$ ($k_x \approx 5$ for $Re_\tau = 800$, and $k_x \approx 10$ for $Re_\tau = 1600$), the convection velocities for the small scales are $\mathcal{U}_c^+ = 10.2$ for SS_P and $\mathcal{U}_c^+ = 8.8$ for SS_N at $Re_\tau = 800$; and $\mathcal{U}_c^+ = 9.4$ for SS_P and $\mathcal{U}_c^+ = 8.4$ for SS_N at $Re_\tau = 1600$.

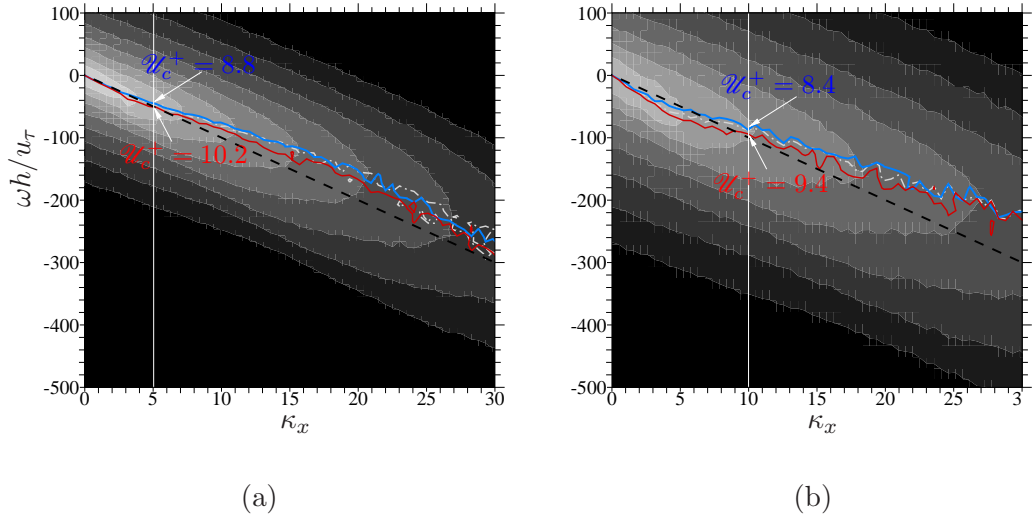


Figure 7.10: Wavenumber-frequency spectra of the wall shear stress fluctuation, τ'_w at (a) $Re_\tau = 800$ and (b) $Re_\tau = 1600$. The contour shows the spectra for no control case; red, blue and white lines are the trajectories of ω_c for SS_P , SS_N and SS , respectively. Black dash line is $\mathcal{U}_c^+ = 10$.

In summary, since $\omega = 2\pi\mathcal{U}_c/\lambda_x$, combining the modulations in both the wavelength λ_x and convection velocity \mathcal{U}_c , this means a higher frequency under the positive VLSMs regions and a lower frequency under the negative VLSMs regions. This frequency modulation agrees with the experimental finding by Ganapathisubramani et al. (2012). As illustrated by the schematics in figure 7.11, at higher Reynolds number, the effect of VLSMs becomes more important. These VLSMs are scaled in the outer units, and carry a significant amount of the streamwise Reynolds

shear stress and contribute to the wall shear stress through their footprints. In the mean time, the VLSMs define the local environment for the small scale structures in the near wall region, and modulate their strength, length, frequency, convection velocity and phase properties. Within the positive VLSMs region, the small scale structures are stronger, shorter, convecting faster and bursting more frequently than those small scale structures within the negative VLSMs regions.

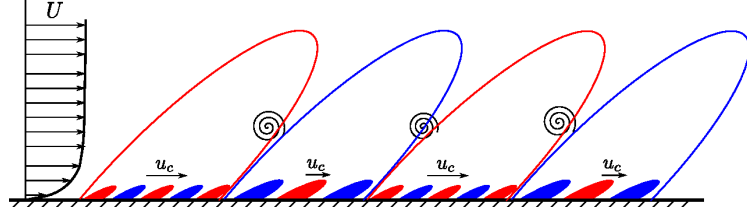


Figure 7.11: Schematics of modulation effects from VLSMs on the near wall small scale structures in a turbulent boundary layer. Contour lines represent VLSMs and shaded contour regions represent the near wall small scale structures. Red colour indicates positive fluctuation and blue colour indicates negative fluctuation.

7.2.3 Phase modulation in Stokes layer

Apart from the amplitude, frequency and wavenumber modulation effects from the VLSMs, a phase modulation was also reported (Ganapathisubramani et al., 2012). Here, an evidence of the phase modulation in the control case by spanwise wall oscillation is documented. The phase variation of the wall shear stress, τ_w was reported by Toubert and Leschziner (2012) and Hurst et al. (2014) for spanwise wall oscillation control. Here, the focus is put on the small scales, and their r.m.s. variation in the positive and the negative VLSMs regions is shown in figure 7.12. Larger variation is observed under the positive VLSMs regions. Another obvious difference of the $\tau_{w,rms,S}$ variations under the positive and the negative VLSMs regions is the phase leading in the positive VLSMs regions compared to the negative VLSMs regions.

Since the variation of $\tau_{w,rms,S}$ is mainly the reflection of the near wall structures, the dynamics of the λ_2 structures is further investigated using the coherent structure identification method described in section 3.2. An instantaneous flow field is shown in figure 7.13 for the spanwise wall oscillation case. The λ_2 structures are mainly located within the positive VLSMs regions, and this is consistent with Marusic et al. (2010). Again, this confirms that the small scale structures under the positive VLSMs regions is more difficult to be damped (see also figure 7.8).

For the spanwise wall oscillation case ($\omega^+ = 0.06$), the ensemble averaged λ_2

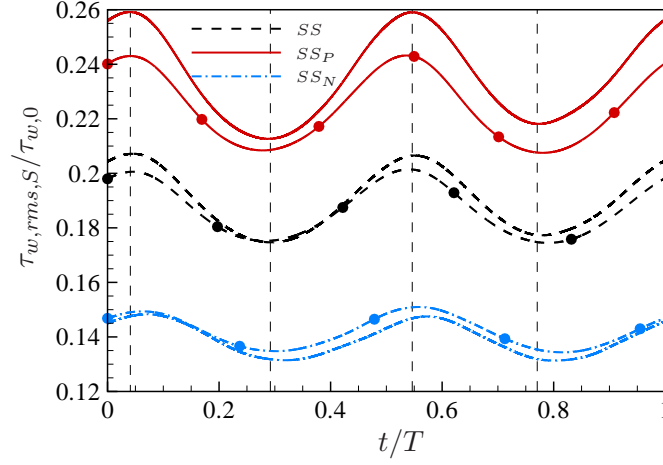


Figure 7.12: Conditional averaged small scale wall shear stress fluctuation r.m.s., $\tau_{w,rms,S}$ under positive and negative VLSMs regions. Lines with (without) symbols are for $Re_\tau = 1600$ (800).

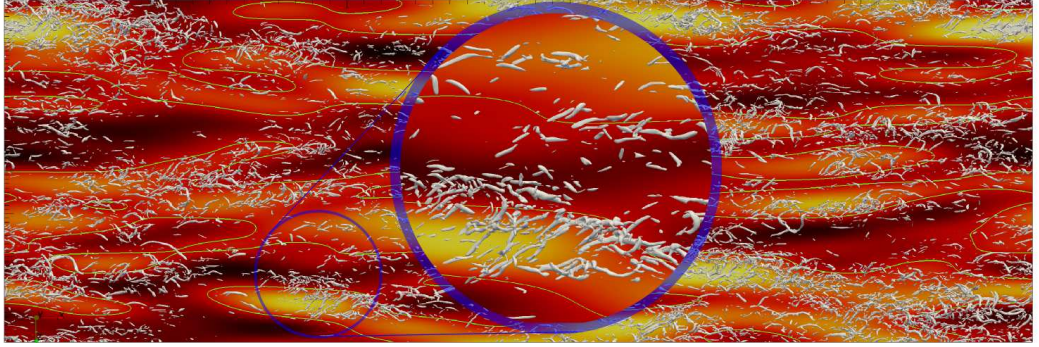


Figure 7.13: Instantaneous near wall λ_2 structures ($\lambda_2^+ = -0.02$) with the background of large scale wall shear stress fluctuation $\tau'_{w,L}$ at $Re_\tau = 800$. Light colour represents positive value and dark colour represents negative value. Contour lines are the interfaces between positive and negative VLSMs. Circle shows a zoomed-in view. Flow goes from left to right. View size is 12×4 .

structures are conditioned for 16 equally separated phases, *i.e.*, $\phi = 0 \sim 15\pi/8$ with an interval $\Delta\phi = \pi/8$. The results for the first 8 phases are shown in figure 7.14(a) at $Re_\tau = 800$. By a first glance, the structure dynamics is very similar to the spanwise wall oscillation case at the lower Reynolds number, $Re_\tau = 200$, shown in figure 4.19. The two types of λ_2 structures are strongly affected by the Stokes layer: 1) the structures gradually move away from the wall during the whole oscillation period; 2) the strength of the structures increases in one half of the period, and decreases in the second half of the period; 3) the structures change the tilting angle in the xz

plane. The generation of one new structure (between phase $\phi = 0 \sim \pi/8$ in figure 7.14(a)) corresponds to one peak of the wall shear stress variation (at $t/T \approx 0.05$ in figure 7.12).

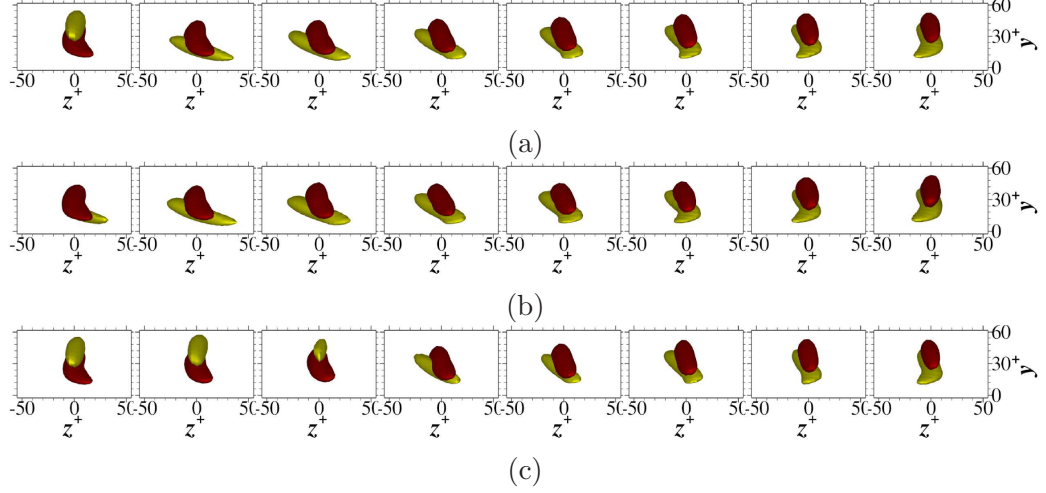


Figure 7.14: Conditional averaged near wall quasi-streamwise vortices ($\lambda_2^+ = -0.005$) for spanwise oscillation case ($\omega^+ = 0.06$) at $Re_\tau = 800$ during the first half oscillation period under (a) all regions; (b) positive VLSMs regions and (c) negative VLSMs regions. Light and dark coloured are positive and negative structures, respectively.

The two types of λ_2 structures are further conditioned based on whether they are fully within the positive or the negative VLSMs regions of the streamwise velocity fluctuation, u_L' . The conditional averaged structures are shown in figures 7.14(b) and 7.14(c) for the positive and the negative VLSMs regions, respectively. The ensemble averaged λ_2 structures are smoothed, and no obvious strength difference is captured between the same type of structures within the positive and the negative VLSMs regions, when the same threshold, $\lambda_2^+ = -0.005$ is used for the visualisation. However, a phase shift is clearly observed: the new structure starts to be generated close to the wall between phase $\phi = 0 \sim \pi/8$ within the positive VLSMs regions (figure 7.14(b)) and between phase $\phi = \pi/4 \sim 3\pi/8$ within the negative VLSMs regions (figure 7.14(c)). These two phases roughly match the two peaks, $t/T = 0.04$ and 0.1 in figure 7.12, though the peak for $\tau_{w,rms,S}$ under the negative VLSMs region is quite broad. Both results suggest that the response of the near wall small scale structures under the negative VLSMs regions is phase lag of those under the positive VLSMs regions.

The tilting angle change of the λ_2 structures is essentially due to the Stokes layer generated by the spanwise wall oscillation. This Stokes layer is conditioned in

the positive and the negative VLSMs regions (same criteria as for the conditioned λ_2 structures used above) at three different wall normal locations: the structure tail, $y^+ \approx 5$; the structure centre, $y^+ \approx 25$; and the structure head, $y^+ \approx 55$. The conditioned result is shown in figure 7.15. At the tail of the structure, the Stokes layers within the positive and the negative VLSMs regions have no difference (figure 7.15(a)), while the phase difference between the Stokes layers become obvious at the structure centre and head (figure 7.15(b)(c)). The spanwise mean velocity within the positive VLSMs regions is always phase leading of that within the negative VLSMs regions, which agrees with the phase relation observed for the small scale wall shear stress r.m.s., $\tau_{w,rms,S}$ variation (figure 7.12) and the conditioned λ_2 structure dynamics (figure 7.14).

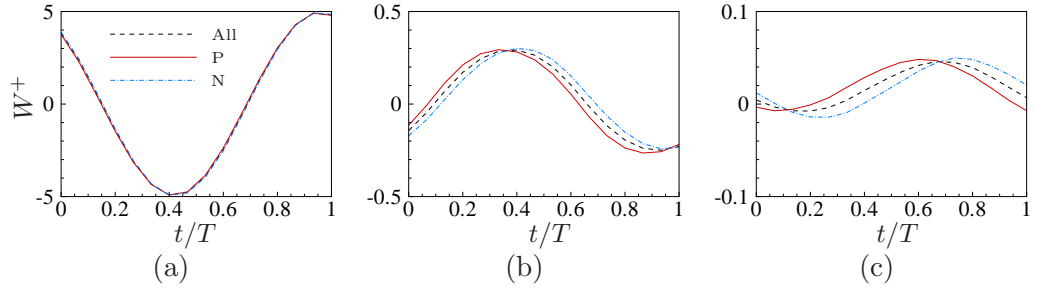


Figure 7.15: Conditioned spanwise mean velocity variation for spanwise wall oscillation ($\omega^+ = 0.06$) at $Re_\tau = 800$ within positive (P) and negative (N) VLSMs regions at: (a) $y^+ \approx 5$; (b) $y^+ \approx 25$; and (c) $y^+ \approx 55$.

7.3 Change in the \mathcal{DR} map

In this section, we focus on the wall shear stress, and perform conditional analysis for the wall shear stress statistics and the relative reduction maps. The analysis is based on 1080 instantaneous snapshots. Appendix H gives the uncertainty estimation due to the sample length used.

7.3.1 Wall shear stress spectra

The wall shear stress, τ_w is directly linked to the drag reduction, thus the two-dimensional pre-multiplied spectra are calculated to understand the contribution to the wall shear stress from different scales. Figure 7.16(a) shows the 2D pre-multiplied spectra for the wall shear stress fluctuation, τ'_w at $Re_\tau = 800$ and 1600 for the no control case. There is a strong energy peak at $\lambda_x^+ \approx 650$ and $\lambda_z^+ \approx 100$, which is associated with the near wall streaks ($\lambda_x^+ \approx 1000$ and $\lambda_z^+ \approx 100$, see figure

3.15). The spectra also show a long tail, which is more obvious at $Re_\tau = 1600$, and this can potentially form an outer peak (Örlü and Schlatter, 2011). The definition of the VLSMs in equation (7.2) is indicated by the vertical and the horizontal lines in figure 7.16(a). With this definition, the VLSMs contain around 15% of the total fluctuation $\overline{\tau_w'^2}$ for both $Re_\tau = 800$ and $Re_\tau = 1600$. The streamwise and the spanwise spectra filter sizes tend to separate the inner peak from the outer scales very well in figure 7.16(a).

The skin-friction can be split via Fukagata-Iwamoto-Kasagi identity (Fukagata et al., 2002) (equation (4.3)). By applying the second term to the co-spectrum of streamwise Reynolds shear stress, $\Phi_{u'v'}$, the mean wall shear stress from the turbulent contribution, $\overline{\tau_{w,t}}$ (non-dimensionalised by ρU_m^2) can be decomposed into wave components,

$$\begin{aligned}\overline{\tau_{w,t}} &\equiv \int_0^\infty \int_0^\infty \Phi_{\tau_w \tau_w} dk_x dk_z \equiv \int_0^\infty \int_0^\infty \left(6 \int_0^1 (y-1) \Phi_{uv}(k_x, k_z) dy \right) dk_x dk_z, \\ \overline{\tau_w} &= \frac{6}{Re} + \overline{\tau_{w,t}}.\end{aligned}\tag{7.5}$$

The derivation of the above equation is given in appendix I. The contour plot is shown in figure 7.16(b). The most energetic region deviates from the 2D pre-multiplied spectra plot for τ_w' , and resides at much larger scales. The region grows as a function of $\lambda_x \sim 3\lambda_z$ and finally tends to saturate at $\lambda_z = 1$. This suggests that the large scale motions carry a significant amount of the Reynolds shear stress and make a large contribution to the wall shear stress (Guala et al., 2006). A similar result has also been observed by Deck et al. (2014). In the following section, it will be shown how $\overline{\tau_w}$ and $\overline{\tau_w'^2}$ are correlated.

7.3.2 \mathcal{DR} deterioration rate

It is noticed that the \mathcal{DR} deterioration is stronger when Reynolds number increases from $Re_\tau = 200$ to $Re_\tau = 400$ than from $Re_\tau = 800$ to $Re_\tau = 1600$. To understand this, the wall oscillation case at $\omega^+ = 0.06$, and the stationary wave case at $\kappa_x^+ = 0.008$ for all four Reynolds numbers are chosen for analysis. Following the approach by Hurst et al. (2014), the contribution to \mathcal{DR} from the inner and outer regions are quantified. Figure 7.17 shows the \mathcal{DR} contribution from the wall oscillation and the stationary wave cases. The two plots are very similar, with the contribution from the outer structures remains almost constant when the Reynolds number increases

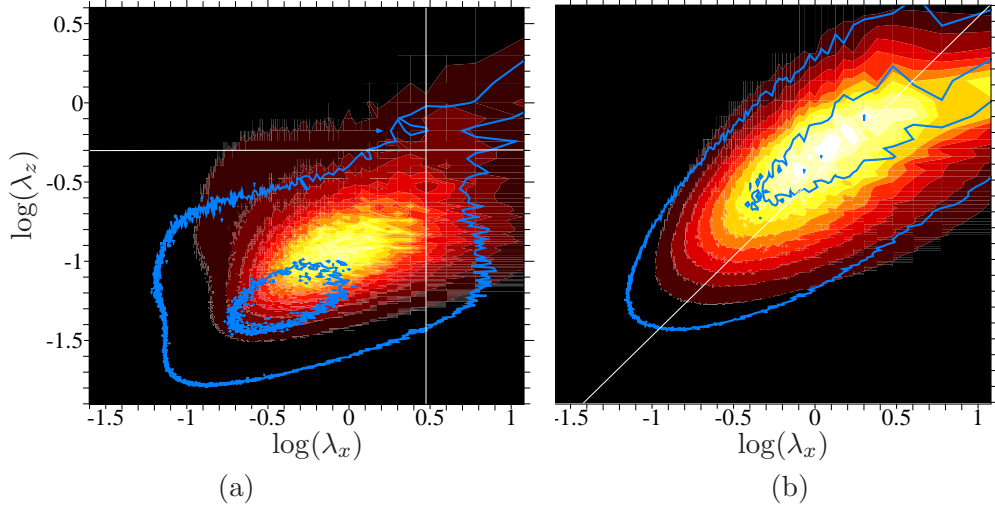


Figure 7.16: 2D pre-multiplied spectra for (a) wall shear stress fluctuation, $k_x k_z \Phi_{\tau'_w \tau'_w}$ and (b) wall shear stress mean component, $k_x k_z \Phi_{\tau_w \tau_w}$. The vertical and horizontal lines indicate $\lambda_x = 3$, $\lambda_z = 0.5$ in (a) and diagonal line indicates $\lambda_x = 3\lambda_z$ in (b). The shaded contour is for $Re_\tau = 800$, and the contour lines are for $Re_\tau = 1600$, with only the 60% and 10% levels of the maximum value shown.

from $Re_\tau = 200$ to 1600. However, the \mathcal{DR} deterioration is very strong for the inner region. This is consistent with the finding by Iwamoto et al. (2002), who showed that the \mathcal{DR} deterioration was only strong for $Re_\tau < 300$ in their opposition control.

At $Re_\tau = 400$, though there is no clear scale separation, the outer structures are still very energetic, which can be seen from the 2D pre-multiplied spectra in figure 3.15. Figure 7.18 shows the contribution to the skin friction from the smallest length scale to a cut off length scale λ_z , with the definition of $C(\lambda_z)$ given as below,

$$C(\lambda_z) = \frac{1}{\overline{\tau_{w,t}}} \int_{2\pi/\lambda_z}^{\infty} \int_0^{\infty} \Phi_{\tau_w \tau_w}(k_x, k_z) dk_x dk_z. \quad (7.6)$$

Clearly, majority of the mean wall shear stress contribution comes from the length scale between $\lambda_z^+ = 100$ and $\lambda_z = 1$, as found by de Giovanetti et al.. This is the case for the lowest Reynolds number $Re_\tau = 200$ as well.

The pre-multiplied spectra for the mean wall shear stress, $k_z \Phi_{\tau_w \tau_w}(k_z)$ are plotted in figure 7.19(a) for both the control and the no control cases. Unlike the inner scaling of the wall shear stress fluctuation spectra as shown in figure 7.9(b), the mean wall shear spectra do not scale in wall units, and the dominant peak location keeps increasing in wall units as the Reynolds number increases. Since the

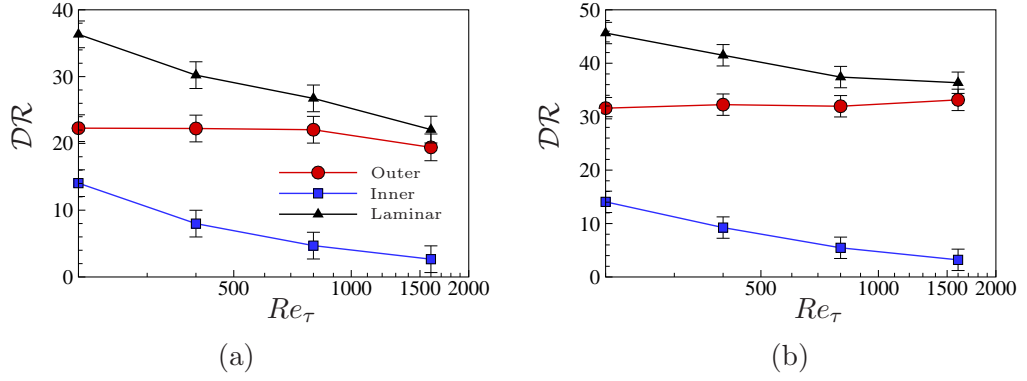


Figure 7.17: \mathcal{DR} contribution from the inner and outer regions for: (a) wall oscillation at $\omega^+ = 0.06$; and (b) stationary wave at $\kappa_x^+ = 0.008$.

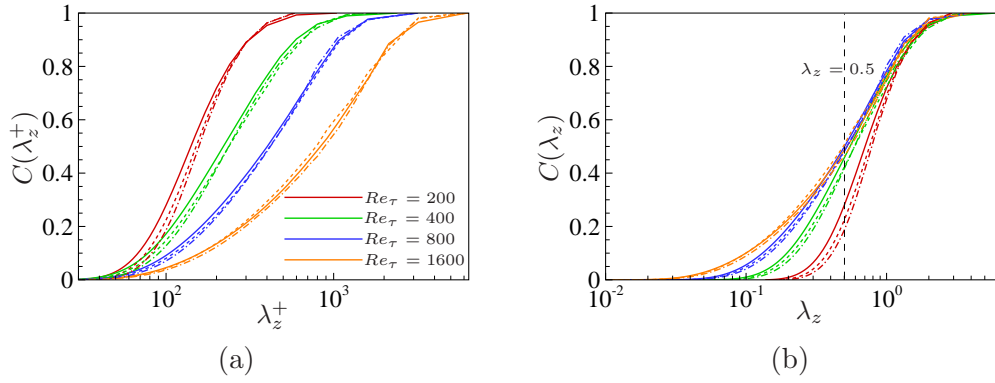


Figure 7.18: Mean wall shear stress contribution from spanwise length scales below a cut off value in: (a) wall units, and (b) outer units, for four different Reynolds numbers. Solid lines are no control cases; dashed lines are wall oscillation cases; and dash-dotted lines are stationary wave case.

level of each curve represents the actual contribution to the mean wall shear stress, the relative change of $k_z \Phi_{\tau_w \tau_w}(k_z)$ from the no control case to the control case gives the \mathcal{DR} values, which are plotted in figure 7.19(b) for both the wall oscillation case and the stationary wave case. In this plot, scales with $\lambda_z^+ < 30$ are not shown due to the high noise level. The high fluctuation at the largest wavelength is due to the less enough samples. It is clear to see that for all the cases in the region $\lambda_z^+ < 400$, \mathcal{DR} decreases monotonically as λ_z^+ increases. For the region $\lambda_z^+ > 400$, though the data is noisy, it suggests a constant \mathcal{DR} level at $Re_\tau = 400, 800$ and 1600 . The increase of \mathcal{DR} at the largest wavelength end for $Re_\tau = 200$ might be due to a low Reynolds number effect. This suggests an expected result that larger scale structures are less effectively controlled than the smaller one, since larger scale structures are

further away from the wall (Flores and Jiménez, 2010; Hwang, 2013). A closer look at the \mathcal{DR} change with the Reynolds number for the wall oscillation case and the stationary wave case, suggests a very similar result as in figure 7.17, namely the \mathcal{DR} deteriorates rate is faster in smaller scale structures, which are closer to the wall. To study the reason for a power law (or log law) for the \mathcal{DR} scaling of the Reynolds number is an interesting question to explore in the future. In the present study, we only focus on the two highest Reynolds numbers explored, *i.e.*, $Re_\tau = 800$ and 1600, which have less low Reynolds number effect.

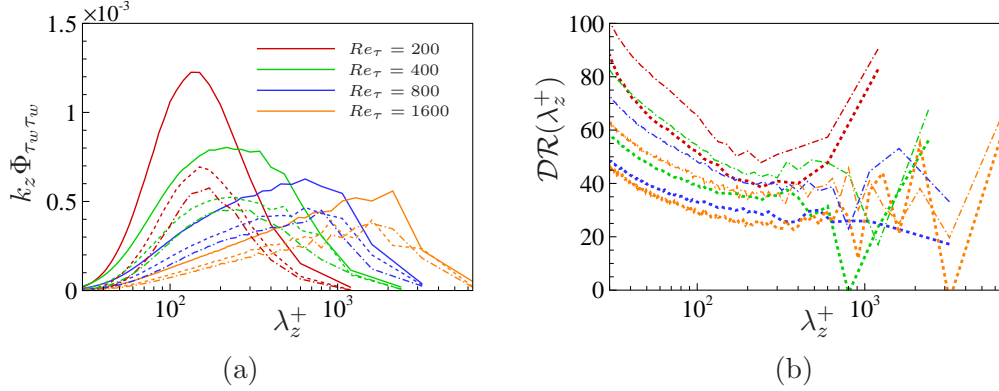


Figure 7.19: (a) Pre-multiplied spectra for mean wall shear stress $\overline{\tau_w}$; (b) \mathcal{DR} contribution from different spanwise length scales.

7.3.3 Influence of the superimposition effect

Figures 7.20 and 7.21 shows the 1D pre-multiplied spectra of τ_w' for all the control cases at $Re_\tau = 800$ and 1600. Comparing to the no control case in the spanwise spectra (figure 7.20), it is clear that majority of the spectrum change by the control comes from the small scales (inner spectrum peak). For the large scales (outer spectrum peak), there are two notable phenomena: 1) the outer peak amplitude is affected by the control, even though the corresponding VLSMs are far away from the wall; 2) the variation of the outer peak amplitude is not in phase with that of the inner peak. For instance, at $\omega^+ = 0.03$, $\kappa_x^+ = 0$, $Re_\tau = 800$, the inner peak is significantly weakened, while the outer peak is strengthened instead. In the streamwise spectra (figure 7.21), the length scales, λ_x^+ associated with the inner peak reduces significantly by the control, even for the drag increase cases, corresponding to the breaking up of the near wall streaks (Choi et al., 1998).

A clearer view of the wall shear stress fluctuation reduction $\mathcal{R}(\tau_w'^2)$ (see equation (7.3) for the definition) is shown in figure 7.22 in the same format as the \mathcal{DR} map

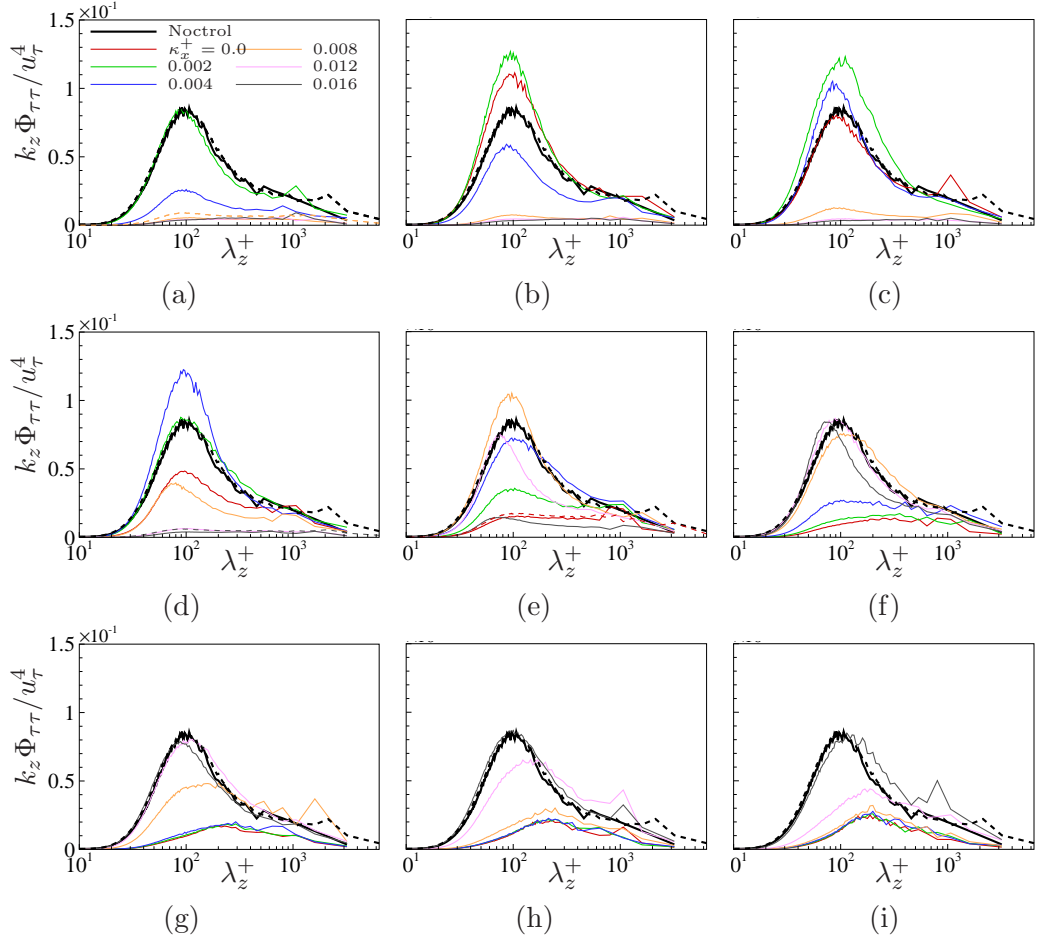


Figure 7.20: 1D pre-multiplied spectra for wall shear stress fluctuation, τ_w' as a function of spanwise wavelength λ_z^+ at different oscillation frequencies: (a) $\omega^+ = 0$; (b) $\omega^+ = 0.01$; (c) $\omega^+ = 0.02$; (d) $\omega^+ = 0.03$; (e) $\omega^+ = 0.06$; (f) $\omega^+ = 0.09$; (g) $\omega^+ = 0.12$; (h) $\omega^+ = 0.15$ and (i) $\omega^+ = 0.18$. Solid lines are for $Re_\tau = 800$, and dashed lines are for $Re_\tau = 1600$. The no control cases at the two Reynolds numbers are indicated by bold black lines in all the plots.

(figure 7.3). The value of $\overline{\tau_w'^2}$ is the integration of each curve along the wavenumber in figures 7.20 and 7.21. By comparing figure 7.22(a) and figure 7.3, a high correlation between $\mathcal{R}(\tau_w'^2)$ and \mathcal{DR} value is observed, though the actual changes are much larger for $\mathcal{R}(\tau_w'^2)$. The high correlation between $\mathcal{R}(\tau_w'^2)$ and \mathcal{DR} value is not surprising, because higher $\mathcal{R}(\tau_w'^2)$ means that turbulent structures are more strongly suppressed, thus corresponding to a higher drag reduction. Negative $\mathcal{R}(\tau_w'^2)$ value is located in the drag increase region with a travelling wave speed of $c^+ \approx 10$, and this is also where the turbulent structures are most amplified. The reduction of $\overline{\tau_w'^2}$ in the large scales, $\mathcal{R}(\tau_{w,L}'^2)$ and in the small scales, $\mathcal{R}(\tau_{w,S}'^2)$ are shown in figures 7.22(b)

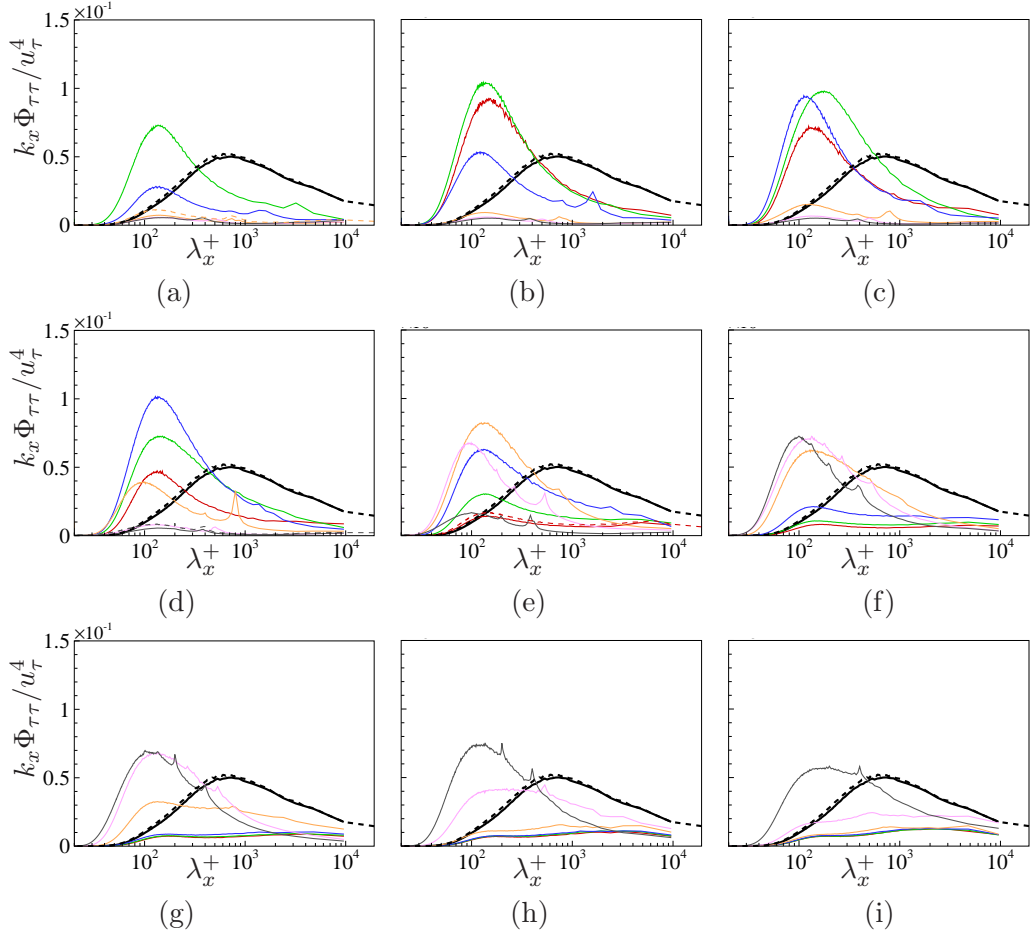


Figure 7.21: Same as in figure 7.20, but for streamwise wavelength, λ_x^+ .

and 7.22(c), respectively. A clear difference in the structure amplified region (yellow coloured) is observed. For the large scales, the most amplified region corresponds to a streamwise travelling wave speed of $c^+ > 10$, which also appears to be streamwise wavelength dependent; while for the small scales, the amplified region corresponds to a streamwise travelling wave speed of $c^+ \approx 8$. This suggests that both the small and the large scales can be amplified by the streamwise travelling wave; similarly, they can also be attenuated by the streamwise travelling wave. The large scales resident much further away from the wall (figure 7.7(a)), but a significant amount of them are attached to the wall, thus the control in the near wall region can still affect those large scale structures (del Álamo et al., 2006). Since the VLSMs are amplified in the regions $c^+ > 10$, this may explain why the optimal drag reduction case appears in the region of $c^+ < 10$ rather than $c^+ > 10$ as reported in figure 7.3 of the present study and also in figure 2 by Quadrio et al. (2009). Moreover,

it also sheds light on why the drag reduction deteriorates stronger for the optimal spanwise wall oscillation cases than the optimal stationary wave cases, as found by Hurst et al. (2014).

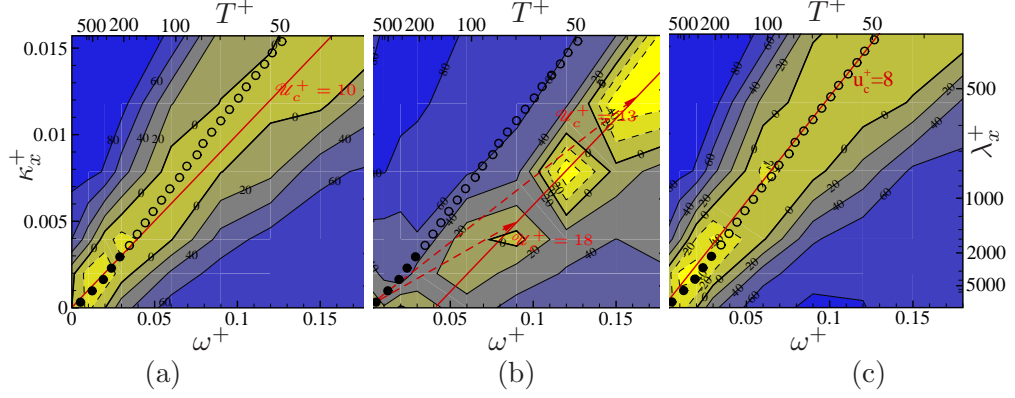


Figure 7.22: Maps for wall shear stress fluctuation reduction for: (a) all scales, $\mathcal{R}(\tau_w'^2)$; (b) large scales, $\mathcal{R}(\tau_{w,L}'^2)$; and (c) small scales, $\mathcal{R}(\tau_{w,S}'^2)$. Circles are the streamwise wavelength dependent convection velocity from figure 7.23(b): $\lambda_x < 3$ for closed circles and $\lambda_x > 3$ for open circles.

The observation of two different streamwise travelling wave speeds for the most amplified region in $\mathcal{R}(\tau_{w,L}'^2)$ and $\mathcal{R}(\tau_{w,S}'^2)$ maps, is actually not surprising, since del Álamo and Jiménez (2009) has shown the convection velocity of the three velocity components, *i.e.*, u' , v' and w' are wavelength dependent. The formula proposed by del Álamo and Jiménez (2009) for the wavelength dependent convection velocity calculation as below,

$$\mathcal{U}_c(k_x, k_z) = -\frac{Im\langle\hat{\phi}^*\partial_t\hat{\phi}\rangle}{k_x\langle|\hat{\phi}|^2\rangle}, \quad (7.7)$$

where $\hat{\cdot}$ is the Fourier coefficient, \cdot^* is the complex conjugate, $\langle\cdot\rangle$ represents the ensemble average and Im is the imaginary part. The same method is used to calculate the convection velocity for τ_w' at $Re_\tau = 800$ and 1600 for the no control cases. The wavelength dependent convection velocity of τ_w' is shown in figure 7.23 in both 2D and 1D formats. In figure 7.23(a), the streamwise and spanwise wavelength dependent convection velocity of τ_w' (shaded contour) at $Re_\tau = 800$ is compared with that of the streamwise velocity fluctuation on the wall (contour lines) calculated from the semi-empirical model by del Álamo and Jiménez (2009) at $Re_\tau = 950$. A good agreement can be seen, especially in the large streamwise and spanwise wavelengths region. By integrating the convection velocity in figure 7.23(a) along the spanwise direction, a streamwise wavelength dependent convection velocity for τ_w' is shown in figure 7.23(b) for both $Re_\tau = 800$ and 1600 , together with the data from Jeon et al.

(1999) at $Re_\tau = 180$. A streamwise wavelength dependent convection velocity of τ'_w is also suggested by Jeon et al. (1999), where the wavenumber-frequency spectrum was used to determine the convection velocity (equation (7.4)), thus the more noisy of the data. When the convection velocities are scaled in wall units, it shows a good collapse between the two Reynolds numbers studied, especially for the near wall dominant structure range, *i.e.*, $\lambda_x^+ \approx 10^3$. There is a plateau for the convection velocity, which is around $\mathcal{U}_c^+ \approx 8$ for $10^2 < \lambda_x^+ < 10^3$, and this appears to agree well with the most amplified region of $\tau'_{w,S}$ in figure 7.22(c). For the rest of the wavelength, *i.e.*, $\lambda_x^+ < 10^2$ and $\lambda_x^+ > 10^3$, the convection velocity shows a strong wavelength dependency. This trend is also suggested by the most amplified region of $\tau'_{w,L}$ shown in figure 7.22(b), where a single convection velocity can not be used to describe the most amplified region of the VLSMs in the map.

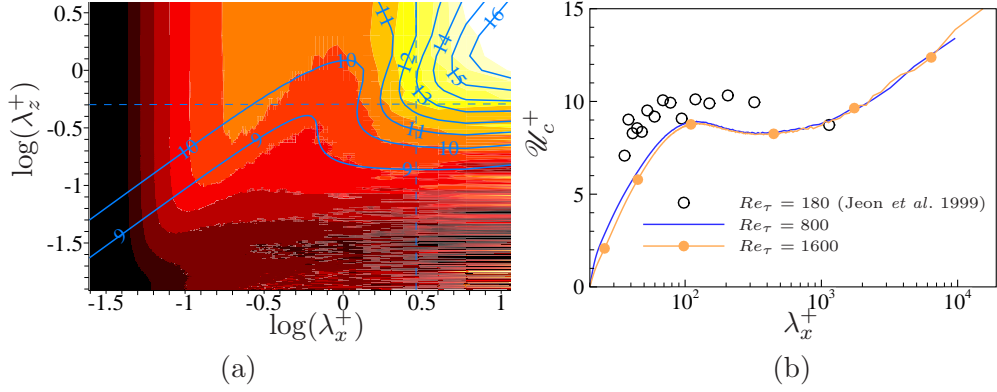


Figure 7.23: Wavelength dependent convection velocity of wall shear stress fluctuation, τ'_w in (a) 2D format for $Re_\tau = 800$, and (b) 1D format for $Re_\tau = 800$ and 1600. The contour lines in (a) is from the semi-empirical model by del Álamo and Jiménez (2009), and the vertical and horizontal dash lines correspond to $\lambda_x = 3$ and $\lambda_z = 0.5$ respectively.

The correlation between \mathcal{DR} and $\tau'_{w,rms}$ is plotted in figure 7.24 for the small scales and the large scales. Despite the scattering of the data, the difference between the large scales and the small scales can be clearly seen. As expected, majority of the change of τ'_w comes from the small scales, $\tau'_{w,S}$, which are closer to the wall and easier to be modulated by the wall motion. The decreasing rate of τ'_w against \mathcal{DR} is much slower for the large scales $\tau'_{w,L}$ compared with the small scales $\tau'_{w,S}$. The trend of the data in small scales indicated by the straight dashed line suggests a limit of the drag reduction by purely damping the small scales. The upper bound of the drag reduction value is around 55%. The data also suggests an asymptotic behaviour for the large scales in the high \mathcal{DR} region, where weakening the large

scales is as efficient as that for the small scales. Overall, the large scale structures can be partially affected by the streamwise travelling wave, but the control on the large scales is less effective than that on the small scales. This explanation for the drag reduction deterioration is in line with the proposal by Touber and Leschziner (2012) for the spanwise wall oscillation case at $Re_\tau = 500$, and later supported by Deng et al. (2015) for the opposition control at $Re_\tau = 1000$. It has to be mentioned that the analysis for both Touber and Leschziner (2012) and Deng et al. (2015) were based on a single control case in the low \mathcal{DR} region only.

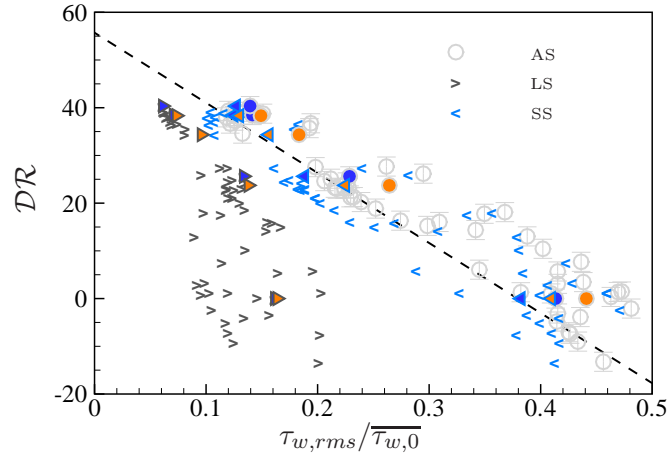


Figure 7.24: Correlation between drag reduction \mathcal{DR} and wall shear stress r.m.s., $\tau_{w,rms}$ for all 54 cases on the drag reduction map at $Re_\tau = 800$ for all scales (AS), large scales (LS) and small scales (SS). The orange colour filled symbols are cases at $Re_\tau = 1600$ (corresponding cases at $Re_\tau = 800$ are indicated by blue colour filled symbols). The trend of the small scales is indicated by a black dashed line.

7.3.4 Influence of the modulation effect

VLSMs define the local environment for the small scale structures, and modulate the behaviours of the small scale structures (Hutchins and Marusic, 2007a). In this section, the modulation effect on the small scales of τ'_w is going to be quantified. The positive and negative VLSMs regions are distinguished by the red and blue islands in figure 7.25, which represent 30% of the extreme positive and the extreme negative VLSMs in the probability density function of $\tau'_{w,L}$. The total wall shear stress τ_w and the small scale wall shear stress fluctuation $\tau'^2_{w,S}$ are sampled within the positive and the negative VLSMs regions for all the 54 cases, and the relative

reduction for any turbulent property ϕ under these two regions are defined as,

$$\begin{aligned}\mathcal{R}_P(\phi) &= \frac{\overline{\phi_{0,P}} - \overline{\phi_P}}{\overline{\phi_{0,P}}} \times 100(\%); \\ \mathcal{R}_N(\phi) &= \frac{\overline{\phi_{0,N}} - \overline{\phi_N}}{\overline{\phi_{0,N}}} \times 100(\%),\end{aligned}\tag{7.8}$$

where subscript P (or N) represents under the positive (or negative) VLSMs regions.

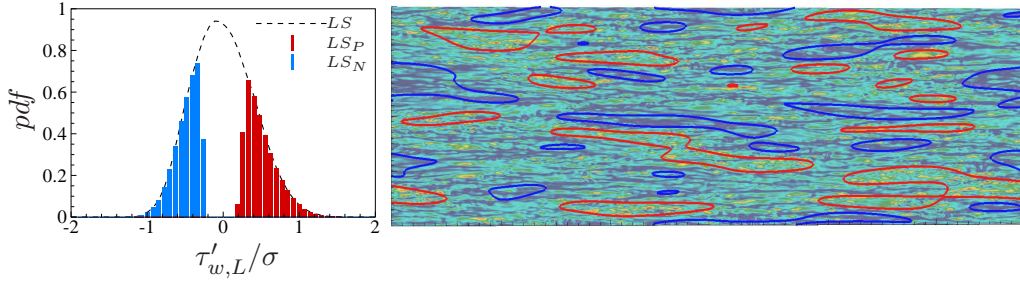


Figure 7.25: The probability density function of the VLSMs and the extreme positive (30%, red) and extreme negative (30%, blue) VLSMs regions in the instantaneous wall shear stress fluctuation field (view size 12×4).

The decomposed wall shear stress τ_w reduction maps under the positive ($\mathcal{R}_P(\tau_w)$) and the negative ($\mathcal{R}_N(\tau_w)$) VLSMs regions are shown in figures 7.26(a) and 7.26(b). These two maps still keep the main features of the original drag reduction map (figure 7.3). However, two differences between the two drag reduction maps can be seen: 1) the drag increase region (yellow) for $\mathcal{R}_P(\tau_w)$ map is narrower than that for the $\mathcal{R}_N(\tau_w)$ map; 2) the optimal drag reduction value (left top corner in the map) is higher in $\mathcal{R}_P(\tau_w)$ map than in $\mathcal{R}_N(\tau_w)$ map: $\mathcal{R}_{P,max}(\tau_w) = 43 \pm 2$ and $\mathcal{R}_{N,max}(\tau_w) = 35 \pm 2$ at $\omega^+ = 0.03$, $\kappa_x^+ = 0.012$. The \mathcal{DR} value difference between the conditioned \mathcal{DR} maps is shown in figure 7.26(c). There is a remarkable similarity between this map and the map shown in figure 7.22(b), thus the $\mathcal{R}_P(\tau_w) - \mathcal{R}_N(\tau_w)$ map shows the signature of the VLSMs. Generally, more \mathcal{DR} comes from the positive VLSMs regions, except the region where the VLSMs are amplified. This positive $\mathcal{R}_P(\tau_w) - \mathcal{R}_N(\tau_w)$ region also exists at $Re_\tau = 1600$ by checking the decomposed drag reduction value for the three control cases (table 7.1): the oscillation case is within the VLSMs amplified region, while the stationary and the streamwise travelling wave cases are outside.

Figures 7.26(d) and 7.26(e) show the conditioned reduction maps for the small scale wall shear stress fluctuation $\tau'^2_{w,S}$ under the positive ($\mathcal{R}_P(\tau'^2_{w,S})$) and the negative ($\mathcal{R}_N(\tau'^2_{w,S})$) VLSMs regions, respectively. And the difference map

Table 7.1: Conditioned wall shear stress, $\overline{\tau_w}$ and relative drag reduction, \mathcal{DR} under positive and negative VLSMs regions. Numbers outside (inside) brackets are for $Re_\tau = 800$ (1600).

	All regions	Positive regions	Negative regions
$C_f \times 10^{-3}$			
No control	5.22 (4.35)	6.32 (5.28)	4.19 (3.52)
Oscillation	3.88 (3.38)	4.86 (4.27)	3.06 (2.40)
Stationary wave	3.21 (2.86)	3.71 (3.38)	2.78 (2.39)
Travelling wave	3.17 (2.73)	3.65 (3.10)	2.77 (2.31)
$\mathcal{DR} \%$			
Oscillation	25 (24) ± 2	23 (19) ± 2	27 (32) ± 2
Stationary wave	39 (34) ± 2	42 (36) ± 2	34 (32) ± 2
Travelling wave	39 (38) ± 2	42 (41) ± 2	34 (34) ± 2

$\mathcal{R}_P(\tau_{w,S}'^2) - \mathcal{R}_N(\tau_{w,S}'^2)$ is shown in figure 7.26(f). Here the discontinuity in the maps is due to the resolution in the $\omega^+ - \kappa_x^+$ space, thus the focus is only put on the trend suggested by figure 7.26(f). Clearly, the small scale wall shear stress fluctuation $\tau_{w,S}'^2$ under the negative VLSMs regions $\mathcal{R}_N(\tau_{w,S}'^2)$ is modulated stronger than that under the positive VLSMs regions $\mathcal{R}_P(\tau_{w,S}'^2)$, *i.e.*, a stronger attenuation for the drag reduction cases and a stronger amplification for the drag increase cases. This result is indeed supported by figure 7.8, where for all the three drag reduction cases, the small scale wall shear stress fluctuation remains strong under the positive VLSMs regions, while the small scales under negative VLSMs regions is almost invisible. It is not clear yet why the small scales under the positive VLSMs regions are more stable, and more difficult to be damped. One possible explanation is that those small scales within the positive VLSMs regions are under the down wash side of the large scale motions, thus more energy is transferred from the outer scales into the small scales. Deng et al. (2015) also reported the small scales under the positive VLSMs regions are less suppressed than those under the negative VLSMs regions for the opposition control. The authors also argued that the overall \mathcal{DR} under the negative VLSMs regions was higher than that under the positive VLSMs regions. However, this is only true when the VLSMs are amplified; and the opposite trend appears when the VLSMs are suppressed (figure 7.26(c)).

In general, majority of the drag reduction comes from the attenuation of the small scales under the VLSMs regions. Since the small scale structures under the positive and the negative VLSMs regions are very different, in terms of their intrinsic strength, length, frequency and convection velocity (section 7.2.2), while

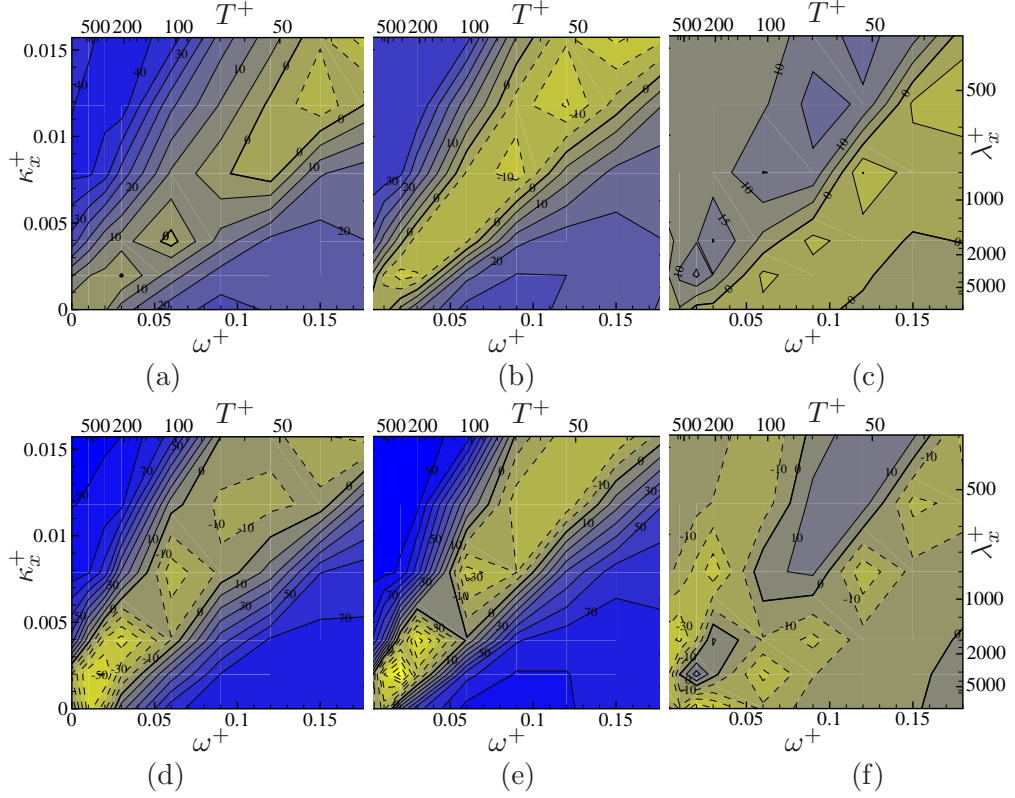


Figure 7.26: Reduction rate maps for mean wall shear stress $\overline{\tau_w}$ conditioned under (a) positive VLSMs regions ($\mathcal{R}_P(\tau_w)$), (b) negative VLSMs regions ($\mathcal{R}_N(\tau_w)$) and (c) the \mathcal{DR} difference map ($\mathcal{R}_P(\tau_w) - \mathcal{R}_N(\tau_w)$); and for small scale wall shear stress fluctuation $\overline{\tau_{w,s}^{\prime 2}}$ under (d) positive VLSMs regions ($\mathcal{R}_P(\tau_{w,s}^{\prime 2})$), (e) negative VLSMs regions ($\mathcal{R}_N(\tau_{w,s}^{\prime 2})$), and (f) the difference map ($\mathcal{R}_P(\tau_{w,s}^{\prime 2}) - \mathcal{R}_N(\tau_{w,s}^{\prime 2})$).

the applied streamwise travelling wave is in a global sense, thus it needs to find a balance between suppressing the small scales under the positive and the negative VLSMs regions. To achieve the maximum drag reduction, the key is to attenuate the small scales under the positive VLSMs regions, because those structures are more stable than those under the negative VLSMs regions. Since the small scales under positive VLSMs regions burst faster and convect faster, this leads to the control parameters being shifted towards higher values for the spanwise wall oscillation and the stationary wave, which is the second Reynolds number effect observed by Hurst et al. (2014).

7.4 Conclusions

The influence of the VLSMs on the turbulent skin-friction control by the streamwise travelling wave of the spanwise wall velocity was quantified using a series of conditional average analysis at moderate Reynolds numbers $Re_\tau = 800$ and 1600 . The drag reduction deterioration and the optimal control parameters shift were found to be linked to the superimposition and the modulation effects of the VLSMs. Firstly, the weakening of the VLSMs was less effective than that of the near wall small scales. Secondly, the attenuation of the small scales under the positive VLSMs regions was more difficult than that under the negative VLSMs regions. The strong modulation effect on the wavenumber and frequency of the small scale structures from the VLSMs resulted in the optimal control parameters unfixed in wall units. To attenuate the small scale structures under the positive VLSMs regions most effectively, the control parameters shifted towards higher values to match the natural frequency and wavenumber of those small scales. The VLSMs were amplified when the wave travelling speed $c^+ > 10$ (see figure 7.22(b)), and this caused the drag reduction deterioration to be even worse in this region of the $\omega^+ - \kappa_x^+$ space. For example, figure 7.17 suggested a stronger \mathcal{DR} deterioration for the wall oscillation case at $\omega^+ = 0.6$ (within the VLSMs amplified region) than the stationary wave case at $\kappa_x^+ = 0.008$ (outside of the VLSMs amplified region). For the optimal drag reduction at high Reynolds numbers, a strategy by controlling both the small scales from the near wall region and the VLSMs from the outer region may be necessary.

Chapter 8

Conclusions and Future Works

8.1 Conclusions

In the present study, the skin-friction drag reduction by the spanwise motion generated by the wall movement and the body forces was studied in a DNS channel. The aim was to bring the skin-friction drag reduction control by spanwise wall oscillation into real engineering applications. Two main challenges were explored: 1) creating the same drag reduction effect as the spanwise wall oscillation using newly developed DBD plasma actuators; 2) understanding the effect of the VLSMs on the drag reduction deterioration at high Reynolds numbers. The following main works were done in the four result chapters:

In chapter 4, the drag reduction mechanism in a three-dimensional turbulent boundary layer by the uni-direction and the oscillating spanwise wall motion was studied. Extensive analysis on the λ_2 structures and the near wall streaks were performed to understand the structure dynamics modulation by spanwise wall oscillation, which provided the guide to implement Lorentz and plasma body forces.

In chapter 5, the travelling wave forms were created by spanwise Lorentz force. Thanks to the continuous variation of the Lorentz force, a whole picture of the drag reduction by forward streamwise travelling wave, spanwise travelling wave, backward streamwise travelling wave and any oblique travelling wave was given. The results provided the confidence that the body force could create a similar drag reduction effect to the wall velocity, thus paving the way for the plasma actuators study.

In chapter 6, a series of configurations was designed for the drag reduction control by the DBD plasma actuators. A new configuration to generate the spanwise oscillation was proposed. It demonstrated the possibility to implement the plasma

actuators to real engineering problems for the drag reduction purpose for at least low Reynolds numbers.

In chapter 7, the effect of the VLSMs was studied based on the high Reynolds number data for the streamwise travelling wave of the spanwise wall velocity generated by Hurst (2013). Due to the similarity between the spanwise wall oscillation and the spanwise oscillating plasma body force, the results in this chapter also shed light on the drag reduction scenario at high Reynolds numbers for the plasma actuators.

The results in the present study leads to the following main conclusions:

- To achieve drag reduction, the oscillation frequency should be high enough to prevent the near wall structures from recovering; but the oscillation frequency also needs to be low enough to maintain a certain thickness of the Stokes layer for the interaction with the near wall structures (Akhavan et al., 1991; Baron and Quadrio, 1996; Quadrio and Ricco, 2004). This optimal frequency for the spanwise wall oscillation is at $\omega^+ = 0.06$ (Quadrio and Ricco, 2004; Blesbois et al., 2013), though it slightly varies in wall units with the Reynolds number.
- The λ_2 structures and the associated high- and low-speed streaks are significantly modulated in the Stokes layer. Their tilting angles and the averaged structure centres change with the wall movement (Ricco, 2004). The period for the structures from growing-up to dying-out, is dominated by the oscillation frequency. The optimal oscillation frequency is around the same value of the structure bursting frequency (Quadrio and Ricco, 2004). At this period, the newly generated structure are quickly pushed away from the wall, and the misalignment between the positive and the negative λ_2 structures prohibits the formation of the long low-speed streaks, thus it generates less skin-friction.
- Spanwise body force can achieve the same effect as the spanwise wall velocity, though less effective. The structure dynamics in the Stokes layer generated by the travelling wave form of the spanwise Lorentz force and by the spanwise wall velocity are very similar.
- The interaction between the “ribbon structure” and the near wall streaks in any oblique travelling wave of the spanwise Lorentz force is similar to the scenario for the spatial homogeneous Lorentz force. There is no fundamental difference in the drag reduction mechanism.
- A “local travelling wave global oscillation” configuration (SO4) was proposed for the skin-friction control by the DBD plasma actuators, which resembles the

drag reduction by the spanwise wall oscillation and the spanwise oscillating Lorentz force most. Drag reduction is still achievable when the gap between the two activated actuators is as large as $s^+ = 100$.

- No net energy saving is obtained for the drag reduction control by plasma actuators for all the configurations explored in this study, even when only considering the fluid power as the power required.
- The VLSMs play an important role at high Reynolds numbers. These VLSMs carry a significant amount of the Reynolds shear stress, but the general near wall skin-friction controls can not damp these VLSMs very effectively. The frequency modulation from these VLSMs on the near wall small scales shifts the optimal control parameters in the wall units.

8.2 Future works

Though the works done in the present study helps improve the understanding of the skin-friction drag reduction control by the spanwise motion to some extent, significant efforts are still needed in the future. Some suggested future works are listed as below:

- Investigating the exact coherent structure within the unsteady Stokes layer (Hwang et al., 2016) is a great topic. The λ_2 structures and the near wall streaks are conditioned from the turbulent fields separately, thus the interaction between those two is still weak in the present analysis. Understanding the modulation on the exact coherent structure by the spanwise wall oscillation can provide a direct view on how the regeneration cycle is weakened by the spanwise motion.
- The ‘local travelling wave global oscillation’ configuration (SO4) for the DBD plasma actuators is a successful drag reduction proposal. However, the plasma actuator model used in the present study is still very simplified, and an experiment validation of SO4 configuration is needed.
- Even though the drag reduction mechanisms for the skin-friction control are similar between the spanwise velocity and the spanwise body force, the result from figures 4.8 and 6.29 suggests that, a more detailed study of the link between the spanwise mean strain and the skin-friction is required to bring the understanding of the drag reduction mechanism to the ground. For this

study, specific spanwise mean strain can be imposed numerically in the DNS, or through simplified turbulent model, such as used by Barkley et al. (2015).

- At the flight Reynolds number, the contribution to skin-friction from the VLSMs are very important, and it is an interesting topic to understand how to control the VLSMs effectively from the outer region.

Appendix A

Estimation of flight Reynolds number

For a commercial aircraft under a cruising condition at an altitude of $10km$ above the sea water, assuming the flight speed is $U_\infty = 225m/s$, we estimate the flight Reynolds number on the wing at $x = 2m$ downstream of the stagnation point ($x = 0$). The air properties at this height are: 1) density $\rho = 4.12707 \times 10^{-1}kg/m^3$; 2) dynamics viscosity $\mu = 1.46884 \times 10^{-5}Ns/m^2$; 3) kinetic viscosity $\nu = \mu/\rho = 3.55904 \times 10^{-5}m^2/s$. For the boundary layer thickness δ , and skin-friction coefficient C_f estimation, the same empirical formulas as in (Ricco and Hahn, 2013) are used:

$$\begin{aligned}\delta &= 0.37xRe_x^{-0.2}, \\ C_f &= 0.37(\log Re_x)^{-2.584}, \\ Re_x &= \frac{xU}{\nu}.\end{aligned}\tag{A.1}$$

At $x = 2m$, $Re_x \approx 1.264 \times 10^7$, $\delta \approx 0.028m$, $C_f \approx 2.335 \times 10^{-3}$, $\tau_w = C_f/(\frac{1}{2}\rho U_\infty) = 24.39Pa$, and $u_\tau = \sqrt{\tau_w/\rho} = 7.69m/s$. Therefore, we have the frictional Reynolds number $Re_\tau = u_\tau\delta/\nu \approx 6072$, which is the order of $O(10^4)$. The viscous length scale is $\nu/u_\tau \approx 4.6 \times 10^{-6}m$, which is the order of $O(1\mu m)$. The viscous time scale is $\nu/u_\tau^2 = 6.1 \times 10^{-7}s$, which is the order of $O(1\mu s)$.

Appendix B

Density spectra

We begin with the forward and backward Fourier transform,

$$\begin{aligned}\widehat{u}(\boldsymbol{\kappa}) &= \mathcal{F}(u(\mathbf{x})) = \frac{1}{4\pi^2} \int_{-\infty}^{\infty} u(\mathbf{x}) e^{-i\boldsymbol{\kappa}\mathbf{x}} d\mathbf{x}, \\ u(\mathbf{x}) &= \mathcal{F}^{-1}(\widehat{u}(\boldsymbol{\kappa})) = \int_{-\infty}^{\infty} \widehat{u}(\boldsymbol{\kappa}) e^{i\boldsymbol{\kappa}\mathbf{x}} d\boldsymbol{\kappa},\end{aligned}\tag{B.1}$$

where the two dimensional vectors are $\mathbf{x} = (x, z)$ and $\boldsymbol{\kappa} = (\kappa_x, \kappa_z)$; $\widehat{\cdot}$ indicates the Fourier coefficient. There are two possible ways to get the spectra tensor $\phi_{ij}(\boldsymbol{\kappa})$. The first method is through the correlation tensor $R_{ij}(\mathbf{r})$, which is defined as below,

$$R_{i,j}(\mathbf{r}) \equiv \overline{u_i(\mathbf{x})u_j(\mathbf{x}') } = \overline{u_i(\mathbf{x})u_j(\mathbf{x} + \mathbf{r})}.\tag{B.2}$$

where overline indicates average in time. Then the spectra tensor can be obtained by taking the Fourier transform of the correlation tensor, *i.e.*,

$$\phi_{ij}(\boldsymbol{\kappa}) = \mathcal{F}(R_{ij}(\mathbf{r})).\tag{B.3}$$

A less computational expensive way to calculate the spectra tensor is through the following multiplication,

$$\phi_{ij}(\boldsymbol{\kappa}) = \overline{\widehat{u}_i(\boldsymbol{\kappa})\widehat{u}_j^*(\boldsymbol{\kappa})},\tag{B.4}$$

where the superscript * indicates the complex conjugate. Then a one-side spectrum $E_{ij}(k_x, k_z)$ can be defined in the wave space for $k_x \geq 0$ and $k_z \geq 0$. Considering

$\phi_{ij}(\boldsymbol{\kappa})$ is symmetric about $\boldsymbol{\kappa} = \mathbf{0}$, $E_{ij}(k_x, k_z)$ can be written as below,

$$\begin{aligned} E_{ij}(k_x, k_z) &= \overline{\widehat{u}_i(k_x, k_z)\widehat{u}_j^*(k_x, k_z)} + \overline{\widehat{u}_i(-k_x, k_z)\widehat{u}_j^*(-k_x, k_z)} \\ &\quad + \overline{\widehat{u}_i(-k_x, -k_z)\widehat{u}_j^*(-k_x, -k_z)} + \overline{\widehat{u}_i(k_x, -k_z)\widehat{u}_j^*(k_x, -k_z)} \\ &= 2 \left[\overline{\widehat{u}_i(k_x, k_z)\widehat{u}_j^*(k_x, k_z)} + \overline{\widehat{u}_i(k_x, -k_z)\widehat{u}_j^*(k_x, -k_z)} \right]. \end{aligned} \quad (\text{B.5})$$

Given $E_{ij}(k_x, k_z)$, the two dimensional density spectrum is defined as,

$$\Phi_{ij}(k_x, k_z) = \frac{\partial^2 E_{ij}(k_x, k_z)}{\partial k_x \partial k_z}. \quad (\text{B.6})$$

With the pre-multiplied density spectrum in a log-log plot, the area underneath the surface gives the total fluctuation energy, *i.e.*,

$$\overline{u'_i u'_j} = \int_{k_z} \int_{k_x} \Phi_{ij}(k_x, k_z) dk_x dk_z \equiv \int_{k_z} \int_{k_x} k_x k_z \Phi_{ij}(k_x, k_z) d \log(k_x) d \log(k_z). \quad (\text{B.7})$$

The one dimensional density spectra along k_x and k_z are given as below,

$$\begin{aligned} \Phi_{ij}(k_x) &= \int_{k_z} \Phi_{ij}(k_x, k_z) dk_z, \\ \Phi_{ij}(k_z) &= \int_{k_x} \Phi_{ij}(k_x, k_z) dk_x. \end{aligned} \quad (\text{B.8})$$

Appendix C

\mathcal{DR} asymptotic at $\omega = 0$ ($T = \infty$)

For the uni-direction wall motion $W_w = A_w$, the xz plane averaged skin-friction C_f is a function of the initial flow field \mathbf{u}_0 , the wall velocity A_w , and time t . $C_f(A_w, \mathbf{u}_0, t)$ trajectory depends on \mathbf{u}_0 only for the transient period ($t_0 < t < t_1$), but in the new steady state $t > t_1$, long time averaged C_f is independent from the initial flow field, shown as below,

$$\begin{aligned}\overline{C_f}(A_w) &= \left(\frac{1}{t_2 - t_1} \int_{t_1}^{t_2} C_f(A_w, \mathbf{u}_0, t) dt \right) \Big|_{t_2 \rightarrow \infty}, \\ &= \left(\frac{1}{t_2 - t_1} \int_{t_0}^{t_2} C_f(A_w, \mathbf{u}_0, t) dt \right) \Big|_{t_2 \rightarrow \infty} - \left(\frac{1}{t_2 - t_1} \int_{t_0}^{t_1} C_f(A_w, \mathbf{u}_0, t) dt \right) \Big|_{t_2 \rightarrow \infty}, \\ &= \left(\frac{1}{t_2 - t_0} \int_{t_0}^{t_2} C_f(A_w, \mathbf{u}_0, t) dt \right) \Big|_{t_2 \rightarrow \infty},\end{aligned}\tag{C.1}$$

where $\overline{C_f}(A_w)$ is independent from \mathbf{u}_0 . Therefore, the steady state $\overline{C_f}(A_w)$ can be predicted using any initial flow field \mathbf{u}_0 subjected to $t \rightarrow \infty$.

For the spanwise wall oscillation case with $W_w = A_w \sin(\omega t)$ (minus sign is dropped from equation 4.2 for convenience), let us set $\phi = \omega t$, and consider a finite change of the phase $\phi \in [\phi_1, \phi_2]$ ($\Delta\phi = \phi_2 - \phi_1$, $\Delta W_w = A_w(\sin(\phi_2) - \sin(\phi_1)) = \cos \phi_1 \Delta\phi$). As $\Delta\phi \rightarrow 0$, $\Delta W_w \rightarrow 0$. At $\omega = 0$, we have $\Delta t = \Delta\phi/\omega = \infty$. Therefore, the wall oscillation problem at the phase interval $[\phi_1, \phi_2]$ is equivalent to a uni-direction wall motion problem, with an initial field $\mathbf{u}_0|_{\phi=\phi_1}$, spanwise wall velocity $W_w = A_w \sin \phi_1$. As shown in equation C.1, the steady value $\overline{C_f}(\phi = \phi_2)$ is independent from $\mathbf{u}_0|_{\phi=\phi_1}$, and it can be taken from figure 4.8, where a no control flow field is used as the initial field. The corresponding drag reduction $\mathcal{DR}(\phi)$ values at different phases are tabulated in table C.1 for one quarter of the oscillation period

at $A_w^+ = 12$. The $\mathcal{DR}(\phi)$ values in the other three quarters are identical to the first quarter, since $\mathcal{DR}(\phi)$ is only a function of $|W_w|$. The overall $\overline{\mathcal{DR}}$ in one oscillation

Table C.1: $\mathcal{DR}(\phi)$ in the first 1/4 period at $A_w^+ = 12$.

W_w^+	0	1	2	4	6	8	10	12
$\sin(\phi_i) = W_w/A_w$	0	0.083	0.167	0.333	0.5	0.667	0.833	1.0
ϕ_i	0	0.0834	0.167	0.340	0.524	0.730	0.985	1.571
$\mathcal{DR}(\phi_i)^\dagger$	0	-0.8	-2.5	-5.9	-8.4	-10.2	-11.0	-11.6
$\mathcal{DR}(\phi_i)^\ddagger$	0	-0.4	-1.8	-6.3	-12.3	-18.7	-25.7	-31.7

\dagger top and bottom walls are in phase; \ddagger top and bottom walls are out of phase.

period can be obtained through a time average (equation C.2). The integration is approximated using a trapezoidal rule with the discretise $\mathcal{DR}(\phi)$ values in table C.1. The predicted asymptotic \mathcal{DR} values are -8.6 when the top and bottom walls are in phase, and -16.1 when they are out of phase.

$$\begin{aligned}
\overline{\mathcal{DR}} &= \frac{1}{T/4} \int_0^{T/4} \mathcal{DR}(t) dt = \frac{2}{\pi} \int_0^{\pi/2} \mathcal{DR}(\phi) d\phi, \\
&\approx \frac{2}{\pi} \sum_i (\mathcal{DR}(\phi_{i-1}) + \mathcal{DR}(\phi_i)) \frac{\phi_i - \phi_{i-1}}{2}.
\end{aligned} \tag{C.2}$$

Appendix D

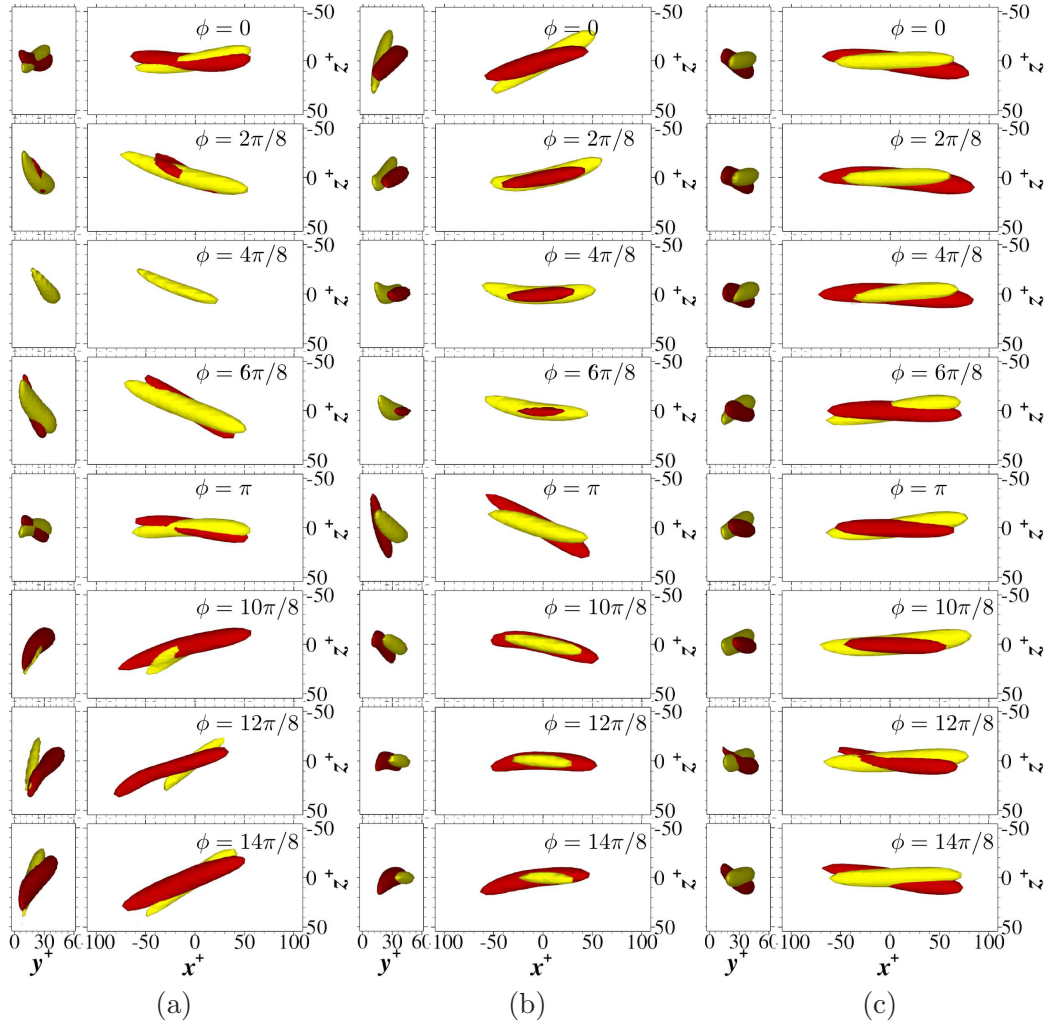
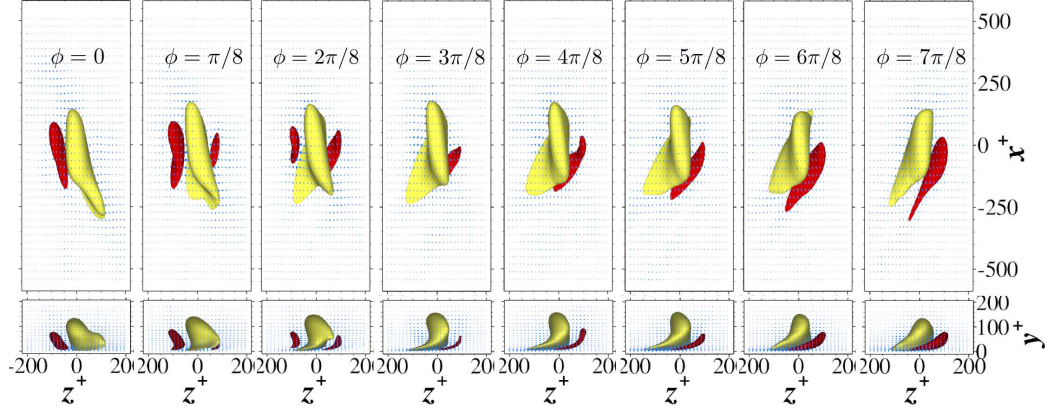
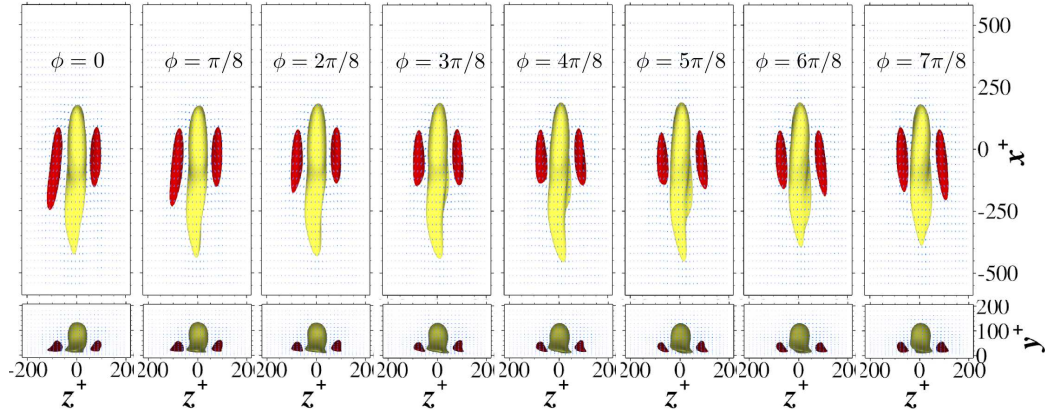


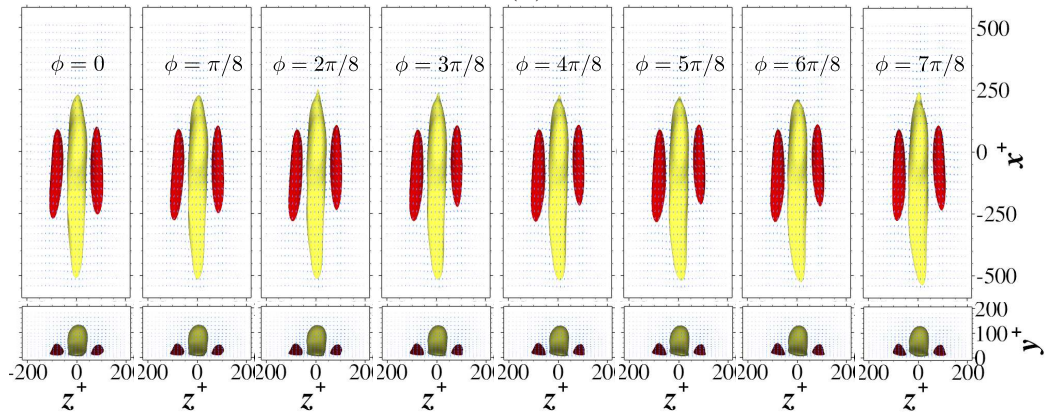
Figure D.1: Ensemble averaged λ_2 structures at 8 equally separated phases during one oscillation period with different oscillation frequencies: (a) $\omega^+ = 0.01$ ($\lambda_2^+ = -0.009$); (b) $\omega^+ = 0.03$ ($\lambda_2^+ = -0.009$); and (c) $\omega^+ = 0.12$ ($\lambda_2^+ = -0.003$).



(a)



(b)



(c)

Figure D.2: The characteristic eddies changes in the first half period for: (a) $\omega^+ = 0.01$ ($T^+ = 628$), (b) $\omega^+ = 0.06$ ($T^+ = 105$), and (c) $\omega^+ = 0.12$ ($T^+ = 52$).

Appendix E

Analytical solution for the Laminar LGSL

For equation (5.16) (the superscript $+$ has been dropped for simplicity), we look for the solution with the following form,

$$W = \mathscr{W}_1 e^{i\omega t} + \mathscr{W}_2 e^{-i\omega t}, \quad (\text{E.1})$$

with the forcing term decomposed as,

$$A_f e^{-y/\Delta} \sin(-\omega t) = \frac{i}{2} A_f e^{-y/\Delta} (e^{i\omega t} - e^{-i\omega t}), \quad (\text{E.2})$$

where \mathscr{W}_1 and \mathscr{W}_2 are complex functions of y . Substitute equations (E.1) and (E.2) into equation (5.16), we have,

$$\left(\frac{\partial^2 \mathscr{W}_1}{\partial y^2} - i\omega \mathscr{W}_1 + \frac{i}{2} A_f e^{-y/\Delta} \right) e^{i\omega t} + \left(\frac{\partial^2 \mathscr{W}_2}{\partial y^2} - i\omega \mathscr{W}_2 - \frac{i}{2} A_f e^{-y/\Delta} \right) e^{-i\omega t} = 0, \quad (\text{E.3})$$

To make equation E.3 valid for any t , we have,

$$\frac{\partial^2 \mathscr{W}_1}{\partial y^2} - i\omega \mathscr{W}_1 + \frac{i}{2} A_f e^{-y/\Delta} = 0, \quad (\text{E.4})$$

$$\frac{\partial^2 \mathscr{W}_2}{\partial y^2} - i\omega \mathscr{W}_2 - \frac{i}{2} A_f e^{-y/\Delta} = 0, \quad (\text{E.5})$$

with the boundary conditions,

$$\mathcal{W}_1|_{y=0} = 0, \quad \mathcal{W}_1|_{y=\infty} = 0; \quad (\text{E.6})$$

$$\mathcal{W}_2|_{y=0} = 0, \quad \mathcal{W}_2|_{y=\infty} = 0. \quad (\text{E.7})$$

We first solve equation (E.4) subjected to boundary equation (E.6). The homogeneous part of equation (E.4) is as below,

$$\frac{\partial^2 \mathcal{W}_1}{\partial y^2} - i\omega \mathcal{W}_1 = 0. \quad (\text{E.8})$$

And the general solution is,

$$\mathcal{W}_1 = Ae^{(1+i)\sqrt{\frac{\omega}{2}}y} + Be^{-(1+i)\sqrt{\frac{\omega}{2}}y}, \quad (\text{E.9})$$

where A and B are constant to be determined later. We then look for a particular solution of the form $\mathcal{W}_1 = be^{ay}$. Substitute it into equation (E.4), we have,

$$a^2 be^{ay} - i\omega be^{ay} + \frac{i}{2} A_f e^{-y/\Delta} = 0. \quad (\text{E.10})$$

Comparing the coefficient of y , we have $a = -1/\Delta$ and $b = A_f / (2(\omega + \frac{i}{\Delta^2}))$. Therefore, the final solution for \mathcal{W}_1 is,

$$\mathcal{W}_1 = Ae^{(1+i)\sqrt{\frac{\omega}{2}}y} + Be^{-(1+i)\sqrt{\frac{\omega}{2}}y} + be^{ay}. \quad (\text{E.11})$$

With the boundary conditions in equation (E.6) we have,

$$\begin{aligned} A + B + b &= 0, \\ A &= 0. \end{aligned} \quad (\text{E.12})$$

Therefore, $B = -b$, and

$$\mathcal{W}_1 = \frac{A_f/2}{\omega + i/\Delta^2} \left(e^{-y/\Delta} - e^{-(1+i)\sqrt{\frac{\omega}{2}}y} \right). \quad (\text{E.13})$$

Similarly, solving equation (E.5) subjected to boundary equation (E.7), we have

$$\mathcal{W}_2 = \frac{A_f/2}{\omega - i/\Delta^2} \left(e^{-y/\Delta} - e^{-(1-i)\sqrt{\frac{\omega}{2}}y} \right). \quad (\text{E.14})$$

Let

$$c \equiv \frac{1}{\Delta^2}, \quad \widehat{A}_f \equiv \frac{A_f}{c^2 + \omega^2}, \quad \widehat{y} \equiv y \sqrt{\frac{\omega}{2}}, \quad \widetilde{y} \equiv \frac{y}{\Delta}, \quad (\text{E.15})$$

and plug equations (E.13) and (E.14) into equation (E.1), the final solution is arrived as below,

$$\begin{aligned} W &= \mathscr{W}_1 e^{i\omega t} + \mathscr{W}_2 e^{-i\omega t}, \\ &= \widehat{A}_f e^{-\widetilde{y}} (\omega \cos(\omega t) + c \sin(\omega t)) - \widehat{A}_f e^{-\widehat{y}} (\omega \cos(\omega t - \widehat{y}) + c \sin(\omega t - \widehat{y})). \end{aligned} \quad (\text{E.16})$$

Appendix F

Parameter selection for starting vortex comparison

To make a comparison with the experimental study of the starting vortex by Whalley and Choi (2012), the three parameters, *i.e.*, σ , λ and A_f in the plasma actuator model need to be chosen first. For convenience, we dimensionalise all the parameters in our channel simulation at $Re_\tau = 200$ ($Re_m = 3150$). The plasma force distribution parameters are set to be $\sigma = 1.8$ mm and $\lambda = 1.6$ mm⁻¹, and this gives a plasma force region with a vertical height of 0.6 mm, and a horizontal extend of 4 mm (estimated from the accumulative density function of the Exponential and the Rayleigh distributions, *i.e.*, $1 - e^{-\lambda y} = 0.9$ and $1 - e^{-z^2/2\sigma^2} = 0.9$), which roughly matches the plasma actuator size used by Whalley and Choi (2012). Other σ and λ values have also been tested, but the effect on the vortex dynamics was found to be weak. The half channel height is set to be $h = 40$ mm, so that the actuator size is the same in wall units as those used by Choi et al. (2011) at $Re_\tau = 475$. The reference velocity in our channel simulation is $U_m = Re_m \nu / h = 1.184$ m/s (provided $\nu = 1.5 \times 10^{-5}$ m²/s, and $\rho = 1.322$ kg/m³ for air). Since the present empirical plasma actuator model does not have the direct link to the applied electric voltage and frequency, the plasma body force parameter strength A_f needs to be tuned. For each case of A_f , the maximum jet velocity W_{max} and the vortex travelling distance in the horizontal direction L are recorded after the steady W_{max} value is just reached. Then W_{max} and ν/W_{max} are used as the correct reference velocity and length scales for the non-dimensionalisation (indicated by a $*$) as used in the experimental data. Since the plasma actuator acts as a momentum source, we tune A_f to give a good comparison with the experimental data in the total volume momentum increase. The best comparison is given in figure F.1(a) with $A_f = 0.26$ kN/m³. The

linear increase of the momentum M_z indicates a constant plasma body force, and they are almost the same between the simulation result and the PIV data. However, the simulation data is upward shifted, which might be due to an initial effect that the PIV data has a negative momentum at the beginning. The steady W_{max} value is reached at $t = 135$ ms ($t^* = 1580$), and $W_{max} = 0.42$ m/s, $L = 6.7$ mm, which are under predicted compared to the experiment ($W_{max} = 0.45$ m/s, $L = 8.3$ mm). The Reynolds number defined as $Re_j = W_{max}L/\nu$ are 250 and 190 for the experiment and the simulation, respectively. The vortex centre coordinate (z_c^*, y_c^*) is also recorded and compared with the experimental data. Generally, the starting vortex in our simulation moves slower in both the horizontal and the vertical directions, but it does suggest a power law scaling of $z_c^* \sim t^{*0.71}$ and $y_c^* \sim t^{*0.71}$ as in the experiment for large t^* .

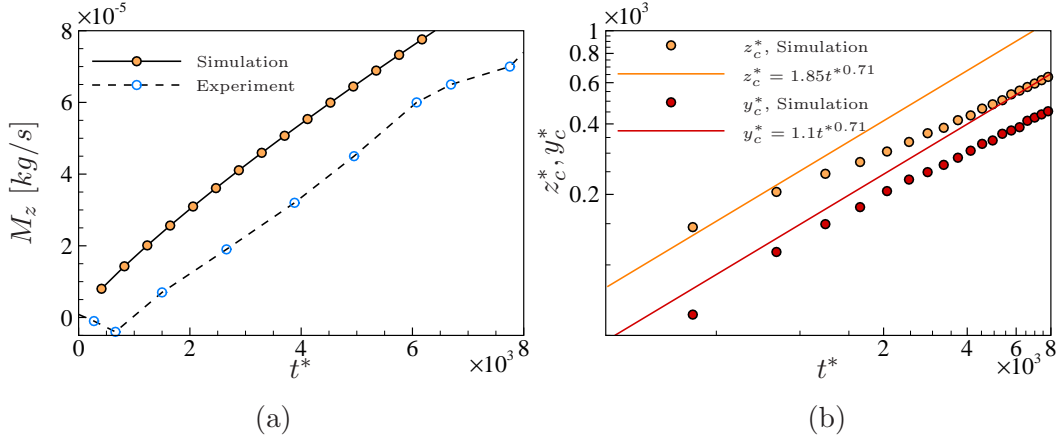


Figure F.1: Comparison of the starting vortex between the simulation and experiment (Case A, (Whalley and Choi, 2012)) for (a) momentum and (b) vortex centre movement.

Appendix G

Validation of the VLSMs definition

The streamwise velocity fluctuation, u' at $y^+ = 15$ for $Re_\tau = 1600$ is decomposed into the large and the small scale components using both the spectra filter definition in equation (7.2) and the Hilbert-Huang empirical decomposition used by Agostini and Leschziner (2014), and the instantaneous snapshots are shown in figure G.1(a) and G.1(b), respectively. The large scale component from the Fourier spectra filter is very similar to the one obtained from the Hilbert-Huang empirical decomposition, except that the latter is more noisy due to the surface fitting and the iteration process.

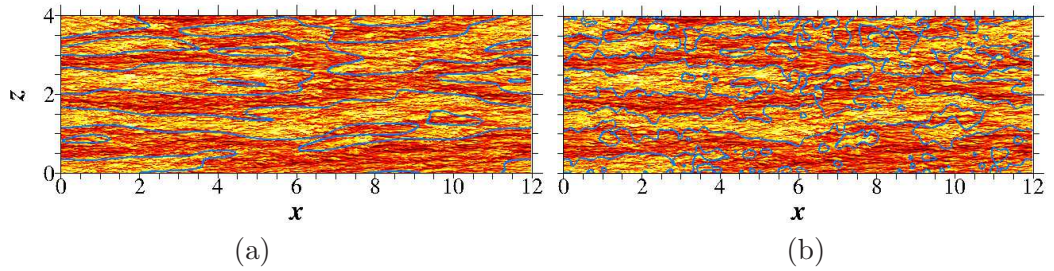


Figure G.1: Streamwise velocity fluctuation, u' contour at $y^+ = 15$, $Re_\tau = 1600$ with the large scales (contour lines) identified by (a) Fourier spectra filter (equation (7.2)), and (b) residual field of Hilbert-Huang empirical decomposition.

The decomposed streamwise velocity fluctuation profile, u' over the whole half channel height is calculated at $Re_\tau = 800$ and compared between the Fourier spectra filter and the Hilbert-Huang empirical decomposition, shown in figure G.2. A good match between the large scale component profiles is observed. The small scale component decomposed from Hilbert-Huang empirical decomposition is higher

than the one obtained from the spectra filter decomposition. This might be due to the fact that Hilbert-Huang empirical decomposition does not perfectly guarantee the orthogonal among the decomposed modes and also the slightly higher Reynolds number data studied by Agostini and Leschziner (2014).

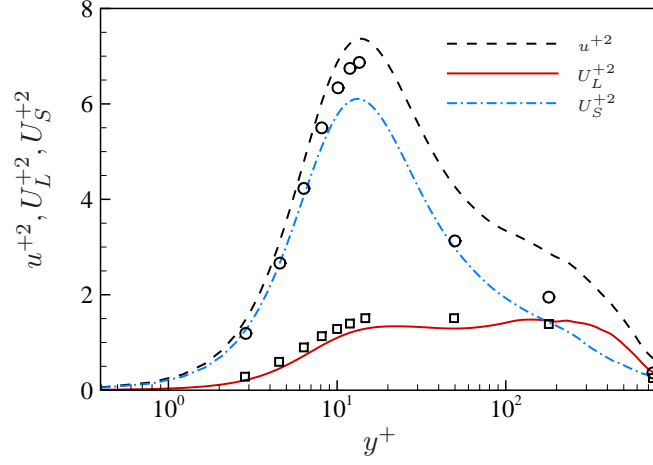


Figure G.2: Comparison of the decomposed streamwise velocity fluctuation profiles between Fourier spectra filter at $Re_\tau = 800$ and Hilbert-Huang empirical decomposition at $Re_\tau = 1000$ (Agostini and Leschziner, 2014).

Appendix H

Uncertainty quantification for VLSMs statistics

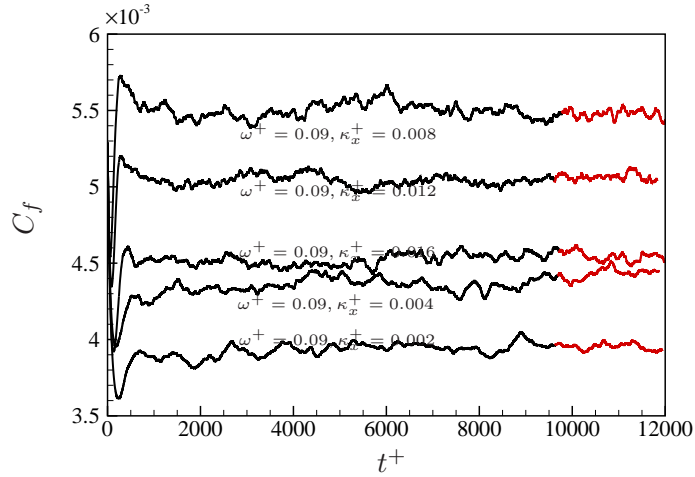


Figure H.1: Typical time history of C_f , with the wall shear stress sampling window indicated by red segment lines.

The instantaneous top and bottom wall shear stress snapshots are saved every 20 steps ($\Delta t^+ = 4$) for 10800 time steps after $t^+ \approx 10000$. The sampling window is indicated by red segment lines in figure H.1. 1080 snapshots are saved in total for each case. The wall shear stress and its conditioned properties are tested in table H.1 for four typical cases at $Re_\tau = 800$. The relative error is estimated by comparing the results obtained from 540 samples and 1080 samples. This error is generally around 1 ~ 3%. For large scale component, the fluctuation is higher, and the error occasionally reaches 10%, for example for $\tau_{w,L}'^2$. Since the study in chapter

7 is mainly on the patterns in the \mathcal{DR} maps, the maximum 10% relative error does not affect the conclusion drew. In figure H.2, we reproduce figures 7.22(b), 7.26(a) and 7.26(d) in chapter 7 with only 540 snapshots, and no obvious difference in the map pattern can be seen. This is the case for all the other maps studied in chapter 7.

Table H.1: Wall shear stress statistics from different sample lengths.

Samples	τ_w^2 ($\times 10^{-6}$)	$\tau_{w,L}^2$ ($\times 10^{-6}$)	$\tau_{w,S}^2$ ($\times 10^{-6}$)	$\tau_{w,P}^2$ ($\times 10^{-6}$)	$\tau_{w,N}^2$ ($\times 10^{-6}$)	$\overline{\tau_w}$ ($\times 10^{-3}$)	$\overline{\tau_{w,P}}$ ($\times 10^{-3}$)	$\overline{\tau_{w,N}}$ ($\times 10^{-3}$)
NC [†]								
540	1.148	0.184	0.973	1.406	0.622	2.628	3.176	2.095
1080	1.162	0.186	0.986	1.396	0.621	2.614	3.159	2.096
Error(%)	1.2	1.1	1.2	0.7	0.2	0.5	0.6	0.0
OC [†]								
540	0.374	0.133	0.247	0.475	0.103	1.960	2.456	1.536
1080	0.357	0.122	0.242	0.471	0.101	1.944	2.430	1.530
Error(%)	4.6	9.0	2.3	0.9	2.4	0.8	1.1	0.4
SW [†]								
540	0.126	0.031	0.099	0.194	0.041	1.585	1.831	1.379
1080	0.137	0.034	0.106	0.204	0.044	1.608	1.859	1.394
Error(%)	7.9	10.0	6.6	4.6	4.9	1.5	1.5	1.0
ST [†]								
540	0.102	0.029	0.076	0.143	0.035	1.586	1.836	1.384
1080	0.098	0.026	0.074	0.139	0.035	1.585	1.827	1.388
Error(%)	4.2	10.1	2.0	2.7	1.5	0.1	0.5	0.3

†: NC - $\omega^+ = 0.0$, $\kappa_x^+ = 0.0$; OC - $\omega^+ = 0.06$, $\kappa_x^+ = 0.0$; SW - $\omega^+ = 0.0$, $\kappa_x^+ = 0.008$; ST - $\omega^+ = 0.03$, $\kappa_x^+ = 0.016$.

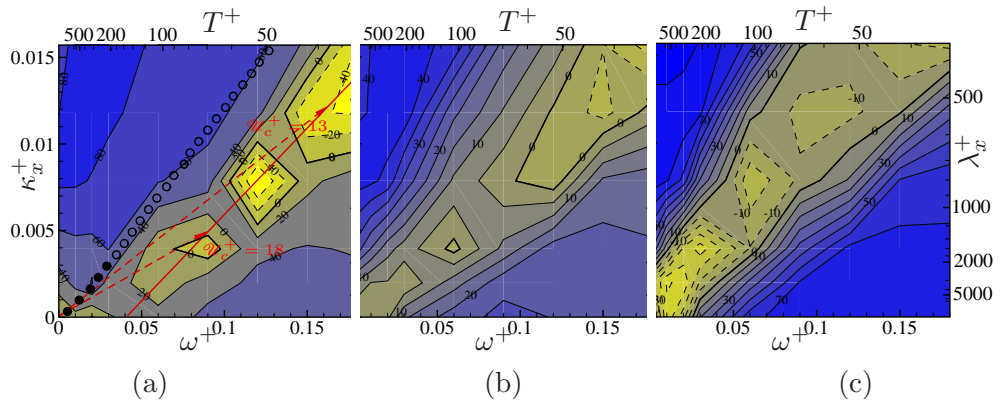


Figure H.2: Reproducing (a) figure 7.22(b); (b) figure 7.26(a) and (c) figure 7.26(d) using 540 sampling snapshots.

Appendix I

Derivation of FIK for each wave component

The FIK identity for channel flow is as below (Fukagata et al., 2002),

$$C_f = \frac{6}{Re} + 6 \int_0^1 (1-y)(-\overline{u'v'})dy, \quad (\text{I.1})$$

where the overbar indicates time average. The Reynolds shear stress can be written in terms of its density spectra tensor $\Phi_{u'v'}(k_x, k_z)$ in Fourier space as below,

$$-\overline{u'v'} = - \int_0^\infty \int_0^\infty \Phi_{u'v'}(k_x, k_z) dk_x dk_z. \quad (\text{I.2})$$

Plug equation I.2 into equation I.1, the skin-friction coefficient C_f can be expressed in wave component form,

$$C_f = \frac{6}{Re} + 6 \int_0^1 \int_0^\infty \int_0^\infty (y-1) \Phi_{u'v'}(k_x, k_z) dk_x dk_z dy. \quad (\text{I.3})$$

Thus a new density spectra tensor $\Phi_{\tau_w \tau_w}$ can be defined for the mean wall shear stress,

$$\Phi_{\tau_w \tau_w} = 6 \int_0^1 (y-1) \Phi_{u'v'}(k_x, k_z) dy. \quad (\text{I.4})$$

And the turbulent contribution to mean wall shear stress, $\overline{\tau_{w,t}}$ can be written in wave component form as below,

$$\overline{\tau_{w,t}} = \int_0^\infty \int_0^\infty \Phi_{\tau_w \tau_w} dk_x dk_z. \quad (\text{I.5})$$

Bibliography

- M. Abdollahzadeh, J. C. Páscoa, and P. J. Oliveira. Modified split-potential model for modeling the effect of DBD plasma actuators in high altitude flow control. *Current Applied Physics*, 14(8):1160–1170, 2014.
- M. Abdollahzadeh, J. C. Pascoa, and P. J. Oliveira. Implementation of the classical plasma-fluid model for simulation of dielectric barrier discharge (DBD) actuators in OpenFOAM. *Comput. Fluids*, 128:77–90, 2016.
- H. Abe, H. Kawamura, and H. Choi. Very large-scale structures and their effects on the wall shear-stress fluctuations in a turbulent channel flow up to $Re_\tau = 640$. *J. Fluids Eng. ASME*, 126(5):835–843, 2004.
- R. Adrian, C. Meinhart, and C. D. Tompkins. Vortex organisation in the outer region of the turbulent boundary layer. *J. Fluid Mech.*, 422:1–54, 2000.
- L. Agostini and M. A. Leschziner. On the influence of outer large-scale structures on near-wall turbulence in channel flow. *Phys. of Fluids*, 26:075107, 2014.
- L. Agostini and M. A. Leschziner. Predicting the response of small-scale near-wall turbulence to large-scale outer motions. In *European Turbulence Conference 15*, 25-28 August, Delft, The Netherlands, 2015.
- L. Agostini, E. Toubert, and M. A. Leschziner. Spanwise oscillatory wall motion in channel flow: drag-reduction mechanisms inferred from dns-predicted phase-wise property variations at $Re_\tau = 1000$. *J. Fluid Mech.*, 743:606–635, 2014.
- J. Ahn, J. H. Lee, S. J. Jang, and H. J. Sung. Direct numerical simulations of fully developed turbulent pipe flows for $Re_\tau = 180$, 544 and 934. *Int. J. Heat Fluid Fl.*, 44:222–228, 2013.
- R. Akhavan, R. D. Kamm, and A. H. Shapiro. An investigation of transition to turbulence in bounded oscillatory Stokes flows. Part 2. Numerical simulation. *J. Fluid Mech.*, 225:423–444, 1991.

- R. Akhavan, W. Jung, and N. Mangiavacchi. Control of wall turbulence by high frequency spanwise oscillations. AIAA Paper 93-3282, 1993.
- T. Albrecht, T. Weier, G. Gerbeth, H. Metzkes, and J. Stiller. A method to estimate the planar, instantaneous body force distribution from velocity field measurements. *Phys. of Fluids*, 23(2):021702, 2011.
- F. Auteri, A. Baron, M. Belan, G. Campanardi, and M. Quadrio. Experimental assessment of drag reduction by traveling waves in turbulent pipe flow. *Phys. of Fluids*, 22(11):115103, 2010.
- W. J. Baars, K. M. Talluru, N. Hutchins, and I. Marusic. Wavelet analysis of wall turbulence to study large-scale modulation of small scales. *Exp. Fluids*, 56(10):188, 2015.
- H. L. Bai, Y. Zhou, W. G. Zhang, S. J. Xu, Y. Wang, and R. A. Antonia. Active control of a turbulent boundary layer based on local surface perturbation. *J. Fluid Mech.*, 750:316–354, 2014.
- S. C. C. Bailey and A. J. Smits. Experimental investigation of the structure of large- and very-large-scale motions in turbulent pipe flow. *J. Fluid Mech.*, 651:339–356, 2010.
- S. C. C. Bailey, M. Hultmark, A. J. Smits, and M. P. Schultz. Azimuthal structure of turbulence in high reynolds number pipe flow. *J. Fluid Mech.*, 615:121–138, 2008.
- B. J. Balakumar and R. J. Adrian. Large- and very-large-scale motions in channel and boundary-layer flows. *Philos. T. Roy. Soc. A*, 365:665–681, 2007.
- K. S. Ball, L. Sirovich, and L. R. Keefe. Dynamical eigenfunction decomposition of turbulent channel flow. *Int. J. Numer. Meth. Fl.*, 12:585–604, 1991.
- D. Barkley, B. Song, V. Mukund, G. Lemoult, M. Avila, and B. Hof. The rise of fully turbulent flow. *Nature*, 526(7574):550–U191, 2015.
- A. Baron and M. Quadrio. Turbulent drag reduction by spanwise wall oscillation. *Appl. Sci. Res.*, 55:311–326, 1996.
- M. Belan and M. Quadrio. A perturbative model for predicting the high-Reynolds-number behaviour of the streamwise travelling waves technique in turbulent drag reduction. *J. Appl. Math. Mech.*, 93(12):944–962, 2013.

- B. A. Belson, R. E. Hanson, D. Palmeiro, P. Lavoie, K. Meidell, and C. W. Rowley. Comparison of plasma actuators in simulations and experiments for control of bypass transition. In *45th AIAA Aerospace Sciences Meeting, Nashville, Tennessee, USA*, AIAA Paper 2012-1141, 2012.
- N. Benard, A. Debien, and E. Moreau. Time-dependent volume force produced by a non-thermal plasma actuator from experimental velocity field. *J. Phys. D Appl. Phys.*, 46(24):245201, 2013.
- T. W. Berger, J. Kim, C. Lee, and J. Lim. Turbulent boundary layer control utilizing the Lorentz force. *Phys. of Fluids*, 12(3):631–649, 2000.
- G. Berkooz, P. Holmes, and J. L. Lumley. The proper orthogonal decomposition in the analysis of turbulent flows. *Annu. Rev. Fluid Mech.*, 25:539–575, 1993.
- M. Bernardini and S. Pirozzoli. Inner/outer layer interactions in turbulent boundary layers: A refined measure for the large-scale amplitude modulation mechanism. *Phys. of Fluids*, 23(6):061701, 2011.
- M. Bernardini, S. Pirozzoli, and P. Orlandi. Velocity statistics in turbulent channel flow up to $Re_\tau = 4000$. *J. Fluid Mech.*, 742:171–191, 2014.
- J. Bird, M. Santer, and J. F. Morrison. In-plane forcing of a turbulent boundary layer, through the actuation of a compliant structure. In *European Drag Reduction and Flow Control Meeting*, 23-26 March, Cambridge, U.K., 2015.
- R. F. Blackwelder and H. Eckelmann. Streamwise vortices associated with the bursting phenomenon. *J. Fluid Mech.*, 94(part 3):577–594, 1979.
- O. Blesbois, S. I. Chernyshenko, E. Toubert, and M. A. Leschziner. Pattern prediction by linear analysis of turbulent flow with drag reduction by wall oscillation. *J. Fluid Mech.*, 724:607–641, 2013.
- J. P. Boeuf and L. C. Pitchford. Electrohydrodynamic force and aerodynamic flow acceleration in surface dielectric barrier discharge. *J. Appl. Phys.*, 97(10):103307, 2005.
- D. G. Bogard and W. G. Tiederman. Burst detection with single-point velocity measurements. *J. Fluid Mech.*, 162:389–413, 1986.
- D. G. Bogard, K. S. Ball, and E. Wassen. Drag reduction for turbulent boundary layer flows using an oscillating wall. Report No. TTCRL 00-2, The University of Texas at Austin, 2000.

- P. Bradshaw and N. Pontikos. Measurements in the turbulent boundary layer of an ‘infinite’ swept wing. *J. Fluid Mech.*, 159:105–130, 1985.
- D. M. Bushnell. Aircraft drag reduction – a review. *J. Aerospace Engineering*, 217:1–18, 2003.
- D Caruana. Plasma for aerodynamic control. *Plasma Phys. Contr. F.*, 52:124045, 2010.
- H. Choi and P. Moin. Effects of the computational time step on numerical solutions of turbulent flow. *J. Comput. Phys.*, 113(1):1–4, 1994.
- H. Choi, P. Moin, and J. Kim. Direct numerical simulation of turbulent flow over riblets. *J. Fluid Mech.*, 255:503–539, 1993.
- J. I. Choi, C. X. Xu, and H. J. Sung. Drag reduction by spanwise wall oscillation in wall-bounded turbulent flows. *AIAA J.*, 40(5):842–850, 2002.
- K.-S. Choi. Near-wall structure of turbulent boundary layer with spanwise-wall oscillation. *Phys. of Fluids*, 14(7):2530–2542, 2002.
- K.-S. Choi and B. R. Clayton. The mechanism of turbulent drag reduction with wall oscillation. *Int. J. Heat Fluid Fl.*, 22(1):1–9, 2001.
- K.-S. Choi and M. Graham. Drag reduction of turbulent pipe flows by circular-wall oscillation. *J. Comput. Phys.*, 10(1):7–9, 1998.
- K.-S. Choi, J.-R. DeBisschop, and B. R. Clayton. Turbulent boundary-layer control by means of spanwise-wall oscillation. *AIAA J.*, 36(7):1157–1163, 1998.
- K.-S. Choi, T. Jukes, and R. Whalley. Turbulent boundary-layer control with plasma actuators. *Philos. T. Roy. Soc. A*, 369:1443–1458, 2011.
- Y. M. Chung and T. Talha. Effectiveness of active flow control for turbulent skin friction drag reduction. *Phys. of Fluids*, 23(2):025102, 2011.
- A. Cimarelli, B. Frohnapfel, Y. Hasegawa, Angelis E. D., and M. Quadrio. Prediction of turbulence control for arbitrary periodic spanwise wall movement. *Phys. of Fluids*, 25(7):075102, 2013.
- G. N. Coleman, J. Kim, and A. T. Le. A numerical study of three-dimensional wall-bounded flows. *Int. J. Heat Fluid Fl.*, 17(3):333–342, 1996.

- G. N. Coleman, J. Kim, and P. R. Spalart. A numerical study of strained three-dimensional wall-bounded turbulence. *J. Fluid Mech.*, 416:75–116, 2000.
- D. Coles. The law of the wake in the turbulent boundary layer. *J. Fluid Mech.*, 1:191–226, 1956.
- T. C. Corke, C. L. Enloe, and S. P. Wilkinson. Dielectric barrier discharge plasma actuators for flow control. *Annu. Rev. Fluid Mech.*, 42:505–529, 2010.
- M. de Giovanetti, Y. Hwang, and H. Choi. Skin-friction generation by attached eddies in turbulent channel flow. to appear. *J. Fluid Mech.*
- R. B. Dean. Reynolds number dependence of skin friction and other bulk flow variables in two-dimensional rectangular duct flow. *J. Fluids Eng. ASME*, 100(2):215–223, 1978.
- A. Debien, N. Benard, and E. Moreau. Streamer inhibition for improving force and electric wind produced by DBD actuators. *J. Phys. D Appl. Phys.*, 45(21):215201, 2012.
- S. Deck, N. Renard, R. Laraufie, and P.-É Weiss. Large-scale contribution to mean wall shear stress in high-Reynolds-number flat-plate boundary layers up to $Re_\theta = 13650$. *J. Fluid Mech.*, 743:202–248, 2014.
- D. B. DeGraaff and J. K. Eaton. Reynolds-number scaling of the flat-plate turbulent boundary layer. *J. Fluid Mech.*, 422:319–346, 2000.
- J. C. del Álamo and J. Jiménez. Spectra of the very large anisotropic scales in turbulent channels. *Phys. of Fluids*, 15(6):L41–L44, 2003.
- J. C. del Álamo and J. Jiménez. Estimation of turbulent convection velocities and corrections to Taylor’s approximation. *J. Fluid Mech.*, 640:5–26, 2009.
- J. C. del Álamo, J. Jiménez, P. Zandonade, and R. D. Moser. Self-similar vortex clusters in the turbulent logarithmic region. *J. Fluid Mech.*, 561:329–358, 2006.
- B.-Q. Deng, C.-X. Xu, W.-X. Huang, and G.-X. Cui. Strengthened opposition control for skin-friction reduction in wall-bounded turbulent flows. *J. Turbul.*, 15(2):122–143, 2014.
- B.-Q. Deng, C.-X. Xu, W.-X. Huang, and G.-X. Cui. Influence of large-scale motions on effectiveness of active drag-reduction control in turbulent channel flow at $Re_\tau = 1000$. In *Turbulence and Shear Flow Phenomena -9*, pages 7A–5, 30 June - 3 July, Melbourne, Australia, 2015.

- M. R. Dhanak and C. Si. On reduction of turbulent wall friction through spanwise wall oscillations. *J. Fluid Mech.*, 383:175–195, 1999.
- G. M. Di Cicca, G. Iuso, P. G. Spazzini, and M. Onorato. Particle image velocimetry investigation of a turbulent boundary layer manipulated by spanwise wall oscillations. *J. Fluid Mech.*, 467:41–56, 2002.
- P. C. Dörr and M. J. Kloker. Numerical investigation of plasma-actuator force-term estimations from flow experiments. *J. Phys. D Appl. Phys.*, 48(39):395203, 2015.
- Y. Du and G. E. Karniadakis. Suppressing wall turbulence by means of a transverse traveling wave. *Science*, 288:1230–1234, 2000.
- Y. Du, V. Symeonidis, and G. E. Karniadakis. Drag reduction in wall-bounded turbulence via a transverse travelling wave. *J. Fluid Mech.*, 457:1–34, 2002.
- A. Dugdaleby, K. S. Ball, and M. R. Paul. The effect of spanwise wall oscillation on turbulent pipe flow structures resulting in drag reduction. *Phys. of Fluids*, 19(12):125107, 2007.
- J. K. Dukowicz and A. S. Dvinsky. Approximate factorization as a high order splitting for the implicit incompressible flow equations. *J. Comput. Phys.*, 102(2):336–347, 1992.
- C. A. Duque-Daza, M. F. Baig, D. A. Lockerby, S. I. Chernyshenko, and C. Davies. Modelling turbulent skin-friction control using linearized Navier-Stokes equations. *J. Fluid Mech.*, 702:403–414, 2012.
- R. Durscher and S. Roy. Evaluation of thrust measurement techniques for dielectric barrier discharge actuators. *Exp. Fluids*, 53(4):1165–1176, 2012.
- J. K. Eaton. Effects of mean flow three dimensionality on turbulent boundary-layer structure. *AIAA J.*, 33(11):2020–2025, 1995.
- D. Elam. *A direct numerical simulation of dielectric barrier discharge (DBD) plasma actuators for turbulent skin-friction control*. PhD thesis, School of Engineering, University of Warwick, UK, June 2012.
- T. Endo, N. Kasagi, and Y. Suzuki. Feedback control of wall turbulence with wall deformation. *Int. J. Heat Fluid Fl.*, 21(5):568–575, 2000.
- O. Flores and J. Jiménez. Hierarchy of minimal flow units in the logarithmic layer. *Phys. of Fluids*, 22(7):071704, 2010.

- B. Frohnapfel, Y. Hasegawa, and M. Quadrio. Money versus time: evaluation of flow control in terms of energy consumption and convenience. *J. Fluid Mech.*, 700:406–418, 2012.
- K. Fukagata and N. Kasagi. Highly energy-conservation finite difference method for the cylindrical coordinate system. *J. Comput. Phys.*, 181(2):478–498, 2002.
- K. Fukagata, K. Iwamoto, and N. Kasagi. Contribution of Reynolds stress distribution to the skin friction in wall-bounded flows. *Phys. of Fluids*, 14(11):L73–L76, 2002.
- K. Fukagata, N. Kasagi, and P. Koumoutsakos. A theoretical prediction of friction drag reduction in turbulent flow by superhydrophobic surfaces. *Phys. of Fluids*, 18(5):051703, 2006.
- K. Fukagata, M. Kobayashi, and N. Kasagi. On the friction drag reduction effect by a control a large-scale turbulent structures. *J. Fluid Sci. Tech.*, 5(3):574–584, 2010.
- I. Galionis and P. Hall. On the stabilization of the most amplified Görtler vortex on a concave surface by spanwise oscillations. *J. Fluid Mech.*, 527:265–283, 2005.
- B. Ganapathisubramani, N. Hutchins, J. P. Monty, D. Chung, and I. Marusic. Amplitude and frequency modulation in wall turbulence. *J. Fluid Mech.*, 712:61–91, 2012.
- R. García-Mayoral and J. Jiménez. Hydrodynamics stability and breakdown of the viscous regime over riblets. *J. Fluid Mech.*, 678:317–347, 2011a.
- R. García-Mayoral and J. Jiménez. Drag reduction by riblets. *Philos. T. Roy. Soc. A*, 369:1412–1427, 2011b.
- D. Gatti, M. Quadrio, C. Tropea, and B. Frohnapfel. Effectiveness of spanwise forcing for turbulent drag reduction at higher Re. In *European Turbulence Conference 14*, 2013.
- D. Gatti, A. Güttler, B. Frohnapfel, and C. Tropea. Experimental assessment of spanwise-oscillating dielectric electroactive surfaces for turbulent drag reduction in an air channel flow. *Exp. Fluids*, 56(5):110, 2015a.
- D. Gatti, M. Quadrio, and B. Frohnapfel. Reynolds number effect on turbulent drag reduction. In *European Turbulence Conference 15*, 25-28 August, Delft, The Netherlands, 2015b.

- M. W. Ge, C. X. Xu, and G. X. Cui. Detection of near-wall streamwise vortices by measurable information at wall. In *European Turbulence Conference 13*, 2011.
- K. Gouder, M. Potter, and J. F. Morrison. Turbulent friction drag reduction using electroactive polymer and electromagnetically driven surfaces. *Exp. Fluids*, 54(1):1441, 2013.
- M. D. Graham. Drag reduction and the dynamics of turbulence in simple and complex fluids. *Phys. of Fluids*, 26(10):101301, 2014.
- M. Guala, S. E. Hommema, and R. J. Adrian. Large-scale and very-large-scale motions in turbulent pipe flow. *J. Fluid Mech.*, 554:521–542, 2006.
- M. Guala, M. Metzger, and B. J. McKeon. Interactions within the turbulent boundary layer at high Reynolds number. *J. Fluid Mech.*, 666:573–604, 2011.
- J. M. Hamilton, J. Kim, and F. Waleffe. Regeneration mechanisms of near-wall turbulence structures. *J. Fluid Mech.*, 287:317–348, 1995.
- R. A. Handler, E. Levich, and L. Sirovich. Drag reduction in turbulent channel flow by phase randomization. *Phys. of Fluids*, 686(5):686–694, 1993.
- M. R. Head and P. Bandyopadhyay. New aspects of turbulent boundary-layer structure. *J. Fluid Mech.*, 107:297–338, 1981.
- A. Holstad, H. I. Andersson, and B. Pettersen. Turbulence in a three-dimensional wall-bounded shear flow. *Int. J. Numer. Meth. Fl.*, 62:875–905, 2010.
- A. Holstad, H. I. Andersson, and B. Pettersen. Turbulence in a skewed three-dimensional wall-bounded shear flow: effect of mean vorticity on structure modification. *Int. J. Numer. Meth. Fl.*, 69:1299–1325, 2012.
- S. Hoyas and J. Jiménez. Scaling of the velocity fluctuations in turbulent channels up to $Re_\tau = 2003$. *Phys. of Fluids*, 18(1):011702, 2006.
- L. Huang, B. Fan, and G. Dong. Turbulent drag reduction via a transverse wave travelling along streamwise direction induced by Lorentz force. *Phys. of Fluids*, 22(1):015103, 2010.
- L. Huang, K. Choi, B. Fan, and Y. Chen. Drag reduction in turbulent channel flow using bidirectional wavy Lorentz force. *Sci. China Phy. Mech. Astron.*, 57(6):1–8, 2014.

- E. Hurst. *A numerical study of turbulent drag reduction using streamwise travelling waves of spanwise wall velocity*. PhD thesis, School of Engineering, University of Warwick, UK, June 2013.
- E. Hurst. *A numerical study of turbulent drag reduction using streamwise travelling waves of spanwise wall velocity*. PhD thesis, School of Engineering, University of Warwick, UK, 2014.
- E. Hurst, Q. Yang, and Y. M. Chung. The effect of Reynolds number on turbulent drag reduction by streamwise travelling waves. *J. Fluid Mech.*, 759:28–55, 2014.
- N. Hutchins and K.-S. Choi. Experimental investigation of turbulence suppression by the imposition of a large-scale vortical control flow. In *15th AIAA Computational Fluid Dynamics Conference, Anaheim, CA, USA*, AIAA Paper 2001-2775, 2001.
- N. Hutchins and I. Marusic. Large-scale influences in near-wall turbulence. *Philos. T. Roy. Soc. A*, 365:647–664, 2007a.
- N. Hutchins and I. Marusic. Evidence of very long meandering features in the logarithmic region of turbulent boundary layers. *J. Fluid Mech.*, 579:1–28, 2007b.
- Y. Hwang. Near-wall turbulent fluctuations in the absence of wide outer motions. *J. Fluid Mech.*, 723:264–288, 2013.
- Y. Hwang. Statistical structure of self-sustaining attached eddies in turbulent channel flow. *J. Fluid Mech.*, 767:254–289, 2015.
- Y. Hwang and C. Cossu. Self-sustained process at large scales in turbulent channel flow. *Phys. Rev. Lett.*, 105(4), 2010.
- Y. Hwang and C. Cossu. Self-sustained processes in the logarithmic layer of turbulent channel flows. *Phys. of Fluids*, 23(6), 2011.
- Y. Hwang, A. P. Willis, and C. Cossu. Invariant solutions of minimal large-scale structures in turbulent channel flow for Re_τ up to 1000. *J. Fluid Mech.*, 802:R1, 2016.
- I. H. Ibrahim and M. Skote. Simulating plasma actuators in a channel flow configuration by utilizing the modified Suzen-Huang model. *Comput. Fluids*, 99:144–155, 2014.
- M. Itoh, S. Tamano, K. Yokota, and S. Taniguchi. Drag reduction in a turbulent boundary layer on a flexible sheet undergoing a spanwise traveling wave motion. *J. Turbul.*, 7(27):1–17, 2006.

- G. Iuso, G. M. Di Cicca, and M. Onorato. Velocity streak structure modifications induced by flow manipulation. *Phys. of Fluids*, 15(9):2602, 2003.
- K. Iwamoto, Y. Suzuki, and N. Kasagi. Reynolds number effect on wall turbulence: Toward effective feedback control. *Int. J. Heat Fluid Fl.*, 23(5):678–689, 2002.
- K. Iwamoto, N. Kasagi, and Y. Suzuki. Dynamical roles of large-scale structures in turbulent channel flow. In *Computational Mechanics, WCCM VI in conjunction with APCOM'04, Sept. 5-10, 2004, Beijing, China*, 2004.
- K. Iwamoto, K. Fukagata, N. Kasagi, and Y. Suzuki. Friction drag reduction achievable by near-wall turbulence manipulation at high Reynolds numbers. *Phys. of Fluids*, 17(1):011702, 2005.
- I. Jacobi and B. J. McKeon. Phase relationship between large and small scales in the turbulent boundary layer. *Exp. Fluids*, 54(3):1481, 2013.
- B. Jayaraman, S. Thakur, and W. Whyy. Modeling of dielectric barrier discharge and resulting fluid dynamics. In *44th AIAA Aerospace Sciences Meeting and Exhibit, Reno, NV, USA*, AIAA Paper 2006-686, 2006.
- T. O. Jelly, S. Y. Jung, and T. A. Zaki. Turbulence and skin friction modification in channel flow with streamwise-aligned superhydrophobic surface texture. *Phys. of Fluids*, 26(9):095102, 2014.
- S. Jeon, H. Choi, J. Y. Yoo, and P. Moin. Space-time characteristics of the wall shear-stress fluctuations in a low-reynolds-number channel flow. *Phys. of Fluids*, 11(10):3084–3094, 1999.
- J. Jeong and F. Hussain. On the identification of a vortex. *J. Fluid Mech.*, 285:69–94, 1995.
- J. Jeong, F. Hussain, W. Schoppa, and J. Kim. Coherent structures near the wall in a turbulent channel flow. *J. Fluid Mech.*, 332:185–214, 1997.
- J. Jiménez. The largest scales of turbulent flows. Annual research briefs, CTR, Stanford University, 1998.
- J. Jiménez. Cascades in wall-bounded turbulence. *Annu. Rev. Fluid Mech.*, 44:27–45, 2012.
- J. Jiménez and P. Moin. The minimal flow unit in near-wall turbulence. *J. Fluid Mech.*, 225:213–240, 1991.

- J. Jiménez and A. Pinelli. The autonomous cycle of near-wall turbulence. *J. Fluid Mech.*, 389:335–359, 1999.
- T. N. Jukes and K.-S. Choi. Dielectric-barrier-discharge vortex generators: characterisation and optimisation for flow separation control. *Exp. Fluids*, 52:329–345, 2012.
- T. N. Jukes and K.-S. Choi. On the formation of streamwise vortices by plasma vortex generators. *J. Fluid Mech.*, 733:370–393, 2013.
- T. N. Jukes, K.-S. Choi, G. A. Johnson, and S. J. Scott. Characterization of surface plasma-induced wall flows through and temperature measurements. *AIAA J.*, 44(4):764–771, 2006a.
- T. N. Jukes, K.-S. Choi, G. A. Johnson, and S. J. Scott. Turbulent drag reduction by surface plasma through spanwise flow oscillation. In *3rd AIAA Flow control conference, San Francisco, CA, USA*, AIAA Paper 2006-3693, 2006b.
- T. N. Jukes, K.-S. Choi, T. Segawa, and H. Yoshida. Jet flow induced by a surface plasma actuator. *J. Syst. Contr. Eng.*, 222(5):347–356, 2008.
- T. N. Jukes, T. Segawa, and H. Furutani. Flow control on a NACA 4418 using dielectric-barrier-discharge vortex generators. *AIAA J.*, 51(2):452–464, 2012.
- S. Y. Jung and Y. M. Chung. Large-eddy simulations of accelerated turbulent flow in a circular pipe. *Int. J. Heat Fluid Fl.*, 33(1):1–8, 2012.
- S. Y. Jung and H. J. Sung. Characterization of the three-dimensional turbulent boundary layer in a concentric annulus with a rotating inner cylinder. *Phys. of Fluids*, 18(11):115102, 2006.
- W. J. Jung, N. Mangiavacchi, and R. Akhavan. Suppression of turbulence in wall-bounded flows by high-frequency spanwise oscillations. *Phys. Fluids A*, 4(8):1605–1607, 1992.
- Y. Kametani, K. Fukagata, R. Örlü, and P. Schlatter. Effect of uniform blowing/suction in a turbulent boundary layer at moderate Reynolds number. *Int. J. Heat Fluid Fl.*, 55:132–142, 2015.
- H. S. Kang, H. Choi, and Y. Y. Jung. On the modification of the near wall coherent structure in a three-dimensional turbulent boundary layer on a free rotating disk. *Phys. of Fluids*, 10(9):2315–2322, 1998.

- G. E. Karniadakis and K.-S. Choi. Mechanisms on transverse motions in turbulent wall flows. *Annu. Rev. Fluid Mech.*, 35:45–62, 2003.
- J. Kim and F. Hussain. Propagation velocity of perturbations in turbulent channel flow. *Phys. of Fluids*, 5:695–706, 1993.
- J. Kim and P. Moin. Application of a fractional-step method to incompressible Navier-Stokes equations. *J. Comput. Phys.*, 59(2):308–323, 1985.
- J. Kim, P. Moin, and R. Moser. Turbulence statistics in fully developed channel flow at low Reynolds number. *J. Fluid Mech.*, 177:133–166, 1987.
- K. Kim, S.-J. Baek, and H. J. Sung. An implicit velocity decoupling procedure for the incompressible Navier-Stokes equations. *Int. J. Numer. Meth. Fl.*, 38(2):125–138, 2002.
- K. C. Kim and R. J. Adrian. Very large-scale motion in the outer layer. *Phys. of Fluids*, 11(2):417422, 1999.
- S. J. Kline, W. C. Reynolds, F. A. Schraub, and P. W. Runstadler. The structure of turbulent boundary layers. *J. Fluid Mech.*, 30(4):741–773, 1967.
- S. Klumpp, M. Meinke, and W. Schröder. Friction drag variation via spanwise transversal surface waves. *Flow Turbul. Combust.*, 87:33–53, 2011.
- S. R. Koh, P. Meysonnat, M. Meinke, and W. Schröder. Drag reduction via spanwise transversal surface waves at high Reynolds numbers. *Flow Turbul. Combust.*, 95(1):169–190, 2015.
- M. Kotsonis, S. Ghaemi, R. Giepmans, and L. Veldhuis. Experimental study on the body force field of dielectric barrier discharge actuators. In *41st AIAA Plasmadynamics and Lasers Conference, Chicago, Illinois, USA*, AIAA Paper 2010-4630, 2010.
- M. Kotsonis, S. Ghaemi, L. Veldhuis, and F. Scarano. Measurement of the body force field of plasma actuators. *J. Phys. D Appl. Phys.*, 44(4):045204, 2011.
- A. G. Kravchenko, H. Choi, and P. Moin. On the relation of near-wall streamwise vortices to wall skin friction in turbulent boundary layers. *Phys. Fluids A*, 5(12):3307–3309, 1993.
- J. Kriegseis, C. Schwarz, C. Tropea, and S. Grundmann. Velocity-information-based force-term estimation of dielectric-barrier discharge plasma actuators. *J. Phys. D Appl. Phys.*, 46(5):055202, 2013.

- F. Laadhari, L. Skandaji, and R. Morel. Turbulence reduction in a boundary layer by local spanwise oscillating surface. *Phys. of Fluids*, 6(10):3218–3220, 1994.
- S. Lardeau and M. A. Leschziner. The streamwise drag-reduction response of a boundary layer subjected to a sudden imposition of transverse oscillatory wall motion. *Phys. of Fluids*, 25(7):075109, 2013.
- A. T. Le, G. N. Coleman, and J. Kim. Near-wall turbulence structures in three-dimensional boundary layers. *Int. J. Heat Fluid Fl.*, 21(5):480–488, 2000.
- C. Lee and J. Kim. Control of the viscous sublayer for drag reduction. *Phys. of Fluids*, 14(7):2523–2529, 2002.
- J. Lee, J. H. Lee, J. I. Choi, and H. J. Sung. Spatial organization of large- and very-large-scale motions in a turbulent channel flow. *J. Fluid Mech.*, 749:818–840, 2014.
- J. Lee, T. O. Jelly, and T. A. Zaki. Effect of Reynolds number on turbulent drag reduction by superhydrophobic textures. *Flow Turbul. Combust.*, 95(2):277–300, 2015.
- J. H. Lee and H. J. Sung. Reponse of a spatially developing turbulent boundary layer to a spanwise oscillating electromagnetic force. *J. Turbul.*, 6(39):1–15, 2005.
- J. H. Lee and H. J. Sung. Comparison of very-large-scale motions of turbulent pipe and boundary layer simulations. *Phys. of Fluids*, 25(4):045103, 2013.
- S. B. Lee, W. Kang, and H. J. Sung. Organized self-sustained oscillations of turbulent flows over an open cavity. *AIAA J.*, 46(11):2848–2856, 2008.
- M. Leschziner, H. Choi, and K.-S. Choi. Flow control approaches in aerodynamics: progress and prospects. *Philos. T. Roy. Soc. A*, 369(1940):1349–1351, 2011.
- N. Li and S. Laizet. 2DECOMP and FFT - a highly scalable 2d decomposition library and FFT interface. In *Cray User Group 2010 Conference*, 2010.
- Z. Li, B. Hu, S. Lan, J. Zhang, and J. Huang. Control of turbulent channel flow using a plasma-based body force. *Comput. Fluids*, 119:26–36, 2015.
- B. K. Lieu, R. Moarref, and M. R. Jovanović. Controlling the onset of turbulence by streamwise travelling waves. Part 2. Direct numerical simulation. *J. Fluid Mech.*, 663:100–119, 2010.

- A. V. Likhanskii, M. N. Shneider, S. O. Macheret, and R. B. Miles. Modeling of dielectric barrier discharge plasma actuator in air. *J. Appl. Phys.*, 103(5):053305, 2008.
- H. S. Littel and J. K. Eaton. Turbulence characteristics of the boundary layer on a rotating disk. *J. Fluid Mech.*, 266:175–207, 1994.
- S. S. Lu and W. W. Willmarth. Measurements of the structure of the reynolds stress in a turbulent boundary layer. *J. Fluid Mech.*, 60:481–511, 1973.
- I. Maden, R. Maduta, J. Kriegseis, S. Jakirlić, C. Schwarz, S. Grundmann, and C. Tropea. Experimental and computational study of the flow induced by a plasma actuator. *Int. J. Heat Fluid Fl.*, 41:80–89, 2013.
- H. Mamori and K. Fukagata. Drag reduction by streamwise traveling wave-like Lorenz force in channel flow. In *European Turbulence Conference 13*, 2011.
- H. Mamori, K. Iwamoto, and A. Murata. Effect of the parameters of traveling waves created by blowing and suction on the relaminarization phenomena in fully developed turbulent channel flow. *Phys. of Fluids*, 26(1):015101, 2014.
- I. Marusic, R. Mathis, and N. Hutchins. Predictive model for wall-bounded turbulent flow. *Science*, 329:193–196, 2010.
- M. Marzali Bermudez, R. Sosa, D. Grondona, A. Márquez, H. Kelly, and G. Artana. Study of a pseudo-empirical model approach to characterize plasma actuators. *Journal of Physics: Conference Series*, 296:012023, 2011.
- R. Mathis, N. Hutchins, and I. Marusic. Large-scale amplitude modulation of the small-scale structures in turbulent boundary layer. *J. Fluid Mech.*, 628:311–337, 2009.
- R. Mathis, N. Hutchins, and I. Marusic. A predictive inner-outer model for stream-wise turbulence statistics in wall-bounded flows. *J. Fluid Mech.*, 681:537–566, 2011a.
- R. Mathis, I. Marusic, N. Hutchins, and K. R. Sreenivasan. The relationship between the velocity skewness and the amplitude modulation of the small scale by the large scale in turbulent boundary layers. *Phys. of Fluids*, 23(12):121702, 2011b.
- R. Mathis, I. Marusic, S. I. Chernyshenko, and N. Hutchins. Estimating wall-shear-stress fluctuations given an outer region input. *J. Fluid Mech.*, 715:163–180, 2013.

- C. D. Meinhart and R. J. Adrian. On the existence of uniform momentum zones in a turbulent boundary layer. *Phys. of Fluids*, 694(7):694–696, 1995.
- B. E. Mertz and T. C. Corke. Time-dependent dielectric barrier discharge plasma actuator modeling. In *47th AIAA Aerospace Sciences Meeting Including the New Horizons Forum and Aerospace Exposition, Orlando, Florida, USA*, AIAA Paper 2009-1083, 2009.
- B. E. Mertz and T. C. Corke. Single-dielectric barrier discharge plasma actuator modelling and validation. *J. Fluid Mech.*, 669:557–583, 2011.
- T. Min, S. M. Kang, J. L. Speyer, and J. Kim. Sustained sub-laminar drag in a fully developed channel flow. *J. Fluid Mech.*, 558:309–318, 2006.
- M. Mishra and M. Skote. Drag reduction in turbulent boundary layers with half wave wall oscillations. *Math. Probl. Eng.*, page 253249, 2015.
- Y. Mito and N. Kasagi. DNS study of turbulence modification with streamwise-uniform sinusoidal wall-oscillation. *Int. J. Heat Fluid Fl.*, 19(5):470–481, 1998.
- Y. Mizuno and J. Jiménez. Wall turbulence without walls. *J. Fluid Mech.*, 723:429–455, 2013.
- R. Moarref and M. R. Jovanović. Model-based design of transverse wall oscillations for turbulent drag reduction. *J. Fluid Mech.*, 707:205–240, 2012.
- P. Moin and R. D. Moser. Characteristic-eddy decomposition of turbulence in a channel. *J. Fluid Mech.*, 200:471–509, 1989.
- P. Moin, T.-H. Shih, D. M. Driver, and N. N. Mansour. Direct numerical simulation of a three dimensional turbulent boundary layer. *Phys. of Fluids*, 187:61–98, 1989.
- P. Moin, T.-H. Shih, D. M. Driver, and N. N. Mansour. Direct numerical simulation of a three dimensional turbulent boundary layer. *Phys. Fluids A*, 2(10):1846–1853, 1990.
- J. P. Monty, J.A. Stewart, R. C. Williams, and M. S. Chong. Large-scale features in turbulent pipe and channel flows. *J. Fluid Mech.*, 589:147–156, 2007.
- J. P. Monty, N. Hutchins, H. C. H. Ng, I. Marusic, and M. S. Chong. A comparison of turbulent pipe, channel and boundary layer flows. *J. Fluid Mech.*, 632:431–442, 2009.

- E. Moreau. Airflow control by non-thermal plasma actuators. *J. Phys. D Appl. Phys.*, 40(3):605–636, 2007.
- R. Moser, J. Kim, and N. Mansour. Direct numerical simulation of turbulent channel flow up to $Re_\tau = 590$. *Phys. of Fluids*, 11(4):943–945, 1999.
- J. P. Murphy, J. Kriegseis, and P. Lavoie. Scaling of maximum velocity, body force, and power consumption of dielectric barrier discharge plasma actuators via particle image velocimetry. *J. Appl. Phys.*, 113(24):243301, 2013.
- M. Nadeem, J. H. Lee, J. Lee, and H. J. Sung. Turbulent boundary layers over sparsely-spaced rod-roughened walls. *Int. J. Heat Fluid Fl.*, 56:16–27, 2015.
- R. Nakanishi, H. Mamori, and K. Fukagata. Relaminarization of turbulent channel flow using travelling wave-like wall deformation. *Int. J. Heat Fluid Fl.*, 35:152–159, 2012.
- P. S. Negi, M. Mishra, and M. Skote. DNS of a single low-speed streak subject to spanwise wall oscillations. *Flow Turbul. Combust.*, 94(4):795–816, 2015.
- H. Nishida and T. Abe. Numerical analysis of plasma evolution on dielectric barrier discharge plasma actuator. *J. Appl. Phys.*, 110(1):013302, 2011.
- P. Orlandi and J. Jiménez. On the generation of turbulent wall friction. *Phys. of Fluids*, 6(2):634–641, 1994.
- D. M. Orlov and T. C. Corke. Electric circuit model for aerodynamic plasma actuator. In *44th AIAA Aerospace Sciences Meeting and Exhibit, Reno, NV, USA*, AIAA Paper 2006-1206, 2006.
- Örlü and P. Schlatter. On the fluctuating wall-shear stress in zero pressure-gradient turbulent boundary layer flows. *Phys. of Fluids*, 23(2):021704, 2011.
- J. Pang and K.-S. Choi. Turbulent drag reduction by Lorentz force oscillation. *Phys. of Fluids*, 16(5):L35–L38, 2004.
- J. Pang, K.-S. Choi, and A. Aessopos. Control of near-wall turbulence for drag reduction by spanwise oscillating Lorentz force. In *2nd AIAA Flow control conference, Portland, Oregon, USA*, AIAA Paper 2004-2117, 2004.
- R. L. Panton. Overview of the self-sustaining mechanisms of wall turbulence. *Prog. Aerosp. Sci.*, 37:341–383, 2001.

- J. B. Perot. An analysis of the fractional step method. *J. Comput. Phys.*, 108(1): 51–58, 1993.
- S. Pirozzoli, M. Bernardini, and P. Orlandi. Large-scale motions and inner/outer layer interactions in turbulent Couette-Poiseuille flows. *J. Fluid Mech.*, 680:534–563, 2011.
- L. Prandtl. Bericht über untersuchungen zur ausgebildeten turbulenz. *Zeitschrift für angewandte Mathematik und Mechanik*, 5:136–139, 1925.
- G. Pujals, M. García-Villalba, C. Cossu, and S. Depardon. A note on optimal transient growth in turbulent channel flow. *Phys. of Fluids*, 21(1):015109, 2009.
- G. Pujals, C. Cossu, and S. Depardon. Forcing large-scale coherent streaks in a zero-pressure-gradient turbulent boundary layer. *J. Turbul.*, 11(25):1–13, 2010.
- M. Quadrio. Drag reduction in turbulent boundary layers by in-plane wall motion. *Philos. T. Roy. Soc. A*, 369:1428–1442, 2011.
- M. Quadrio and D. Gatti. Skin-friction drag reduction by spanwise forcing: the Reynolds-number effect. In *European Drag Reduction and Flow Control Meeting*, 23-26 March, Cambridge, U.K., 2015.
- M. Quadrio and P. Ricco. Initial response of a turbulent channel flow to spanwise oscillation of the walls. *J. Turbul.*, 4:007, 2003.
- M. Quadrio and P. Ricco. Critical assessment of turbulent drag reduction through spanwise wall oscillations. *J. Fluid Mech.*, 521:251–271, 2004.
- M. Quadrio and P. Ricco. The laminar generalized stokes layer and turbulent drag reduction. *J. Fluid Mech.*, 667:135–157, 2011.
- M. Quadrio and S. Sibilla. Numerical simulation of turbulent flow in a pipe oscillating around its axis. *J. Fluid Mech.*, 424:217–241, 2000.
- M. Quadrio and W. Xie. Turbulent drag reduction by traveling waves of spanwise forcing. In *European Turbulence Conference 15*, 25-28 August, Delft, The Netherlands, 2015.
- M. Quadrio, P. Ricco, and C. Viotti. Streamwise-travelling waves of spanwise wall velocity for turbulent drag reduction. *J. Fluid Mech.*, 627:161–178, 2009.

- O. Reynolds. An experimental investigation of the circumstances which determine whether the motion of water shall be direct or sinuous, and the law of resistance in parallel channels. *Philos. T. Roy. Soc.*, 174:935, 1883.
- P. Ricco. Modification of near-wall turbulence due to spanwise wall oscillations. *J. Turbul.*, 5(1):024, 2004.
- P. Ricco and S. Hahn. Turbulent drag reduction through rotating discs. *J. Fluid Mech.*, 722:267–290, 2013.
- P. Ricco and M. Quadrio. Wall-oscillation conditions for drag reduction in turbulent channel flow. *Int. J. Heat Fluid Fl.*, 29(4):891–902, 2008.
- P. Ricco and S. Wu. On the effects of lateral wall oscillations on a turbulent boundary layer. *Exp. Therm Fluid Sci.*, 29:41–52, 2004.
- P. Ricco, C. Ottonelli, Y. Hasegawa, and M. Quadrio. Changes in turbulent dissipation in a channel flow with oscillating walls. *J. Fluid Mech.*, 700:77–104, 2012.
- S. K. Robinson. Coherent motions in the turbulent boundary layer. *Annu. Rev. Fluid Mech.*, 23:601–639, 1991.
- J. R. Roth. Aerodynamic flow acceleration using piezoelectric and peristaltic electrohydrodynamic effects of a one atmosphere uniform glow discharge plasma. *Phys. Plasmas*, 10(5):2117–2126, 2003.
- J. R. Roth, D. M. Sherman, and S. P. Wilkinson. Electrohydrodynamic flow control with a flow-dishcharge surface plasma. *AIAA J.*, 38(7):1166–1172, 2000.
- S. Satake and N. Kasagi. Turbulence control with wall-adjacent thin layer damping spanwise velocity fluctuations. *Int. J. Heat Fluid Fl.*, 17(3):343–352, 1996.
- P. Schlatter, R. Örlü, C. Chin, and N. Hutchins. Large-scale friction control in turbulent wall flow. In *Turbulence and Shear Flow Phenomena -9*, pages 9A–2, 30 June - 3 July, Melbourne, Australia, 2015.
- H. Schlichting. *Boundary Layer Theory*. New York, McGraw-Hill, 8th edition, 1968.
- W. Schoppa and F. Hussain. A large-scale control strategy for drag reduction in turbulent boundary layers. *Phys. of Fluids*, 10(5):1049–1051, 1998.
- M. Sen, K. Bhaganagar, and V. Juttijudata. Application of proper orthogonal decomposition (POD) to investigate a turbulent boundary layer in a channel with rough walls. *J. Turbul.*, 8(41):1–21, 2007.

- O. Sendstad and P. Moin. The near wall mechanics of three-dimensional turbulent boundary layers. Report TF-57, Thermosciences Division, Department of Mechanical Engineering, Stanford University, USA, 1992.
- W. Shyy, B. Jayaraman, and A. Andersson. Modeling of glow discharge-induced fluid dynamics. *J. Appl. Phys.*, 92(11):6434–6443, 2002.
- L. Sirovich. Turbulence and the dynamics of coherent structures, part I: coherent structures. *Q. Appl. Math.*, 45:561–571, 1987.
- L. Sirovich and S. Karlsson. Turbulent drag reduction by passive mechanisms. *Nature*, 388(6644):753–755, 1997.
- M. Skote. Turbulent boundary layer flow subject to streamwise oscillation of spanwise wall velocity. *Phys. of Fluids*, 23:081703, 2011.
- M. Skote. Temporal and spatial transients in turbulent boundary layer flow over an oscillating wall. *Int. J. Heat Fluid Fl.*, 38:1–12, 2012.
- M. Skote. Comparison between spatial and temporal wall oscillations in turbulent boundary layer flows. *J. Fluid Mech.*, 730:273–294, 2013.
- M. Skote. Scaling of the velocity profile in strongly drag reduced turbulent flows over an oscillating wall. *Int. J. Heat Fluid Fl.*, 50:352–358, 2014.
- M. Skote, M. Mishra, and Y. Wu. Drag reduction of a turbulent boundary layer over an oscillation wall and its variation with Reynolds number. *Int. J. Aerosp. Eng.*, 2015:1–9, 2015.
- S. Solbakken and H. I. Andersson. The generic skin-friction pattern underneath coherent near-wall structures. *Fluid Dyn. Res.*, 34:167–174, 2004.
- Y. B. Suzen, P. G. Huang, J. D. Jacob, and D. E. Ashpis. Numerical simulations of plasma based flow control applications. In *35th AIAA Fluid Dynamics Conference and Exhibit, Toronto, Ontario, Canada*, AIAA Paper 2005-4633, 2005.
- Y. B. Suzen, P. G. Huang, and D. E. Ashpis. Numerical simulations of flow separation control in low-pressure turbines using plasma actuators. In *45th AIAA Aerospace Sciences Meeting and Exhibit, Reno, NV, USA*, AIAA Paper 2007-937, 2007.
- J. D. Swearingen and R. F. Blackwelder. The growth and breakdown of streamwise vortices in the presence of a wall. *J. Theor. Biol.*, 182:255–290, 1987.

- T. Talha. *A numerical investigation of three-dimensional unsteady turbulent channel flow subjected to temporal acceleration*. PhD thesis, School of Engineering, University of Warwick, UK, March 2012.
- K. M. Talluru, R. Baidya, N. Hutchins, and I. Marusic. Amplitude modulation of all three velocity components in turbulent boundary layers. *J. Fluid Mech.*, 746:R1, 2014.
- S. Tamano and M. Itoh. Drag reduction in turbulent boundary layers by spanwise traveling waves with wall deformation. *J. Turbul.*, 13(9):1–26, 2012.
- R. Temam. Remark on the pressure boundary condition for the projection method. *Theor. Comp. Fluid Dyn.*, 3:181–184, 1991.
- S. Toh and T. Itano. Interaction between a large-scale structure and near-wall structures in channel flow. *J. Fluid Mech.*, 524:249–262, 2005.
- N. Tomiyama and K. Fukagata. Direct numerical simulation of drag reduction in a turbulent channel flow using spanwise traveling wave-like wall deformation. *Phys. of Fluids*, 25(10):105115, 2013.
- E. Toubert and M. A. Leschziner. Near-wall streak modification by spanwise oscillatory wall motion and drag-reduction mechanisms. *J. Fluid Mech.*, 693:150–200, 2012.
- A. A. Townsend. Equilibrium layers and wall turbulence. *J. Fluid Mech.*, 11:97–120, 1961.
- A. A. Townsend. *The structure of turbulent shear flow*. Cambridge University Press, 1976.
- S. M. Trujillo, D. G. Bogard, and K. S. Ball. Turbulent boundary layer drag reduction using an oscillating wall. AIAA Paper 97-1870, 1997.
- T. Unfer. An asynchronous framework for the simulation of the plasma/flow interaction. *J. Comput. Phys.*, 236:229–246, 2013.
- T. Unfer and J.-P. Boeuf. Modelling of a nanosecond surface discharge actuator. *J. Phys. D Appl. Phys.*, 42(19):194017, 2009.
- T. Unfer and J.-P. Boeuf. Modeling and comparison of sinusoidal and nanosecond pulsed surface dielectric barrier discharges for flow control. *Plasma Phys. Contr. F.*, 52(12):124019, 2010.

- C. Viotti, M. Quadrio, and P. Luchini. Streamwise oscillation of spanwise velocity at the wall of a channel for turbulent drag reduction. *Phys. of Fluids*, 21(11):115109, 2009.
- I. S. Vodop'yanov, N. V. Nikitin, and S. I. Chernyshenko. Turbulent drag reduction by spanwise oscillations of a ribbed surface. *Fluid Dyn.*, 48(4):461–470, 2013.
- T. Von Kármán. Mechanische ähnlichkeit und turbulenz. *Sonderdrucke aus den Nachrichten von der Gesellschaft der Wissenschaften zu Göttingen: Mathematisch-physische Klasse*, 1930.
- F. Waleffe. Exact coherent structures in channel flow. *J. Fluid Mech.*, 435:93–102, 2001.
- J.-J. Wang, K.-S. Choi, L.-H. Feng, T. N. Jukes, and R. D. Whalley. Recent developments in DBD plasma flow control. *Prog. Aerosp. Sci.*, 62:52–78, 2013.
- R. D. Whalley and K.-S. Choi. Turbulent boundary-layer control with spanwise travelling waves. *Journal of Physics: Conference Series*, 318:022039, 2011.
- R. D. Whalley and K.-S. Choi. The starting vortex in quiescent air induced by dielectric-barrier-discharge plasma. *J. Fluid Mech.*, 703:192–203, 2012.
- R. D. Whalley and K.-S. Choi. Turbulent boundary-layer control with plasma spanwise travelling waves. *Exp. Fluids*, 55:1796, 2014.
- B. Wilke. *Aerodynamische strömungssteuerung mittels dielektrischen barriereentladungs-plasmaaktuatoren*. PhD thesis, Technische Universität Darmstadt, DLR Göttingen, 2009.
- S. P. Wilkinson. Investigation of an oscillating surface plasma for turbulent drag reduction. In *41st AIAA Aerospace Sciences Meeting and Exhibit, Reno, NV, USA*, AIAA Paper 2003-1023, 2003.
- D. J. Wise, C. Alvarenga, and P. Ricco. Spinning out of control: Wall turbulence over rotating discs. *Phys. of Fluids*, 26(12):125107, 2014.
- X. Wu and P. Moin. Direct numerical simulation of turbulence in a nominally zero-pressure-gradient flat-plate boundary layer. *J. Fluid Mech.*, 630:5–41, 2009.
- X. Wu, J. R. Baltzer, and R. J. Adrian. Direct numerical simulation of a $30R$ long turbulent pipe flow at $R^+ = 685$: large- and very-large-scale motions. *J. Fluid Mech.*, 698:235–281, 2012.

- W. Xie and M. Quadrio. Wall turbulence control by spanwise travelling waves. In *European Turbulence Conference 14*, 2013.
- C.X Xu and W.X Huang. Transient response of reynolds stress transport to spanwise wall oscillation in a turbulent channel flow. *Phys. of Fluids*, 17:018101, 2005.
- J. Xu, S. Dong, M. R. Maxey, and G.E. Karniadakis. Turbulent drag reduction by constant near-wall forcing. *J. Fluid Mech.*, 582:79–101, 2007.
- A. Yakeno, Y. Hasegawa, and N. Kasagi. Spatio-temporally periodic control for turbulent friction drag reduction. In *Turbulence and Shear Flow Phenomena -6*, pages 598–602, 22-24 June, Seoul, Korea, 2009.
- A. Yakeno, Y. Hasegawa, and N. Kasagi. Modification of quasi-streamwise vortical structure in a drag-reduced turbulent channel flow with spanwise wall oscillation. *Phys. of Fluids*, 26(8):085109, 2014.
- I. Yudhistira and M. Skote. Direct numerical simulation of a turbulent boundary layer over an oscillating wall. *J. Turbul.*, 12(9):1–17, 2011.
- H. Zhao, J.-Z. Wu, and J.-S. Luo. Turbulent drag reduction by trveling wave of flexible wall. *Fluid Dyn. Res.*, 34:175–198, 2004.
- D. Zhou and K. S. Ball. Turbulent drag reduction by spanwise wall oscillations. *IJE T. A Bas.*, 21(1):85–104, 2008.
- J. Zhou, R. J. Adrian, S. Balachandar, and T. M. Kendall. Mechanisms for generating coherent packets of hairpin vortices in channel flow. *J. Fluid Mech.*, 387:353–396, 1999.